Current-induced spin-orbit torques in ferromagnetic and antiferromagnetic systems

A. Manchon[*]

King Abdullah University of Science and Technology (KAUST),
Physical Science and Engineering Division (PSE), and Computer, Electrical,
and Mathematical Science and Engineering (CEMSE),
Thuwal, 23955-6900, Saudi Arabia

J. Železný

Institute of Physics, Academy of Sciences of the Czech Republic,
162 00 Praha, Czech Republic

I. M. Miron

University of Grenoble Alpes, CNRS, CEA, INAC-SPINTEC, F-38000 Grenoble, France

T. Jungwirth[†]

Institute of Physics, Academy of Sciences of the Czech Republic,
162 00 Praha, Czech Republic
and School of Physics and Astronomy, University of Nottingham,
Nottingham NG7 2RD, United Kingdom

J. Sinova[‡]

Institut für Physik, Johannes Gutenberg Universität Mainz, 55128 Mainz Germany
and Institute of Physics, Academy of Sciences of the Czech Republic,
162 00 Praha, Czech Republic

A. Thiaville[§]

Laboratoire de Physique des Solides, Univ. Paris-Sud,
CNRS UMR 8502-91405 Orsay Cedex, France

K. Garello

IMEC, Kapeldreef 75, 3001 Leuven, Belgium

P. Gambardella[‖]

ETH Zürich, Hönggerbergring 64, CH-8093 Zürich, Switzerland

(published 9 September 2019)

Spin-orbit coupling in inversion-asymmetric magnetic crystals and structures has emerged as a powerful tool to generate complex magnetic textures, interconvert charge and spin under applied current, and control magnetization dynamics. Current-induced spin-orbit torques mediate the transfer of angular momentum from the lattice to the spin system, leading to sustained magnetic oscillations or switching of ferromagnetic as well as antiferromagnetic structures. The manipulation of magnetic order, domain walls, and skyrmions by spin-orbit torques provides evidence of the microscopic interactions between charge and spin in a variety of materials and opens novel strategies to design spintronic devices with potentially high impact in data storage, nonvolatile logic, and magnonic applications. This paper reviews recent progress in the field of spin orbitronics, focusing on theoretical models, material properties, and experimental results obtained on bulk noncentrosymmetric conductors

---

[*]aurelien.manchon@kaust.edu.sa
[†]jungw@fzu.cz
[‡]sinova@uni-mainz.de
[§]andre.thiaville@u-psud.fr
[‖]pietro.gambardella@mat.ethz.ch

and multilayer heterostructures, including metals, semiconductors, and topological insulator systems. Relevant aspects for improving the understanding and optimizing the efficiency of nonequilibrium spin-orbit phenomena in future nanoscale devices are also discussed.

CONTENTS

I. INTRODUCTION

The interplay between spin and orbital degrees of freedom in condensed matter physics has been intensively studied for more than a century, starting from the seminal experiments of Barnett (1915) and Einstein and de Haas (1915). At the time of these pioneering experiments on the transfer between magnetic and lattice angular momenta, the electron's spin was unknown and the phenomena could be explained only on the level of macroscopic angular momentum conservation principles. A microscopic insight into spin-orbit coupling emerged later from the relativistic quantum-mechanical Dirac equation. In magnetic materials, the relativistic spin-orbit coupling is now understood to play a fundamental role in a number of phenomena, including magnetocrystalline anisotropy, magnetization precession damping (Stöhr and Siegmann, 2006), anomalous Hall effect (AHE) (Nagaosa *et al.*, 2010), anisotropic magnetoresistance (AMR) (McGuire and Potter, 1975), and spin relaxation (Dyakonov, 2008). In nonmagnetic semiconductors, the correlation between nonequilibrium charge and spin currents has been extensively studied since the 1970s (D'yakonov and Perel', 1971; Ivchenko and Pikus, 1978; Aronov and Lyanda-Geller, 1989), allowing for the manipulation of spin states using both electrical and optical techniques

(Rashba and Sheka, 1991; Ganichev *et al.*, 2002; Kato and Awschalom, 2008). In the past 15 years, the interest in materials with strong spin-orbit coupling has substantially intensified. Heterostructures, surfaces, and interfaces displaying unprecedentedly large spin-momentum locking have been recognized as powerful platforms for investigating the relativistic motion of electrons in condensed matter systems (Hasan and Kane, 2010; Manchon *et al.*, 2015) as well as the formation of chiral magnetic textures (Nagaosa and Tokura, 2013; Soumyanarayanan *et al.*, 2016). In this context, recent predictions (Bernevig and Vafek, 2005; Tan, Jalil, and Liu, 2007; Manchon and Zhang, 2008, 2009; Obata and Tatara, 2008; Garate and MacDonald, 2009; Železný *et al.*, 2014) and observations of current-induced magnetization dynamics mediated by spin-orbit coupling in ferromagnets and antiferromagnets (Ando *et al.*, 2008; Chernyshov *et al.*, 2009; Miron *et al.*, 2010, 2011; Liu *et al.*, 2011; Wadley *et al.*, 2016) have revolutionized the field of spintronics, leading to new opportunities to integrate electronic and magnetic functionalities in a wide variety of materials and devices.

Research in spintronics explores the possibilities to add the spin degree of freedom to conventional charge-based microelectronic devices or to completely replace charge with spin functionalities (Wolf *et al.*, 2001; Zutic, Fabian, and Das Sarma, 2004). Over the past three decades of research and development, spintronics has offered means to replace magnetic fields for reading and writing information in nanomagnets by more scalable current-induced spin torques (Chappert, Fert, and Dau, 2007; Brataas, Kent, and Ohno, 2012). Spin-transfer torques (STT), which mediate the transfer of spin-angular momentum between two magnetic layers having noncollinear magnetizations (Berger, 1996; Slonczewski, 1996; Ralph and Stiles, 2008), are currently the method of choice for controlling the bit states in magnetic random access memories (MRAMs) (Kent and Worledge, 2015; Apalkov, Dieny, and Slaughter, 2016). In STT, spin-orbit coupling already plays an important, but passive role: by inducing spin relaxation and magnetic damping, it enables the spin polarization of the charge current passing through the reference layer and permits the magnetization switching. This review focuses on a new family of spin torques, whose physical origin is the transfer of orbital angular momentum from the lattice to the spin system. These torques rely on the conversion of electrical current to spin (Gambardella and Miron, 2011; Sinova *et al.*, 2015) and are called *spin-orbit torques* (SOTs) in order to underline their direct link to the spin-orbit interaction.

Because of the ubiquity of spin-orbit coupling, SOTs provide efficient and versatile ways to control the magnetic state and dynamics in different classes of materials, as schematically shown in Fig. 1. Several microscopic mechanisms can give rise to SOT. In one picture, a charge current flowing parallel to an interface with broken inversion symmetry generates a spin density due to spin-orbit coupling, which in turn exerts a torque on the magnetization of an adjacent magnetic layer via the exchange coupling (Manchon and Zhang, 2008). Several names have appeared in the literature for this model mechanism, such as the Rashba-Edelstein effect (Edelstein, 1990) or the inverse spin galvanic effect (iSGE) (Belkov and Ganichev, 2008). In this review we use the term iSGE-SOT.

In the other model scenario, spin-orbit coupling generates a spin current in the nonmagnetic metal layer due to the spin
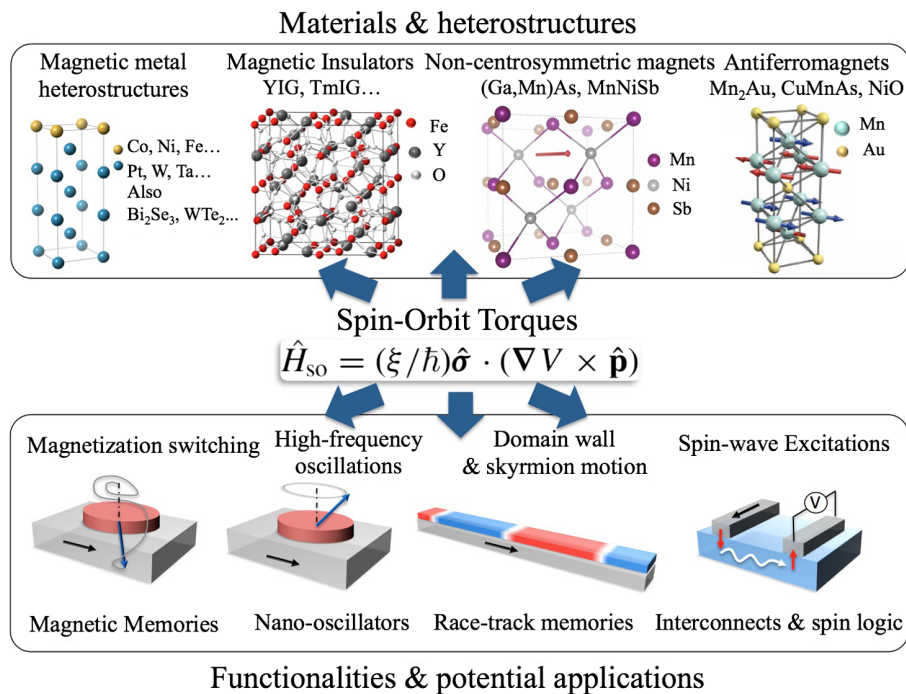
FIG. 1. Materials in which spin-orbit torques have been observed range from metallic heterostructures involving transition metals, topological insulators, and other heavy element substrates to bulk noncentrosymmetric ferromagnets and antiferromagnets. Spin-orbit torque is a promising candidate mechanism to drive disruptive spintronics devices such as magnetic memories, nano-oscillators, racetrack storage devices, as well as interconnects and spin logic gates.

Hall effect (SHE) (Dyakonov and Perel, 1971; Hirsch, 1999; Sinova *et al.*, 2015). The spin current propagates toward the interface, where it is absorbed in the form of a magnetization torque in the adjacent ferromagnet (Ando *et al.*, 2008; Liu *et al.*, 2011). The SHE-SOT and iSGE-SOT can act in parallel. This is reminiscent of the early observations in semiconductors of the SHE and iSGE as companion phenomena, both allowing for electrical alignment of spins in the same structure (Kato *et al.*, 2004a, 2004b; Wunderlich *et al.*, 2004, 2005).

Considering the SOT as originating from either the iSGE or SHE model scenarios can provide useful physical and materials guidance. The necessary condition for the iSGE-induced nonequilibrium spin polarization is the broken inversion symmetry, which is automatically fulfilled in the previously mentioned interfaces. However, uniform crystals can also have unit cells that lack a center of symmetry. The initial discovery of the iSGE-SOT was made in such a crystal, namely, in the zinc-blende diluted magnetic semiconductor (Ga,Mn)As (Chernyshov *et al.*, 2009) and later also reported in asymmetric metal multilayers (Miron *et al.*, 2010). This line of research was subsequently extended to crystals whose individual atomic positions in the unit cell are locally noncentrosymmetric, leading to the discovery of a staggered iSGE polarization and current-induced switching in an antiferromagnet (Železný *et al.*, 2014; Wadley *et al.*, 2016).

The notion of the SHE-induced SOT, on the other hand, led to systematic studies correlating trends in the magnitude and sign of the SOT in ferromagnetic/nonmagnetic metal bilayers (Ando *et al.*, 2008; Liu, Pai *et al.*, 2012; Pai *et al.*, 2012) with the magnitude and sign of the SHE in the nonmagnetic material calculated by *ab initio* methods (Tanaka *et al.*, 2008; Freimuth, Blügel, and Mokrousov, 2010; Qiao *et al.*,

2018) or measured by spin absorption in nonlocal spin valves (Morota *et al.*, 2011; Hiroshi, Fukuma, and Otani, 2015). However, in the commonly used bilayers with a nm-scale spin-diffusion length and nm-thick magnetic film, the distinction between SOTs generated by "bulk"-SHE and "interface"-iSGE remains principally blurred. Moreover, the experimentally observed complex SOT phenomenology in the bilayer structures is often not captured by either of the two idealized model scenarios (Garello *et al.*, 2013; Junyeon Kim *et al.*, 2013). Other studies have pointed out further contributions to the SOT due to interface oxidation (Miron, Garello *et al.*, 2011; Qiu *et al.*, 2015; Demasius *et al.*, 2016; An, Kanno *et al.*, 2018) and spin-dependent scattering of the spin-polarized current flowing in the ferromagnet (Saidaoui and Manchon, 2016; Amin, Zemen, and Stiles, 2018), which can add to the SHE-induced SOT.

Independently on their origin, SOTs allow for new device architectures and efficient control of the magnetization. Figure 2 compares the out-of-plane current geometry employed in STT-MRAMs for both the write and read operations of a magnetic tunnel junction (MTJ), shown in Fig. 2(a), with the in-plane writing geometry enabled by SOT based on either SHE [Fig. 2(b)] or iSGE [Fig. 2(c)]. SOT-induced magnetization switching, first demonstrated by Miron, Garello *et al.* (2011) and Liu, Pai *et al.*, 2012, allows for decoupling the write and read current paths, with great advantages in terms of endurance of the junction and switching speed relative to STT (Prenat *et al.*, 2016; Fukami and Ohno, 2017; Cubukcu *et al.*, 2018). Differently from STT, SOT allows also for the switching of magnetic insulators (Avci, Quindeau *et al.*, 2017) and antiferromagnets (Wadley *et al.*, 2016), as well as for the generation of coherent spin
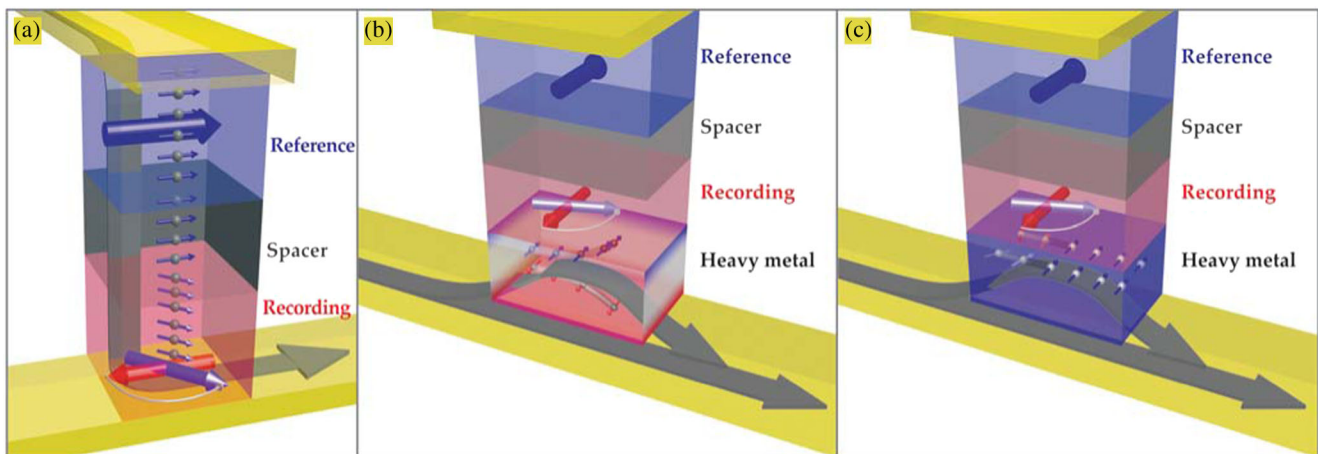
FIG. 2. STT vs SOT switching of a magnetic tunnel junction. (a) In the STT case, a current of spin-polarized electrons (gray arrow) flows from a reference ferromagnet through a spacer layer into the recording ferromagnetic layer. Within a few atomic monolayers of entering the recording magnet, the flowing electrons' spin aligns with the instantaneous magnetization due to the exchange interaction (large purple arrow in the recording medium). This alignment results in a torque (curved white arrow) on the recording ferromagnet that ultimately causes the magnetization to switch from its original orientation (large red arrow). In the snapshot shown here, the magnetization is about 2/3 of the way to being switched. Note that the time scale for the full reversal is much greater than the time needed for the current to flow from the reference ferromagnet through the recording ferromagnet. A second mechanism, SOT, can be driven by the SHE or by the iSGE. (b) In the SHE variant, as current flows along the contact and the nonmagnetic metal layer, a spin current is generated that flows upward into the recording ferromagnet and switches its magnetization. (c) In the iSGE mechanism, electrons become spin polarized at the interface of a nonmagnetic metal and a ferromagnet; the polarized electrons then switch the magnetization of the recording ferromagnet. From Sinova and Jungwirth, 2017.

waves (Demidov *et al.*, 2012; Collet *et al.*, 2016) and interconversion of electric and magnon currents (Kajiwara *et al.*, 2010; Cornelissen *et al.*, 2015; Goennenwein *et al.*, 2015) in single-layer ferromagnets and ferrimagnets.

We review the present theoretical understanding of the SOT in various types of material systems and summarize the experimentally established SOT phenomenology. We also discuss links of SOT to other currently highly active research fields, such as the topological phenomena in condensed matter, and outline foreseen technological applications of the SOT. A brief overview is given in Sec. II. Readers interested in a more detailed discussion of theoretical and experimental aspects of SOT are referred to the subsequent sections.

II. OVERVIEW

A. Magnetization dynamics induced by spin-orbit torques

The dynamics of the recording layer subject to STT or SOT is governed by the Landau-Lifshitz-Gilbert (LLG) equation,

$$\frac{d\mathbf{m}}{dt} = -\gamma\mathbf{m} \times \mathbf{B_M} + \alpha\mathbf{m} \times \frac{d\mathbf{m}}{dt} + \frac{\gamma}{M_s}\mathbf{T}, \quad (1)$$

where $\gamma > 0$ is the absolute value of the gyromagnetic ratio (1.76×10^{11} s^{-1} T^{-1} for free electrons), α is the Gilbert damping parameter (dimensionless), M_s is the saturation magnetization, and $\mathbf{m} = \mathbf{M}/M_s$ is the magnetization unit vector. The first term accounts for the precession of the magnetization $\mathbf{m}$ about the effective field $\mathbf{B_M}$ defined as the functional derivative of the magnetic energy density $\mathcal{E}$, $\mathbf{B_M} = -\delta\mathcal{E}/\delta\mathbf{M}$. The second term accounts for the relaxation of the magnetization toward its equilibrium position, and the third term represents the other torques $\mathbf{T}$ that may not derive from an energy density, notably the torques induced by an electrical current. Such torques are by definition orthogonal to the magnetization $\mathbf{m}$ and adopt the most general form

$$\mathbf{T} = \tau_{FL}\mathbf{m} \times \boldsymbol{\zeta} + \tau_{DL}\mathbf{m} \times (\mathbf{m} \times \boldsymbol{\zeta}). \quad (2)$$

Here $\boldsymbol{\zeta}$ is a unit vector that depends on the microscopic mechanism at the origin of the torques, and the coefficients $\tau_{FL,DL}$ may depend on the magnetization angle. In the STT configuration depicted in Fig. 2(a), $\boldsymbol{\zeta}$ is the polarization vector and is oriented along the magnetization direction of the reference layer. In the case of SOT, $\boldsymbol{\zeta}$ is determined by the charge-spin conversion process induced by spin-orbit coupling. In the literature, τ_{DL} is usually referred to as the longitudinal (Slonczewski-like) component, which lies in the $(\mathbf{m}, \boldsymbol{\zeta})$ plane. In contrast, τ_{FL} is normally referred to as the perpendicular (or transverse) component, which lies normal to the $(\mathbf{m}, \boldsymbol{\zeta})$ plane. The directions of these two torque components are represented in Fig. 3. To understand the impact of these torques on the magnetization dynamics, it is instructive to remark that, when independent on the magnetization $\mathbf{m}$, the perpendicular torque τ_{FL} acts on the magnetization like an effective magnetic field [first term in Eq. (1)], while the longitudinal torque τ_{DL} acts like an effective magnetic damping [second term in Eq. (1), to the lowest
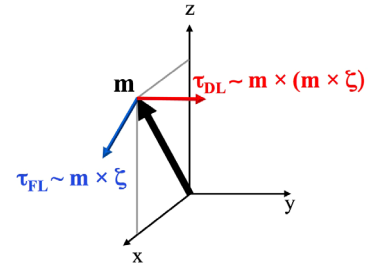
FIG. 3. Directions of the fieldlike and dampinglike SOT components. In the present configuration and for clarity, we take $\boldsymbol{\zeta} = \mathbf{y}$.

order in α]. Because of these similarities, these two torque components τ_{FL} and τ_{DL} are also commonly called *fieldlike* and *dampinglike* terms, respectively, a denomination we adopt in this review.

Initially, the dampinglike component of the SOT was identified by measuring the damping of the ferromagnetic resonance (FMR) in nonmagnetic metal/ferromagnetic metal bilayers (NM/FM) (Ando *et al.*, 2008). A change of the damping factor was induced in the experiment by an in-plane dc current and interpreted as a consequence of the SHE-SOT. This was a new concept in which a dc electrical current driven through a conductor adjacent to the ferromagnet controls the FMR damping, in contrast to traditional means of controlling the FMR frequency by the dc current-induced Oersted field. Since the SHE in nonmagnetic metals was an emerging topic at the time of these pioneering SOT experiments, one of the key perceived merits of the SOT then was in providing an experimental measure of the spin Hall angle in the nonmagnetic material (Ando *et al.*, 2008). From our present perspective, however, we emphasize that such measurements have to be taken with great caution as the "spin Hall angles" inferred from these experiments are only effective parameters capturing, besides the bulk SHE, also the iSGE and other potential spin-orbit coupling and spin current contributions originating from the spin-orbit coupling from the interface (Lifshits and Dyakonov, 2009; Miron, Garello *et al.*, 2011; Sinova *et al.*, 2015; Amin and Stiles, 2016a, 2016b; Saidaoui and Manchon, 2016; Kyoung Whan Kim *et al.*, 2017).

While in experiments pioneered by Ando *et al.* (2008) the FMR is generated externally and the SOT modifies only the dynamics, Liu *et al.* (2011) demonstrated that the SOT itself can drive the FMR when an alternating in-plane current is applied to the NM/FM bilayer. The method was again conceived to provide additional means to utilize ferromagnet dynamics for measuring the SHE in the adjacent nonmagnetic metal layer (Liu *et al.*, 2011). A remarkable turn of events appeared, however. Miron, Garello *et al.* (2011) and, subsequently, Liu, Pai *et al.*, 2012 observed that SOTs can not only trigger small angle FMR precession but, for large enough electrical currents, it can fully and reversibly switch the ferromagnetic moments. The roles of the ferromagnetic and nonmagnetic metallic layers got reversed: In the original experiment by Ando *et al.* (2008), the ferromagnet provided the tool and the relativistic effects in the nonmagnetic metal layer were the object of interest. From now on, the new means to manipulate the magnetization takes central stage.

Phenomenologically, SHE-SOT may appear as a mere counterpart of the STT (Ando *et al.*, 2008; Liu, Pai *et al.*, 2012). At first sight, the spin current injected from the nonmagnetic metal layer due to the SHE just replaces the spin injection from the reference to the recording ferromagnet in the STT stack (see Fig. 2). However, the change in the writing electrical current geometry from out of plane in the STT to in plane in the SOT has major consequences for the operation of memory devices as well as for the transport properties of layered structures.

In the STT, each electron injected perpendicular to the plane of the heterostructure transfers one quantum unit of spin-angular momentum as it travels from the reference to the recording ferromagnet. This transfer can be enhanced by using resonant tunneling (Vedyayev *et al.*, 2006; Theodonis, Kalitsov, and Kioussis, 2007), which is difficult to realize experimentally. In the relativistic SOT utilizing no reference spin polarizer and where electrons are injected in the plane of the heterostructure, the spin-angular momentum generated from the linear momentum in between collisions gives a little kick in every collision or acceleration that the electron feels, all along the plane. This configuration inherently enables the effective transfer of more than one spin unit per electron and allows for exerting spin torque on large sample areas. This fact has opened an entirely new space for material and device optimization of the switching process in SOT-MRAMs.

Present MRAM bit cells utilize the tunneling magneto-resistance (TMR) for readout (Chappert, Fert, and Dau, 2007). The TMR effect is maximized when the recording and reference magnetizations switch between parallel and anti-parallel configurations. For STT writing in such a device, however, the injected spin from the reference ferromagnet with a precisely aligned or antialigned orientation to the recording magnetization exerts no torque. This implies that the STT mechanism relies on thermal fluctuations of magnetization and the associated incubation time for initializing the magnetization dynamics slows down the switching process. A means to limit the incubation time is to engineer the polarizing and recording layers with orthogonal magnetizations. In this configuration, however, the polarizing layer cannot be used as a TMR sensor to probe the magnetic state of the recording layer and a third reference layer needs to be inserted in the device for this purpose (Kent, Özyilmaz, and Del Barco, 2004; Ye *et al.*, 2014).

In the SOT approach, the orientation of the current-induced spin polarization that exerts the torque in the recording ferromagnet is independent of the magnetization in the reference ferromagnet of the TMR stack and can be engineered to be misaligned with the recording magnetization. Therefore, the in-plane writing current geometry can make the SOT more efficient and faster than STT (Garello *et al.*, 2014; Aradhya *et al.*, 2016; Prenat *et al.*, 2016; Baumgartner *et al.*, 2017; Fukami and Ohno, 2017).

Sharing the read and write current paths in STT-MRAMs is also problematic (Kent and Worledge, 2015; Apalkov, Dieny, and Slaughter, 2016). The distributions of read and write current values need to be well separated to avoid undesired writing while reading the memory. However, high writing currents go against energy efficiency. They also require a thin tunnel barrier separating the recording and reference ferromagnetic layers, resulting in reliability issues due to barrier damage at high writing currents. Moreover, optimizing the tunnel barrier (and other components of the STT-MRAM stack) for writing can have a detrimental effect on the magnitude of the readout TMR. In contrast, the three-terminal SOT-MRAM bit cell with separate write and read paths allows for separately optimizing these two basic memory function-alities and removing the endurance issue by not exposing the tunnel barrier to the writing current. These advantages come at the expense of a larger area of the three-terminal SOT-MRAM cell (that is, a lower memory density) compared to the two-terminal STT-MRAM. Overall, SOT-MRAMs can find a broad utility and appear to be particularly well suited for the top of the memory hierarchy, namely, for the embedded processor caches (Hanyu *et al.*, 2016; Prenat *et al.*, 2016; Fukami and Ohno, 2017).

B. Nonuniform magnetic textures

Nonuniform magnetic textures are the basis of the racetrack memory concept illustrated in Fig. 4 (Parkin, Hayashi, and Thomas, 2008; Parkin and Yang, 2015). A domain wall racetrack memory consists of a series of alternating up and down magnetization domains that can be synchronously shifted along the corresponding multibit track and by this sequentially read by a single magnetoresistive sensor [see Fig. 4(a)].

An applied uniform (easy-axis) magnetic field cannot be used to operate the racetrack since it favors one of the two types of domains and thus pushes neighboring domain walls in opposite directions. Initially this problem was resolved by replacing magnetic field with the STT that is induced by an in-plane current driven along the racetrack (Parkin, Hayashi, and Thomas, 2008). The physics is analogous to STT switching by a vertical current in an MRAM stack where the preferred magnetization direction is controlled by the direction of the applied spin current. In the racetrack, one direction of the applied electrical current moves electrons from, say, the up domain to the down domain at one domain wall, and from the down domain to the up domain at the neighboring domain wall. As a result, the sense of the spin current is opposite at the two domain walls. It implies that, say, the up domain is preferred at the first domain wall while the down domain is preferred at the second domain wall and the two domain walls then move in the same direction.

At first sight, SOT in a racetrack fabricated from a NM/FM bilayer cannot be used to synchronously move multiple domain walls along the track. For example, a fieldlike SOT would act as a uniform magnetic field. Also the dampinglike SOT seems unfavorable as it is driven by a uniform vertical spin current that acts all along the racetrack. This makes the dampinglike SOT fundamentally distinct in the domain wall racetrack geometry from the STT mechanism that exploits the repolarization of the in-plane spin current when carriers enter successive domains.

Remarkably, theory and experiment have shown that the dampinglike SOT can also move neighboring domain walls in the same direction, provided that the walls are of Néel type and have the same spin chirality (Thiaville *et al.*, 2012; Emori *et al.*, 2013; Ryu *et al.*, 2013). Chiral Néel domain walls are
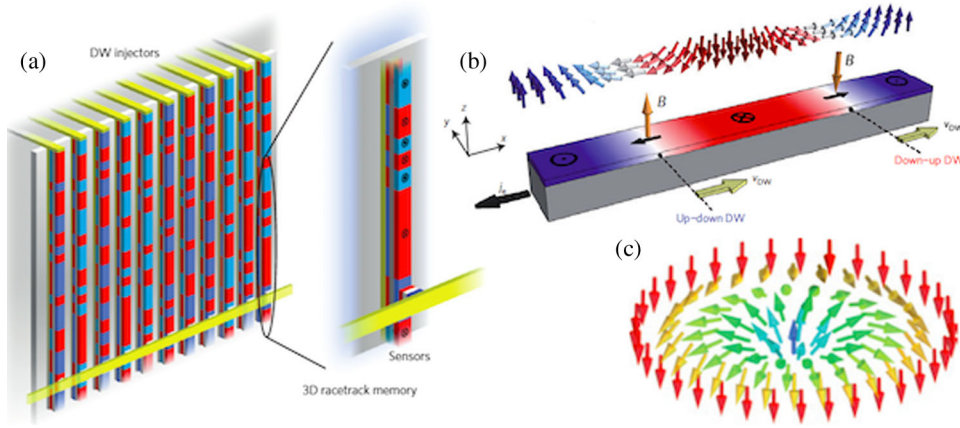
FIG. 4. (a) Domain wall racetrack memory with red and blue regions representing areas that are oppositely magnetized. Adapted from Parkin and Yang, 2015. (b) Illustration of left-handed chiral Néel domain walls in a NM/FM bilayer. The effective field B of the dampinglike SOT moves adjacent up-down and down-up domains (with velocity v_{DW}) in the same direction. Adapted from Emori *et al.*, 2013. (c) Skyrmions in a 2D ferromagnet with uniaxial magnetic anisotropy along the vertical axis. Magnetization is pointing down on the edges and pointing up in the center. Moving along a diameter, the magnetization rotates by 2π around an axis perpendicular to the diameter due to the DMI. Adapted from Fert, Cros, and Sampaio, 2013.

stabilized by the Dzyaloshinskii-Moriya interaction (DMI) which relies on the interfacial spin-orbit coupling and broken inversion symmetry, similarly to the SOT. In this chiral case, the effective field associated with the dampinglike SOT in the domain wall is oriented along the easy axis in a direction that alternates from one domain wall to the next so that current drives them in the same direction [see Fig. 4(b)]. Moreover, in analogy to switching in MRAMs, the racetrack SOT can be more efficient than STT, resulting in higher current-induced domain wall velocities (Miron *et al.*, 2011; Yang, Ryu, and Parkin, 2015).

In an alternative racetrack memory concept, the one-dimensional (1D) chiral domain walls are replaced with the skyrmion topological 2D chiral textures [see Fig. 4(c)] (Fert, Cros, and Sampaio, 2013). While current-driven depinning can be achieved at substantially lower current density in skyrmion lattices (Jonietz *et al.*, 2010), individual metastable skyrmions are expected to behave as pointlike particles and are in principle less sensitive to the boundaries and pinning to boundary defects as compared to domain walls (Sampaio *et al.*, 2013). Research is currently focusing on current-driven motion of individual skyrmions (Woo *et al.*, 2016; Jiang *et al.*, 2017; Legrand *et al.*, 2017; Litzius *et al.*, 2017).

C. Microscopic origin of spin-orbit torques

We mentioned in the Introduction that two main model mechanisms have been proposed to generate SOT. SHE originates from asymmetric spin deflection in the bulk of, e.g., a nonmagnetic metal induced by spin-orbit coupling. Such a deflection induces a pure spin current, transverse to the direction of the applied electrical current, that is subsequently absorbed in the adjacent magnetic layer, as depicted in Fig. 2(b). The SHE-SOT model mechanism shares with the STT the basic concept of the angular momentum transfer from a carrier spin current to magnetization torque. As a consequence, the dominant component of the SHE-SOT in this picture is dampinglike and takes the form (Ando *et al.*, 2008)

$$\mathbf{T} = (j_s^{SHE}/t_F)\mathbf{m} \times (\mathbf{m} \times \boldsymbol{\zeta}), \tag{3}$$

in units of eV/m^3. Here j_s^{SHE} is the SHE spin current density absorbed by the recording magnet of thickness t_F, and $\boldsymbol{\zeta}$ is a unit vector of the in-plane spin polarization of the out-of-plane SHE spin current. The magnitude of the injected SHE spin current density into the magnet is modeled as $j_s^{SHE} = (\hbar/2e)\eta\theta_{sh}\sigma_N E$, where η is the spin-injection efficiency across the NM/FM interface, also called transparency, $\theta_{sh} = \sigma_{sh}/\sigma_N$ is the spin Hall angle in the nonmagnetic material of spin Hall conductivity σ_{sh} (expressed in units of Ω^{-1} m^{-1}) and electrical conductivity σ_N, and $\mathbf{E} \perp \boldsymbol{\zeta}$ is the applied in-plane electric field. The SHE-SOT, being dampinglike, directly competes with the damping term in the LLG equation of magnetization dynamics. This situation favors the current-induced switching of in-plane magnetized layers, as, for a dampinglike torque, the critical current has to overcome the magnetic anisotropy barrier multiplied by the Gilbert damping factor α, the latter being typically $\ll 1$ (Ralph and Stiles, 2008).

Another common favorable feature of both SOTs and STT is that the switching condition is given by the applied current density and not the absolute current, which makes the mechanism scalable and, therefore, suitable for high-density memories. In contrast, for the traditional writing method by the current-induced Oersted magnetic field, the switching condition is determined by the absolute current.

The iSGE-SOT, as depicted in Fig. 2(c), arises from spin-orbit coupling in noncentrosymmetric systems such as interfaces [see Fig. 2(c)], or zinc-blende (Ga,Mn)As crystals (see Sec. II.D). In such systems, the band structure acquires a spin texture that is *odd* in momentum k. An example of such a spin texture is given in Fig. 5 for the prototypical case of the Pt/Co interface. This interfacial spin texture exhibits several features similar to the ideal case of Rashba spin-orbit coupling (Manchon *et al.*, 2015) and promotes iSGE. The iSGE-SOT resembles at first glance a mechanism in which the applied current generates a field rather than a dampinglike torque.
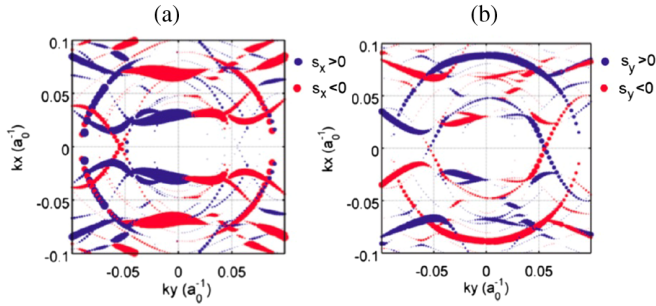
FIG. 5. Spin texture in momentum space calculated for the interfacial Co layer of Pt(8 ML)/Co(2 ML) slab using density functional theory. ML stands for monolayer. Both in-plane spin components, (a) S_x and (b) S_y, are *odd* in momentum space, enabling iSGE. Adapted from Paul M. Haney *et al.*, 2013.

In the iSGE mechanism in a NM/FM bilayer, the carrier spin density and the corresponding nonequilibrium effective magnetic field acting on the magnetization form directly at the inversion-asymmetric interface. The dampinglike SHE-SOT, on the other hand, has been primarily viewed as a consequence of the spin current pumped from the bulk of the nonmagnetic material (which can be centrosymmetric) to the ferromagnet where it transfers its angular momentum to the magnetization. In the SHE, however, the spin current also yields a nonequilibrium spin density at the edges of the nonmagnetic material where the inversion symmetry is broken. This implies an alternative picture of the SHE-SOT caused by the nonequilibrium spin density at the NM/FM interface. Correspondingly, the SHE can also be expected to contribute to the fieldlike SOT. Vice versa, as further discussed in Sec. III, the iSGE mechanism can yield not only fieldlike but also dampinglike SOT terms (Miron, Garello *et al.*, 2011; Kurebayashi *et al.*, 2014). While the original iSGE models consider the effect of a uniform spin density on the magnetization dynamics, additional torques arise in models where the spin density generated at the interface is allowed to diffuse away from the interface (Manchon, 2012; P. M. Haney *et al.*, 2013; Amin and Stiles, 2016a, 2016b). An example of numerical results is shown on Fig. 6, where the torque magnitude is plotted against the nonmagnetic metal thickness in the case of pure SHE and pure iSGE (Amin and Stiles, 2016b). For the reasons mentioned, the decomposition
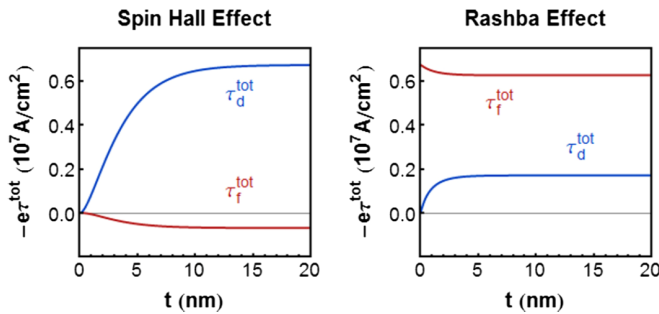

FIG. 6. Torque components as a function of the nonmagnetic metal thickness in the case of SHE (left) and iSGE (right). Both mechanisms produce fieldlike and dampinglike components. From Amin and Stiles, 2016b.

into fieldlike torque, $\mathbf{T}_{FL}$, and dampinglike torque, $\mathbf{T}_{DL}$, does not allow one to disentangle the microscopic iSGE and SHE mechanisms of the SOT. Moreover, the factors τ_{FL} and τ_{DL} can depend on the angle of $\mathbf{m}$ (Garello *et al.*, 2013). This not only makes the microscopic analysis but also the phenomenological LLG description of the SOT more complex.

In general, SOT can be directly linked to the applied electric field $\mathbf{E}$ by a linear response expression $\mathbf{T} = \chi_T \mathbf{E}$ (Freimuth, Blügel, and Mokrousov, 2014b). Alternatively, SOT can be written as $\mathbf{T} = \mathbf{M} \times \mathbf{B}_T$, where $\mathbf{B}_T \approx -\Delta \mathbf{S}/M_s$ is an effective current-induced spin-orbit field, Δ is the exchange coupling between carrier spins and magnetic moments, and $\mathbf{S} = \chi_S \mathbf{E}$ is the current-induced carrier spin density expressed again in the linear response. The different torque terms in the LLG equation are obtained from the expansion $\chi_{S,ij} = \chi_{S,ij}^{(0)} + \chi_{S,ij,k}^{(1)} m_k + \chi_{S,ij,kl}^{(2)} m_k m_l + \cdots$, where m_i are the components of the magnetization unit vector. Here the response function coefficients for each order in $\mathbf{m}$ are independent of $\mathbf{m}$ and their matrix form reflects the underlying crystal symmetry of the considered material or structure (Hals and Brataas, 2013a, 2013b; Wimmer *et al.*, 2016; Železný, Gao *et al.*, 2017). For example, the fieldlike SOT corresponds to the zeroth order term while the dampinglike SOT term appears in the first order of the expansion of χ_S.

Note that an analogous expansion can be written for χ_T and that the approaches using χ_T or χ_S expansion are in principle equivalent. Using χ_S appeals to the two-step physical picture of the SOT in which, first, the applied current polarizes the carriers (which can also appear in nonmagnetic metals) and, second, the nonequilibrium carrier spins generate the torque on magnetic moments via exchange coupling Δ. When considering χ_T, the physical intuition based on SHE, iSGE, or other nonequilibrium spin-density phenomena may be less apparent but the experimentally measured quantity, which is the SOT, is accessed directly. In microscopic theories, SOT has been calculated from either χ_S or χ_T. In the former case, one obtains a spin density averaged over the unit cell which is then multiplied by an averaged exchange field to obtain the net torque. In the latter case, the cross product of the spin density and exchange field is calculated locally and then averaged over the unit cell to get the torque. Hence, using χ_T always represents the more rigorous approach.

In the Kubo linear response formalism, the microscopic expression for χ_S (or χ_T) can be split into the intraband contribution (Boltzmann theory) and the interband term (Garate and MacDonald, 2009). The former one scales with conductivity, i.e., diverges in the absence of disorder, and contributes to the fieldlike SOT (Manchon and Zhang, 2008). The latter one is finite in the disorder-free intrinsic limit (Freimuth, Blügel, and Mokrousov, 2014a; Kurebayashi *et al.*, 2014) and contributes to the dampinglike SOT. As a result, the fieldlike SOT tends to dominate the dampinglike SOT in clean systems while the trend reverses in more disordered structures (Freimuth, Blügel, and Mokrousov, 2014b; Hang Li *et al.*, 2015). This is an example of basic guidelines that theory can provide when analyzing SOT experiments. We emphasize, however, that other terms beyond the lowest order fieldlike and dampinglike torques can also significantly contribute to

the total SOT, as seen in experiments (Garello *et al.*, 2013; Yabin Fan *et al.*, 2014).

Finally, we note that unlike the rigorous and systematic methods based on the response functions χ_S or χ_T, considering the SHE spin current as an intermediate step between the applied electrical current and the resulting SOT is an intuitive but not rigorous approach. This is because other mechanisms beyond the bulklike SHE can contribute, and because in spin-orbit coupled systems the spin current is not uniquely defined, in contrast to the well-defined and directly measurable spin density or torque. As a result, the "Hall angle" $\theta_{\rm sh}$ inferred from Eq. (3), relating the measured torque to a hypothetical SHE spin current, should not be understood in the original sense of the term "Hall angle" but rather as an effective experimental parameter providing a simple, and therefore rather vague, characterization of the charge-to-spin conversion efficiency in a given structure. For similar reasons, the spin current approach has not been applied for the systematic crystal and magnetization symmetry analysis of the series of SOT terms identified in experiment. From now on, to avoid unnecessary confusion we use ξ to designate the charge-to-spin conversion efficiency (see Sec. IV.A) and $\theta_{\rm sh}$ in the specific context of SHE.

D. Spin-orbit torques in antiferromagnets

For antiferromagnets, the STT or SOT phenomenology is modified by considering a current-induced spin density at a particular atomic site that tends to produce a torque which acts locally on the magnetic moment centered on that site (MacDonald and Tsoi, 2011; Gomonay and Loktev, 2014; Železný *et al.*, 2014; Jungwirth *et al.*, 2016). In analogy to ferromagnets, the local torques acting on the *a*th antiferromagnetic sublattice magnetization $\mathbf{M}_a$ have a fieldlike component of the form $\mathbf{T}_a = \mathbf{M}_a \times \mathbf{B}_a$, with $\mathbf{B}_a \sim \boldsymbol{\zeta}_a$, and a dampinglike component $\mathbf{T}_a = \mathbf{M}_a \times \mathbf{B}'_a$, with $\mathbf{B}'_a \sim \mathbf{M}_a \times \boldsymbol{\zeta}_a$, respectively. Note that in a rigorous systematic theory, these and all other torque terms acting in an antiferromagnet can be again obtained from the linear response expressions in which the coefficients of the magnetization expansion of $\chi_{T,a}$ (or $\chi_{S,a}$) reflect local crystal symmetries of the *a*th antiferromagnetic sublattice (Železný, Gao *et al.*, 2017). Assuming a collinear antiferromagnet, two model scenarios can be considered for the fieldlike and dampinglike SOTs: One with $\boldsymbol{\zeta}_1 = \boldsymbol{\zeta}_2 = \boldsymbol{\zeta}$ and the other one with $\boldsymbol{\zeta}_1 = -\boldsymbol{\zeta}_2$.

The former case corresponds, e.g., to injection of uniformly polarized carriers from an external reference ferromagnet, from a nonmagnetic SHE material, or to the generation of a uniform spin density at a nonmagnetic metal/antiferromagnetic metal (NM/AF) interface by iSGE [see, e.g., Manchon (2017)]. The fieldlike torque in the antiferromagnet would then be driven by a uniform nonstaggered effective field $\mathbf{B}_1 = \mathbf{B}_2 \sim \boldsymbol{\zeta}$, i.e., would be equally inefficient in switching an antiferromagnet as a uniform external magnetic field acting on an antiferromagnet. On the other hand, the local nonequilibrium effective field $\mathbf{B}'_a \sim \mathbf{M}_a \times \boldsymbol{\zeta}$ driving the dampinglike torque has an opposite sign on the two spin sublattices since $\mathbf{M}_1 = -\mathbf{M}_2$. This staggered effective field cants the magnetizations of the two sublattices and triggers the dynamics of the antiferromagnetic order resulting in current-driven
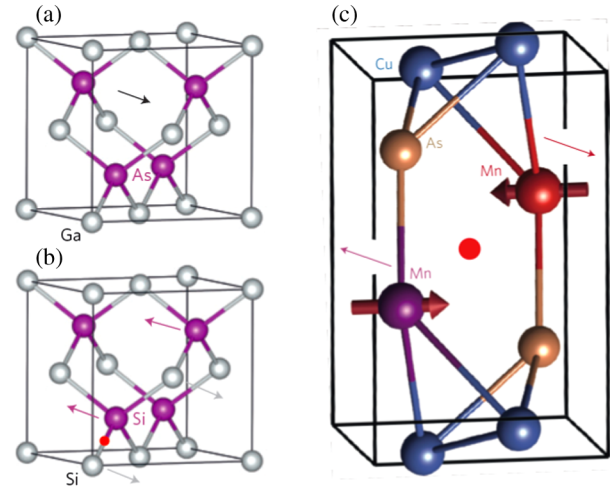
FIG. 7. (a) Global uniform nonequilibrium spin density generated by electrical current in a nonmagnetic lattice with global inversion asymmetry (e.g., GaAs) due to the iSGE. (b) Local staggered, antiferromagneticlike nonequilibrium spin density in a nonmagnetic lattice with local inversion asymmetry (e.g., Si) due to the iSGE. The red dot shows the inversion-symmetry center of the Si lattice. The two Si atoms on either side of the center occupy inversion-partner lattice sites with locally asymmetric environments. In GaAs lattice, the inversion-symmetry center is absent since the two inversion-partner sites in the unit cell are occupied by different atoms. (c) Local staggered nonequilibrium spin density inducing a local staggered effective field in an antiferromagnetic lattice with local inversion asymmetry (e.g., CuMnAs). Thin arrows represent the current-induced staggered effective field and thick arrows the antiferromagnetic moments. Adapted from Jungwirth *et al.*, 2016.

switching and excitations, somewhat similar to what is obtained in ferromagnets subject to a dampinglike torque (Gomonay and Loktev, 2010; Cheng, Xiao, and Brataas, 2016; Khymyn *et al.*, 2017).

The microscopic realization of the second scenario in which $\boldsymbol{\zeta}_1 = -\boldsymbol{\zeta}_2$ is illustrated in Fig. 7 (Železný *et al.*, 2014; Ciccarelli *et al.*, 2016; Jungwirth *et al.*, 2016). It is the staggered counterpart of the uniform iSGE spin density previously discussed. As mentioned in the previous section, iSGE exists only in noncentrosymmetric systems. For instance, the unit cell of zinc-blende GaAs [Fig. 7(a)] lacks a center of inversion, enabling an electrical current to induce a nonequilibrium uniform spin density in the bulk crystal. In contrast, the related diamond lattice of, e.g., Si [Fig. 7(b)] has global inversion symmetry and therefore cannot promote a net iSGE spin density when integrated over the unit cell. However, the two identical atoms in the unit cell sitting on the inversion-partner sites have locally noncentrosymmetric environments. As a result, the diamond lattice is an example where the iSGE can generate *local* nonequilibrium spin density with opposite sign and equal magnitude on the two inversion-partner atoms while the global spin density integrated over the whole unit cell vanishes. Here a uniform electrical current induces a nonequilibrium *staggered* spin density in the bulk crystal.

In Si there is no equilibrium antiferromagnetic order that could be manipulated by these local staggered nonequilibrium

spin densities. However, antiferromagnets like CuMnAs shown in Fig. 7(c) share the crystal symmetry allowing for the current-induced staggered spin density whose sign alternates between the inversion-partner atoms. Moreover, one inversion-partner lattice site is occupied by the magnetic atom belonging to the first antiferromagnetic spin sublattice and the other inversion partner is occupied by the magnetic atom belonging to the second spin sublattice. As a result, the corresponding fieldlike Néel SOT can reorient antiferromagnetic moments with an efficiency similar to the reorientation of ferromagnetic moments by an applied uniform field. This scenario has been confirmed experimentally in CuMnAs and Mn$_2$Au memory devices (Wadley *et al.*, 2016; Bodnar *et al.*, 2018; Meinert, Graulich, and Matalla-Wagner, 2018; Zhou *et al.*, 2018).

E. Spin-orbit torques in topological materials

The distribution of spin texture in momentum space is a crucial ingredient to understand SOT. In semiconductor materials where the iSGE and SHE were initially discovered, and even more in metal structures, multiple bands cross the Fermi level and their respective contributions to the current-induced spin density tend to compensate each other. Also the spin textures are more complex, which can further reduce the net effect.

From this perspective, topological insulators (Hasan and Kane, 2010; Pesin and MacDonald, 2012b) are regarded as optimal materials for the SOT. The surface states of a three-dimensional (3D) topological insulator form a Dirac cone with a single Fermi surface and a helical locking of the relative orientations of the spin and the momentum [see Fig. 8(a)]. Indeed, SOT-FMR measurements in a metallic ferromagnet interfaced with a topological insulator showed an exceptionally large spin conversion efficiency ξ (Mellnik *et al.*, 2014). However, compared to common nonmagnetic metals, the

increase of ξ in the studied topological insulators turned out to be primarily due to its decreased electrical conductivity while the inferred effective spin Hall conductivity was similar to the nonmagnetic metals (see Table II).

Interfacing a highly resistive topological insulator with a low resistive metal FM has also a practical disadvantage that most of the applied electrical current is shunted through the metallic magnet and does not contribute to the generation of the spin density at the topological insulator surface. A possible remedy is in using an insulating magnet. An example is a study of highly efficient magnetization switching at cryogenic temperatures in a topological insulator/magnetic topological insulator bilayer, in which the inferred spin conversion efficiency ξ was 3 orders of magnitude larger than in nonmagnetic metals (Yabin Fan *et al.*, 2014; Fan and Wang, 2016).

In the previously discussed studies, Dirac quasiparticles exhibiting strong spin-momentum locking are considered to enhance the efficiency of the SOT control of magnetic moments. Vice versa, a scheme has been recently proposed for the electric control of Dirac band crossings by reorienting magnetic moments via SOT (Šmejkal *et al.*, 2017). Instead of 2D surface states of a topological insulator, these predictions consider Dirac bands in the bulk of a topological 3D semimetal. Since Dirac bands can exist only in systems with a combined space-inversion and time-inversion ($\mathcal{P}T$) symmetry, ferromagnets are excluded. On the other hand, the combined $\mathcal{P}T$ symmetry in an antiferromagnet is equivalent to a magnetic crystal symmetry in which antiferromagnetic spin sublattices occupy inversion-partner lattice sites. This in turn allows for an efficient SOT, as discussed in the previous section.

F. Inverse effect of the spin-orbit torque

The Onsager reciprocity relations imply that there is an inverse phenomenon to the SOT, which we call the spin-orbit charge pumping (Hals, Brataas, and Tserkovnyak, 2010; Kim, Moon *et al.*, 2012; Tölle, Eckern, and Gorini, 2017). The underlying physics of the spin-orbit charge pumping generated from magnetization dynamics is the direct conversion of magnons into charge currents via spin-orbit coupling, as illustrated in Fig. 9. This effect evolves from the spin pumping predicted by Brataas *et al.* (2002) and Tserkovnyak, Brataas, and Bauer (2002b) when spin-orbit coupling is included, either in the bulk of the nonmagnetic metal or at the interface. Thus, any external force that drives magnetization precession can generate spin-orbit charge pumping. Similar to the SOT, two model microscopic mechanisms can be considered for the spin-orbit charge pumping: one due to the inverse effect of the iSGE (Rojas-Sánchez *et al.*, 2013; Ciccarelli *et al.*, 2015), called the spin galvanic effect (SGE), and the other one due to the inverse SHE (Saitoh *et al.*, 2006). Together with the nonlocal detection in a lateral structure (Valenzuela and Tinkham, 2006), the spin-orbit charge pumping across the NM/FM interface provided the first experimental demonstration of the inverse SHE (Saitoh *et al.*, 2006). Since then it has evolved into one of the most common tools for electrical detection of magnetization dynamics.
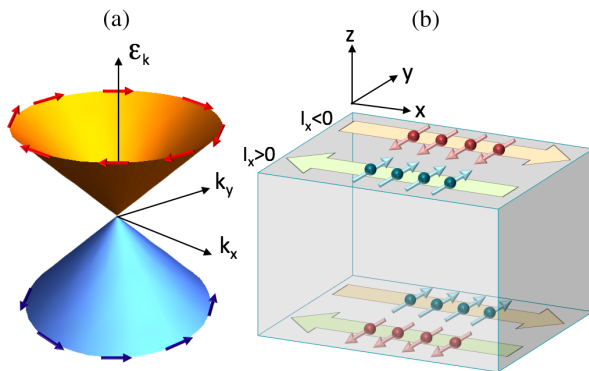

FIG. 8. Charge current-induced surface spin density in a topological insulator. (a) Schematic illustration of the spin-momentum locked helical spin texture of the surface states in a topological insulator: clockwise spin texture above the Dirac point while anticlockwise spin texture below the Dirac point. (b) Schematic of surface spin density on two opposite surfaces for a charge current flowing along the $-x$ direction (i.e., $I_x < 0$, thick yellow arrow) and for a charge current flowing along the $+x$ direction (i.e., $I_x > 0$, thick green arrow).
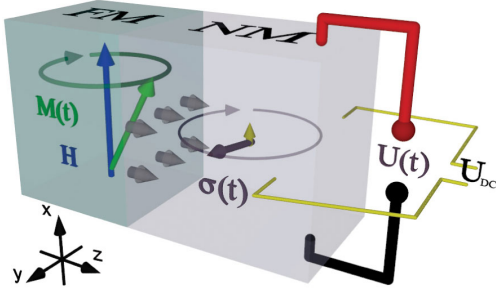
FIG. 9. A spin current is generated by spin pumping at the NM/FM interface (gray arrows). The time-dependent spin density $\sigma(t)$ of this current (dark gray arrow) rotates almost entirely in the *y-z* plane. The small time averaged dc component (yellow arrow) appears along the *x* axis. Both components lead to charge currents in the nonmagnetic metal and can be converted into ac and dc voltages, $U(t)$ and U_{DC}, by placing probes along the *x* and *y* directions, respectively. From Wei *et al.*, 2014.

III. THEORY OF SPIN-ORBIT TORQUES

In this section we review the progress that has been made toward the theoretical understanding of SOTs in both layered heterostructures and bulk materials. The most general treatment of the SOT that has been considered so far is based on the (spin-)density functional theory, in which the system is described by a Hamiltonian for noninteracting particles

$$\hat{H} = \hat{\mathcal{K}} + \hat{V}_{\text{eff}}(\mathbf{r}) + \hat{\boldsymbol{\sigma}} \cdot \boldsymbol{\Omega}_{\text{xc}}(\mathbf{r}) + \hat{H}_{\text{so}}, \qquad (4)$$

where $\hat{\mathcal{K}}$ is the kinetic energy, $\hat{V}_{\text{eff}}$ is the effective crystal potential, $\boldsymbol{\Omega}_{\text{xc}}$ is the exchange-correlation energy, and $\hat{H}_{\text{so}}$ is the spin-orbit coupling. Assuming this form of the Hamiltonian, the torque on magnetization at point $\mathbf{r}$ is given by (Haney *et al.*, 2008; Manchon and Zhang, 2011)

$$\mathbf{T}(\mathbf{r}) = -\mathbf{S}(\mathbf{r}) \times \boldsymbol{\Omega}_{\text{xc}}(\mathbf{r}), \qquad (5)$$

where $\mathbf{S} = \langle \hat{\boldsymbol{\sigma}} \rangle$ is the current-induced spin density. Equation (5) is valid for the STT as well as for the SOT. When spin-orbit coupling is neglected, the torque can be equivalently expressed as a divergence of a spin current (Ralph and Stiles, 2008)

$$T_i(\mathbf{r}) = -\nabla \cdot \mathcal{J}_{\text{s}}^i, \qquad (6)$$

where $\mathcal{J}_{\text{s}}^i = (\hbar/4)\langle\{\hat{\sigma}_i, \hat{\mathbf{v}}\}\rangle$ is a vector representing the *i*th spin component of the spin current tensor. The *j*th component of the vector $\mathcal{J}_{\text{s}}^i$ is noted as $j_{\text{s},i}^j$ and denotes a spin current polarized along the *i*th direction and propagating along the *j*th direction. In the absence of spin-orbit coupling, the torque is thus directly given by the absorption of the spin current. However, when spin-orbit coupling is not neglected, the spin-angular momentum is not a conserved quantity and the spin current in Eq. (6) is then not uniquely defined, while Eq. (5) remains valid.

The total torque is obtained by integrating Eq. (5) over the whole unit cell, and a local torque is obtained by integrating over a particular magnetic atom. This torque can then be

inserted into the LLG equation to evaluate the magnetic dynamics induced by the SOT. When using this approach it is necessary to ensure that the dynamics of the nonequilibrium carrier spins is much faster than the dynamics of magnetic moments arising from equilibrium electrons; otherwise the dynamics of the two could not be separated. This is well justified in ferromagnets whose magnetization dynamics lies in the GHz range but it could become an issue when discussing antiferromagnets whose dynamics can reach several THz. We also note that Eq. (5) assumes that Eq. (4) accurately describes the electronic system. This is reasonable for most materials of interest, namely, metals, but fails in strongly correlated systems. In these systems, more sophisticated many-body approaches are necessary. So far SOTs have been studied using only noninteracting model (free electron or $\mathbf{k} \cdot \mathbf{p}$) Hamiltonians or Kohn-Sham Hamiltonians originating from density functional theory.

At weak applied electric fields, the SOT is well described by linear response theory $\mathbf{T} = \chi_T \mathbf{E}$, where the response tensor χ_T can be calculated using Eq. (5). Equivalently, the torque can be rewritten as $\mathbf{T} = \mathbf{M} \times \mathbf{B}_T$, with the effective field obtained from the linear response expression $\mathbf{B}_T = \chi_B \mathbf{E}$. In many calculations of the SOT, especially those based on model Hamiltonians, an approximation is used in which the effective magnetic field is made directly proportional to the current-induced spin density $\mathbf{B}_T \approx -\Delta \mathbf{S}/M_{\text{s}}$. Here Δ is an exchange coupling energy corresponding to exchange between the carrier spins and magnetic moments, and $\mathbf{S}$ is again evaluated using linear response $\mathbf{S} = \chi_S \mathbf{E}$.

As discussed in Sec. II, the origin of the SOT in the bilayer systems is often attributed to two different effects, the SHE and the iSGE, where the SHE-SOT is assumed to originate from the absorption of a spin current generated in the nonmagnetic metal [see Fig. 10(a)] and the iSGE-SOT is due to spin density generated locally in the ferromagnet or at the interface [see Fig. 10(b)]. Equation (5) shows however that the torque always originates from a current-induced spin density. Thus the SHE-SOT can be more fundamentally

$$T_{FL} \sim \mathbf{m} \times (\mathbf{z} \times \mathbf{j}_e)$$
$$T_{DL} \sim \mathbf{m} \times [(\mathbf{z} \times \mathbf{j}_e) \times \mathbf{m}]$$
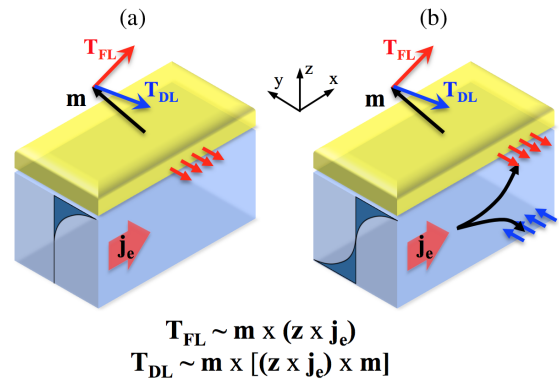
FIG. 10. Two main model spin-charge conversion mechanisms at the NM/FM interface: (a) iSGE and (b) SHE. Both mechanisms produce dampinglike and fieldlike torques. The small red and blue arrows denote the nonequilibrium spin density accumulating at the interfaces, and their corresponding spatial distribution is sketched as a shaded area on the structure's side. The large red and blue arrows represent the fieldlike and dampinglike torques, respectively.

understood not in terms of the absorption of a spin current but in terms of a spin density induced by the spin Hall current. Consequently, both contributions can be treated on the same footing and there is no clear way how to theoretically separate them.

Still, it is intuitively appealing to separate the total torque into a contribution associated with the absorption of a spin current, as given by Eq. (6), and a contribution due to a locally generated spin density, described by Eq. (5). One could then attribute the former contribution to SHE and the latter one to iSGE. However, such an approach has several drawbacks. First, spin currents are not necessarily due to the bulk SHE alone and substantial contributions can also come from the interface with the ferromagnet (Amin and Stiles, 2016a, 2016b; Lei Wang *et al.*, 2016; Kyoung Whan Kim *et al.*, 2017; Ghosh and Manchon, 2018). Second, even in bulk noncentrosymmetric materials where SOT is considered of purely iSGE origin, local spin currents within the unit cell can contribute to the torque. Third, in a slab geometry, interface and bulk are not well-defined notions, and the terminology of what should be referred to as iSGE or SHE becomes unclear (Freimuth, Blügel, and Mokrousov, 2014b). Conventionally, iSGE refers to spin density generated internally in the material. However, even the spin density induced by SHE in the bilayers could be referred to as iSGE, since it is also a spin density induced by a charge current. In conclusion, although models based on bulk SHE or iSGE due to interfacial Rashba spin-orbit coupling can be useful to explain some aspects of the experiments, in real systems there is not much point in trying to rigorously parse the torque into these two contributions.

In many experimental studies, the origin of the SOT is analyzed in terms of its symmetries. The dampinglike torque $\mathbf{T}_{\text{DL}}$ is often referred to as *spin Hall* or *Slonczewski torque*, and the fieldlike torque $\mathbf{T}_{\text{FL}}$ as *spin orbit* or *Rashba torque*. This is based primarily on the assumption that any torques associated with transfer and absorption of spin-angular momentum would have dissipativelike character and the one arising from the iSGE would be primarily of fieldlike character. This is however not the case, as interband transitions, spin-dependent scattering, spin relaxation, spin precession, and size effects significantly complicate the SOT scenario. Hence, symmetry considerations alone cannot directly disentangle the two contributions. However, symmetry analysis remains a powerful tool. SOTs obey Neumann's principle and must be invariant under the symmetry operations of the material system. This can significantly restrict the forms of the response coefficients and aids the formulation of the proper phenomenological description of the SOTs, reflecting the underlying crystal symmetry of the considered material or structure (Hals and Brataas, 2013a; Wimmer *et al.*, 2016; Železný, Gao *et al.*, 2017).

This section is organized as follows. We review the linear response formalism commonly used for microscopic calculations of the SOT in Sec. III.A, and the general symmetry properties of SOT are then discussed in Sec. III.B. Because of the great challenge of incorporating the full complexity of the bilayer systems at once, almost all theoretical studies have been focused either on iSGE in model systems or on the SHE mechanism only, with a handful of them attempting a comprehensive modeling. In Sec. III.C we review calculations of the SOT in bilayer systems based on the SHE mechanism. In Sec. III.D we review calculations of the SOT in bulk systems which includes the 2D Rashba model and 3D non-centrosymmetric materials. Microscopic calculations carried out using density functional theory calculations for bilayer structures are presented in Sec. III.E. In Sec. III.F we review calculations of the SOT in bulk antiferromagnets, and a discussion of SOTs in topological insulators and other systems is presented in Secs. III.G and III.H, respectively.

A. Kubo linear response: Intraband versus interband transitions

From a microscopic linear response perspective, basic quantum mechanics states that the statistical average of an operator $\hat{\mathcal{O}}$ reads $\mathcal{O} = \sum_{n,\mathbf{k}} \langle n, \mathbf{k} | \hat{\mathcal{O}} | n, \mathbf{k} \rangle f_{n,\mathbf{k}}$, where $f_{n,\mathbf{k}}$ is the carrier distribution function and $|n, \mathbf{k}\rangle$ is the quantum eigenstate of the system. Under a small perturbation, such as an external electric field, both the distribution function $f_{n,\mathbf{k}}$ and the eigenstates $|n, \mathbf{k}\rangle$ are modified, giving rise to different nonequilibrium contributions to the observable $\mathcal{O}$ as consistently modeled by quantum field theory (Rammer and Smith, 1986; Mahan, 2000). Within the constant relaxation time approximation, the distribution function and eigenstates become

$$f_{n,\mathbf{k}} \to f_{n,\mathbf{k}}^0 + \tau \langle n, \mathbf{k} | e\mathbf{E} \cdot \hat{\mathbf{v}} | n, \mathbf{k} \rangle_0 \frac{\partial}{\partial \epsilon} f_{n,\mathbf{k}}^0, \qquad (7)$$

$$|n, \mathbf{k}\rangle \to |n, \mathbf{k}\rangle_0 - \sum_{n'} \frac{\langle n', \mathbf{k} | e\mathbf{E} \cdot \hat{\mathbf{r}} | n, \mathbf{k} \rangle_0}{\epsilon_{n,\mathbf{k}} - \epsilon_{n',\mathbf{k}}} |n', \mathbf{k}\rangle_0, \quad (8)$$

where $f_{n,\mathbf{k}}^0$ is the Fermi-Dirac distribution, $\mathbf{E}$ is the electric field, $\hat{\mathbf{v}}$ and $\hat{\mathbf{r}}$ are the velocity and position operators, $\epsilon_{n,\mathbf{k}}$ is the eigenenergy associated with the unperturbed eigenstate $|n, \mathbf{k}\rangle_0$, and $e > 0$ is the absolute value of the electron charge. As a result, within the linear response approximation and to the lowest order in relaxation time, $\mathcal{O} = \mathcal{O}^{\text{Intra}} + \mathcal{O}^{\text{Inter}}$, where

$$\mathcal{O}^{\text{Intra}} = \tau \sum_{n,\mathbf{k}} \text{Re}\langle n, \mathbf{k} | e\mathbf{E} \cdot \hat{\mathbf{v}} | n, \mathbf{k} \rangle \langle n, \mathbf{k} | \hat{\mathcal{O}} | n, \mathbf{k} \rangle \frac{\partial}{\partial \epsilon} f_{n,\mathbf{k}}^0, \quad (9)$$

$$\mathcal{O}^{\text{Inter}} = -\hbar \sum_{n,n',\mathbf{k}} \text{Im}\langle n, \mathbf{k} | e\mathbf{E} \cdot \hat{\mathbf{v}} | n', \mathbf{k} \rangle \langle n', \mathbf{k} | \hat{\mathcal{O}} | n, \mathbf{k} \rangle$$
$$\times \frac{(f_{n,\mathbf{k}} - f_{n',\mathbf{k}})}{(\epsilon_{n,\mathbf{k}} - \epsilon_{n',\mathbf{k}})^2}. \qquad (10)$$

The first contribution, Eq. (9), is proportional to the relaxation time $\sim\tau$ and involves only intraband transitions, $|n, \mathbf{k}\rangle \to |n, \mathbf{k}\rangle$. The second one, Eq. (10), is weakly dependent on disorder and is sometimes called *intrinsic*. It involves only interband transitions $|n, \mathbf{k}\rangle \to |n', \mathbf{k}\rangle$. The intrinsic contribution can be related to the Berry curvature of the material that connects intrinsic transport properties to the topology of the phase space (Xiao *et al.*, 2010; Sinova *et al.*, 2015). Equations (9) and (10) are valid only under the assumption of a constant and large relaxation time. More generally, the linear response can be expressed in terms of the Kubo-Bastin

formula (Freimuth, Blügel, and Mokrousov, 2014b; Wimmer *et al.*, 2016)

$$\mathcal{O} = \mathcal{O}^{I(a)} + \mathcal{O}^{I(b)} + \mathcal{O}^{II}, \tag{11}$$

$$\mathcal{O}^{I(a)} = \frac{e}{h} \int_{-\infty}^{\infty} d\varepsilon \frac{\partial}{\partial \varepsilon} f_\varepsilon^0 \text{Tr} \langle \hat{\mathcal{O}} \hat{G}_\varepsilon^R (\mathbf{E} \cdot \hat{\mathbf{v}}) \hat{G}_\varepsilon^A \rangle_c, \tag{12}$$

$$\mathcal{O}^{I(b)} = -\frac{e}{h} \int_{-\infty}^{\infty} d\varepsilon \frac{\partial}{\partial \varepsilon} f_\varepsilon^0 \text{ReTr} \langle \hat{\mathcal{O}} \hat{G}_\varepsilon^R (\mathbf{E} \cdot \hat{\mathbf{v}}) \hat{G}_\varepsilon^R \rangle_c, \tag{13}$$

$$\mathcal{O}^{II} = \frac{e}{h} \int_{-\infty}^{\infty} d\varepsilon f_\varepsilon^0 \text{ReTr} \left\langle \hat{\mathcal{O}} \hat{G}_\varepsilon^R (\mathbf{E} \cdot \hat{\mathbf{v}}) \frac{\partial}{\partial \varepsilon} G_\varepsilon^R \right.$$
$$\left. - \hat{\mathcal{O}} \frac{\partial}{\partial \varepsilon} \hat{G}_\varepsilon^R (\mathbf{E} \cdot \hat{\mathbf{v}}) \hat{G}_\varepsilon^R \right\rangle_c, \tag{14}$$

where $\hat{G}_\varepsilon^{R(A)}$ denotes the retarded (advanced) Green's function, respectively, and $\langle \cdots \rangle_c$ denotes an average over disorder configurations. Tr is the trace over spin, momentum, and orbital spaces. For concreteness, the operator $\hat{\mathcal{O}}$ is simply the spin operator $\hat{\boldsymbol{\sigma}}$ or the spin current operator $\mathcal{J}_s^i$ previously defined. This formula is often simplified by assuming that the only effect of disorder is to induce a constant energy broadening $\Gamma = \hbar/2\tau$, such that $\hat{G}_\varepsilon^{R(A)} = \hbar(\varepsilon - \hat{H} \pm i\Gamma)^{-1}$. In the limit of large relaxation time, $\Gamma \to 0$ and the Kubo-Bastin formula reduces to Eqs. (9) and (10). Notice that extrinsic contributions to SHE (side jump and skew scattering) are overlooked within this approximation (Sinova *et al.*, 2015). Thus for a complete treatment, more sophisticated approaches are necessary.

B. Symmetry of spin-orbit torques

As previously mentioned, the torque can always be rewritten in terms of an effective magnetic field $\mathbf{B}_T$, $\mathbf{T} = \mathbf{M} \times \mathbf{B}_T$. The symmetry of the SOT can be studied either in terms of the linear response tensor χ_T or, equivalently, in terms of χ_B. Here we focus on the effective field since its symmetry relations are simpler. In terms of symmetry, the effective magnetic field is equivalent to the iSGE, i.e., the tensors χ_B and χ_S have the same form (although they are not necessarily proportional, as often assumed in model calculations). To understand the symmetry properties of the SOT, it is convenient to parse the effective field into two parts, even and odd under time reversal (or, equivalently, under the reversal of all magnetic moments). This is similar to the case of conductivity in magnetic systems (Grimmer, 1993). However, unlike for conductivity, the even and odd parts do not correspond to the symmetric and antisymmetric parts of the effective field tensor. Thus a separate linear response tensor has to be assigned to each part,

$$\mathbf{B}_{\text{eff}}^{\text{even}} = \chi_B^{\text{even}} \mathbf{E}, \tag{15}$$

$$\mathbf{B}_{\text{eff}}^{\text{odd}} = \chi_B^{\text{odd}} \mathbf{E}. \tag{16}$$

The same parsing can also be done for the torque. We note that the odd part of the torque corresponds to the even part of the effective field and vice versa. Noticeably, the odd and even parts have very different properties and correspond to different contributions of the Kubo formula: the intraband formula, Eq. (9), corresponds to the even field, whereas the interband formula, Eq. (10), corresponds to the odd field. Similar separation can be done for the full Kubo-Bastin formula (Freimuth, Blügel, and Mokrousov, 2014b). Furthermore, such a separation is also commonly done for experimental measurements of SOT (see Secs. IV and VI). Since the following applies equally to χ_B and χ_S we denote the tensor simply by χ. Following Neumann's principle, the tensors χ have to be invariant under all symmetry operations of the crystal. The two parts transform differently for symmetry operations that contain time-reversal symmetry. For a symmetry operation represented by a matrix $\mathcal{R}$ (Železný, Gao *et al.*, 2017),

$$\chi^{\text{even}} = \det(\mathcal{R}) \mathcal{R} \chi^{\text{even}} \mathcal{R}^{-1}, \tag{17}$$

$$\chi^{\text{odd}} = \pm \det(\mathcal{R}) \mathcal{R} \chi^{\text{odd}} \mathcal{R}^{-1}, \tag{18}$$

where $\pm$ refers to a symmetry operation with and without time reversal, respectively, and $\det(\mathcal{R})$ is the determinant of $\mathcal{R}$. By considering all the symmetry operations in the magnetic point group of the given crystal, the general form of the response tensors is found from these equations. It is also possible to treat the whole tensor together without separating it into the even and odd parts, although then some information about the structure of the torque is lost. See Wimmer *et al.* (2016) for a table of total χ_T tensors for all the magnetic point groups.

In systems with more than one magnetic atom in the unit cell, such as antiferromagnets, it is furthermore useful to study the symmetry of SOT on each magnetic site. Then Eqs. (17) and (18) are modified as follows (Železný, Gao *et al.*, 2017):

$$\chi_{a'}^{\text{even}} = \det(\mathcal{R}) \mathcal{R} \chi_a^{\text{even}} \mathcal{R}^{-1}, \tag{19}$$

$$\chi_{a'}^{\text{odd}} = \pm \det(\mathcal{R}) \mathcal{R} \chi_a^{\text{odd}} \mathcal{R}^{-1}, \tag{20}$$

where a denotes a given site and a' is the site to which site a transforms under symmetry operation $\mathcal{R}$. In this case it is necessary to consider the full magnetic space group and atomic positions of magnetic moments. The symmetry of χ_a is determined by symmetry operations that leave site a invariant (such symmetry operations form the so-called site symmetry group), whereas the symmetry operations that transform a to a different site a' relate tensor χ_a to tensor $\chi_{a'}$.

A key conclusion that can be made from Eqs. (17) and (18) is that there can be no net SOT (or iSGE) if the system has inversion symmetry. However, from Eqs. (19) and (20) we see that even in a system with inversion symmetry there can still be a local SOT if the inversion symmetry is broken locally, i.e., there can be SOT on site a, if there is no inversion symmetry which would leave site a invariant.

To understand the dependence of SOT on the direction of magnetic moments, it is helpful to expand the SOT in the direction of magnetic moments. For a collinear magnetic material,

$$\chi_{ij}(\mathbf{n}) = \chi_{ij}^{(0)} + \chi_{ij,k}^{(1)} n_k + \chi_{ij,kl}^{(2)} n_k n_l + \cdots, \tag{21}$$

where **n** is the magnetic order parameter (the magnetization direction in ferromagnets or the Néel order parameter in antiferromagnets). The even terms in the expansion correspond to the even effective field and conversely the odd terms correspond to the odd field. The symmetry of the **n**-independent expansion tensors in Eq. (21) is determined by the symmetry group of the *nonmagnetic* system. For a global SOT in a ferromagnet or a local SOT in a bipartite antiferromagnet the following transformation rule is found for the expansion tensors:

$$\chi^{(\nu)}_{ij,mn\cdots} = \det(\mathcal{R})^{\nu-1} \mathcal{R}_{ik} \mathcal{R}^{-T}_{jl} \mathcal{R}^{-T}_{mo} \mathcal{R}^{-T}_{np\cdots} \chi^{(\nu)}_{kl,op\cdots}. \quad (22)$$

For the global case, the nonmagnetic point group has to be used, whereas for the local case, the nonmagnetic site symmetry group has to be used instead. Since there are only 21 nonmagnetic point groups with broken inversion symmetry, it is feasible to calculate all allowed leading terms of the expansion (21). This was done for the zeroth-, first-, and some second-order terms in Ciccarelli *et al.* (2016) and Železný,

TABLE I. Zeroth- and first-order terms in the expansion (21) for the point groups with broken inversion symmetry. The tensors $\chi^{(1)}$ have the spin-axis direction included: $\chi^{(1)}_{ij} = \chi^{(1)}_{ij,k}\hat{n}_k$. The x parameters can be chosen arbitrarily for each tensor. The tensors are given in Cartesian coordinate systems defined by Železný, Gao *et al.* (2017).

Crystal system	Point group	$\chi^{(0)}$	$\chi^{(1)}$
Triclinic	1	$\begin{pmatrix} x_{11} & x_{12} & x_{13} \\ x_{21} & x_{22} & x_{23} \\ x_{31} & x_{32} & x_{33} \end{pmatrix}$	$\begin{pmatrix} \hat{n}_x x_{111} + \hat{n}_y x_{112} + \hat{n}_z x_{113} & \hat{n}_x x_{121} + \hat{n}_y x_{122} + \hat{n}_z x_{123} & \hat{n}_x x_{131} + \hat{n}_y x_{132} + \hat{n}_z x_{133} \\ \hat{n}_x x_{211} + \hat{n}_y x_{212} + \hat{n}_z x_{213} & \hat{n}_x x_{221} + \hat{n}_y x_{222} + \hat{n}_z x_{223} & \hat{n}_x x_{231} + \hat{n}_y x_{232} + \hat{n}_z x_{233} \\ \hat{n}_x x_{311} + \hat{n}_y x_{312} + \hat{n}_z x_{313} & \hat{n}_x x_{321} + \hat{n}_y x_{322} + \hat{n}_z x_{323} & \hat{n}_x x_{331} + \hat{n}_y x_{332} + \hat{n}_z x_{333} \end{pmatrix}$
Monoclinic	2	$\begin{pmatrix} x_{11} & 0 & x_{13} \\ 0 & x_{22} & 0 \\ x_{31} & 0 & x_{33} \end{pmatrix}$	$\begin{pmatrix} \hat{n}_y x_1 & \hat{n}_x x_{13} + \hat{n}_z x_{12} & \hat{n}_y x_3 \\ \hat{n}_x x_5 + \hat{n}_z x_6 & \hat{n}_y x_{11} & \hat{n}_x x_4 + \hat{n}_z x_7 \\ \hat{n}_y x_{10} & \hat{n}_x x_8 + \hat{n}_z x_9 & \hat{n}_y x_2 \end{pmatrix}$
	m	$\begin{pmatrix} 0 & x_{12} & 0 \\ x_{21} & 0 & x_{23} \\ 0 & x_{32} & 0 \end{pmatrix}$	$\begin{pmatrix} \hat{n}_x x_{12} + \hat{n}_z x_9 & \hat{n}_y x_{14} & \hat{n}_x x_{13} + \hat{n}_z x_8 \\ \hat{n}_y x_3 & \hat{n}_x x_{11} + \hat{n}_z x_{10} & \hat{n}_y x_4 \\ \hat{n}_x x_7 + \hat{n}_z x_6 & \hat{n}_y x_5 & \hat{n}_x x_1 + \hat{n}_z x_2 \end{pmatrix}$
Orthorhombic	222	$\begin{pmatrix} x_{11} & 0 & 0 \\ 0 & x_{22} & 0 \\ 0 & 0 & x_{33} \end{pmatrix}$	$\begin{pmatrix} 0 & \hat{n}_z x_5 & \hat{n}_y x_4 \\ \hat{n}_z x_1 & 0 & \hat{n}_x x_6 \\ \hat{n}_y x_3 & \hat{n}_x x_2 & 0 \end{pmatrix}$
	$mm2$	$\begin{pmatrix} 0 & x_{12} & 0 \\ x_{21} & 0 & 0 \\ 0 & 0 & 0 \end{pmatrix}$	$\begin{pmatrix} \hat{n}_z x_4 & 0 & \hat{n}_x x_6 \\ 0 & \hat{n}_z x_5 & \hat{n}_y x_7 \\ \hat{n}_x x_3 & \hat{n}_y x_2 & \hat{n}_z x_1 \end{pmatrix}$
Tetragonal	4	$\begin{pmatrix} x_{11} & -x_{21} & 0 \\ x_{21} & x_{11} & 0 \\ 0 & 0 & x_{33} \end{pmatrix}$	$\begin{pmatrix} \hat{n}_z x_6 & -\hat{n}_z x_2 & \hat{n}_x x_5 - \hat{n}_y x_7 \\ \hat{n}_z x_2 & \hat{n}_z x_6 & \hat{n}_x x_7 + \hat{n}_y x_5 \\ \hat{n}_x x_4 - \hat{n}_y x_3 & \hat{n}_x x_3 + \hat{n}_y x_4 & \hat{n}_z x_1 \end{pmatrix}$
	-4	$\begin{pmatrix} x_{11} & x_{21} & 0 \\ x_{21} & -x_{11} & 0 \\ 0 & 0 & 0 \end{pmatrix}$	$\begin{pmatrix} \hat{n}_z x_5 & \hat{n}_z x_1 & \hat{n}_x x_4 + \hat{n}_y x_6 \\ \hat{n}_z x_1 & -\hat{n}_z x_5 & \hat{n}_x x_6 - \hat{n}_y x_4 \\ \hat{n}_x x_3 + \hat{n}_y x_2 & \hat{n}_x x_2 - \hat{n}_y x_3 & 0 \end{pmatrix}$
	422	$\begin{pmatrix} x_{11} & 0 & 0 \\ 0 & x_{11} & 0 \\ 0 & 0 & x_{33} \end{pmatrix}$	$\begin{pmatrix} 0 & -\hat{n}_z x_3 & -\hat{n}_y x_2 \\ \hat{n}_z x_3 & 0 & \hat{n}_x x_2 \\ -\hat{n}_y x_1 & \hat{n}_x x_1 & 0 \end{pmatrix}$
	$4\,mm$	$\begin{pmatrix} 0 & -x_{21} & 0 \\ x_{21} & 0 & 0 \\ 0 & 0 & 0 \end{pmatrix}$	$\begin{pmatrix} \hat{n}_z x_4 & 0 & \hat{n}_x x_1 \\ 0 & \hat{n}_z x_4 & \hat{n}_y x_1 \\ \hat{n}_x x_3 & \hat{n}_y x_3 & \hat{n}_z x_2 \end{pmatrix}$
	$-42m$	$\begin{pmatrix} x_{11} & 0 & 0 \\ 0 & -x_{11} & 0 \\ 0 & 0 & 0 \end{pmatrix}$	$\begin{pmatrix} 0 & \hat{n}_z x_3 & \hat{n}_y x_2 \\ \hat{n}_z x_3 & 0 & \hat{n}_x x_2 \\ \hat{n}_y x_1 & \hat{n}_x x_1 & 0 \end{pmatrix}$
Trigonal	3	$\begin{pmatrix} x_{11} & -x_{21} & 0 \\ x_{21} & x_{11} & 0 \\ 0 & 0 & x_{33} \end{pmatrix}$	$\begin{pmatrix} \hat{n}_x x_7 + \hat{n}_y x_2 + \hat{n}_z x_8 & \hat{n}_x x_2 - \hat{n}_y x_7 - \hat{n}_z x_3 & \hat{n}_x x_6 - \hat{n}_y x_9 \\ \hat{n}_x x_2 - \hat{n}_y x_7 + \hat{n}_z x_3 & -\hat{n}_x x_7 - \hat{n}_y x_2 + \hat{n}_z x_8 & \hat{n}_x x_9 + \hat{n}_y x_6 \\ \hat{n}_x x_5 - \hat{n}_y x_4 & \hat{n}_x x_4 + \hat{n}_y x_5 & \hat{n}_z x_1 \end{pmatrix}$
	312	$\begin{pmatrix} x_{11} & 0 & 0 \\ 0 & x_{11} & 0 \\ 0 & 0 & x_{33} \end{pmatrix}$	$\begin{pmatrix} \hat{n}_y x_3 & \hat{n}_x x_3 - \hat{n}_z x_4 & -\hat{n}_y x_2 \\ \hat{n}_x x_3 + \hat{n}_z x_4 & -\hat{n}_y x_3 & \hat{n}_x x_2 \\ -\hat{n}_y x_1 & \hat{n}_x x_1 & 0 \end{pmatrix}$
	$3m1$	$\begin{pmatrix} 0 & -x_{21} & 0 \\ x_{21} & 0 & 0 \\ 0 & 0 & 0 \end{pmatrix}$	$\begin{pmatrix} \hat{n}_y x_4 + \hat{n}_z x_5 & \hat{n}_x x_4 & \hat{n}_x x_2 \\ \hat{n}_x x_4 & -\hat{n}_y x_4 + \hat{n}_z x_5 & \hat{n}_y x_2 \\ \hat{n}_x x_3 & \hat{n}_y x_3 & \hat{n}_z x_1 \end{pmatrix}$

(Table continued)

TABLE I. *(Continued)*

Crystal system	Point group	$\chi^{(0)}$	$\chi^{(1)}$
Hexagonal	6	$\begin{pmatrix} x_{11} & -x_{21} & 0 \\ x_{21} & x_{11} & 0 \\ 0 & 0 & x_{33} \end{pmatrix}$	$\begin{pmatrix} \hat{n}_z x_6 & -\hat{n}_z x_2 & \hat{n}_x x_5 - \hat{n}_y x_7 \\ \hat{n}_z x_2 & \hat{n}_z x_6 & \hat{n}_x x_7 + \hat{n}_y x_5 \\ \hat{n}_x x_4 - \hat{n}_y x_3 & \hat{n}_x x_3 + \hat{n}_y x_4 & \hat{n}_z x_1 \end{pmatrix}$
	-6	$\begin{pmatrix} 0 & 0 & 0 \\ 0 & 0 & 0 \\ 0 & 0 & 0 \end{pmatrix}$	$\begin{pmatrix} \hat{n}_x x_1 + \hat{n}_y x_2 & \hat{n}_x x_2 - \hat{n}_y x_1 & 0 \\ \hat{n}_x x_2 - \hat{n}_y x_1 & -\hat{n}_x x_1 - \hat{n}_y x_2 & 0 \\ 0 & 0 & 0 \end{pmatrix}$
	622	$\begin{pmatrix} x_{11} & 0 & 0 \\ 0 & x_{11} & 0 \\ 0 & 0 & x_{33} \end{pmatrix}$	$\begin{pmatrix} 0 & -\hat{n}_z x_3 & -\hat{n}_y x_2 \\ \hat{n}_z x_3 & 0 & \hat{n}_x x_2 \\ -\hat{n}_y x_1 & \hat{n}_x x_1 & 0 \end{pmatrix}$
	6 *mm*	$\begin{pmatrix} 0 & -x_{21} & 0 \\ x_{21} & 0 & 0 \\ 0 & 0 & 0 \end{pmatrix}$	$\begin{pmatrix} \hat{n}_z x_4 & 0 & \hat{n}_x x_1 \\ 0 & \hat{n}_z x_4 & \hat{n}_y x_1 \\ \hat{n}_x x_3 & \hat{n}_y x_3 & \hat{n}_z x_2 \end{pmatrix}$
	$-6m2$	$\begin{pmatrix} 0 & 0 & 0 \\ 0 & 0 & 0 \\ 0 & 0 & 0 \end{pmatrix}$	$\begin{pmatrix} \hat{n}_y x_1 & \hat{n}_x x_1 & 0 \\ \hat{n}_x x_1 & -\hat{n}_y x_1 & 0 \\ 0 & 0 & 0 \end{pmatrix}$
Cubic	23	$\begin{pmatrix} x_{11} & 0 & 0 \\ 0 & x_{11} & 0 \\ 0 & 0 & x_{11} \end{pmatrix}$	$\begin{pmatrix} 0 & \hat{n}_z x_2 & \hat{n}_y x_1 \\ \hat{n}_z x_1 & 0 & \hat{n}_x x_2 \\ \hat{n}_y x_2 & \hat{n}_x x_1 & 0 \end{pmatrix}$
	432	$\begin{pmatrix} x_{11} & 0 & 0 \\ 0 & x_{11} & 0 \\ 0 & 0 & x_{11} \end{pmatrix}$	$\begin{pmatrix} 0 & -\hat{n}_z x_1 & \hat{n}_y x_1 \\ \hat{n}_z x_1 & 0 & -\hat{n}_x x_1 \\ -\hat{n}_y x_1 & \hat{n}_x x_1 & 0 \end{pmatrix}$
	$-43m$	$\begin{pmatrix} 0 & 0 & 0 \\ 0 & 0 & 0 \\ 0 & 0 & 0 \end{pmatrix}$	$\begin{pmatrix} 0 & \hat{n}_z x_1 & \hat{n}_y x_1 \\ \hat{n}_z x_1 & 0 & \hat{n}_x x_1 \\ \hat{n}_y x_1 & \hat{n}_x x_1 & 0 \end{pmatrix}$

Gao *et al.* (2017). The results for the zeroth- and first-order terms are given in Table I.

The lowest order even field is typically given by $\chi^{(0)}$, which corresponds to a fieldlike torque. In some cases such a term is, however, prohibited by symmetry and the lowest order even field is second order in magnetization. This is the case of the cubic zinc-blende or half-heusler crystal ferromagnets with space group $F\bar{4}3m$, for instance. Under strain, however, these materials exhibit an even field at the zeroth order in magnetization (in other words, a fieldlike torque) (Chernyshov *et al.*, 2009). In contrast, MnSi and its parent compounds adopt the $P2_13$ space group and display a fieldlike torque even without strain (Hals and Brataas, 2013b).

More generally, the connection between the SOT field and the applied electric field can be categorized in three different types illustrated in Fig. 11: Rashba and Dresselhaus coupling schemes [Figs. 11(a) and 11(b)], and a coupling such that the SOT field is collinear to the electric field that we refer to as Weyl coupling [Fig. 11(e)]. These denominations are taken in analogy with the spin textures in the momentum space of the Rashba, Dresselhaus, and Weyl spin-orbit couplings further discussed in Sec. III.D. The Rashba and Dresselhaus fields are confined to a plane and appear only for an electric field lying in the plane. They differ in how the effective field is changed when the electric field is rotated. In the case of a standard Rashba coupling, the effective field rotates in the same direction as the electric field [Fig. 11(a)], whereas in the case of a standard Dresselhaus coupling the effective field rotates in the opposite direction [Fig. 11(b)]. The generalized Rashba coupling differs

from a conventional Rashba coupling in that the angle between the electric and the effective field is not necessarily 90° [Fig. 11(c)]. The generalized Dresselhaus coupling differs from the conventional Dresselhaus coupling in that the effective field is not necessarily parallel or perpendicular to the electric field along the crystalline axes [Fig. 11(d)].

As seen in Table I, $\chi^{(1)}$ always has some nonzero components. These generate the lowest order odd field. It often has a dampinglike character, i.e., can be written as $\mathbf{B}_T \sim \mathbf{m} \times \boldsymbol{\zeta}$, where $\boldsymbol{\zeta}$ is a vector independent of magnetization. However, in some cases the first-order field does not have the dampinglike form. An example of a system where no dampinglike torque is allowed by symmetry is again cubic zinc-blende or half-heusler crystals. Even if the dampinglike torque is allowed by
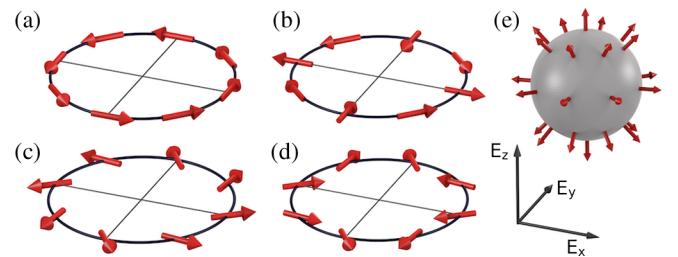

FIG. 11.   Various types of the fieldlike torques as a function of the electric field direction. The red arrows denote the corresponding effective field direction for (a) Rashba, (b) Dresselhaus, (c) generalized Rashba, (d) generalized Dresselhaus, and (e) Weyl coupling schemes.

symmetry there can be other first-order contributions. Magnetic dynamics induced by such torques can differ from the effect of a dampinglike torque and has not been studied so far.

The lowest order terms frequently describe qualitative aspects of the torque both in experiments and in the theoretical calculations. The usefulness of the lowest order term is illustrated by the fact that materials with very different electronic structures but the same symmetry have very similar SOTs. For instance this is the case of ferromagnetic (Ga,Mn)As and NiMnSb, or systems modeled by the 2D Rashba Hamiltonian, or antiferromagnets Mn$_2$Au and CuMnAs, discussed in Sec. III.F. For an accurate quantitative description of the SOT, higher order terms can be important. These are not tabulated but can be produced by the publicly available code that was used for generating Table I (Železný, 2017). This code can also be used to determine the full tensors χ_a^{even} and χ_a^{odd} for a given crystal. For the case of an interface with inversion-symmetry breaking only (e.g., in the case of a Rashba 2D gas), one obtains

$$\chi^{(0)} = x_0 \begin{pmatrix} 0 & 1 & 0 \\ -1 & 0 & 0 \\ 0 & 0 & 0 \end{pmatrix}, \qquad \chi^{(1)} = x_1 \begin{pmatrix} -\hat{n}_z & 0 & 0 \\ 0 & \hat{n}_z & 0 \\ \hat{n}_x & \hat{n}_y & 0 \end{pmatrix}. \tag{23}$$

C. Spin-orbit torques due to the spin Hall effect

The SHE-SOT contribution in bilayer systems arises from the absorption of angular momentum coming from a SHE spin current generated outside the ferromagnet, e.g., in the proximate nonmagnetic metal layer (Dyakonov and Perel, 1971). This is effectively the mechanism of STT where the polarizing ferromagnet in a trilayer device is replaced in this instance by the nonmagnetic metal (Stiles and Zangwill, 2002; Brataas *et al.*, 2012). In analogy to STT, the SHE-SOT mechanism in common metal structures is primarily dampinglike in character, assuming a full absorption of the carrier spin-angular momentum in the ferromagnet. Therefore in many experiments, the dampinglike SOT is associated with SHE, and the extracted spin Hall angle is calculated on the basis that this is the only contribution to the dampinglike SOT component. Since this is generally not the case, the spin Hall angle values extracted from these experiments should be considered only as effective phenomenological descriptions of the SOT efficiency. On the other hand, in many experiments a clear correlation between the magnitude and sign of SHE, e.g., obtained by nonlocal measurements (Morota *et al.*, 2011), and dampinglike SOT is observed. We do not review here the calculations of the SHE, which has been done elsewhere (Sinova *et al.*, 2015), and focus instead on effective theoretical treatments using the spin Hall angle as a phenomenological parameter.

The SHE-SOT is present in structures where the ferromagnet is adjacent to a nonmagnetic (Pt, W, Ta, WTe$_2$, conductive Bi$_2$Se$_3$, etc.) or magnetic metal (IrMn, PtMn, etc.). To model this torque, one needs to compute the spin density originating from this metal and diffusing into the ferromagnet. The

simplest method is to solve the drift-diffusion equation in the presence of spin-orbit coupling and match the spin currents and accumulations at the boundary between the ferromagnet and the nonmagnetic metal using, for instance, the spin mixing conductance (P. M. Haney *et al.*, 2013; Wei Chen *et al.*, 2015; Amin and Stiles, 2016b). The charge and spin currents in a nonmagnetic metal with spin-orbit coupling read (Dyakonov and Perel, 1971; Shchelushkin and Brataas, 2005; Shen, Raimondi, and Vignale, 2014; Pauyac *et al.*, 2018)

$$\mathbf{j}_c/\sigma_{\text{N}} = -\nabla\mu_c + \theta_{\text{sh}}\nabla \times \boldsymbol{\mu}, \tag{24}$$

$$(2e/\hbar)\mathcal{J}_s^i/\sigma_{\text{N}} = -\nabla\mu_i - \theta_{\text{sh}}\mathbf{e}_i \times \nabla\mu_c - \theta_{\text{sw}}\nabla \times (\mathbf{e}_i \times \boldsymbol{\mu}), \tag{25}$$

where σ_{N} is the bulk conductivity and θ_{sw} is the spin swapping coefficient (Lifshits and Dyakonov, 2009; Pauyac *et al.*, 2018) (we comment on the spin swapping term in more detail at the end of this section). $\mu_c = n/e\mathcal{N}$ and $\boldsymbol{\mu} = \mathbf{S}/e\mathcal{N}$ are the charge and spin chemical potentials, respectively, with $\mathcal{N}$ the density of states at the Fermi level. Formally, the drift-diffusion approach for the current-in-plane geometry is applicable only as long as the mean free path is much shorter than the layer thickness and assuming uniform spin Hall angle and conductivity in the nonmagnetic metal. This model also neglects interfacial spin flips or spin-memory loss (Bass and Pratt, 2007; Belashchenko, Kovalev, and Van Schilfgaarde, 2016; Dolui and Nikolic, 2017). As discussed later, this assumption is not always accurate. Using the spin mixing conductance $g^{\uparrow\downarrow}$ as a boundary condition, the spin transfer arises from the absorption of the incoming transverse spin current at the interface $\mathbf{T} = \mathcal{J}_s/t_{\text{F}}$, t_{F} being the thickness of the magnet. It is composed of two components, as described in Eq. (2), which read (P. M. Haney *et al.*, 2013)

$$\tau_{\text{DL}} = \frac{\hbar\theta_{\text{sh}}}{2e} \frac{\tilde{g}_r^{\uparrow\downarrow} + |\tilde{g}^{\uparrow\downarrow}|^2}{(1 + \tilde{g}_r^{\uparrow\downarrow})^2 + \tilde{g}_i^{\uparrow\downarrow 2}} \left(1 - \cosh^{-1}\frac{t_{\text{N}}}{\lambda_{\text{sf}}}\right)\sigma_{\text{N}}E, \tag{26}$$

$$\tau_{\text{FL}} = -\frac{\hbar\theta_{\text{sh}}}{2e} \frac{\tilde{g}_i^{\uparrow\downarrow}}{(1 + \tilde{g}_r^{\uparrow\downarrow})^2 + \tilde{g}_i^{\uparrow\downarrow 2}} \left(1 - \cosh^{-1}\frac{t_{\text{N}}}{\lambda_{\text{sf}}}\right)\sigma_{\text{N}}E. \tag{27}$$

Here we omitted the spin swapping term in Eq. (25), and $\boldsymbol{\zeta}\|\mathbf{z} \times \mathbf{j}_c$, $\mathbf{z}$ being normal to the interface. We also define the applied electric field $E = -\partial\mu_c/\partial x$, and the reduced mixing conductance $\tilde{g}^{\uparrow\downarrow} = g^{\uparrow\downarrow}\lambda_{\text{sf}}/\sigma_{\text{N}}\tanh(t_{\text{N}}/\lambda_{\text{sf}})$, while t_{N} and λ_{sf} are the thickness and spin relaxation length of the nonmagnetic metal, respectively. Finally, $\tilde{g}_r^{\uparrow\downarrow}$ and $\tilde{g}_i^{\uparrow\downarrow}$ refer to the real and imaginary parts of $\tilde{g}^{\uparrow\downarrow}$, respectively. In the limit of the small imaginary part of the mixing conductance, $\tau_{\text{DL}} \propto \eta\theta_{\text{sh}}$ and $\tau_{\text{FL}} \propto \eta\theta_{\text{sh}}g_i^{\uparrow\downarrow}/g_r^{\uparrow\downarrow}$. The transparency coefficient $\eta = g_r^{\uparrow\downarrow}/[g_r^{\uparrow\downarrow} + \sigma_{\text{N}}\tanh(t_{\text{N}}/\lambda_{\text{sf}})/\lambda_{\text{sf}}]$ accounts for the spin current transmission through the interface, with $\eta \to 1$ when $g_r^{\uparrow\downarrow} \gg \sigma_{\text{N}}/\lambda_{\text{sf}}$. Equations (26) and (27) assume that all the spin current impinging on the interface is either reflected back to the nonmagnetic metal or absorbed by the ferromagnet. Allowing for spin-memory loss at the interface opens an

additional spin dissipation channel (Bass and Pratt, 2007; Belashchenko, Kovalev, and Van Schilfgaarde, 2016; Dolui and Nikolic, 2017) and reduces the effective spin mixing conductance, leading to an *underestimation* of the spin Hall angle (Rojas-Sánchez *et al.*, 2014; Berger, Edwards, Nembach, Karis *et al.*, 2018).

These expressions, although quite extensively used to interpret experimental data, must be handled with care as they disregard any corrections emerging from thickness-dependent conductivity, spin Hall angle, and spin-dependent scattering at interfaces, and assume the simplest form of the interfacial spin mixing conductance. To overcome these limitations, several methods have been employed, such as the Boltzmann transport equation where SHE is explicitly contained in the collision integral (Engel, Halperin, and Rashba, 2005; P. M. Haney *et al.*, 2013; Amin and Stiles, 2016b), the Kubo formula with real-space Green's function in a slab geometry (Chen and Zhang, 2017), the tight-binding model with random impurity potential (Saidaoui and Manchon, 2016), or transport calculations based on first principles (Freimuth, Blügel, and Mokrousov, 2014b, 2015; Lei Wang *et al.*, 2016; Dolui and Nikolic, 2017).

Several additional features beyond the "conventional" SHE model have been identified. First, because the thickness of the nonmagnetic metal is of the same order as the mean free path (5–10 nm), the conductivity depends on the thickness of the slab (Sondheimer, 2001). In fact, it is well known that spin transport in a current-in-plane configuration is governed by mean free path effects, rather than by the spin-diffusion length (Camley and Barnas, 1989; Zhang and Levy, 1993). A direct consequence is that the spin Hall current estimated using the drift-diffusion models, Eq. (26) and (27), is generally *overestimated* (Chen and Zhang, 2017).

A second important aspect was revealed by *ab initio* calculations (Freimuth, Blügel, and Mokrousov, 2015; Lei Wang *et al.*, 2016). These studies suggest that the SHE itself can be significantly enhanced close to the interface. The computed interfacial Hall angle can be an order of magnitude larger than the bulk spin Hall angle and possibly dominate the total SHE signal. On the other hand, increasing the disorder leads to a progressive reduction of the interfacial spin Hall angle (Freimuth, Blügel, and Mokrousov, 2015). Realistic modeling based on *ab initio* simulations are further discussed in Sec. III.E.

Finally, it was recently realized that the precession of spin currents around the spin-orbit field can substantially impact the SOT. This mechanism was originally proposed by Lifshits and Dyakonov (2009) in a different context and called *spin swapping*. In this mechanism, a primary spin current with spin polarization $\mathcal{J}_s \sim \boldsymbol{\sigma}$ precesses around the spin-orbit field $\mathbf{B}_{so}$, resulting in a secondary spin current $\mathcal{J}_s \sim \boldsymbol{\sigma} \times \mathbf{B}_{so}$. This secondary spin current can be absorbed by an adjacent ferromagnet, resulting in additional SOT components. Several flavors of this scenario have been proposed, depending on the source of the primary spin current and on the nature of the spin-orbit field. Saidaoui and Manchon (2016) suggested that spin-polarized electrons scattering off the ferromagnetic layer inject a primary spin current $\mathcal{J}_s \sim \mathbf{m}$ in the nonmagnetic metal. This primary spin current precesses around the spin-orbit field oriented normal to the scattering
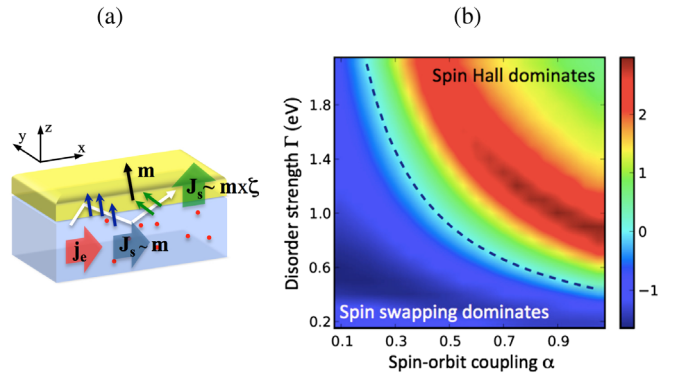

(a)   (b)

FIG. 12.   Spin precession around the spin-orbit field. (a) Schematic of the extrinsic spin swapping effect in a bilayer composed of a nonmagnetic metal (blue) and a ferromagnet (yellow) with magnetization $\mathbf{m}$. The spin current flowing from the ferromagnet into the nonmagnetic metal is polarized along $\mathbf{m}$ and precesses about the impurity-driven spin-orbit field normal to the scattering plane $\boldsymbol{\zeta}$. It produces a secondary spin current polarized along $\mathbf{m} \times \boldsymbol{\zeta}$. (b) Ratio between the magnitude of the fieldlike and dampinglike torques τ_{DL}/τ_{FL} as a function of disorder strength and spin-orbit coupling in the extrinsic spin swapping scenario. The ratio is given in logarithmic scale and the dashed line indicates $\tau_{DL} = \tau_{FL}$. Adapted from Saidaoui and Manchon, 2016.

plane, which produces a secondary spin current $\mathcal{J}_s \sim \mathbf{m} \times \boldsymbol{\zeta}$ [Fig. 12(a)]. Once absorbed into the ferromagnet, this spin swapping spin current induces a fieldlike SOT. This mechanism survives only as long as the nonmagnetic metal thickness is comparable to the mean free path, as shown in Fig. 12(b).

While the SHE-SOTs previously discussed occur in bilayers composed of a spin current source (e.g., a nonmagnetic metal) and a spin current absorber, another configuration involving a single ferromagnet was recently investigated. By computing the spin-diffusion equation in a centrosymmetric ferromagnet with spin-orbit coupling, Pauyac *et al.* (2018) showed how the interplay between SHE, spin swapping, and spin precession about the magnetic exchange can lead to local torques acting at the edges of the magnet. These local torques can nucleate reversed magnetic domains and initiate current-driven magnetization dynamics (Wang *et al.*, 2019).

D. Spin-orbit torques due to the inverse spin galvanic effect

In this section we review calculations of the SOT in 2D and 3D bulk magnetic systems. Such a torque is considered to be due to the iSGE, which refers to the electrical generation of spin density when a current flows in a system lacking (bulk or interfacial) inversion symmetry. Its reciprocal effect, the SGE, is the generation of a charge current in the presence of nonequilibrium spin density (generated, e.g., by photoexcitation). Microscopically, iSGE and SGE are associated with the presence of a spin-orbit coupling that is odd in momentum k, due to inversion-symmetry breaking (Winkler, 2003; Manchon *et al.*, 2015). As a consequence, the spin texture in momentum space becomes antisymmetric in k as shown in Fig. 5 for the Pt/Co interface. To keep the results tractable, theories usually consider simpler forms of odd-in-k spin-orbit

coupling, valid close to high symmetry points. For instance, strained zinc-blende crystals display a *k*-linear Dresselhaus spin-orbit coupling close to the Γ point (D'yakonov *et al.*, 1986),

$$\hat{H}_{\mathrm{D}} = \beta(\hat{\sigma}_x p_x - \hat{\sigma}_y p_y), \tag{28}$$

whereas interfaces display a so-called Rashba spin-orbit coupling (Vasko, 1979; Bychkov and Rashba, 1984),

$$\hat{H}_{\mathrm{R}} = \alpha_{\mathrm{R}}\hat{\boldsymbol{\sigma}} \cdot (\mathbf{p} \times \mathbf{z}). \tag{29}$$

The coefficients β and α_{R} are the Dresselhaus and Rashba parameters, respectively. In Weyl semimetals, the low-energy bulk Hamiltonian directly connects the spin with the linear momentum $\hat{H}_{\mathrm{W}} = v\hat{\boldsymbol{\sigma}} \cdot \mathbf{p}$ (Weyl, 1929; Wan *et al.*, 2011). Although the spin-momentum locking scheme of real materials is in general much more complex (see Fig. 5), these various forms of spin-orbit coupling have been widely used theoretically to study the SGE and iSGE.

SGE was first predicted by Ivchenko, Lyanda-Geller, and Pikus (1989) and observed by Ganichev *et al.* (2001, 2002). The iSGE was predicted originally by Ivchenko and Pikus (1978), followed by Aronov and Lyanda-Geller (1989) and Edelstein (1990), and observed in noncentrosymmetric systems such as tellurium (Vorobev *et al.*, 1979), strained semiconductors (Kato *et al.*, 2004a), and quantum wells (Ganichev *et al.*, 2004; Silov *et al.*, 2004; Wunderlich *et al.*, 2004, 2005). More recently, current-driven spin density has also been observed at the surface of transition metals (Zhang *et al.*, 2014; Stamm *et al.*, 2017). In magnets lacking inversion symmetry, such as zinc-blende semiconductors (Bernevig and Vafek, 2005; Garate and MacDonald, 2009; Hals, Brataas, and Tserkovnyak, 2010), or magnetic 2D electron gas with Rashba spin-orbit coupling (Tan, Jalil, and Liu, 2007; Manchon and Zhang, 2008; Obata and Tatara, 2008), the current-driven spin density can be used to control the magnetic order parameter.

The iSGE-induced SOT can be derived from the dynamics of the carrier spin density **S**, brought out of equilibrium by the applied electric field, in the presence of both magnetic exchange and spin-orbit interaction. For this discussion, let us consider the following model Hamiltonian:

$$\hat{H} = \hat{H}_0 + \hat{H}_{\mathrm{ex}} + \hat{H}_{\mathrm{so}}, \tag{30}$$

where $\hat{H}_0$ is the spin-independent part, and $\hat{H}_{\mathrm{ex}} = (\Delta/2)\hat{\boldsymbol{\sigma}} \cdot \mathbf{m}$ is the *s-d* exchange. The Heisenberg equation for the spin motion reads

$$\frac{d\mathbf{S}}{dt} = \frac{\Delta}{\hbar}\mathbf{S} \times \mathbf{m} + \frac{1}{i\hbar}\langle[\hat{\boldsymbol{\sigma}}, \hat{H}_{\mathrm{so}}]\rangle. \tag{31}$$

Here $\langle \cdots \rangle$ represents quantum-mechanical averaging over the nonequilibrium carrier states and $\langle \hat{\boldsymbol{\sigma}} \rangle = \mathbf{S}$. The SOT is obtained by taking the steady-state solution of Eq. (31) ($d\mathbf{S}/dt = 0$) into Eq. (5),

$$\mathbf{T} = \Delta\mathbf{m} \times \mathbf{S} = \frac{1}{i}\langle[\hat{\boldsymbol{\sigma}}, \hat{H}_{\mathrm{so}}]\rangle. \tag{32}$$

The right side of Eq. (32) explicitly shows the spin-orbit coupling origin of the SOT. For discerning qualitatively distinct SOT contributions (i.e., the extrinsic versus intrinsic terms introduced in Sec. III.A), we now use the middle expression.

Let us first discuss the extrinsic (intraband) contribution to the spin density which, in the limit of spin-independent disorder, corresponds to the usual Boltzmann contribution. In the limit $\hat{H}_{\mathrm{ex}} \ll \hat{H}_{\mathrm{so}}$, this term is independent of the *s-d* exchange (Edelstein, 1990; Manchon and Zhang, 2008). For illustration, we consider the Rashba spin-orbit coupling, Eq. (29), such that the spins align perpendicular to the wave vector, $\boldsymbol{\sigma}_{\mathbf{k}} \sim \mathbf{z} \times \mathbf{k}$, as illustrated in Fig. 13(a). In the absence of the electric field, $\langle \mathbf{k} \rangle = 0$, and the equilibrium distribution of these eigenstate spin vectors adds up into a zero net spin density [Fig. 13(a), top panel]. Under the applied electric field, however, the states are repopulated with a deficit or excess of left or right moving carriers with respect to the applied electric field [Fig. 13(a), bottom panel]. The steady-state nonequilibrium distribution is reached when balancing the carrier acceleration in the electric field with scattering against disorder; see Eq. (9). Because of the noncentrosymmetric spin texture of the eigenstates, the nonequilibrium distribution leads to a nonzero net spin density aligned perpendicular to the electric field $\mathbf{S} \sim \tau\alpha_{\mathrm{R}}\mathbf{z} \times \mathbf{E}$. In analogy to the Boltzmann theory of conductivity, the spin density is proportional to the momentum lifetime τ and, hence, associated with an extrinsic iSGE. Since we neglected $\hat{H}_{\mathrm{ex}}$ in the carrier Hamiltonian, the iSGE generated spin density **S** in this approximation is independent of **m** and, when introduced into the middle expression of Eq. (32), yields a fieldlike SOT $\mathbf{T}_{\mathrm{FL}} \sim \mathbf{m} \times (\mathbf{z} \times \mathbf{E})$. Incorporating the exchange field creates only a small angular dependence of an otherwise constant spin density.

Let us now consider the intrinsic (interband) contribution, assuming the same Rashba spin-orbit coupling. Such a term is labeled intrinsic because it has a weak dependence on scattering in metallic systems. This contribution can also be derived from an intuitive picture of the Bloch dynamics of carrier spins. To do so we consider for simplicity the limit $\hat{H}_{\mathrm{ex}} \gg \hat{H}_{\mathrm{so}}$ (i.e., the opposite limit than considered before). In equilibrium, the carrier spins are then approximately aligned with the exchange field $\boldsymbol{\sigma}_{\mathbf{k}} \approx s\mathbf{m}$, independent of their momentum. This is depicted in Figs. 13(b) and 13(c), bottom panels, for $\mathbf{m} \| \mathbf{E}$ and $\mathbf{m} \perp \mathbf{E}$, respectively. The Bloch equations describe the carrier spin dynamics during their acceleration in the applied electric field, i.e., between the scattering events. Without loss of generality, we take $\mathbf{E} = E_x\mathbf{x}$. For $\mathbf{m} \| \mathbf{E}$, the equilibrium effective magnetic field acting on the carrier spins due to the exchange term is $\mathbf{B}_{\mathrm{eff}}^{\mathrm{eq}} \approx (\Delta, 0, 0)$ in units of energy. During the acceleration in the applied electric field $dp_x/dt = eE_x$, and the effective magnetic field acquires a time-dependent *y* component due to $\hat{H}_{\mathrm{so}}$ for which

$$\frac{dB_{\mathrm{eff,y}}}{dt} = (\alpha_{\mathrm{R}}/\hbar)\frac{dp_x}{dt},$$

as illustrated in Fig. 13(b). For small tilts of the spins from equilibrium, the Bloch equation
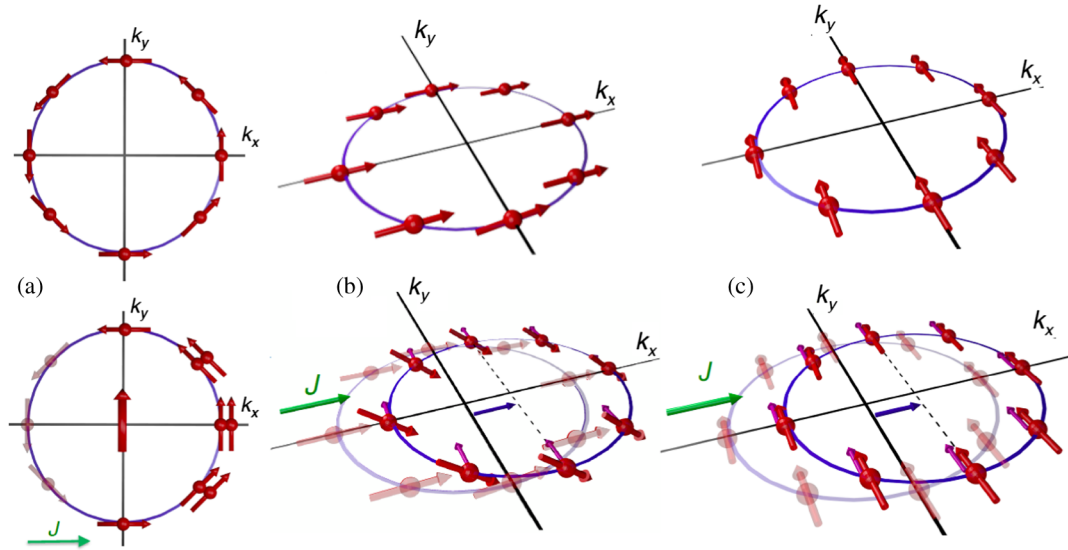
FIG. 13. (a) Top panel: Rashba spin texture for one of the chiral states in equilibrium with zero net spin density. Bottom panel: Nonequilibrium redistribution of eigenstates in an applied electric field resulting in a nonzero spin density due to broken inversion symmetry of the spin texture. When combined with the exchange coupling of the carrier spin density to magnetization, this mechanism corresponds to the extrinsic (Boltzmann transport), fieldlike iSGE-SOT. (b) Top panel: A model equilibrium spin texture in a 2D Rashba spin-orbit coupled system with an additional time-reversal symmetry breaking exchange field of a strength much larger than the spin-orbit field. In equilibrium, all spins in this case align approximately with the *x* direction of the exchange field (magnetization). Bottom panel: In the presence of an electrical current along the *x* direction the Fermi surface (circle) is displaced along the same direction. When moving in momentum space, electrons experience an additional spin-orbit field (purple arrows). In reaction to this nonequilibrium current-induced field, spins tilt and generate a uniform, nonequilibrium out-of-plane spin density. (c) Top panel: Same as in (b) for the *y* direction of the exchange field. Bottom panel: Same as in (b) but now with the current-induced spin-orbit field align with the exchange field, resulting in zero tilt of the carrier spins. (b), (c) The intrinsic (Berry curvature) dampinglike iSGE-SOT. Adapted from Kurebayashi *et al.*, 2014.

$$\frac{d\boldsymbol{\sigma_k}}{dt} = \frac{1}{\hbar}(\boldsymbol{\sigma_k} \times \mathbf{B}_{\mathrm{eff}})$$

yields $\sigma_{\mathbf{k},x} \approx s$, $\sigma_{\mathbf{k},y} \approx sB_{\mathrm{eff},y}/B_{\mathrm{eff}}^{\mathrm{eq}}$, and

$$\sigma_{\mathbf{k},z} \approx -\frac{\hbar s}{(B_{\mathrm{eff}}^{\mathrm{eq}})^2}\frac{dB_{\mathrm{eff},y}}{dt} = -\frac{s}{\Delta^2}\alpha_{\mathrm{R}}eE_x. \qquad (33)$$

The nonequilibrium spin orientation of the carriers acquires a time- and momentum-independent $\sigma_{\mathbf{k},z} = \sigma_z$ component. For a general angle $\theta_{\mathbf{m}-\mathbf{E}}$ between $\mathbf{m}$ and $\mathbf{E}$ we obtain

$$\sigma_{\mathbf{k},z}(\mathbf{m}) = \sigma_z(\mathbf{m}) \approx \frac{s}{\Delta^2}\alpha_{\mathrm{R}}eE_x\cos\theta_{\mathbf{m}-\mathbf{E}}. \qquad (34)$$

The total nonequilibrium spin density $S_z = 2g_{2\mathrm{D}}\Delta\sigma_z(\mathbf{m})$ is obtained by integrating $\sigma_{\mathbf{k},z}$ over all occupied states ($g_{2\mathrm{D}}$ is the density of states). The nonequilibrium spin density produces an out-of-plane field which exerts a torque on the in-plane magnetization. From Eqs. (32) and (34) we obtain an intrinsic dampinglike SOT (Kurebayashi *et al.*, 2014),

$$\mathbf{T}_{\mathrm{DL}} = \frac{\Delta}{\hbar}(\mathbf{m} \times S_z\mathbf{z}) \sim \mathbf{m} \times [\mathbf{m} \times (\mathbf{z} \times \mathbf{E})]. \qquad (35)$$

It is worth pointing out the analogy and differences between the intrinsic iSGE and the intrinsic SHE (Murakami, Nagaosa, and Zhang, 2003; Sinova *et al.*, 2004). In the SHE case where $\hat{H}_{\mathrm{ex}} = 0$ in the paramagnet,

$B_{\mathrm{eff}}^{\mathrm{eq}}$ depends on the angle $\theta_{\mathbf{k}}$ of the carrier momentum with respect to $\mathbf{E}$ which implies a momentum-dependent z component of the nonequilibrium spin,

$$\sigma_{\mathbf{k},z} \approx \frac{s}{\alpha_{\mathrm{R}}k^2}\alpha_{\mathrm{R}}eE_x\sin\theta_{\mathbf{k}}. \qquad (36)$$

The same spin rotation mechanism that generates the uniform bulk spin density in the case of the intrinsic iSGE in a ferromagnet [Fig. 13(b)] is responsible for the scattering-independent spin current of the SHE in a paramagnet (Sinova *et al.*, 2004). Note that the SHE spin current yields zero spin density in the bulk while a net spin density accumulates only at the edges of the conduction channel.

1. Inverse spin galvanic torque in a magnetic two-dimensional electron gas

Because of the symmetry present in most bilayer systems considered in experiments, the Rashba spin-orbit coupling given by Eq. (29) is the natural model to study, and therefore the iSGE-SOT has been alternatively called Rashba-SOT in this context. As discussed, the Rashba torque can possess two components corresponding to the fieldlike and dampinglike torques; see Eq. (2). While the origin of the fieldlike torque is well understood and consistently attributed to the extrinsic intraband iSGE (Rashba-Edelstein) effect (Edelstein, 1990), several mechanisms contribute to the dampinglike torque. The different contributions have been investigated using the

semiclassical Boltzmann transport equation (Tan, Jalil, and Liu, 2007; Manchon and Zhang, 2008; Matos-Abiague and Rodriguez-Suárez, 2009; van der Bijl and Duine, 2012; Kim, Seo *et al.*, 2012; Kyoung-Whan Kim *et al.*, 2013; Lee *et al.*, 2015) or quantum-mechanical Kubo formula approaches (Pesin and MacDonald, 2012a; Wang, Pauyac, and Manchon, 2014; Hang Li *et al.*, 2015; Qaiumzadeh, Duine, and Titov, 2015; Freimuth, Blügel, and Mokrousov, 2017).

As discussed, interband transitions produce an intrinsic dampinglike torque in the limit of weak scattering (Freimuth, Blügel, and Mokrousov, 2014b; Kurebayashi *et al.*, 2014) and can be related to the Berry curvature of the electronic band structure in the mixed spin-momentum phase space (Freimuth, Blügel, and Mokrousov, 2014b; Kurebayashi *et al.*, 2014; Lee *et al.*, 2015; Hang Li *et al.*, 2015). As a result, one can expect "hot spots" in the band structure, i.e., points where neighboring bands get very close to each other, to give a very large contribution, similar to the case of intrinsic SHE (Tanaka *et al.*, 2008). Notice that in the specific case of the pure 2D Rashba gas, at the first order in the Rashba parameter, vertex corrections cancel the intrinsic dampinglike torque unless the momentum relaxation time is spin dependent (Qaiumzadeh, Duine, and Titov, 2015; Freimuth, Blügel, and Mokrousov, 2017), similar to the cancellation occurring for the intrinsic SHE in pure 2D Rashba gas (Inoue, Bauer, and Molenkamp, 2004). Nevertheless, such cancellations are highly sensitive to this specific model band structure and can be considered as accidental, as discussed by Sinova *et al.* (2015) in the context of intrinsic SHE.

Extrinsic iSGE mechanisms related to spin scattering were also theoretically shown to generate a dampinglike component of the SOT. In Kim, Seo *et al.* (2012), the dampinglike term arises from the momentum-scattering induced spin relaxation, an effect initially proposed in metallic spin valves and domain walls (Zhang, Levy, and Fert, 2002; Zhang and Li, 2004). In fact, when a nonequilibrium spin density **S** is injected into a magnet, spin relaxation generates a corrective term of the form $\sim\beta_{\rm sf}\mathbf{m}\times\mathbf{S}$, where $\beta_{\rm sf}$ is a parameter that depends on the ratio between spin precession and spin-flip scattering. In other works, this component is obtained within a quantum kinetic formalism and ascribed to spin-dependent carrier lifetimes or to a term arising from the weak-diffusion limit which in the leading order is proportional to a constant carrier lifetime (Pesin and MacDonald, 2012a; Wang and Manchon, 2012; Wang, Pauyac, and Manchon, 2014).

Finally, we stress that the coefficients $\tau_{\rm FL,DL}$ are in principle angular dependent and display terms proportional to $\sin^{2n}\theta_{\mathbf{m}-\mathbf{E}}$, $n\in\mathbb{N}^*$. This angular dependence reflects the distortion of the band structure when changing the magnetization direction (Lee *et al.*, 2015), as well as the anisotropic spin relaxation in the system due to D'yakonov-Perel's mechanism (Pauyac *et al.*, 2013).

2. Noncentrosymmetric bulk magnets

The dilute magnetic semiconductor (Ga,Mn)As has been a test-bed material for observing and exploring the bulk SOT. Hence, unlike in the case of bilayer systems, all torques observed in these bulk materials arise internally with no
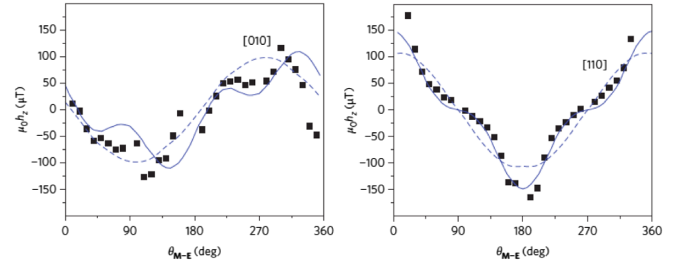

FIG. 14.   Microscopic modeling of the intrinsic SOT in bulk (Ga, Mn)As. The solid lines correspond to the numerical results and the symbols correspond to the experimental data. The dashed lines correspond to the free electron approximation. From Kurebayashi *et al.*, 2014.

contribution from externally injected spin currents. Current-driven torques in dilute magnetic semiconductors were first studied by Bernevig and Vafek (2005). They considered the Kohn-Lüttinger Hamiltonian in the spherical approximation, augmented by a *k*-linear spin-orbit coupling term arising from strain of the form $\lambda\cdot\hat{\mathbf{J}}$, where $\hat{\mathbf{J}}$ is the total angular momentum operator, $\lambda_x = C_4(\epsilon_{xy}k_y - \epsilon_{xz}k_z)$ and $\lambda_{y,z}$ are obtained from cyclic permutation of indices. The current-driven spin density reads

$$\mathbf{S} = -\frac{e\tau}{\hbar^2}\frac{15}{4}\left(\sum_{s=\pm1}\frac{\sqrt{3n/\pi}}{(\gamma_1 + 2s\gamma_2)^{3/2}}\right)^{2/3}(e\mathbf{E}\cdot\mathbf{\nabla_k})\lambda, \quad (37)$$

where *n* is the charge density. Because in their calculation they did not consider an exchange coupling directly, the torque induced by this iSGE is therefore a fieldlike torque. The intrinsic dampinglike torque originating from interband transitions was later proposed by Kurebayashi *et al.* (2014) to interpret the experimental observation of such a dampinglike torque in (Ga,Mn)As; see Fig. 14. The theoretical investigation of SOT in dilute magnetic semiconductors was also pursued by Hang Li *et al.* (2013, 2015). Besides some subtleties related to the complex band structure, the numerical results they obtained qualitatively confirm the general picture obtained in the context of the magnetic Dresselhaus and Rashba gases.

Apart from (Ga,Mn)As, the SOT has been studied in several other bulk systems. One of them is the ferromagnet NiMnSb (Ciccarelli *et al.*, 2016). This half-heusler material has the same crystalline symmetry as zinc blende (Ga,Mn)As; however, it is not a dilute-moment random alloy like (Ga,Mn)As, but a dense-moment ordered compound. Despite these differences, the SOTs found in NiMnSb are quite similar to those in (Ga,Mn)As because the torque is mostly determined by the lowest order terms in the magnetization expansion, Eq. (21), which are the same for the two systems.

3. Spin-orbit torques in magnetic textures

When itinerant electrons flow in a magnetic domain wall, their spin slightly misaligns with the local texture, resulting in STT (Tatara and Kohno, 2004; Zhang and Li, 2004); see Sec. VI for details. When spin-orbit coupling is present, the flowing spins experience an additional precession around the

spin-orbit field, resulting in enhanced spin torque (Nguyen, Skadsem, and Brataas, 2007; Stier, Egger, and Thorwart, 2013; Stier and Thorwart, 2015; Yuan and Kelly, 2016). An interesting consequence is the emergence of additional torque components that are proportional to the magnetization gradient (Hals and Brataas, 2013b). Some of these contributions can be directly assigned to the presence of the anomalous Hall effect and anisotropic magnetoresistance (van der Bijl and Duine, 2012), while others genuinely come from the interplay between magnetic texture and precession around the spin-orbit field. For instance, Kim, Seo *et al.* (2012) and Kyoung-Whan Kim *et al.* (2013) showed that in the presence of Rashba spin-orbit coupling, a 2D magnetic texture (i.e., a magnetic skyrmion or vortex) experiences a torque of the form $\mathbf{T} \propto (\boldsymbol{\nabla} \cdot \mathbf{m})[(\mathbf{z} \times \mathbf{u}) \cdot \boldsymbol{\nabla}]\mathbf{m}$, where $\mathbf{u}$ is the direction of injection. Such SOTs open interesting perspectives for the electrical manipulation of magnetic textures, discussed in Sec. VI, but have received little attention to date.

E. *Ab initio* modeling of spin-orbit torques in bilayer systems

Following after the studies in bulk magnets, the SOTs have been most extensively studied experimentally in NM/FM bilayer (or multilayer) structures (Sec. IV). Theories of SOT in bilayer systems based on iSGE and SHE as exposed in the previous sections present two major limitations. First, both mechanisms formally apply in very distinct situations: in the widely used diffusive model, SHE in the nonmagnetic metal is considered uniform, neglecting semiclassical size effects and possible variation of the spin Hall angle close to the interface (Freimuth, Blügel, and Mokrousov, 2015; Lei Wang *et al.*, 2016b), as discussed in Sec. III.C. In contrast, iSGE in magnetic multilayers is often modeled using the Rashba interaction, Eq. (29), which applies to 2D gases and ideally sharp interfaces only. Both approaches overlook the details of the interfacial orbital overlap, which can be quite subtle in transition-metal interfaces and lead to enhanced orbital moment and related spin-orbit phenomena (Blügel and Bihlmayer, 2007; Grytsyuk *et al.*, 2016; Marmolejo-Tejada *et al.*, 2017).

To overcome these issues, SOTs in Co/Pt bilayer systems have been computed within the relaxation time approximation using an *ab initio* density functional theory description of the whole bilayer structure (Paul M. Haney *et al.*, 2013; Freimuth, Blügel, and Mokrousov, 2014b, 2015). Paul M. Haney *et al.* (2013) focused on the extrinsic iSGE, disregarding the SHE and intrinsic contributions to iSGE. In spite of the high complexity of the band structure (see Fig. 5), these calculations confirm the intuitive picture elaborated based on the Rashba model. In particular, they showed that SOT is mostly driven by spin-orbit coupling in Pt, while the influence of induced magnetization is negligible; see Fig. 15. Moreover, the torque acquires a nontrivial angular dependence and depends dramatically on the quality of the interface. Using a similar method, neglecting intrinsic contributions to both SHE and iSGE, Amin, Zemen, and Stiles (2018) computed the interfacial spin current in Co/Cu bilayers, obtaining both fieldlike and dampinglike components, as well as an additional torque $\mathbf{T} \propto \boldsymbol{\zeta} \times (\mathbf{m} \times \boldsymbol{\zeta})$. These results were confirmed by Freimuth, Blügel, and Mokrousov (2018).
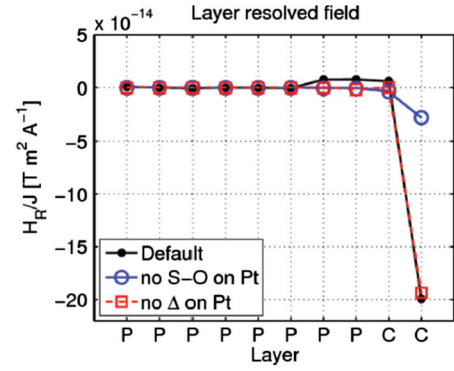

FIG. 15. Layer-resolved fieldlike torque in normal Pt/Co(111) (black symbols), when turning off the induced magnetization on Pt (red symbols) and when turning off the spin-orbit coupling on Pt (blue symbols). From Paul M. Haney *et al.*, 2013.

Alternatively, Freimuth, Blügel, and Mokrousov (2014b) and Géranton *et al.* (2015) computed the full Kubo-Bastin formula, thereby accounting for both intrinsic SHE and intrinsic iSGE. These calculations confirmed that SOTs are composed of both fieldlike and dampinglike torques, the latter being produced by interband transitions only; see Fig. 16. An interesting aspect revealed through these calculations is the high sensitivity of SOTs to interfacial engineering. In fact, they found that by capping the Co layer by either Al or O atoms, the dampinglike torque is only slightly affected (its magnitude changes up to 50%—see Fig. 16) while the fieldlike torque is dramatically altered and can even change its sign. In a follow-up work, Freimuth, Blügel, and Mokrousov (2015) reported an enhancement of SHE close to the interface, also predicted by Lei Wang *et al.* (2016) for Pt/NiFe. These studies suggest that the assumption of the uniform spin Hall angle made in the diffusive approach may be valid in the strong disorder limit only. Similar results were recently obtained by Mahfouzi and Kioussis (2018) in Co/Pt and Co/Pd bilayers.
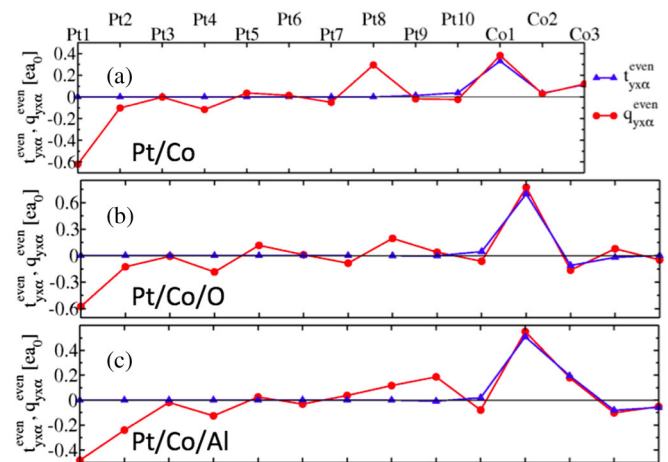

FIG. 16. Layer-resolved dampinglike torque $t_{x\text{-}y}^{\text{even}}$ (blue symbols) and spin current $q_{x\text{-}y}^{\text{even}}$ (red symbols) in (a) Pt/Co, (b) Pt/Co/O, and (c) Pt/Co/Al. From Freimuth, Blügel, and Mokrousov, 2014b.

Whereas all these studies are based on the relaxation time approximation (i.e., the effect of impurities is captured by a homogeneous broadening), Wimmer *et al.* (2016) calculated the torque in Pt/Fe$_x$Co$_{1-x}$/Cu superlattices using the Kubo-Bastin formula and coherent potential approximation to account for the alloy disorder. This allows for treating extrinsic scattering mechanisms (i.e., side jump and skew scattering) within the framework of density functional theory. The influence of impurities and phonon scattering on the SOT was investigated by Géranton *et al.* (2016) within the Korringa-Kohn-Rostoker Green's function method. Finally, Belashchenko, Kovalev, and Van Schilfgaarde (2019) investigated the angular dependence of the SOTs in Co/Pt bilayers using a two-terminal nonequilibrium Green's function approach with real-space Anderson disorder, uncovering a planar Hall-like contribution.

F. Spin-orbit torques in antiferromagnets

Since the first proposal of STT in antiferromagnets (Núñez *et al.*, 2006; MacDonald and Tsoi, 2011), several configurations have been theoretically investigated to enable large spin-torque efficiency. In the course of the search for such torques it was realized that in order to efficiently manipulate the order parameter of a collinear, bipartite antiferromagnet one needs a torque that corresponds to a staggered effective magnetic field, i.e., a field with an opposite sign on the two magnetic sublattices. Such a field, unlike a homogeneous field, couples directly to the Néel order. The torque resulting from a staggered field has been referred to as a Néel SOT (Železný *et al.*, 2014; Železný, Gao *et al.*, 2017).

The dampinglike torque due to a spin current (from a SHE or a ferromagnetic polarizer) is a Néel torque, assuming that it has the same form on each magnetic sublattice as in ferromagnets, i.e., $\mathbf{T}_a = \tau_{\text{DL}}\mathbf{m} \times (\mathbf{m} \times \boldsymbol{\zeta})$. This form of the torque was predicted theoretically (Gomonay, Kunitsyn, and Loktev, 2012; Cheng *et al.*, 2014; Železný *et al.*, 2014) and it was shown that it can indeed efficiently manipulate the antiferromagnetic order (Gomonay and Loktev, 2010; Gomonay, Kunitsyn, and Loktev, 2012). A recent drift-diffusion theory confirmed that spin current injected from an adjacent ferromagnetic polarizer or induced by SHE indeed generates such a Néel dampinglike torque (Manchon, 2017). An experimental indication of the presence of the SHE generated SOT in an NM/AF bilayer was reported by Reichlova *et al.* (2015).

The bulk SOT can also have the Néel order form if the current-induced spin density has an opposite sign on the two sublattices (Železný *et al.*, 2014). In a collinear antiferromagnet, the two sublattices with opposite magnetizations are connected by some symmetry operation. Typically, this is either a translation or an inversion. This symmetry operation combined with time reversal is then a symmetry of the magnetic system which, using Eqs. (19) and (20), relates the current-induced spin densities on the two sublattices (Železný, Gao *et al.*, 2017). If the sublattices are connected by translation then

$$\chi_{B,a}^{\text{even}} = \chi_{B,b}^{\text{even}}, \tag{38}$$

$$\chi_{B,a}^{\text{odd}} = -\chi_{B,b}^{\text{odd}}, \tag{39}$$

where a and b denote the two sublattices. If they are connected by inversion

$$\chi_{B,a}^{\text{even}} = -\chi_{B,b}^{\text{even}}, \tag{40}$$

$$\chi_{B,a}^{\text{odd}} = \chi_{B,b}^{\text{odd}}. \tag{41}$$

Thus in both cases there exists both a staggered component and a uniform component of the current-induced spin density and the corresponding effective field. For the magnetic dynamics only the staggered component has an appreciable effect for the achievable magnitudes of the effective fields (a few mT). Since the component that is staggered is different in the two cases, the dynamics will differ. As discussed in Sec. III.B, the even field typically has a fieldlike character, whereas the odd field is commonly dampinglike. Thus in systems where magnetic sublattices are connected by translation we can expect an efficient dampinglike torque, whereas in systems where the sublattices are connected by inversion a fieldlike torque is expected.

SOTs in antiferromagnets were first studied in two tight-binding models (Železný *et al.*, 2014; Železný, Gao *et al.*, 2017): (i) the antiferromagnetic 2D Rashba gas and (ii) the bulk Mn$_2$Au. Both systems possess collinear antiferromagnetism. Together they illustrate the two main types of symmetry previously discussed. In the Rashba model the two sublattices are connected by translation and thus the lowest order Néel SOT has a dampinglike character. In the Mn$_2$Au crystal, on the other hand, the two sublattices are connected by inversion and the lowest order Néel torque has consequently a fieldlike character. Microscopic calculations based on the Kubo formula with constant relaxation time indeed show that the Néel SOT in the Rashba model is primarily dampinglike, whereas in Mn$_2$Au it is predominantly of fieldlike character.

The origin of the fieldlike torque in the Mn$_2$Au crystal can be understood in terms of the symmetry of the nonmagnetic crystal. Without magnetism, the crystal has inversion symmetry and thus there is no net current-induced spin density. Yet, the Mn sublattices each have locally broken inversion symmetry and thus can have current-induced spin densities that have to be precisely opposite. An intuitive explanation of this behavior is that the local inversion breaking is opposite for the two sublattices and thus the induced spin densities are also opposite. When magnetism is added these opposite spin densities generate a staggered effective field. In the Rashba model, the inversion breaking is the same for both sublattices and thus the field generating the fieldlike torque is not staggered. On the other hand, the field generating the dampinglike torque is staggered, since it is proportional to the magnetic moment which is staggered in the antiferromagnet. The fieldlike torque in Mn$_2$Au has a Rashba-like symmetry, i.e., the effective field is on each sublattice proportional to $\boldsymbol{\zeta}$. This is because the local symmetry of the Mn sublattices is the same as that of the 2D Rashba model. Additional symmetry analysis for various types of crystalline antiferromagnets was

provided by Železný, Gao *et al.* (2017) and Watanabe and Yanase (2018).

Following the calculations based on tight-binding models, the SOT was also calculated in antiferromagnets using density functional theory. Such calculations were done for Mn_2Au (Železný, Gao *et al.*, 2017) and CuMnAs (Wadley *et al.*, 2016), which has a symmetry analogous to Mn_2Au. These results agree well with the tight-binding calculations in terms of the magnetization and current dependence and in addition show a relatively large torque. The magnitude of the effective field is around 2 mT per 10^7 Acm^{-2} current density for Mn_2Au and 3 mT per 10^7 Acm^{-2} for CuMnAs. The switching attributed to this fieldlike Néel order torque has been observed in CuMnAs (Wadley *et al.*, 2016) and subsequently in Mn_2Au (Bodnar *et al.*, 2018; Meinert, Graulich, and Matalla-Wagner, 2018; Zhou *et al.*, 2018).

G. Spin-orbit torques in topological insulators

Topological insulators are a class of materials displaying intriguing properties such as insulating bulk and conductive chiral and helical surfaces (Hasan and Moore, 2011; Qi and Zhang, 2011; Wehling, Black-Schaffer, and Balatsky, 2014). Considering the large spin-charge conversion efficiency recently reported in these systems (see Sec. IV.C.4), they deserve special attention. The category of topological materials we are interested in is characterized by time-reversal symmetry and helical surface states: their low-energy surface states are represented by a Dirac Hamiltonian of the form $\sim p_i \sigma_j$; see Fig. 8. When electrons flow on the surface of these systems, they acquire a nonequilibrium spin density, similar to the case of the 2D Rashba gas, as demonstrated in a Bi_2Se_3 slab using *ab initio* calculations (Chang *et al.*, 2015). Since the strength of the spin-momentum coupling is quite large ($\sim 4 \times 10^{-10}$ eV m at Bi_2Se_3 surfaces, comparable to Bi/Ag surfaces, and 2 orders of magnitude larger than in InAlAs/InGaAs 2D gases), iSGE is expected to be very large. In addition, the absence of bulk conduction in ideal topological insulators further strongly enhances the spin-charge conversion efficiency.

Spin-charge conversion processes in topological insulator/insulating ferromagnet bilayers have been studied by several authors (Fujimoto and Kohno, 2014; Linder, 2014; Sakai and Kohno, 2014; Taguchi, Shintani, and Tanaka, 2015; Tserkovnyak, Pesin, and Loss, 2015). The low-energy Hamiltonian reads $\hat{H} = v\hat{\boldsymbol{\sigma}} \cdot (\hat{\mathbf{p}} \times \mathbf{z}) + (\Delta/2)\hat{\boldsymbol{\sigma}} \cdot \mathbf{m}$, where the first term models the Dirac cone and the second term is the exchange. This model applies when the Dirac states are preserved, so typically when the topological insulator surfaces are interfaced with magnetic insulators (Lang *et al.*, 2014; Mingda Li *et al.*, 2015; Katmis *et al.*, 2016). The eigenenergies read

$$\epsilon_k^s = s\sqrt{\left(vk_x + \frac{\Delta}{2}m_y\right)^2 + \left(vk_y - \frac{\Delta}{2}m_x\right)^2 + \frac{\Delta^2}{4}m_z^2}. \quad (42)$$

When $m_z \neq 0$ the surface states are gapped, whereas when $m_z = 0$, the origin of the band dispersion is shifted only in the $\mathbf{k}$ plane. If the Fermi energy lies in the gap, a quantum anomalous Hall effect emerges, accompanied by a quantized magnetoelectric effect $\mathbf{S} = -(e\hbar/2\pi v)\mathbf{E}$ (Qi, Hughes, and Zhang, 2008; Nomura and Nagaosa, 2011). On the other hand, when the Fermi level lies above the gap, the system is metallic and the SOT possesses both fieldlike and dampinglike components of the form (Garate and Franz, 2010; Ndiaye *et al.*, 2017)

$$\mathbf{T} = \tau_{FL}\mathbf{m} \times \boldsymbol{\zeta} + \tau_{DL}m_z\mathbf{m} \times (\mathbf{z} \times \boldsymbol{\zeta}), \quad (43)$$

where $\boldsymbol{\zeta} \| \mathbf{z} \times \mathbf{E}$. While the fieldlike torque arises from the conventional extrinsic iSGE, the dampinglike torque arising from the intrinsic interband contribution is proportional to m_z and therefore *vanishes* when the magnetization lies in the plane of the surface, in sharp contrast with the usual dampinglike torque given in Eq. (2) (Ndiaye *et al.*, 2017).

These calculations are based on the 2D Dirac gas model, i.e., assuming that the transport is confined to the interface and that surface states remain intact in the presence of the proximate ferromagnetic layer. Such a model presents two major drawbacks though. First, orbital hybridization between the transition metal and the topological insulator substantially alters the surface states at Fermi energy. The presence of magnetic adatoms shifts the Dirac cone downward in energy (Honolka *et al.*, 2012; Scholz *et al.*, 2012; Ye *et al.*, 2012), and favors the presence of additional metallic bands with Rashba-like character across the Fermi level (Jia Zhang *et al.*, 2016; Marmolejo-Tejada *et al.*, 2017).

A second limitation comes from the 3D nature of the transport. Indeed, most experiments involve topological insulators with sizable bulk conductivity, suggesting that bulk states might participate in the spin-charge conversion mechanism. Spin transport in such systems was recently investigated using a drift-diffusion model (Fischer *et al.*, 2016), a nonequilibrium Green's function technique (Mahfouzi, Nikolić, and Kioussis, 2016), and a Kubo formula on a slab geometry (Ghosh and Manchon, 2018). The first two studies show that spin diffusion in the ferromagnet and spin-flip scattering at the interface can enhance the dampinglike torque. The latter work accounts for interfacial and bulk transport on equal footing and demonstrates that a large dampinglike torque is driven by the Berry curvature of the interfacial states, whereas the SHE of the bulk states is inefficient.

Finally, spin-orbit charge pumping, the reciprocal effect of SOT, has also been investigated theoretically in topological insulators (Ueda *et al.*, 2012; Mahfouzi, Nagaosa, and Nikolić, 2014), providing a charge current of the form

$$\mathbf{j}_c = \chi_{DL}m_z\frac{\partial}{\partial t}\mathbf{m} + \chi_{FL}\mathbf{z} \times \frac{\partial}{\partial t}\mathbf{m}$$

(Ndiaye *et al.*, 2017), where $\tau_{DL,FL} = \chi_{DL,FL}E$. A direct consequence of this current is the induction of an anisotropic magnetic damping on the ferromagnetic layer (Yokoyama, Zang, and Nagaosa, 2010).

SOT and spin-orbit charge pumping have also been studied in various configurations involving 2D topological insulators (Soleimani *et al.*, 2017). These studies reveal that SOT experiences a significant enhancement depending on the topological phase (Mahfouzi *et al.*, 2010; Li and Manchon,

2016): the emergence of edge currents promotes a quantized charge pumping when the magnetization is perpendicular to the plane. Such investigations have been recently extended to antiferromagnetic 2D topological insulators, where time reversal combined with a half unit cell translation is a symmetry of the system which preserves topological protection, despite the broken time-reversal symmetry of the magnetic state (Ghosh and Manchon, 2017).

SOTs have also been theoretically studied in magnetic 2D hexagonal lattices such as, but not limited to, graphene, silicene, germanene, stanene, transition-metal dichalcogenides, etc. (Dyrdał and Barnas, 2015; Li, Wang, and Manchon, 2016). The parametric dependencies of the torque in these materials do not significantly differ from the one obtained with the Rashba model. Nonetheless, in these systems the low-energy transport occurs mostly through two independent valleys, which opens the possibility to obtain valley-dependent SOTs.

H. Other spin-orbit torques

1. Anisotropic magnetic tunnel junctions

MTJs composed of a single ferromagnet with interfacial spin-orbit coupling display tunneling anisotropic magnetoresistance, i.e., a change of resistance when varying the magnetization direction (Gould *et al.*, 2004; Park *et al.*, 2008); see Fig. 17(a). One naturally expects that spin-polarized electrons impinging on the spin-orbit coupled interface precess around the spin-orbit field, resulting in a torque on the local magnetization (A. Manchon, 2011). This SOT is of the form given by Eq. (2) with $\boldsymbol{\zeta} = \mathbf{z}$. The fieldlike torque possesses an equilibrium contribution [which is nothing but the perpendicular magnetic anisotropy (Aurelien Manchon, 2011)] and the dampinglike torque is purely non-equilibrium. Both torques are linear as a function of the bias voltage, but their magnitude is quadratic in the Rashba parameter; see Fig. 17. A similar idea was proposed by Mahfouzi, Nagaosa, and Nikolic (2012) by considering a topological insulator as a tunnel barrier.

2. Spin-transfer torque assisted by spin-orbit coupling

When a spin-polarized current penetrates into a ferromagnet with spin-orbit coupling, the spin momentum precesses around an effective field that is the sum of the exchange
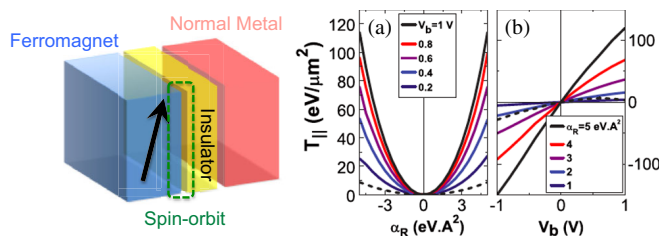

FIG. 17. Left: Schematics of a MTJ composed of a ferromagnet and a nonmagnetic metal separated by a tunnel barrier. Spin-orbit coupling is present at the interface between the ferromagnet and the tunnel barrier. Right: (a) Rashba dependence and (b) bias dependence of the dampinglike torque. Adapted from A. Manchon, 2011.
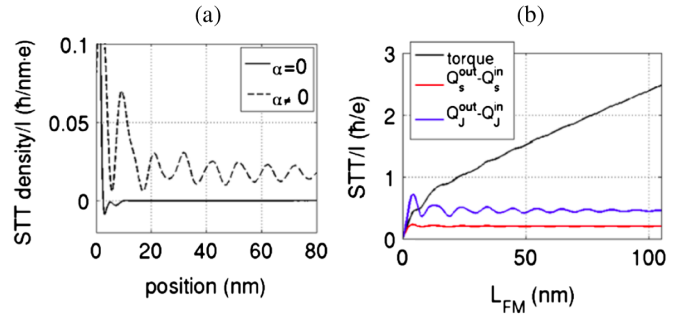

FIG. 18. (a) Spatial profile of the transverse spin density injected in the free layer of a (Ga,Mn)As-based MTJ in the presence and absence of spin-orbit coupling in the band structure; (b) spin-torque efficiency as a function of the free layer thickness. Adapted from Haney and Stiles, 2010.

and spin-orbit fields. This precession results in additional angular dependences of the SOT in Rashba (Lee *et al.*, 2015) and Kohn-Lüttinger systems as previously discussed (Li *et al.*, 2013; Kurebayashi *et al.*, 2014). Interestingly, Haney and Stiles (2010) showed that in a metallic spin valve where spin-orbit coupling is present, such a precession results in an overall STT enhancement. Considering the general Hamiltonian, Eq. (30), with $\hat{H}_{\mathrm{so}} = \xi \hat{\mathbf{L}} \cdot \hat{\boldsymbol{\sigma}}$, the total angular momentum $\hat{\mathbf{J}} = \hat{\mathbf{L}} + \hat{\boldsymbol{\sigma}}$ obeys the continuity equation

$$\frac{d\hat{\mathbf{J}}}{dt} - \boldsymbol{\nabla} \cdot \boldsymbol{\mathcal{J}}_{\mathbf{J}} = -\hat{\boldsymbol{\tau}}_{\mathrm{STT}} - \hat{\boldsymbol{\tau}}_{\mathrm{lat}}, \tag{44}$$

where $\boldsymbol{\mathcal{J}}_{\mathbf{J}}$ is the current density tensor for the total angular momentum, $\hat{\boldsymbol{\tau}}_{\mathrm{STT}}$ is the STT, and $\hat{\boldsymbol{\tau}}_{\mathrm{lat}} = i\langle[\hat{H}, \hat{\mathbf{L}}]\rangle/\hbar$ is the mechanical torque. The latter is nothing but the precession of itinerant spins around the spin-orbit field, such that the total spin torque in a spin valve survives away from the interface; see Fig. 18(a). Because of this additional precession, the total torque extends over the whole thickness of the free layer, as displayed in Fig. 18(b). A similar effect has been identified in magnetic domain walls where spin-orbit coupling enhances spin reflection and thereby STT (Nguyen, Skadsem, and Brataas, 2007; Yuan and Kelly, 2016).

I. Open theoretical questions

After a decade of theoretical progress, the key mechanisms giving rise to SOTs are now well understood at the qualitative level. Although the involved mechanisms are very different (SHE, iSGE, etc.), they can all be unified using Eq. (5), i.e., any SOT can be associated with a current-induced spin density. The various mechanisms differ in the way this spin density is generated. In the iSGE, the spin density is generated locally, whereas in the other mechanisms (SHE, spin swapping, etc.), it is due to spin currents that transfer spin-angular momentum from one part of the system to another. In addition, when a magnetic texture is present, the SOTs acquire new components that depend on the spatial gradient of the magnetization. The key ingredients in all these mechanisms are inversion-symmetry breaking and the spin-orbit coupling.

The general form of the torques can be determined using symmetry analysis.

Nonetheless, a number of challenges remain to be addressed on the theory side. First of all, quantitative agreement between theory and experiments is still missing. While important progress has been made using density functional theory (Freimuth, Blügel, and Mokrousov, 2014b; Géranton *et al.*, 2015; Wimmer *et al.*, 2016), most calculations adopt a simplified, unrealistic model of scattering. Including realistic disorder (structural imperfections, interfacial roughness), but also scattering from phonons and magnons will certainly improve such calculations. Moreover, understanding the interplay between bulk transport and interfacial effects, as well as the impact of interfacial orbital hybridization in magnetic multilayers will lead to the design of better SOT devices. These tasks require the development of accurate first-principles quantum transport methods (Nikolić *et al.*, 2018).

Comprehensive first-principles models would be particularly useful in the context of novel materials. Among these, topological materials such as topological insulators and Weyl semimetals display exotic surface states with strong spin-orbit coupling and are regarded as promising for SOT generation. However, we lack an accurate understanding of how proximate transition metals modify these surface states (Jia Zhang *et al.*, 2016; Marmolejo-Tejada *et al.*, 2017) and how bulk and surface transport cooperate to produce large SOTs (Ghosh and Manchon, 2018). Another important class of materials exhibiting remarkable properties is the antiferromagnets. While the basic principles of SOTs and current-driven dynamics are understood, a proper description of the magnetic texture and dynamics of realistic, disordered antiferromagnets is still lacking. In addition, noncollinear antiferromagnets such as Mn_3X compounds host a variety of novel phenomena, such as the AHE (Nakatsuji, Kiyohara, and Higo, 2015) or "magnetic SHE" (Železný, Zhang *et al.*, 2017; Kimata *et al.*, 2019), that could be exploited in the context of SOT. These various aspects call for further theoretical endeavors.

Although the single-particle density functional theory provides a good description of the electronic structure of most transition metals and semiconductors, it fails in describing strongly correlated systems, such as Mott or Kondo insulators (Cohen, Mori-Sanchez, and Yang, 2008; Jones, 2015). Utilizing more advanced many-body approaches, such as the dynamical mean field theory, might thus be necessary for an accurate description of the SOT in such materials. These calculations are, however, numerically very expensive. We note also that Eq. (5) relies on a density functional theory description, and a more general expression that would be valid even in a many-body system has not yet been established.

The SOT in bilayer systems is often explained in terms of a spin current, which provides useful (but sometimes misleading) insight into the physics at stake. This concept is, however, controversial on a theoretical level. In the presence of spin-orbit coupling, the spin-angular momentum is not a conserved quantity and adopting the conventional definition of the spin current tensor $j_{s,i}^j \sim \{\hat{s}_i, \hat{v}_j\}$ can give rise to dissipationless equilibrium spin currents (Rashba, 2003). For instance, in centrosymmetric crystals Shi *et al.* (2006) circumvented this hurdle by defining the spin current tensor $j_{s,i}^j \sim (d/dt)\{\hat{s}_i, \hat{r}_j\}$,

accounting for a "torque dipole" term that ensures overall spin conservation. Until now, this new definition, restricted to centrosymmetric crystals, has not been widely adopted and the question of its applicability to heterostructures remains open. Another way to consider this problem would be to compute the current of total angular momentum (An *et al.*, 2012). However, doing so complicates the problem because the total angular momentum of the electronic system alone is not conserved as it interacts with phonons and magnons.

Along this line of thought, the orbital analogs of spin phenomena, such as the orbital Hall effect (Tanaka *et al.*, 2008; Go *et al.*, 2018) and the orbital iSGE (Yoda, Yokoyama, and Murakami, 2018), have attracted attention, but their possible connection to the SOT is yet to be explored. Unlike the SHE and the iSGE, the orbital effects exist even in the absence of spin-orbit coupling. When spin-orbit coupling is present, these effects can in principle couple to the magnetic moments and thus contribute to the SOT (Go and Lee, 2019). This indicates a route for the optimization of SOT via orbital engineering. The recent claim of "maximal," Rashba spin splitting suggests a direction toward this end (Sunko *et al.*, 2017).

IV. SPIN-ORBIT TORQUES IN MAGNETIC MULTILAYERS

This section reviews recent experimental progress in the measurement and characterization of SOT in multilayer systems. We first introduce the phenomenological description of SOT commonly used in experiments (Sec. IV.A) and the main techniques employed to measure SOT (Sec. IV.B). Next, we present a survey of different layered materials, namely, nonmagnetic metals, semiconductors, and topological insulators coupled to either ferromagnets, ferrimagnets, or antiferromagnets (Sec. IV.C), summarizing the most salient features of the SOT observed in these systems. Finally, we describe the SOT-induced magnetization dynamics (Sec. IV.D) and switching (Sec. IV.E), and conclude by highlighting examples and perspectives for the implementation of SOT in magnetic devices (Sec. IV.F).

A. Phenomenological description

Current injection in heterostructures composed of a magnetic layer adjacent to a nonmagnetic conductor with either bulk or interfacial spin-orbit coupling gives rise to a transverse spin density $\zeta \| \mathbf{z} \times \mathbf{j}_c$ at the interface of the magnetic layer. This spin density induces both dampinglike and fieldlike SOT components, as shown in Fig. 19(a), and described by Eq. (2). For experimental purposes, it is useful to introduce two effective magnetic fields $\mathbf{B}_{\mathrm{DL,FL}}$, which correspond to the dampinglike and fieldlike torques and are defined by $\mathbf{T}_{\mathrm{DL,FL}} = \mathbf{M} \times \mathbf{B}_{\mathrm{DL,FL}}$. The advantage of the effective field formulation in the SOT characterization is that their action on the magnetization can be directly compared to that of a reference external field of known magnitude and direction. To the lowest order in the magnetization, for a current $\mathbf{j}_c \| \mathbf{x}$ and assuming C_v symmetry (see below), Eq. (2) gives

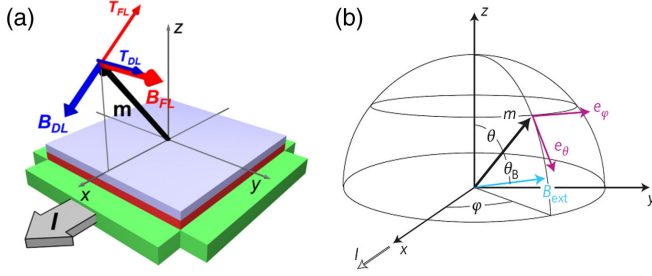$$\mathbf{B}_{\mathrm{FL}} = B_{\mathrm{FL}}\mathbf{y}, \tag{45}$$

FIG. 19. (a) Spin-orbit torques and corresponding effective fields measured in Pt/Co/AlO$_x$ layers when the magnetization is tilted parallel to the current direction. (b) Schematic of the coordinate system.

$$\mathbf{B}_{\mathrm{DL}} = B_{\mathrm{DL}}\mathbf{m} \times \mathbf{y}, \qquad (46)$$

where the field amplitudes are simply $B_{\mathrm{FL}} = \tau_{\mathrm{FL}}$ and $B_{\mathrm{DL}} = \tau_{\mathrm{DL}}$ if the torques are calculated for the unitary magnetization $\mathbf{m}$, as assumed in Eq. (2).[1] Thus, for positive values of the SOT coefficients τ_{FL} and τ_{DL}, $\mathbf{B}_{\mathrm{FL}}\|\mathbf{y}$, whereas $\mathbf{B}_{\mathrm{DL}}$ rotates clockwise in the *x-z* plane, corresponding to $\mathbf{T}_{\mathrm{DL}}\| - \mathbf{y}$. Figure 19(a) shows the orientation of the torques and effective fields for the model system Pt/Co/AlO$_x$, in which $\tau_{\mathrm{FL}} > 0$ and $\tau_{\mathrm{DL}} < 0$ (Garello *et al.*, 2013). Typical values of $B_{\mathrm{FL,DL}}$ in NM/FM systems are in the range 0.1–10 mT for a current density $j_c = 10^7$ A/cm^2. Note also that the Oersted field due to the current flowing in the nonmagnetic layer produces an additional field $B_{\mathrm{Oe}} \approx \mu_0 j_c t_N/2$ antiparallel (parallel) to $\mathbf{y}$ for bottom (top) stacking relative to the magnetic layer.

In the typical NM/FM bilayer geometry shown in Fig. 19(a), the SOTs are interfacial torques whose magnitude, to a first approximation, does not depend on the thickness t_F of the ferromagnet. However, the measurable effects of the SOTs on the magnetization, namely, B_{FL} and B_{DL}, scale inversely with t_F because the magnetic inertia is proportional to the volume of the ferromagnet. Keeping into account the proportional relationship between SOTs and the injected current, it is thus useful to define the spin-torque efficiencies

$$\xi^j_{\mathrm{DL,FL}} = \frac{2e}{\hbar} M_{\mathrm{s}} t_F \frac{B_{\mathrm{DL,FL}}}{j_c}, \qquad (47)$$

where M_{s} is the saturation magnetization. The parameters $\xi^j_{\mathrm{DL,FL}}$ represent the ratio of the effective spin current absorbed by the ferromagnet relative to the charge current injected in the nonmagnetic metal layer and can thus be considered as effective spin Hall angles for a particular combination of nonmagnetic metal and ferromagnet. In the pure SHE-SOT picture, ξ^j_{DL} is equal to the bulk spin Hall angle of the nonmagnetic metal in the limit of a transparent interface and negligible spin-memory loss. Although the SOT efficiencies are useful parameters to compare the strength of the SOT in different systems, ambiguities remain on how to estimate j_c in

[1]To emphasize the direction of the effective fields in perpendicularly magnetized layers, B_{FL} and B_{DL} are sometimes called "transverse field" (H_{T}) and "longitudinal field" (H_{L}), respectively (Junyeon Kim *et al.*, 2013).

layered heterostructures. While some consider j_c to be the average current density, others apply a parallel resistor model to separate the currents flowing in the nonmagnetic metal and ferromagnetic layers. However, thickness inhomogeneities and interface scattering can significantly alter the current distribution in bilayer systems relative to such a model (Chen and Zhang, 2017). Even in homogeneous films, the conductivity is a strong function of the thickness (Fuchs, 1938; Sambles, 1983) so that j_c changes in the bulk and interface regions of a conductor. For these reasons, the current normalization should be performed with care. Alternatively, it is possible to measure the torque efficiency per unit electric field (Nguyen, Ralph, and Buhrman, 2016)

$$\xi^E_{\mathrm{DL,FL}} = \frac{2e}{\hbar} M_{\mathrm{s}} t_F \frac{B_{\mathrm{DL,FL}}}{E} = \xi^j_{\mathrm{DL,FL}}/\rho, \qquad (48)$$

where $E = \rho j_c$ is the electric field driving the current, which is independent of the sample thickness and can be easily adjusted in voltage-controlled experiments. Note that, in the framework of the SHE-SOT model, ξ^E_{DL} can be considered as an effective spin Hall conductivity.

Equations (45) and (46) correspond to the lowest order terms of the SOT, which are sufficient to describe many experimental results, at least on a qualitative level. On a more general level, however, higher order terms in the magnetization are allowed by symmetry. The typical polycrystalline metal bilayers have C_v symmetry, corresponding to broken inversion symmetry along the $\mathbf{z}$ axis and in-plane rotational symmetry. For such systems, the torques can be decomposed into the following terms (Garello *et al.*, 2013):

$$\mathbf{T}_{\mathrm{FL}} = \left[\tau^{\{0\}}_{\mathrm{FL}} + \sum_{n\geq 1}\tau^{\{2n\}}_{\mathrm{FL}}(\sin\theta)^{2n}\right]\mathbf{m} \times \mathbf{y} \\ + \mathbf{m} \times (\mathbf{m} \times \mathbf{z})m_x\sum_{n\geq 1}\tau^{\{2n\}}_{\mathrm{FL}}(\sin\theta)^{2(n-1)}, \quad (49)$$

$$\mathbf{T}_{\mathrm{DL}} = \tau^{\{0\}}_{\mathrm{DL}}\mathbf{m} \times (\mathbf{m} \times \mathbf{y}) + m_x\mathbf{m} \times \mathbf{z}\sum_{n\geq 1}\tau^{\{2n\}}_{\mathrm{DL}}(\sin\theta)^{2(n-1)}, \\ (50)$$

where θ is the polar angle of the magnetization defined in Fig. 19(b). Equation (50) is general and does not depend on the particular mechanism, SHE or iSGE, responsible for the spin density. In a material displaying additional symmetries, such as epitaxial films or single crystals, additional angular dependencies arise (Hals and Brataas, 2013a; Wimmer *et al.*, 2016; Železný, Gao *et al.*, 2017). This complex dependence of the SOT on the magnetization direction is best captured by writing the effective fields in spherical coordinates,

$$\mathbf{B}_{\mathrm{DL}} = B^\theta_{\mathrm{DL}}\cos\varphi\,\mathbf{e}_\theta - B^\varphi_{\mathrm{DL}}\cos\theta\sin\varphi\,\mathbf{e}_\varphi, \qquad (51)$$

$$\mathbf{B}_{\mathrm{FL}} = -B^\theta_{\mathrm{FL}}\cos\theta\sin\varphi\,\mathbf{e}_\theta - B^\varphi_{\mathrm{FL}}\cos\varphi\,\mathbf{e}_\varphi, \qquad (52)$$

where $\mathbf{e}_\theta$ and $\mathbf{e}_\varphi$ are the polar and azimuthal unit vectors, respectively, and $B^\theta_{\mathrm{DL,FL}}$ and $B^\varphi_{\mathrm{DL,FL}}$ are functions of the magnetization orientation, defined by the angles θ and φ

[see Fig. 19(b)]. In polycrystalline bilayers with C_{2v} symmetry, the angular dependence of the polar components simplifies to a Fourier series expansion of the type $B_{\mathrm{DL,FL}}^{\theta} = B_{\mathrm{DL,FL}}^{\{0\}} + B_{\mathrm{DL,FL}}^{\{2\}}\sin^2\theta + B_{\mathrm{DL,FL}}^{\{4\}}\sin^4\theta + \cdots$. The azimuthal components, on the other hand, are found by experiments to be only weakly angle dependent and are given by $B_{\mathrm{DL,FL}}^{\varphi} \approx B_{\mathrm{DL,FL}}^{\{0\}}$ (Garello *et al.*, 2013).

B. Measurement techniques

Experimental measurements of SOT rely on probing the effect of the electric current on the orientation of the magnetization, e.g., by inducing resonant and nonresonant oscillations, switching, or domain wall motion. Schematically, one must first determine the magnetization angle as a function of the amplitude and phase of the applied current and then extract the effective magnetic fields that are responsible for the observed dynamics. In electrical and optical measurements, the magnetization dynamics is detected through changes of the transverse or longitudinal conductivity, which are mainly due to the AHE and AMR, but also include the linear spin Hall magnetoresistance (SMR) (Nakayama *et al.*, 2013; Kim *et al.*, 2016), linear Rashba-Edelstein magnetoresistance (Kobs *et al.*, 2011; Nakayama *et al.*, 2016), as well as nonlinear magnetoresistance terms proportional to the current-induced spin density (Avci, Garello, Ghosh *et al.*, 2015; Avci, Garello, Mendil *et al.*, 2015; Olejník *et al.*, 2015; Yasuda *et al.*, 2016, 2017; Avci *et al.*, 2018). Further, current injection always results in magnetothermal effects due to the thermal gradients induced by Joule heating and asymmetric heat dissipation (Avci, Garello *et al.*, 2014), which affect the conductivity proportionally to j_c^2. The thermal gradients that develop along ($\nabla_x T$) or perpendicular to the magnetic layer ($\nabla_z T$) contribute to the conductivity through the anomalous Nernst effect (ANE) and, to a smaller extent, through the spin Seebeck effect and the inverse spin Nernst effect. The direction of the induced voltage is $\sim \boldsymbol{\nabla} T \times \mathbf{m}$, which modifies both the longitudinal ($\sim m_y$) and transverse conductivities ($\sim m_x$). The relative influence of these effects on SOT measurements depends on the system under investigation and experimental technique. The AMR, AHE, and ANE usually dominate the magnetization dependence of the conductivity and can be properly separated owing to their different symmetry and magnetic field dependence (Garello *et al.*, 2013; Avci, Garello *et al.*, 2014) or frequency-dependent optical response (Montazeri *et al.*, 2015; Fan *et al.*, 2016). In the following, we describe the three main techniques used to characterize the SOT measurements: harmonic Hall voltage analysis, spin-torque ferromagnetic resonance (ST-FMR), and magneto-optical Kerr effect (MOKE). Less precise SOT estimates can be obtained from magnetization switching and domain wall displacements, which are discussed separately in Secs. IV.E and VI.

1. Harmonic Hall voltage analysis

This method detects the harmonic response of the magnetization to a low frequency ac current, typically up to a few kHz. Originally, this approach was developed by assuming the simplest form of fieldlike torque (Pi *et al.*, 2010) and
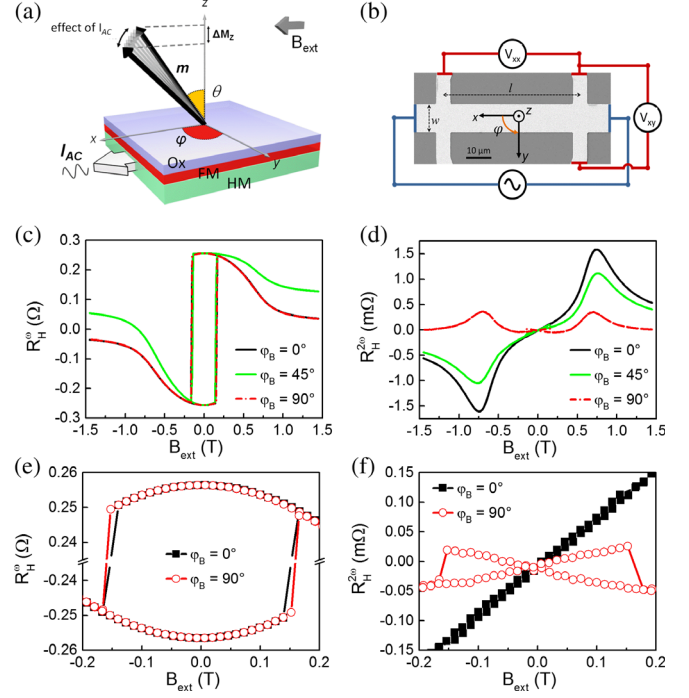

FIG. 20. (a) Schematic of the effect of an ac current on the magnetization and (b) experimental setup for harmonic Hall voltage measurements. (c) R_{xy}^{ω} and (d) $R_{xy}^{2\omega}$ of a Pt(5 nm)/Co(1 nm)/AlO$_x$ layer measured with a sinusoidal current of amplitude $j_c = 10^7$ A/cm^2 and external magnetic field applied at $\varphi_B = 0°$, 45°, and 90°. (e), (f) Closeup of the curves in (c), (d) showing the field range where the small angle approximation can be applied. From Baumgartner, 2018.

neglecting the dampinglike torque and the transverse AMR [the planar Hall effect (PHE)]. It was soon extended to the components of the torques accounting for both the AHE and PHE (Garello *et al.*, 2013; Junyeon Kim *et al.*, 2013; Hayashi *et al.*, 2014), as well as for the torque angular dependence (Garello *et al.*, 2013; Qiu *et al.*, 2014) and magnetothermal effects (Avci, Garello *et al.*, 2014; Ghosh *et al.*, 2017). SOT measurements are performed by analyzing the second harmonic Hall voltage that arises due to the homodyne mixing of the ac current with the Hall resistance modulated by the oscillations of the magnetization induced by the SOTs; see Fig. 20(a). Since the magnetization dynamics is much faster than the current frequency ω, the magnetization is assumed to be in quasistatic equilibrium at all times, at a position determined by the sum of the anisotropy field, external magnetic field, and current-induced fields. To first order in the current, the time-dependent Hall resistance $R_{xy}(t)$ is given by

$$R_{xy}[\mathbf{B}_{\mathrm{ext}} + \mathbf{B}_I(t)] \approx R_{xy}(\mathbf{B}_{\mathrm{ext}}) + \frac{dR_{xy}}{d\mathbf{B}_I} \cdot \mathbf{B}_I \sin(\omega t), \quad (53)$$

where $\mathbf{B}_{\mathrm{ext}}$ is the external magnetic field and $\mathbf{B}_I = \mathbf{B}_{\mathrm{DL}} + \mathbf{B}_{\mathrm{FL}} + \mathbf{B}_{\mathrm{Oe}}$ is the effective current-induced field due to the sum of the dampinglike and fieldlike SOT and the Oersted field. The Hall voltage $V_{xy}(t) = R_{xy}(t)I_0\sin(\omega t)$ then reads

$$V_{xy}(t) \approx I_0[R_{xy}^0 + R_{xy}^{\omega}\sin(\omega t) + R_{xy}^{2\omega}\cos(2\omega t)], \quad (54)$$

where I_0 is the current amplitude,

$$R_{xy}^0 = \frac{1}{2}\frac{dR_{xy}}{d\mathbf{B}_I} \cdot \mathbf{B}_I,$$

$$R_{xy}^\omega = R_{xy}(\mathbf{B}_\text{ext}),$$

and

$$R_{xy}^{2\omega} = -\frac{1}{2}\frac{dR_\omega}{d\mathbf{B}_I} \cdot \mathbf{B}_I + R_{\nabla T}^{2\omega}$$

are the zero, first, and second harmonic components of R_{xy}, respectively. The first harmonic term, shown in Fig. 20(c) as a function of the external field, is analogous to the dc Hall resistance and given by

$$R_{xy}^\omega = R_\text{AHE}\cos\theta + R_\text{PHE}\sin^2\theta\sin(2\varphi), \quad (55)$$

where R_AHE and R_PHE are the anomalous and planar Hall coefficients. This term serves two purposes, namely, to determine the polar angle of the magnetization using Eq. (55) when $\varphi = 0°, 90°$ and to measure the susceptibility of the magnetization to the magnetic field, providing self-calibration to the SOT measurement. The second harmonic term includes the SOT modulation of the Hall resistance as well as an extra contribution due to Joule heating, $R_{\nabla T}^{2\omega}$. In general, the two contributions may have a comparable magnitude and must be separated by either symmetry or magnetic field-dependent measurements (Avci, Garello *et al.*, 2014; Ghosh *et al.*, 2017). Assuming that $R_{\nabla T}^{2\omega}$ is negligible or has been subtracted from $R_{xy}^{2\omega}$, it is straightforward to show that

$$R_{xy}^{2\omega} = A_\theta\mathbf{B}_I \cdot \mathbf{e}_\theta + A_\varphi\mathbf{B}_I \cdot \mathbf{e}_\varphi, \quad (56)$$

where

$$A_\theta = \frac{dR_{xy}^\omega}{dB_\text{ext}}[\sin(\theta_B - \theta)]^{-1}$$

and

$$A_\varphi = R_\text{PHE}\sin^2\theta\frac{d\sin(2\varphi)}{d\varphi}[\sin\theta_B\cos(\varphi_B - \varphi)B_\text{ext}]^{-1}.$$

Here θ_B and φ_B are the polar and azimuthal angles of the applied magnetic field. Equation (56) allows one to find the polar and azimuthal components of B_DL and B_FL as a function of the magnetization angle by measuring the dependence of $R_{xy}^{2\omega}$ on B_ext. Figure 20(d) shows an example of $R_{xy}^{2\omega}$ measured at $\varphi_B = 0°$ and $90°$. These curves are, respectively, odd and even with respect to magnetization reversal, reflecting the different symmetry of B_DL and B_FL (Garello *et al.*, 2013). Because the dampinglike torque is larger when $\mathbf{m}$ lies in the x-z plane, whereas the fieldlike torque tends to align $\mathbf{m}$ toward y, measurements taken at $\varphi_B = 0°$ ($\varphi_B = 90°$) reflect the character of the dampinglike (fieldlike) effective fields. In general, four independent measurements at different azimuthal angles are required to determine the four effective field components in Eqs. (51) and (52).

In uniaxial and easy plane systems the number of independent measurements can be reduced to 2, typically at $\varphi_B = 0$, $\pi/2$ or $\varphi_B = \pi/4$, $3\pi/4$ (Garello *et al.*, 2013; Avci, Garello *et al.*, 2014). A further simplification is achieved using the small angle approximation, which is valid for perpendicularly magnetized samples when the magnetization deviates by at most a few degrees from the z axis (Junyeon Kim *et al.*, 2013; Hayashi *et al.*, 2014). In this case, $R_{xy}^{2\omega}$ varies linearly with the external field, as shown in Fig. 20(f) and the SOTs are extracted by performing two sets of measurement at $\varphi_B = 0$ and $\pi/2$,

$$B_\text{DL} = -\frac{2}{1-4r^2}(b_x + 2rb_y), \quad (57)$$

$$B_\text{FL} = -\frac{2}{1-4r^2}(b_y + 2rb_x), \quad (58)$$

where $r = R_\text{PHE}/R_\text{AHE}$ is the ratio between planar and anomalous Hall coefficients,

$$b_i = \frac{\partial R_{xy}^{2\omega}}{\partial B_\text{ext}} \Big/ \frac{\partial^2 R_{xy}^\omega}{\partial B_\text{ext}^2}$$

is measured for $B_\text{ext}\|i = x, y$, and the partial derivatives are calculated by linear fits of the curves shown in Fig. 20(f). This approximation provides only the lowest order contribution to the SOTs. However, because of its simple implementation, it is widely used for characterizing the SOTs in systems with perpendicular anisotropy. Harmonic Hall voltage measurements can also be generalized to angular scans of the magnetization at constant external field, which is particularly suited for in-plane magnetized samples (Avci, Garello *et al.*, 2014), thus providing a versatile and sensitive method to characterize the SOTs in a variety of systems.

2. Spin-torque ferromagnetic resonance

This method consists of exciting the magnetization of the ferromagnet using a radio-frequency (rf) charge current. The magnetization of the sample is excited through the spin torque and exhibits FMR when varying either the applied magnetic field or the current magnitude. This concept was initially developed in the context of MTJs (Tulapurkar *et al.*, 2005; Kubota *et al.*, 2008; Sankey *et al.*, 2008) and spin valves (Sankey *et al.*, 2006) and more recently extended to the case of ultrathin magnetic bilayers (Liu *et al.*, 2011; Liu, Pai *et al.*, 2012; Berger, Edwards, Nembach, Karenowska *et al.*, 2018) and bulk noncentrosymmetric magnetic semiconductors (Fang *et al.*, 2011; Kurebayashi *et al.*, 2014).

The dc voltage that develops across the sample [Fig. 21(a)] arises from the mixing of the rf current and the rf AMR due to the oscillating magnetization. It corresponds to the zero harmonic component in Eq. (54), which is strongly amplified due to the resonant magnetization dynamics. This rectified voltage gives information on the physical parameters of the magnetic material as well as on the nature of the torques that drive the excitation. For an in-plane system with AMR driven
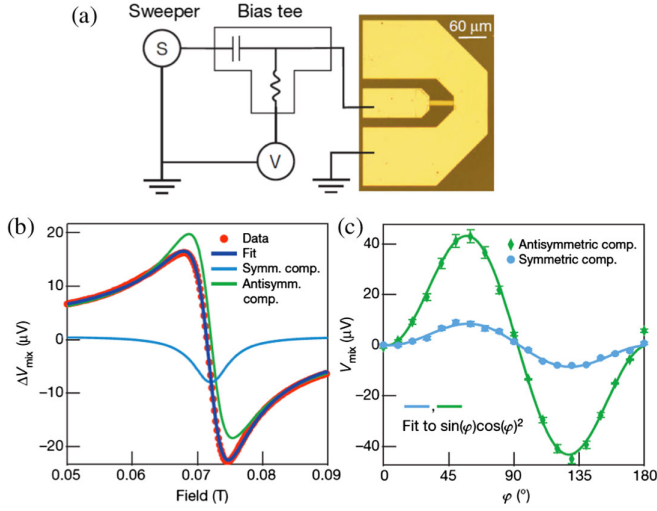
FIG. 21. (a) Schematic of the circuit used for the ST-FMR measurement and the sample contact geometry. (b) Measured ST-FMR at room temperature with microwave frequency $\omega/2\pi = 58$ GHz for $\text{Bi}_2\text{Se}_3(8\ \text{nm})/\text{Ni}_{80}\text{Fe}_{20}(16\ \text{nm})$. A fixed microwave power of 5 dBm is absorbed by the device ($I_{\text{rf}} = 7.7 \pm 1.1$ mA) and B is oriented at an angle $\varphi = \pi/4$ from the current direction. The lines are fits to Eq. (59) showing the symmetric and antisymmetric resonance components. (c) Measured dependence on the magnetic field angle φ for the symmetric and antisymmetric resonance components for a different sample. Adapted from Mellnik *et al.*, 2014.

by SOTs, the mixing voltage reads (Liu *et al.*, 2011; Reynolds *et al.*, 2017)

$$V_{\text{mix}} = -\frac{\gamma^2}{2M_s} I_{\text{rf}} \frac{\partial}{\partial \varphi} R \cos \varphi_B [\tau_{\text{DL}} F_S(B) + \tau_{\text{FL}} F_A(B)], \quad (59)$$

$$F_S(B) = \frac{\alpha \omega^2 (2B + \mu_0 M_s)}{(\omega^2 - \omega_0^2)^2 + \alpha^2 \gamma^2 \omega^2 (2B + \mu_0 M_s)^2}, \quad (60)$$

$$F_A(B) = \frac{\gamma^2 B (B + \mu_0 M_s)^2 - \omega^2 (B + \mu_0 M_s)}{(\omega^2 - \omega_0^2)^2 + \alpha^2 \gamma^2 \omega^2 (2B + \mu_0 M_s)^2}, \quad (61)$$

where ω is the frequency of the rf current I_{rf} and $\omega_0 = \gamma \sqrt{B(B + \mu_0 M_s)}$ is the resonance frequency. In Eq. (59), we remind one that the torque $\tau_{\text{DL,FL}}$ is in units of eV/m^3. The first contribution has a symmetric Lorentzian shape ($\sim F_S$) that is directly proportional to the dampinglike torque, while the second has an antisymmetric shape ($\sim F_A$), providing information about the fieldlike torque (including the Oersted field torque). A picture of the experimental apparatus is given in Fig. 21(a), together with the field-dependent and angular-dependent mixing voltages in Figs. 21(b) and 21(c), respectively. This method is used extensively to probe torques in magnetic bilayers with in-plane magnetization, as well as in noncentrosymmetric bulk magnets, as explained in Sec. V. ST-FMR is the reciprocal to spin pumping, where the field-excited precessing magnetization pumps a spin current in the adjacent nonmagnetic metal (Tserkovnyak, Brataas, and Bauer, 2002a; Saitoh *et al.*, 2006).

Similar to other techniques, applying this method to ultrathin bilayer systems requires extreme care. First, the amplitude of the rf current generating the torques needs to be precisely calibrated using a network analyzer. Such a calibration might require thickness-dependent measurements to characterize possible size-dependent effects (Nguyen, Ralph, and Buhrman, 2016). Second, Eqs. (59) and (61) account only for the rectification arising from AMR, but other sources such as SMR can also contribute to the mixing voltage (Nakayama *et al.*, 2013), which should be properly accounted for (P. Wang *et al.*, 2016; Wenxu Zhang *et al.*, 2016). Third, the phase difference between the rf current and the rf field can also have a significant impact on the output signal (Harder *et al.*, 2011). We refer the interested reader to the specialized literature for more information (Harder, Gui, and Hu, 2016). A fourth issue is that this method assumes the simplest form of the torques, Eq. (2), neglecting the angular dependence of SOTs (Garello *et al.*, 2013).

3. Magneto-optic Kerr effect

The MOKE allows for detecting the in-plane and out-of-plane components of the magnetization through the rotation of the light polarization upon reflection from a magnetic surface (Qiu and Bader, 2000). MOKE microscopy, with a wavelength-limited resolution of about 1 μm, has been used extensively to characterize SOT-induced domain nucleation and displacement (Miron *et al.*, 2010; Emori *et al.*, 2013; Ryu *et al.*, 2013; Safeer *et al.*, 2016) as well as the current-induced spin density in bare Pt and W layers (Stamm *et al.*, 2017). MOKE-based detection schemes have also been used to estimate the SOT amplitude by measuring the oscillations of the magnetization induced by an ac current in thin metal bilayers (Xin Fan *et al.*, 2014).

Vector measurements of the SOTs are based on the separate calibration of the first- and second-order magneto-optic coefficients $f_\perp$ and $f_\parallel$, which parametrize the coupling of the light to the out-of-plane and in-plane magnetization, respectively (Montazeri *et al.*, 2015; Fan *et al.*, 2016). Such a technique measures the dampinglike and fieldlike components of the SOT as a function of the magnetization angle via the polar and quadratic MOKE response, respectively, using only normally incident light; see Fig. 22(a). Similar to the Hall resistance, Eq. (53), the Kerr rotation measured during the ac current injection can be Taylor expanded as

$$\theta_K[\mathbf{B}_{\text{ext}} + \mathbf{B}_I(t)] \approx \theta_K(\mathbf{B}_{\text{ext}}) + \frac{d\theta_K}{d\mathbf{B}_I} \cdot \mathbf{B}_I \sin(\omega t). \quad (62)$$

Here the first term is the equilibrium Kerr angle given by $\theta_K = f_\perp m_z + f_\parallel [(1/2)(m_y^2 - m_x^2)\sin 2\phi_p + m_x m_y \cos 2\phi_p]$, with ϕ_p the angle between the light polarization and $\mathbf{B}_{\text{ext}}$, and the second term results in the differential Kerr signal $\Delta\theta_K = (d\theta_K/dI)I_0$ due to the current-induced fields. In analogy with the harmonic Hall voltage analysis technique, measurements of $\Delta\theta_K$ are mostly sensitive to changes of m_z. Thus, measurements taken with $\mathbf{B}_{\text{ext}} \| \mathbf{x}$ reflect the strength of the dampinglike effective field,

$$\Delta\theta_K = \frac{f_\perp B_{\text{DL}}}{B_{\text{ext}} - B_K} + \frac{f_\parallel \cos 2\phi_p (B_{\text{FL}} + B_{\text{Oe}})}{B_{\text{ext}}}, \quad (63)$$
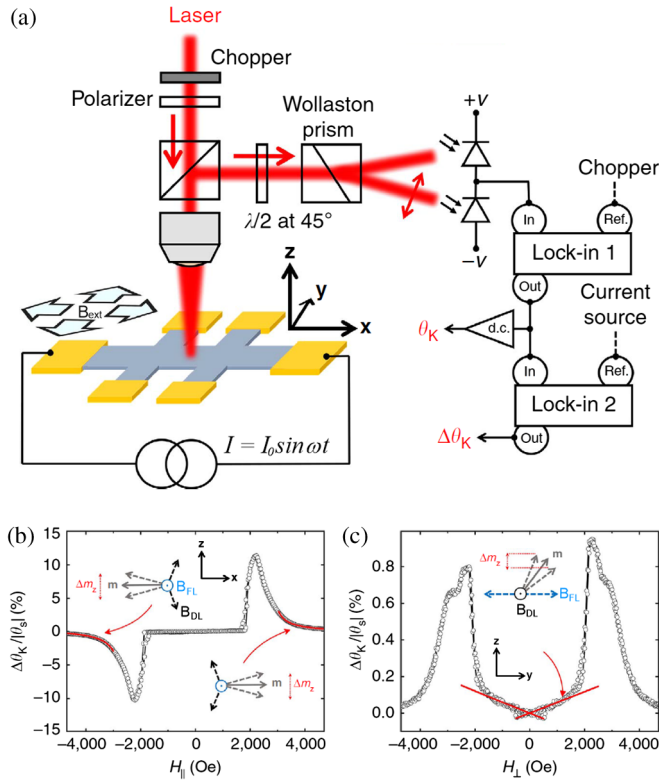
(a)

(b)

(c)

FIG. 22. (a) Schematic of a MOKE setup for SOT detection. (b), (c) Differential Kerr angle $\Delta\theta_K$ measured on a Ta(5 nm)/ CoFeB(1.1 nm)/MgO(2.0 nm) trilayer with perpendicular magnetic anisotropy for (b) $\mathbf{B}_{\text{ext}}\|\mathbf{j}_c$ and (c) $\mathbf{B}_{\text{ext}}\perp\mathbf{j}_c$ with current amplitude $j_c = 4.6 \times 10^6$ A cm^{-2}. Adapted from Montazeri *et al.*, 2015.

where B_K is the magnetic anisotropy field and $f_\| \ll f_\perp$. Conversely, measurements taken with $\mathbf{B}_{\text{ext}}\|\mathbf{y}$ reflect the strength of the fieldlike effective field,

$$B_{\text{FL}} = \frac{-2\partial(\Delta\theta_K)/\partial B_{\text{ext}}}{\partial^2\theta_K/\partial B_{\text{ext}}^2}. \quad (64)$$

Figure 22(b) shows that $\Delta\theta_K$ exhibits an antisymmetric (symmetric) line shape consistent with the symmetry of B_{DL} (B_{FL}) under magnetization reversal, in close analogy with $R_{xy}^{2\omega}$; see Fig. 20(d). SOT vector measurements performed by MOKE agree well with harmonic Hall voltage (Montazeri *et al.*, 2015) and ST-FMR measurements (Fan *et al.*, 2016) and can be used to characterize the SOT in metallic as well as insulating ferromagnets. An advantage of this technique is that it is less sensitive to thermoelectric and inductive effects compared to all-electrical SOT probes, and that it offers spatial resolution comparable to the wavelength of the probing laser beam.

C. Materials survey

1. Ferromagnet/nonmagnetic metal layers

The most studied SOT systems are composed of a metallic ferromagnet deposited on a nonmagnetic metal layer, often capped by an amorphous or crystalline oxide layer. These systems present strong dampinglike and fieldlike SOTs, of the order of a few mT per 10^7 A/cm^2 ($\xi^j \approx 0.1$, see Table II), are easy to fabricate, and compatible with established processing of magnetic materials for memory applications. An early experimental observation of the dampinglike SOT in ferromagnetic metals was reported by Ando *et al.* (2008) in a Pt/NiFe bilayer resonantly excited by an external microwave field, by measuring the change of magnetic damping upon injection of a dc current. This effect was attributed to the SHE of the Pt layer and later extended to the excitation of FMR upon injection of an rf current (Liu *et al.*, 2011). Evidence for the fieldlike SOT was first reported by Miron *et al.* (2010) by observing that the current-induced nucleation of magnetic domains in perpendicularly magnetized Pt/Co/AlO$_x$ wires is either enhanced or quenched by applying an in-plane magnetic field at an angle of $\pm 90°$ relative to the current. This effect was attributed to the action of a Rashba-like effective field and later quantitatively estimated by harmonic Hall voltage analysis measurements (Pi *et al.*, 2010; Garello *et al.*, 2013).

A major breakthrough was achieved in 2011 when bipolar magnetization switching was demonstrated in perpendicular Pt/Co/AlO$_x$ dots (Miron, Garello *et al.*, 2011), establishing the relevance of SOT for applications. Miron, Garello *et al.* (2011) observed that the symmetry of the switching field corresponds to a dampinglike torque consistent with either the SHE or the iSGE, and argued that the SHE of Pt alone could not account for the magnitude of the torque. Other experiments favored a SHE-only explanation of the switching mechanism (Liu, Lee *et al.*, 2012), triggering an ongoing debate on the origin of the torques (see Sec. IV.C.7). These experiments were rapidly followed by measurements of SOTs and magnetization switching in Ta/CoFeB/MgO (Liu, Pai *et al.*, 2012; Emori *et al.*, 2013; Garello *et al.*, 2013; Junyeon Kim *et al.*, 2013; Avci *et al.*, 2014) and W/CoFeB/MgO layers (Pai *et al.*, 2012), which showed that the dampinglike SOT correlates with the sign of the spin-orbit coupling constant and the SHE of the nonmagnetic metal layer, whereas the fieldlike torque has a more erratic behavior depending on the type of ferromagnet and interface structures (Pai *et al.*, 2015).

The largest SOT efficiencies are found in the 5d metals, in particular, for the highly resistive β phase of W and Ta as well for fcc Pt; see Fig. 23. In metals where the spin Hall conductivity σ_{sh} is of intrinsic origin, the spin Hall angle is directly proportional to the longitudinal resistivity, given by $\theta_{\text{sh}} = \sigma_{\text{sh}}\rho$. Pt and Pd display a large SOT efficiency despite their moderate resistivity (Nguyen, Ralph, and Buhrman, 2016; Ghosh *et al.*, 2017), which is attributed to their large intrinsic σ_{sh} and density of states at the Fermi level (Freimuth, Blügel, and Mokrousov, 2010, 2015). Large dampinglike and fieldlike SOT efficiencies have also been reported by replacing the nonmagnetic metal by an intermetallic antiferromagnet such as IrMn (Tshitoyan *et al.*, 2015; Oh *et al.*, 2016; Wu *et al.*, 2016; W. Zhang *et al.*, 2016) and PtMn (Ou *et al.*, 2016), which allows for including exchange-biased systems in SOT devices (Sec. IV.E.3).

Enhanced efficiencies can be obtained in multilayers where the ferromagnet is sandwiched between two nonmagnetic metals with opposite spin Hall angle, giving rise to parallel

TABLE II. SOTs in magnetic multilayers. The thickness of the layers is given in nm with the topmost layer on the right. The following units are used for the effective fields and SOT efficiencies: $B_{DL,FL}/j$ [mT/(10^{11} A/m^2)], $\xi_{DL,FL}^j$ (adimensional), and $\xi_{DL,FL}^E$ [10^5 (Ωm)$^{-1}$]. The sign of B_{DL} and B_{FL} is defined as in Eqs. (51) and (52). $\xi_{DL} > 0$ corresponds to the same sign of the dampinglike torque as for Pt, whereas $\xi_{FL} < 0$ indicates that B_{FL} is opposite to the Oersted field. The magnetic anisotropy (MA) of the ferromagnetic layers is indicated as out of plane (OP) or in plane (IP). The values for the OP samples are given for the magnetization lying close to the easy axis. All measurements have been carried out at room temperature. Here HHV stands for harmonic Hall voltage analysis.

| Structure		MA	Method	B_{DL}/j	B_{FL}/j	ξ_{DL}^j	ξ_{FL}^j	ξ_{DL}^E	ξ_{FL}^E
Nonmagnetic metals									
Pt(3)/Co(0.6)/AlO$_x$(1.6)	Garello *et al.* (2013)	OP	HHV	−6.9	4	0.13	−0.073	3.5	−2.0
Pt(3)/CoFe(0.6)/MgO(1.8)	Emori *et al.* (2013)	OP	HHV	−5	2	0.064	−0.024		
Ti(1)/CoFe(0.6)/Pt(5)	Xin Fan *et al.* (2014)	IP	MOKE	3.2	−0.3	0.074	−0.008		
Pt(5)/Co(1)/MgO(2)	Nguyen, Ralph, and Buhrman (2016)	OP	HHV	−4.5	1	0.11	−0.024	2.43	−0.53
Pt(5)/Ni$_{80}$Fe$_{20}$(8)/AlO$_x$(2)	Fan *et al.* (2016)	IP	MOKE	−0.49	0.71	0.082	−0.12	2.64	−3.88
YIG(50)/Pt(4)	Montazeri *et al.* (2015)	IP	MOKE	0.29		0.03			
TmIG(8)/Pt(5)	Avci, Quindeau *et al.* (2017)	OP	HHV	0.59		0.014			
Ta(4)/CoFeB(1.1)/MgO(1.6)	Liu, Pai *et al.* (2012)	OP	HHV	3.5		−0.13		−0.68	
Ta(3)/CoFeB(0.9)/MgO(2)	Avci *et al.* (2014)	OP	HHV	3.2	−2.1	−0.06	0.04	−0.34	0.22
Ta(3)/CoFeB(0.9)/MgO(2)^a	Garello *et al.* (2013)	OP	HHV	2.4	−4.5	−0.07	0.12	−0.36	0.67
Ta(1.5)/CoFeB(1)/MgO(2)^a	Junyeon Kim *et al.* (2013)	OP	HHV	1.35	−4.46	−0.03	0.11	−0.14	0.48
Ta(2)/CoFeB(0.8)/MgO(2)^a	Qiu *et al.* (2014)	OP	HHV	4.4	−19.4	−0.11	0.47		
Ta(5)/CoFeB(1.1)/MgO(2)^a	Montazeri *et al.* (2015)	OP	MOKE	2.0	−3.3	−0.05	0.08		
W(5)/CoFeB(0.85)/Ti(1)^a	Pai *et al.* (2012)	IP	ST-FMR			−0.33			
Hf(3.5)/CoFeB(1)/MgO(2)^a	Torrejon *et al.* (2014)	OP	HHV	0.8	−2.6	−0.02	0.06		
Hf(3.5)/CoFeB(1.1)/MgO(2)^a	Akyol *et al.* (2016)	OP	HHV	5		−0.17			
Hf(10)/CoFeB(1.1)/MgO(2)^a	Akyol *et al.* (2016)	OP	HHV	−1		0.03			
Hf(1)/CoFeB(1)/MgO(2)	Ramaswamy *et al.* (2016)	OP	HHV	−0.24	0.9	0.007	−0.03		
Hf(6)/CoFeB(1)/MgO(2)	Ramaswamy *et al.* (2016)	OP	HHV	9	−27	−0.28	0.82		
Pd(7)/Co(0.6)/AlO$_x$(1.6)	Ghosh *et al.* (2017)	OP	HHV	−1.3	0.7	0.03	−0.015	1.0	−0.55
Oxidized metals									
WO$_x$(6)/CoFeB(6)/TaN(2)	Demasius *et al.* (2016)	IP	ST-FMR			−0.49			
SiO$_2$/Ni$_{80}$Fe$_{20}$(8)/CuO$_x$(10)	An *et al.* (2016)	IP	ST-FMR			0.08	−0.08		
Ti(1.2)/Ni$_{80}$Fe$_{20}$(1.5)/AlO$_x$(1.5)	Emori *et al.* (2016)	IP	ST-FMR			0.15		−0.01	
PtO$_x$(32)/Ni$_{81}$Fe$_{19}$(5)/SiO2(4)	An, Kanno *et al.* (2018)	IP	ST-FMR			0.9	−0.2	8.7	−1.8
Metal alloys									
CuAu(8)/Ni$_{80}$Fe$_{20}$(1.5)	Wen *et al.* (2017)	IP	HHV	−1.9	0.58	0.01	−0.003	0.33	−0.1
Au$_{25}$Pt$_{75}$(4)/Co(0.8)/MgO(2)	Zhu, Ralph, and Buhrman (2018)	OP	HHV	−8.0	3.2	0.28	−0.11	3.3	−1.3
Ni$_{80}$Fe$_{20}$(9)/Ag(2)/Bi(4)	Jungfleisch *et al.* (2016)	IP	ST-FMR			0.18	0.14^{b,c}		
Antiferromagnets									
IrMn(8)/ Ni$_{80}$Fe$_{20}$(4)/Al(2)	Tshitoyan *et al.* (2015)	IP	ST-FMR	−2.2	−1.7	0.22	0.17		
IrMn$_3$[001](6)/ Ni$_{80}$Fe$_{20}$(6)/TaN	W. Zhang *et al.* (2016)	IP	ST-FMR			0.20			
IrMn$_3$[111](6)/Ni$_{80}$Fe$_{20}$(6)/TaN	W. Zhang *et al.* (2016)	IP	ST-FMR			0.12			
IrMn$_3$(5)/CoFeB(1)/MgO^a	Wu *et al.* (2016)	OP	HHV	−1.8	0.7	0.06	−0.02		
PtMn(8)/Co(1)/MgO(1.6)	Ou *et al.* (2016)	IP	ST-FMR			0.16	−0.04		
MgO(1.6)/Co(1)/PtMn(8)	Ou *et al.* (2016)	IP	ST-FMR			0.19	≃0		
Semiconductors and semimetals									
(Ga, Mn)As(20)/Fe(2)/Al(2)	Skinner *et al.* (2015)	IP	ST-FMR	−0.34^b	0.26^c	0.03^b	−0.02^c		
MoS$_2$(0.8)/CoFeB(3)/TaO$_x$(3)	Shao *et al.* (2016)	IP	HHV	≃0	≃0.008	≃0	−0.14	≃0	−0.03
WSe$_2$(0.8)/CoFeB(3)/TaO$_x$(3)	Shao *et al.* (2016)	IP	HHV	≃0	0.012	≃0	≃ − 0.3	≃0	−0.06
WTe$_2$/Ni$_{80}$Fe$_{20}$(6)/Al(1)	MacNeill *et al.* (2017)	IP	ST-FMR			0.04^b		0.12^b	0.09^c
Topological insulators									
Bi$_2$Se$_3$(8)/Ni$_{80}$Fe$_{20}$(16)/Al(2)	Mellnik *et al.* (2014)	IP	ST-FMR			1	1.3	0.5	0.7
Bi$_2$Se$_3$(20)/CoFeB(5)/MgO(2)	Wang *et al.* (2015)	IP	ST-FMR			0.08^b	0.05^b		
Bi$_2$Se$_3$(10)/Ag(8)/ CoFeB(7)/MgO(2)	Shuyuan Shi *et al.* (2018)	IP	ST-FMR	5.3	3.2	0.49	0.3		
(Bi, Sb)$_2$Te$_3$(8)/CoTb(8)/SiN$_x$(3)	Han *et al.* (2017)	OP	Coercivity	−8		0.4			
Mn$_{0.4}$Ga$_{0.6}$(3)/Bi$_{0.9}$Sb$_{0.1}$(10)	Khang, Ueda, and Hai (2018)	OP	Coercivity	−2300		52		130	

^{a}Annealed.
^{b}Average value.
^{c}Sign uncertain.

(a)

(b)
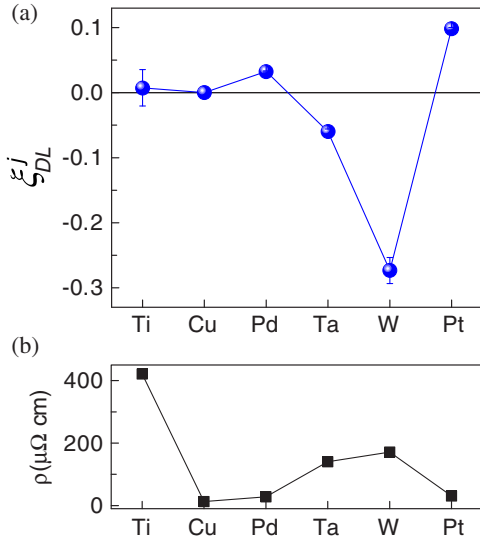
FIG. 23. (a) Dampinglike SOT efficiency in $X(8\ \text{nm})/\text{Co}/$ $\text{AlO}_x(2)$ trilayers, where $X =$ Ti, Cu, Pd, Ta, W, or Pt. The data are measured using the harmonic Hall voltage analysis method. The Co thickness is 2.5 nm except for the Pd sample where it is 0.6 nm. (b) Room-temperature resistivity of the nonmagnetic metal. Adapted from Avci, Garello, Mendil *et al.*, 2015, and Ghosh *et al.*, 2017.

dampinglike torques at opposite interfaces (Woo *et al.*, 2014; Jiawei Yu *et al.*, 2016). In such systems, the spin current associated with the PHE in the bulk of the ferromagnet can give rise to an additional dampinglike torque if the spin transfer to the nonmagnetic metals is asymmetric (Safranski, Montoya, and Krivorotov, 2019). Results obtained on symmetric multilayers such as $[\text{Co}/\text{Pd}]_n$ (Jamali *et al.*, 2013), on the other hand, are more controversial because of the expected compensation of the SOT from the top and bottom interfaces and the missing analysis of thermal voltages.

In general, significant variations of the torque efficiencies have been observed depending on multilayer composition, thickness, thermal annealing protocols, interface oxidation, and dusting, as well as temperature, which we briefly describe next.

a. Thickness dependence

Assuming that the charge-spin conversion in multilayer systems occurs outside the ferromagnetic volume, one expects the SOTs to be simply inversely proportional to the ferro-magnet thickness ($\sim 1/t_F$), as the effects of the current-induced fields are inversely proportional to the magnetic volume on which they act upon, and strongly dependent on the nonmagnetic metal thickness (t_N) as well as on interfacial properties. The influence of t_F on the SOT has been systematically investigated in Ta/CoFeB/MgO (Junyeon Kim *et al.*, 2013), NiFe/Cu/Pt (Fan *et al.*, 2013), Ti/CoFeB/ Pt (Xin Fan *et al.*, 2014), Co/Pt (Skinner *et al.*, 2014), Pt/Co/MgO and Pt/Co$_{50}$Fe$_{50}$/MgO (Pai *et al.*, 2015), and Pd/FePd (Hwang-Rae Lee *et al.*, 2014), all deposited on thermally oxidized Si. Junyeon Kim *et al.* (2013) found that B_{FL} decreases strongly while B_{DL} remains approximately constant in Ta/CoFeB/MgO when increasing t_F from 0.8

to 1.4 nm. Xin Fan *et al.* (2014) showed that both fields decrease when increasing t_F from 0.7 to 6 nm, with B_{FL} dropping significantly faster than $1/t_F$. The spin-torque efficiencies $\xi^j_{DL,FL}$ have been found to decrease in annealed Pt/Co$_{50}$Fe$_{50}$/MgO layers between 0.6 and 1 nm, but to increase in as-grown Pt/Co/MgO (Pai *et al.*, 2015), possibly because the Co thickness has to exceed the spin absorption length (i.e., the length over which the spin current is absorbed in the ferromagnet) in order to develop the full torque or because of strain relaxation in the Pt/Co layer. Interestingly, the sign of the fieldlike torque is opposite in these two systems. Skinner *et al.* (2014) found a sign inversion of the fieldlike torque in Co/Pt for a 2-nm-thick Co layer, which suggests that two mechanisms with different dependence on t_F compete to determine the total torque.

The dependence of the SOT on t_N has been the focus of many studies aimed at distinguishing the bulk and interfacial nature of the torques. In the simplest theoretical models, effects coming from the interfacial Rashba interaction should be independent of t_N, whereas effects emerging from the bulk SHE should scale as $1 - \text{sech}(t_N/\lambda_{sf})$ according to the profile of the spin density in the nonmagnetic metal layer (Liu *et al.*, 2011). In addition, the Oersted field should increase linearly with t_N. Therefore, assuming that the overall structure (crystallinity, interface and interdiffusion processes) is unchanged upon modifying t_N, analyzing the thickness dependence of ξ^j_{DL} and ξ^j_{FL} should provide information about the physical origin of the torques. Figure 24 shows that ξ^j_{DL} of as-grown Co/AlO$_x$ layers deposited on β-Ta, β-W, and Pt increases monotonically with t_N up to saturation, which agrees well with the SHE model assuming a spin-diffusion length of the order of 1.5 nm for all metals. Such a trend is common to a variety of systems based on Ta (Torrejon *et al.*, 2014), W (Hao and Xiao, 2015), Pt (Nguyen, Ralph, and Buhrman, 2016), and Pd (Ghosh *et al.*, 2017), suggesting that the SHE is the dominant source of the spin current causing the dampinglike torque. Recent theoretical work, however, has pointed out that a similar t_N dependence is expected for a
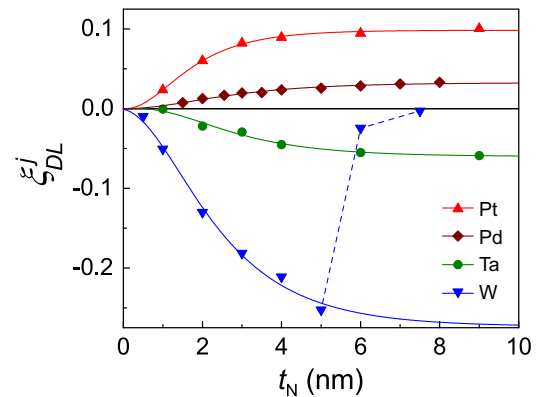
FIG. 24. Dampinglike torque efficiency as a function of thickness in NM(t_N)/Co/AlO$_x$ layers, where NM = Pt, Pd, Ta, and W. The solid lines are fit to the function $\xi^j_{DL}[1 - \text{sech}(t_N/\lambda_{sf})]$. Note that the efficiency ξ^j_{DL} of W drops abruptly between 5 and 6 nm as the crystal structure changes from the β to the α phase. From Garello *et al.*, 2017.

Rashba-like dampinglike torque due to interfacial spin-dependent scattering (P. M. Haney *et al.*, 2013; Amin and Stiles, 2016b), so that separating the bulk and interface contributions to ξ_{DL}^j is not straightforward. Moreover, a change of sign of both ξ_{DL}^j and ξ_{FL}^j has been reported for Ta/CoFeB/MgO (Junyeon Kim *et al.*, 2013; Allen *et al.*, 2015) and Hf/CoFeB/MgO (Akyol *et al.*, 2016; Ramaswamy *et al.*, 2016) at $t_{Ta} \approx 0.5$ nm and $t_{Hf} \approx 2$ nm, respectively, indicating that there are different mechanisms contributing to the torques that may compete or reinforce each other.

Calculations based on the drift-diffusion model of the SHE predict that the dampinglike and fieldlike torques should have a similar dependence on t_N and be proportional to the real and imaginary parts of the spin mixing conductance of the FM/NM interface, respectively, which naturally leads to $\xi_{DL}^j \gg \xi_{FL}^j$ (P. M. Haney *et al.*, 2013).

Several reports, however, show that $\xi_{FL}^j \gtrsim \xi_{DL}^j$ in out-of-plane as well as in-plane magnetized layers (Table II) and that the dependence of ξ_{FL}^j on t_N differs from that of ξ_{DL}^j in systems based on Ta (Junyeon Kim *et al.*, 2013), Pt (Xin Fan *et al.*, 2014; Nguyen, Ralph, and Buhrman, 2016), and Pd (Ghosh *et al.*, 2017), particularly at low thickness ($t_N < 2$ nm). An example of this behavior is reported in Fig. 25(a) for a perpendicularly magnetized Pd/Co/AlO$_x$ layer, where ξ_{FL}^j clearly departs from the monotonic increase of ξ_{DL}^j as a function of t_{Pd}. Remarkably, the thickness dependence changes when the SOT efficiency is normalized to the electric field, as in Fig. 25(b), showing that ξ_{DL}^E and ξ_{FL}^E do not saturate up to $t_N = 8$ nm and that ξ_{FL}^E extrapolates to a finite value at $t_{Pd} = 0$. The difference between $\xi_{DL,FL}^E$ and $\xi_{DL,FL}^j$ also suggests that the thickness dependence should be analyzed with care in films when the resistivity is not homogeneous (Nguyen, Ralph, and Buhrman, 2016; Ghosh *et al.*, 2017).

b. Interfacial tuning

The transport of charge and spin in multilayer systems is strongly affected by interface scattering and discontinuities in the electronic band structure, as is well known from early studies of the giant magnetoresistance (Parkin, 1993; Levy, 1994). Thus, significant variations of the SOTs are expected upon modification of the interfaces, even when the
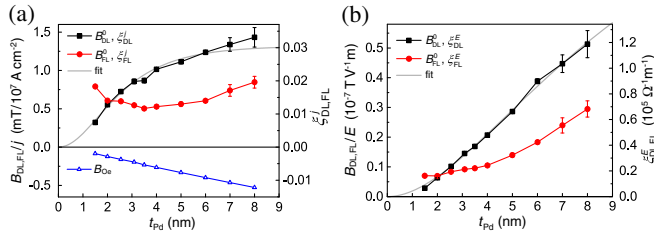
nonequilibrium spin density originates in the bulk of the nonmagnetic metal layer. Experimentally, it has been shown that the dampinglike and fieldlike SOTs change dramatically upon annealing and consequent intermixing of Pt/Co/AlO$_x$ (Garello *et al.*, 2013) and Ta/CoFeB/MgO (Avci *et al.*, 2014), as well as upon the insertion of different spacer layers between the ferromagnet and the nonmagnetic metal that is considered to be the main source of spin density (Fan *et al.*, 2013; Pai *et al.*, 2014; Weifeng Zhang *et al.*, 2015). The insertion of a light metal such as Cu has been pursued with the intention of removing the interfacial spin-orbit coupling. Xin Fan *et al.* (2013, 2014) measured a fieldlike torque that decreases smoothly with the thickness of the Cu spacer in Pt/Cu/NiFe, indicating a nonlocal origin, but also that the ξ_{FL}^j/ξ_{DL}^j ratio of CoFeB/Cu/Pt has a discontinuity around $t_{Cu} = 0.7$ nm, which points toward a modified interface effect. In fact, the insertion of a light metal, while reducing the magnetic proximity effect between the nonmagnetic metal and the ferromagnet, does not completely eliminate the interfacial spin-orbit coupling. Rather, it creates two additional interfaces on either sides of the light metal layer, with different iSGE and scattering properties. The latter effect is evident when considering that the SOTs change by as much as 50% for a Cu spacer thickness of the order of 1 nm (Xin Fan *et al.*, 2014; Rojas-Sánchez *et al.*, 2014; Nan *et al.*, 2015), which is 2 orders of magnitude shorter than the spin-diffusion length in Cu.

The insertion of a spacer layer can also modify the ability of the ferromagnet to absorb the incoming spin current by modifying both the transparency (Nguyen *et al.*, 2015; Weifeng Zhang *et al.*, 2015) and the spin-memory loss at the interface (Rojas-Sánchez *et al.*, 2014; Dolui and Nikolic, 2017; Berger, Edwards, Nembach, Karis *et al.*, 2018; Tao *et al.*, 2018). The former accounts for the spin current backflow in the nonmagnetic metal (the larger the backflow, the smaller the spin current transmission into the ferromagnet), while the latter opens an additional spin dissipation channel at the interface (see Sec. III.C). Both effects reduce the effective spin injection. A typical case is that of Hf, which has been shown to improve the SOT efficiency in W/Hf/CoFeB/MgO and Pt/Hf/CoFeB/MgO while promoting perpendicular magnetic anisotropy (Pai *et al.*, 2014) and reducing the magnetic damping (Nguyen *et al.*, 2015). Changes in the SOT efficiency in such cases are usually interpreted in terms of an enhanced spin mixing conductance, which may also explain why the dampinglike torque efficiency changes for different ferromagnets coupled to the same nonmagnetic metal, as observed, e.g., in Pt/Co/TaN ($\xi_{DL}^j = 0.11$) and Pt/NiFe/TaN ($\xi_{DL}^j = 0.05$) (Weifeng Zhang *et al.*, 2015). Such a phenomenological parameter, however, accounts for the transmission of the bulk spin current as much as for the generation of interfacial spin currents, so that its use to estimate an asymptotic value of the bulk SHE in nonmagnetic metals can be questioned. Moreover, the spacer layer itself can be regarded as a source of spin current, as has been shown in the case of Hf (Akyol *et al.*, 2016; Ramaswamy *et al.*, 2016).

Another interesting aspect is the control of magnetic properties through interfacial oxidation (Monso *et al.*,

FIG. 25. SOT efficiency in Pd(t)/Co(0.6)/AlO$_x$ trilayers as a function of Pd thickness. (a) $\xi_{DL,FL}^j$ and (b) $\xi_{DL,FL}^E$ differ significantly from each other due to the strong decrease of the Pd resistivity with increasing thickness. The fieldlike torque efficiency is shown after subtraction of the Oersted field contribution $B_{Oe} = \mu_0 j_{Pd} t_{Pd}/2$ shown by the open triangles in (a). From Ghosh *et al.*, 2017.

2002; Manchon *et al.*, 2008; Rodmacq *et al.*, 2009) or gate voltage (Weisheit *et al.*, 2007; Maruyama *et al.*, 2009; Shiota *et al.*, 2012; Wei-Gang Wang *et al.*, 2012; Bauer, Lide, and Beach, 2015). Using photoemission spectroscopy, Manchon *et al.* (2008) showed that both the perpendicular magnetic anisotropy and AHE reach a maximum in Pt/Co/AlO$_x$ trilayers when the Co/AlO$_x$ interface is optimally oxidized. This effect is connected to the dependence of the interfacial magnetic anisotropy on the electron density and orbital character of the interface atoms (Yang *et al.*, 2011; Dieny and Chshiev, 2017). It is therefore natural to expect that other spin-orbit coupling properties, such as SOT (Freimuth, Blügel, and Mokrousov, 2014b) or DMI (Belabbes *et al.*, 2016; Srivastava *et al.*, 2018), can be controlled by tuning the interfacial electron density through oxidation or by applying a gate voltage (Emori *et al.*, 2014; Liu, Lim, and Urazhdin, 2014; Qiu *et al.*, 2015). Miron, Garello *et al.* (2011) first showed that moderate oxidation of Pt/Co/AlO$_x$ favors current-induced switching, as recently confirmed in Pt/Co/CoO$_x$ layers oxidized in air, in which up to a twofold enhancement of the SOT efficiency was measured relative to Pt/Co/MgO (Hibino *et al.*, 2017). On the other hand, Liu, Lim, and Urazhdin (2014) demonstrated that both fieldlike and dampinglike torques can be modified by gating Pt/Co/Al$_2$O$_3$ multilayers [Fig. 26(a)], obtaining an enhancement of 4% (1%) of the fieldlike (dampinglike) torque for a gate voltage of about 7 V. Since the gate voltage essentially modifies the electric dipole of the Co/Al$_2$O$_3$ interface and leaves the SHE from Pt unaffected, this observation provides some indication about the origin of the SOTs in this system. Liu, Lim, and Urazhdin (2014) estimated that the SHE does not contribute to more than 20% of the fieldlike torque, while the interfacial spin-orbit coupling produces about 50% of the dampinglike torque. Emori *et al.* (2014) carried out measurements on gated Pt/Co/GdO$_x$, showing that oxidation of the top Co interface leads to a 10-fold increase of the dampinglike torque due to oxygen ion migration, which also affects the magnetic anisotropy. Qiu *et al.* (2015) demonstrated the spectacular impact of interfacial oxidation on SOTs in Pt/CoFeB/SiO$_2$, where the oxidation of the CoFeB/SiO$_2$ layer is varied continuously. They reported that the sign of both dampinglike and fieldlike torques changes from positive
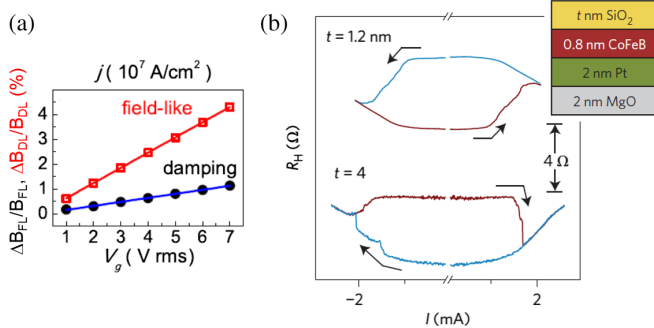
to negative when increasing the oxidation of CoFeB; see Fig. 26(b). They attributed this change of sign to the increase of the orbital moment of Fe and Co upon oxidation (Nistor *et al.*, 2011; Yang *et al.*, 2011). This results in an enhancement of the interfacial SOT at the upper CoFeB/SiO$_2$ interface that can even dominate over the SOT arising from the bottom Pt/CoFeB.

Oxidation of the bottom Pt interface in Pt/Ni$_{81}$Fe$_{19}$ bilayers also leads to drastic enhancements of both dampinglike and fieldlike torque efficiencies, which can be controlled by the oxygen flow during sputter deposition as well as by a gate voltage (An, Kanno *et al.*, 2018; An, Ohno *et al.*, 2018). Interestingly, the maximum SOT efficiency in this system $\xi_{\mathrm{DL}}^j = 0.92$ ($\xi_{\mathrm{DL}}^E = 9 \times 10^3$ $\Omega^{-1}m^{-1}$) is reached for a fully oxidized nonconducting Pt layer. Other reports reveal an enhancement of ξ_{DL}^j from -0.14 to -0.49 upon oxidation of W in W/CoFeB/TaN (Demasius *et al.*, 2016) and the emergence of strong SOT in as-grown SiO$_x$/Co/Cu (Verhagen *et al.*, 2015) and oxidized SiO$_x$/NiFe/Cu layers (An *et al.*, 2016), with contrasting evidence on the role played by the oxidized interfaces. These experiments show that interfacial spin-orbit coupling can produce significant fieldlike and dampinglike torques, but also that a detailed microstructural analysis of the bulk versus interface oxidation is required to understand the role of oxygen in inducing or modifying the SOT.

Finally, Qiu *et al.* (2016) demonstrated a threefold enhancement of the SOT magnitude in a Pt/Co/Ni/Co multilayer by capping the system with Ru. This result is interpreted in terms of enhanced spin absorption induced by the negative spin polarization arising at the Co/Ru interface (Nozaki *et al.*, 2004) and could partly explain the very large SOT magnitude measured in synthetic antiferromagnetic domain walls (Yang, Ryu, and Parkin, 2015). Recent work on IrMn$_3$/NiFe epitaxial layers also shows that ξ_{DL}^j has a facet-dependent contribution, which arises from the different orientation of the Mn magnetic moments at different interfaces (W. Zhang *et al.*, 2016).

c. Angular dependence

As mentioned in Sec. IV.A, the SOTs are anisotropic, i.e., their magnitude changes depending on the magnetization direction in a way that is more complex than described by Eq. (2). In polycrystalline systems with C_{2v} symmetry, the magnitude of this anisotropy is characterized by the coefficients $\tau_{\mathrm{DL,FL}}^{\{2n\}}$ in Eqs. (49) and (50). As measured in Pt/Co/AlO$_x$ (Garello *et al.*, 2013), Pt/Co/MgO (Gweon, Lee, and Lim, 2019), Ta/CoFeB/MgO (Avci *et al.*, 2014; Qiu *et al.*, 2014), and Pd/Co/AlO$_x$ (Ghosh *et al.*, 2017), the SOT anisotropy can be quite large. Figure 27 shows that both fieldlike and dampinglike torques increase in absolute value when the magnetization points in plane, which is the typical behavior observed in metal layers. The anisotropies of the fieldlike and dampinglike components differ from each other and can reach up to a factor of 4 depending on the material and annealing conditions.

The angular dependence of the SOT, although quite general, provides additional clues about the physics taking place in these ultrathin layers. Different physical mechanisms can

FIG. 26. (a) Effect of gate voltage on the fieldlike and dampinglike SOT in Pt/Co/Al$_2$O$_3$. From Liu, Lim, and Urazhdin, 2014. (b) Inversion of the polarity of current-induced switching for different thickness of the oxide capping layer in Pt/CoFeB/SiO$_2$. From Qiu *et al.*, 2015.
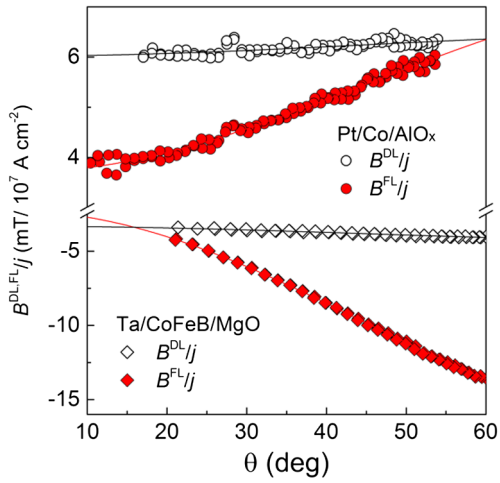
FIG. 27. Angular dependence of B_{DL} and B_{FL} measured in as-grown $Pt(3)/Co(0.6)/AlO_x$ (Garello *et al.*, 2013) and $Ta(3)/CoFeB(0.9)/MgO$ (Avci *et al.*, 2014) at room temperature. The angle θ between the magnetization and the z axis is determined by anomalous Hall resistance measurements. The solid lines are fits to the function $B_\theta^{DL,FL} = B_0^{DL,FL} + B_2^{DL,FL} \sin^2 \theta$.

FIG. 28. Temperature dependence of (a) B_{FL}/j ($\Delta H_T/j$) and (b) B_{DL}/j ($\Delta H_L/j$) in $Ta/CoFeB(1)/MgO(2)$ layers with different Ta thickness. The bottom panels show a magnified view of the fields for the thinner Ta layers. Solid and open symbols correspond to the magnetization pointing along $+\mathbf{z}$ and $-\mathbf{z}$, respectively. From Kim *et al.*, 2014.

generate such an angular dependence: (i) the presence of D'yakonov-Perel relaxation (Pauyac *et al.*, 2013), (ii) the distortion of the Fermi surface when changing the magnetization direction due to strong spin-orbit coupling (Paul M. Haney *et al.*, 2013; Lee *et al.*, 2015), and (iii) the angular dependence of the interfacial mixing conductance, i.e., the change of spin absorption and reflection as a function of the magnetization direction (Amin and Stiles, 2016a; Baek *et al.*, 2018). Additional effects related to spin scattering in the nonmagnetic metal may also be relevant, such as, e.g., spin swapping (Saidaoui and Manchon, 2016). Interestingly, Qiu *et al.* (2014) reported that the angular dependence of the two torque components vanishes when decreasing the temperature, an observation that highlights the importance of scattering events in the emergence of the angular dependence of the SOTs. Finally, systems characterized by low crystalline symmetry may display additional contributions not included in Eqs. (49) and (50) due to the specific symmetry of the spin and orbital textures (Chen *et al.*, 2016; MacNeill *et al.*, 2017).

d. Temperature dependence

A way to obtain information on the physics governing the SOTs is to measure their magnitude as a function of temperature. In Ta/CoFeB/MgO, Qiu *et al.* (2014) reported that the fieldlike torque decreases linearly when reducing the sample temperature, while the dampinglike torque remains mostly unaffected. A qualitatively similar behavior was observed by Kim *et al.* (2014) in similar structures, i.e., the fieldlike torque decreases strongly with decreasing temperature, while the dampinglike torque increases from 400 to 300 K and saturates at lower temperatures; see Fig. 28. Since the Ta resistivity is almost constant between 100 and 400 K, the relative independence of the dampinglike torque on temperature is consistent with the dampinglike torque being driven by the intrinsic SHE of Ta. In contrast, the strong decrease of the
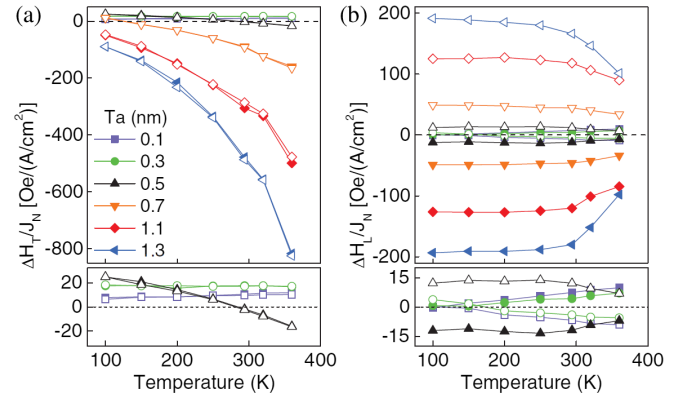
fieldlike torque suggests that scattering events involving phonons and magnons (usually stronger at disordered interfaces) play an important role in the emergence of this component. Studies of the temperature dependence of the SOTs in Pt-based structures, on the other hand, show that the fieldlike and dampinglike SOTs are both approximately constant with temperature in as-grown Pt/Co/MgO, whereas both increase with temperature in annealed Pt/CoFeB/MgO (Pai *et al.*, 2015). In the latter case, the fieldlike torque shows a much stronger change compared to the dampinglike torque and even changes sign, from parallel to antiparallel to the Oersted field, at around 125 K.

In bilayers including disordered alloys of nonmagnetic metals such as $Cu_x Au_{1-x}$, where extrinsic effects dominate, the dampinglike torque decreases upon reducing the temperature, consistently with an extrinsic bulklike SHE, whereas the fieldlike torque increases (Wen *et al.*, 2017). On the other hand, alloys that present a ferromagnetic to paramagnetic transition, such as $Fe_x Pt_{1-x}$ in combination with a ferromagnet such as CoFeB, display a maximum of the dampinglike torque near the Curie temperature, which is attributed to spin fluctuation enhancement of the SHE arising from the interaction between the conduction electrons and the localized magnetic moments (Ou, Ralph, and Buhrman, 2018). *Ab initio* calculations additionally show that the generation and absorption of spin currents in an ordered FePt alloy are extremely sensitive to the distribution of defects near the interface (Géranton *et al.*, 2016). Overall, these studies support the view that intrinsic as well as extrinsic mechanisms contribute in different proportion to the fieldlike and dampinglike torques.

2. Ferrimagnet and antiferromagnet/nonmagnetic metal layers

Ferrimagnetic films were once widely used as recording media in bubble memories (Bobeck, Bonyhard, and Geusic, 1975) and magneto-optic memories (Jenkins *et al.*, 2003). Applications included both insulating garnets (Nielsen, 1976) and amorphous rare-earth $3d$ transition-metal alloys

(Buschow, 1984). Depending on their composition, ferrimagnets can exhibit a magnetization compensation temperature (T_M) where the magnetizations of the two antiparallel coupled sublattices cancel each other and, similarly, an angular momentum compensation temperature (T_A) where the total angular momentum of the two sublattices vanishes (Nielsen, 1976; Buschow, 1984; Hirata *et al.*, 2018). The frequency of the uniform spin precession mode as well as the magnetic damping is expected to diverge at T_A (Wangsness, 1954; Stanciu *et al.*, 2006), which makes these materials extremely interesting for ultrafast switching (Stanciu *et al.*, 2007; Mangin *et al.*, 2014) as well as fast domain wall motion (Kobayashi *et al.*, 2005; Kab-jin Kim *et al.*, 2017; Caretta *et al.*, 2018; Siddiqui *et al.*, 2018).

SOT-induced switching of ferrimagnets has been reported for amorphous ferrimagnetic alloys, such as Ta/TbFeCo (Zhao *et al.*, 2015), Ta/TbCo (Finley and Liu, 2016), Pt/GdCo (Mishra *et al.*, 2017), and Pt/GdFeCo (Roschewsky, Lambert, and Salahuddin, 2017), as well as rare-earth garnets such as $Tm_3Fe_5O_{12}$/Pt (Avci, Quindeau *et al.*, 2017; Avci, Rosenberg *et al.*, 2017; Vélez *et al.*, 2019) and $Tm_3Fe_5O_{12}$/W (Shao *et al.*, 2018). In contrast to ferromagnets, the reduced saturation magnetization of these systems allows for switching relatively thick layers, up to 30 nm (Roschewsky, Lambert, and Salahuddin, 2017), at current densities of the order of 10^7 A/cm^2. Moreover, because of the alternance of magnetic moments with opposite orientation on neighboring atomic sites, spin dephasing due to spin precession in metallic ferrimagnets partially cancels out, which allows a spin current to propagate for several nm inside these materials, as reported for $Pt/[Co/Tb]_N$ multilayers and Pt/CoTb amorphous alloys (Yu *et al.*, 2019). These properties, combined with the bulk perpendicular magnetic anisotropy of rare-earth 3*d* transition-metal compounds, make ferrimagnets interesting for applications requiring relatively thick magnetic layers.

Measurements of the SOT as a function of temperature (Ham *et al.*, 2017; Ueda *et al.*, 2017) and composition (Finley and Liu, 2016; Roschewsky, Lambert, and Salahuddin, 2017; Je *et al.*, 2018) show that the dampinglike effective field tends to diverge as $B_{DL} \propto 1/M_s$ near T_M, whereas ξ_{DL}^j is roughly constant across T_M, as expected. In some cases, however, a disproportionate scaling between B_{DL} and $1/M_s$ has been observed, leading to a considerable enhancement of ξ_{DL}^j of yet unclear origin (Mishra *et al.*, 2017; Je *et al.*, 2018; Yu *et al.*, 2019). As not only M_s and T_M, but also the magnetic anisotropy, Gilbert damping, spin-orbit scattering, and spin dephasing depend on the composition and thickness of these systems, it is not surprising that the simple $1/M_s$ scaling has no general validity. An interesting point is that, even in systems where $B_{DL} \propto 1/M_s$, the threshold switching current does not decrease at T_M, but rather changes smoothly as a function of composition (Je *et al.*, 2018) or thickness (Yu *et al.*, 2019). This behavior agrees with a macrospin model based on the LLG equation for two antiferromagnetically coupled lattices, which shows that the threshold switching current scales with the effective perpendicular anisotropy (Je *et al.*, 2018). The latter depends on the sum of effective anisotropy energy of each lattice, which does not cancel out at the compensation point.

In fully compensated bipartite antiferromagnets, simulations predict that the Néel order can be manipulated via dampinglike SOT (Gomonay and Loktev, 2010) (see Sec. III.F). It was recently shown that current injection in Pt/NiO (X. Z. Chen *et al.*, 2018) and Pt/NiO/Pt (Moriyama *et al.*, 2018) leads to switching of the Néel vector of up to 90-nm-thick films of NiO, independently of the strain state and crystallographic orientation (Baldrati *et al.*, 2018). Contrasting mechanisms have been proposed to explain this type of switching, based on the coherent rotation of the Néel vector (X. Z. Chen *et al.*, 2018), fieldlike SOT acting on uncompensated interfacial spins (Moriyama *et al.*, 2018), as well as rotation of the Néel vector inside individual domains combined with the displacement of the domain walls driven by the dampinglike SOT (Baldrati *et al.*, 2018).

3. Ferromagnet/semiconductor layers

We now turn from purely metallic systems to ferromagnet/semiconductor bilayers, in which the semiconductor has a specific crystal structure that brings about additional symmetries on top of the one arising from interfacial inversion symmetry. For instance, in zinc-blende lattices under strain, such as GaAs, a spin accumulation can be generated via the iSGE driven by Rashba and Dresselhaus spin-orbit coupling as well as by the bulk SHE (see Sec. V). Differently from the commonly studied polycrystalline NM/FM samples, where the iSGE-based and the SHE-based mechanisms are indistinguishable in the lowest order terms (Garello *et al.*, 2013), the dependence of the torques on the angle of the current relative to the high symmetry directions of the semiconductor crystal provides a direct means to disentangle the SHE and iSGE contributions. Skinner *et al.* (2015) proved this point by investigating the SOTs of an epitaxial Fe(2 nm)/(Ga, Mn)As(20 nm) bilayer using the ST-FMR technique; see Fig. 29. The GaAs host was doped with high enough concentration of substitutional Mn acceptors to increase the semiconductor conductivity, but low enough so that (Ga,Mn)As remains paramagnetic at room temperature. It was then shown that the fieldlike and dampinglike torques have similar magnitude, with the first originating from the iSGE with Dresselhaus symmetry and the second from the SHE-like spin current generated inside the paramagnetic *p*-doped GaAs layer. Chen *et al.* (2016), on the other hand, showed that the SOT of epitaxial Fe films grown on nonconducting GaAs(001) originate from the interfacial iSGE and have mixed Rashba and Dresselhaus symmetry, which also leads to the emergence of an unusual crystalline magnetoresistance (Hupfauer *et al.*, 2015). The interfacial spin-orbit interaction and SOT can further be modulated by applying a gate voltage across the Schottky barrier at the Fe/GaAs interface (L. Chen *et al.*, 2018).

Evidence of strong SOTs due to the iSGE has been observed also in heterostructures involving transition-metal dichalcogenides and metallic ferromagnets. van der Waals crystals provide a unique platform for generating SOTs because they have strong spin-orbit coupling, a range of broken crystal symmetries, and can be prepared as monolayer crystalline films by exfoliation or chemical vapor deposition methods (Xu *et al.*, 2014; Manchon *et al.*, 2015).
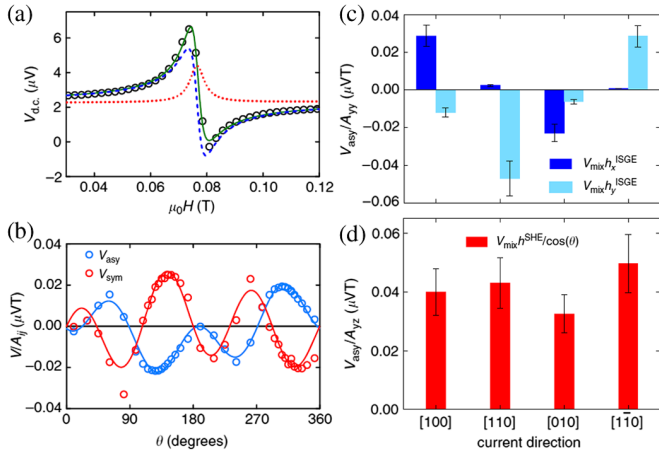
FIG. 29. (a) Electrical excitation and detection of FMR induced by a 16.245 GHz rf current in a Fe(2 nm)/(Ga, Mn)As(20 nm) bilayer. A typical ST-FMR curve (points) is shown as a function of the external field. The dc voltage is fitted (solid green line) by a combination of symmetric (red dotted line) and antisymmetric (blue dashed line) Lorentzians. (b) Dependence of the fitted Lorentzian amplitudes on the in-plane magnetization angle for a device with current in the [010] direction. (c) iSGE dependence on the direction of the current. The fitted in-plane field coefficients (representing the fieldlike torque) for a set of devices in different crystal directions. (d) The fitted out-of-plane field coefficient (representing the dampinglike torque) for the same devices. Adapted from Skinner *et al.*, 2015.

Shao *et al.* (2016) showed that the fieldlike torque in 1 nm CoFeB deposited on monolayer MoS_2 and WSe_2 is of the order of 0.1–0.14 mT/(10^7 A/cm^2), independently of temperature, and is consistent with iSGE-induced spin density, whereas the dampinglike torque is negligibly small. Sizable dampinglike SOTs have been reported for NiFe deposited on MoS_2 (Wei Zhang *et al.*, 2016) and on the Weyl semimetal WTe_2 (MacNeill *et al.*, 2017). The latter case is of particular interest as the surface crystal structure of WTe_2 has only one mirror plane and no twofold rotational invariance about the *c* axis, which allows for a dampinglike torque that is directed out of plane when the current is applied along a low-symmetry axis of the surface. Such a dampinglike torque is forbidden by symmetry in NM/FM bilayers, where the direction of the incoming spin polarization is in plane. The possibility of controlling the allowed symmetry of the dampinglike SOT in multilayer samples is particularly attractive for counteracting the torque due to magnetic damping during magnetization reversal in systems with perpendicular magnetic anisotropy. Further, the current-induced spin density in two-dimensional materials is expected to be extremely sensitive to gating, thus allowing for tuning the SOT efficiency.

4. Ferromagnet/topological insulator layers

Three-dimensional topological insulators are materials that have insulating bulk and conductive surface states (Hasan and Moore, 2011; Roche *et al.*, 2015). The surface states are protected by time-reversal symmetry and have a Dirac-like linear dispersion characterized by spin-momentum locking (Fig. 8), a property that makes them attractive in the context of SOT and spintronics. Moreover, owing to hexagonal warping of the Dirac cone (Kuroda *et al.*, 2010), a current carried by the topological surface states can generate a nonequilibrium spin density with both in-plane and out-of-plane components, which can induce out-of-plane and in-plane torques onto an adjacent magnetic layer.

The most thoroughly investigated topological insulators to date are the bismuth and antimony chalcogenides M_2Q_3, where $M =$ Bi, Sb and $Q =$ Se, Te. In intrinsic systems, the Fermi level resides in the bulk energy gap and thus intersects the topological surface states only. However, these materials are narrow gap semiconductors that are very sensitive to doping by impurities or crystalline defects, which typically shifts the Fermi level to the conduction band. Furthermore, unintentional surface doping caused by the formation of extrinsic defects or the adsorption of impurities leads to the emergence of a two-dimensional electron gas with strong Rashba-split bands that are wrapped by the topological Dirac states (King *et al.*, 2011). These effects have a strong influence on SOT, which has not yet been fully understood.

Topological insulator thin films are usually grown by molecular beam epitaxy (He, Kou, and Wang, 2013). In order to favor surface transport over bulk conduction, it is necessary to minimize defects such as Se or Te vacancies, dislocations, and twin domains. This task has proven to be quite challenging, requiring careful optimization of the lattice matching with the substrate and growth kinetics (Richardella *et al.*, 2015; Bonell *et al.*, 2017). Bulk insulating materials can also be obtained by growing naturally compensated ternary alloys such as $(Bi_{1-x}Sb_x)_2Te_3$, which exploit the tendency of Bi_2Se_3 and Bi_2Te_3 to be *n* type and of Sb_2Te_3 to be *p* type (Zhang *et al.*, 2011).

Since topological insulators involve heavy elements and spin-momentum locked electron states, they are expected to show large charge-spin conversion and SOT efficiency when interfaced with a magnetic layer. However, three issues arise when considering these systems. First, the proximity between a ferromagnet and a topological insulator induces complex electronic hybridization effects, which go beyond the simple notion of a magnetic exchange field breaking time-reversal symmetry and opening a gap in the surface states (Wray *et al.*, 2011). Using first-principles calculations, Jia Zhang *et al.* (2016) and Marmolejo-Tejada *et al.* (2017) showed that charge transfer between Bi_2Se_3 and 3*d* metal layers such as Co, Ni, and Cu shifts the topological surface states below the Fermi energy, where hybridization with the metal bands destroys or heavily distorts the helical spin structure. Crucially for SOTs, it was found that proximity spin-orbit coupling also modifies the electronic states of the ferromagnet adjacent to Bi_2Se_3, leading to a Rashba-like spin texture (Marmolejo-Tejada *et al.*, 2017). Thus, the properties of magnetic/topological insulator bilayers, even in the theoretical approximation of ideal materials and interfaces, cannot be extrapolated from those of the parent layers. Second, the interface chemistry between a topological insulator such as Bi_2Se_3 and typical contact metals (Pd, Ir, Cr, Co, Fe, Ni) leads to the formation of metal selenides, metallic Bi, or intermetallic alloys, which can evidently alter the properties of the pristine materials (Walsh *et al.*, 2017). Third, because of the

competition between bulk and surface conduction, which depends on temperature and extrinsic factors, it is hardly possible to determine the current distribution in magnetic/topological insulator bilayers. This uncertainty makes it difficult to identify the electronic states responsible for charge-spin conversion as well as to provide consistent estimates of the SOT efficiency in different systems.

Regardless of the role played by the topological surface states, mounting experimental evidence suggests that strong spin-momentum coupling can be achieved in these materials. Spin-charge conversion has been reported by spin pumping for bismuth and antimony chalcogenide layers adjacent to metallic ferromagnets (Deorani *et al.*, 2014; Shiomi *et al.*, 2014; Jamali *et al.*, 2015; Kondou *et al.*, 2016; Mendes *et al.*, 2017) and insulating ferrimagnets (Hailong Wang *et al.*, 2016; Tang *et al.*, 2018) as well as by magnetoresistance measurements (Ando, 2014; Li, Vincent Liu, and Balents, 2014; Yasuda *et al.*, 2016). Current-induced SOTs have been demonstrated by ST-FMR in Bi$_2$Se$_3$/NiFe and Bi$_2$Se$_3$/CoFeB bilayers (Mellnik *et al.*, 2014; Wang *et al.*, 2015), gate control of the torque efficiency (Fan *et al.*, 2016), and magnetization switching (Yabin Fan *et al.*, 2014; Han *et al.*, 2017; Wang *et al.*, 2017; Yasuda *et al.*, 2017; Khang, Ueda, and Hai, 2018). In these experiments, the reported damping-like torque efficiency is widely distributed from 0.01 to 2 for Bi$_2$Se$_3$, reaching ∼50 in Bi$_2$Sb$_3$/MnGa (Khang, Ueda, and Hai, 2018) and even larger values in (Bi$_{0.5}$Sb$_{0.5}$)$_2$Te$_3$/(Cr$_{0.08}$Bi$_{0.54}$Sb$_{0.38}$)$_2$Te$_3$ (Yabin Fan *et al.*, 2014). In the latter case, however, the SOT analysis is complicated by nonlinear Hall effects (Yasuda *et al.*, 2017).

Demonstrations of room-temperature SOT-driven switching with threshold currents that are about 1 order of magnitude smaller compared to NM/FM bilayers are particularly interesting in view of possible applications. Wang *et al.* (2017) reported switching of in-plane magnetized Bi$_2$Se$_3$/NiFe with a critical current of ∼6 × 10^5 A/cm^2, while Han *et al.* (2017) demonstrated switching of perpendicularly magnetized Bi$_2$Se$_3$/CoTb at ∼3 × 10^6 A/cm^2 and Khang, Ueda, and Hai (2018) obtained a similar switching threshold for the high coercivity system Bi$_2$Sb$_3$/MnGa. Whereas all these studies were performed on topological insulators grown by molecular beam epitaxy, Mahendra *et al.* (2018) used sputtering to grow Bi$_2$Se$_3$/Ta/CoFeB/Gd/CoFeB heterostructures with perpendicular anisotropy promoted by the 0.5-nm-thick Ta layer. Because of its polycrystalline nature, the Bi$_2$Se$_3$ layer is highly resistive, 10 times more than epitaxial Bi$_2$Se$_3$ (Mellnik *et al.*, 2014), thereby enabling the current to flow mostly through the interface and in the ferromagnetic layer, which enhances the SOT efficiency. However, the role, if any, of the topological surface states in these sputtered layers remains to be proven, together with the stoichiometric profile of the Bi$_2$Se$_3$ films. Other strategies to improve the SOT efficiency in these systems rely on the use of spacer layers, such as Ag, which favor the formation of Rashba-split bands with strong spin-momentum coupling (Shuyuan Shi *et al.*, 2018), the creation of Rashba-Dirac coupled systems (Eremeev *et al.*, 2015), and the search for novel topological materials (Rojas-Sánchez, Laczkowski *et al.*, 2016; Manna *et al.*, 2018).

5. Two-dimensional alloys and oxide interfaces

Spin-pumping measurements performed on heterostructures consisting of a ferromagnetic layer and an interface alloy with strong Rashba-like spin-orbit coupling, such as Ag/Bi (Rojas-Sánchez *et al.*, 2013), Cu/Bi (Isasa *et al.*, 2016), and Cu/Bi$_2$O$_3$ (Karube, Kondou, and Otani, 2016), have revealed large spin-to-charge conversion efficiencies due to the SGE. This effect converts a nonequilibrium spin density **S** into an interfacial 2D charge current $\tilde{j}_c$ (Ivchenko and Pikus, 1978). Owing to the interfacial nature of $\tilde{j}_c$, the spin-to-charge conversion is given by the inverse Rashba-Edelstein "length"

$$\lambda_{\text{IREE}} = \frac{\hbar}{2e} \frac{\tilde{j}_c}{j_s}, \tag{65}$$

where j_s is the spin current density pumped by the ferromagnet and associated with the spin density **S**, expressed in $(\hbar/2e)$ A/m^2, and $\tilde{j}_c$ is measured in A/m. In the framework of the Rashba model, it can be shown that $\lambda_{\text{IREE}} = \alpha_R \tau / \hbar$, where α_R is the Rashba coupling strength and τ the momentum relaxation time at the Rashba-split Fermi surface (Gambardella and Miron, 2011; Shen, Raimondi, and Vignale, 2014). Typical values of λ_{IREE} range from 0.1–0.3 nm in NiFe/Ag/Bi (Rojas-Sánchez *et al.*, 2013; Wei Zhang *et al.*, 2015) to −0.6 nm in NiFe/Cu/Bi$_2$O$_3$ (Karube, Kondou, and Otani, 2016).

Comparison with the inverse SHE in NM/FM bilayers is achieved by converting the effective spin Hall angle (or the SOT efficiency) into λ_{IREE} by taking

$$\lambda_{\text{IREE}} = \theta_{\text{sh}} \lambda_{\text{sf}} \tanh(t_I / 2\lambda_{\text{sf}}), \tag{66}$$

where t_I is the "thickness" of the interface layer in which the spin-to-charge conversion takes place (Rojas-Sánchez *et al.*, 2013, 2016). The maximum attainable length is therefore $\lambda_{\text{IREE}}^{\max} = \theta_{\text{sh}} \lambda_{\text{sf}}$ for $t_I \gg \lambda_{\text{sf}}$. For values of θ_{sh} between 0.1 and 0.3, and $\lambda_{\text{sf}} = 1.5$–2 nm as typical of Pt, Ta, and W, one obtains $\lambda_{\text{IREE}} = 0.15$–0.6 nm, which is comparable to λ_{IREE} of the Ag/Bi interface.

Current injection in such systems results in sizable dampinglike and fieldlike SOT due to the iSGE, as demonstrated by ST-FMR for NiFe/Ag/Bi (Jungfleisch *et al.*, 2016) as well as for the oxidized heavy metal interfaces described in Sec. IV.C.1.b (Fujiwara *et al.*, 2013; An *et al.*, 2016; Demasius *et al.*, 2016; An, Kanno *et al.*, 2018; An, Ohno *et al.*, 2018). In this situation, a 2D charge current produces a 3D nonequilibrium spin density, and the relation between the effective spin Hall angle and the Rashba-Edelstein length reads (Laczkowski *et al.*, 2017)

$$\frac{1}{\lambda_{\text{REE}}} = \frac{2e}{\hbar} \frac{j_s}{\tilde{j}_c} = \frac{\theta_{\text{sh}}}{t_I} \tanh(t_I / 2\lambda_{\text{sf}}). \tag{67}$$

Therefore, the maximum charge-to-spin conversion is

$$\left(\frac{1}{\lambda_{\text{REE}}}\right)^{\max} = \frac{\theta_{\text{sh}}}{2\lambda_{\text{sf}}}$$

when $t_I \ll \lambda_{\mathrm{sf}}$. In other words, within this picture a figure of merit of spin-to-charge conversion is $\theta_{\mathrm{sh}}\lambda_{\mathrm{sf}}$, while for charge-to-spin conversion it is $\theta_{\mathrm{sh}}/\lambda_{\mathrm{sf}}$.

Prominent spin-charge interconversion effects are observed also in 2D electron gases confined at the interface between two insulating oxides, such as LaAlO₃ and SrTiO₃ (Ohtomo and Hwang, 2004). These systems host a variety of unusual electronic phases (Zubko *et al.*, 2011) as well as tunable carrier density and Rashba spin-orbit interaction (Caviglia *et al.*, 2010). Even in the absence of heavy metals, the large interfacial electric fields and long electron relaxation times result in extraordinarily large λ_{IREE}, which can be further modulated by electric gating (Lesne *et al.*, 2016; Song *et al.*, 2017). Spin-pumping experiments on SrTiO₃/LaAlO₃/NiFe reveal that λ_{IREE} changes from 2 to -6 nm as the Fermi level is raised through the crystal-field split interface states, namely, from a single low-lying band with d_{xy} character to the higher-lying heavier $d_{xz,yz}$ bands, where α_{R} is largest (Lesne *et al.*, 2016; Seibold *et al.*, 2017). The observation of strong SOT in SrTiO₃/LaAlO₃/CoFeB at room temperature (Wang, Ramaswamy *et al.*, 2017) shows that the spin current generated by the iSGE at the oxide interface can be effectively absorbed by a magnetic layer deposited on a few nm-thick LaAlO₃, likely via inelastic electron tunneling promoted by defect states in the oxide layer. Interfaces between complex oxides thus represent a notable alternative to heavy metal systems for the generation of SOT, offering additional tools to tune λ_{REE} by controlling the interplay of crystal field and spin-orbit effects in multifunctional heterostructures.

6. Metallic spin valves

Recent theoretical (Taniguchi, Grollier, and Stiles, 2015; Freimuth, Blügel, and Mokrousov, 2018) and experimental works (Humphries *et al.*, 2017; Baek *et al.*, 2018; Bose *et al.*, 2018) pointed out the possibility to induce SOT in all-metallic spin valves by in-plane current injection. These structures, similar to those employed for generating STT (Fig. 2), are FM$_{\mathrm{ref}}$/spacer/FM$_{\mathrm{free}}$ trilayers where FM$_{\mathrm{ref}}$ is a fixed reference ferromagnet with magnetization along $\mathbf{p}$, FM$_{\mathrm{free}}$ is the ferromagnet on which the SOT is measured, and the spacer is a light metal (e.g., Cu or Ti) such that no or little SHE or iSGE is expected from it. According to Taniguchi, Grollier, and Stiles (2015), a spin current polarized along $\boldsymbol{\zeta}\|\mathbf{p}$ is generated by either the AHE or PHE in the bulk of the reference layer and absorbed by the free layer, giving rise to both dampinglike and fieldlike SOTs according to Eq. (2). However, Humphries *et al.* (2017) and Baek *et al.* (2018) pointed out that spin filtering caused by spin-orbit scattering and spin-orbit precession experienced by electrons flowing at the interface between magnetic and nonmagnetic layers give rise to spin currents polarized along $\boldsymbol{\zeta}\|\mathbf{z}\times\mathbf{j}_c$ and $\boldsymbol{\zeta}\|\mathbf{p}\times(\mathbf{z}\times\mathbf{j}_c)$, respectively, which are potentially stronger than the bulk spin currents generated by the AHE and PHE. These predictions have been verified in trilayers with both in-plane (Baek *et al.*, 2018; Bose *et al.*, 2018) and out-of-plane $\mathbf{p}$ (Humphries *et al.*, 2017), for which the SOT symmetry is consistent with the latter mechanisms and allows also for field-free switching of the free layer (Baek *et al.*, 2018).

7. Established features and open questions

The complexity and interplay of the different charge-spin conversion mechanisms outlined in Sec. III underpins an ongoing debate on the origin of SOTs and on strategies to improve their efficiency. Next we summarize the most important findings drawn from experimental investigations of metallic layers:

- In most NM/FM systems, the sign of the dampinglike torque is consistent with that of the SHE of the bulk nonmagnetic metal. Additionally, nonmagnetic metal elements with strong SHE present large dampinglike torques. The magnitude and the sign of the dampinglike torque can be modified by changing the oxidation state or the capping layer of the ferromagnet interface that is not in contact with the nonmagnetic metal. Significant dampinglike torques have been reported also for ferromagnetic layers adjacent to metal alloys and oxide layers with a strong iSGE.

- The fieldlike torque is of the same order of magnitude as the dampinglike torque. The sign and magnitude of the fieldlike torque are not consistent with the predictions of the drift-diffusion model based on the bulk SHE.

- The dampinglike and fieldlike torques typically increase with the thickness of the nonmagnetic metal layer and saturate after a few nm. The dependence of the two torques on the nonmagnetic metal thickness is not the same.

- The temperature dependences of the fieldlike and dampinglike torques are different, indicating the distinct role of electron scattering by magnons or phonons.

- Extrinsic effects related to both interface and bulk electron scattering are significant and can give rise to both dampinglike and fieldlike torques. The SOTs are typically large in high resistivity metals and correlate with the presence of strong SMR in NM/FM bilayers and crystalline AMR in ferromagnet/semiconductor layers.

- The angular dependence of the torques shows that interfacial spin-orbit coupling, through either D'yakonov-Perel relaxation, Fermi surface distortion, or anisotropic mixing conductance, plays a relevant role.

- The insertion of a nonmagnetic light metal spacer between the ferromagnet and a nonmagnetic metal reduces magnetic proximity effects in the nonmagnetic metal, but creates additional interfaces that can contribute to the generation of spin currents. Both the dampinglike and fieldlike torques change upon the insertion of nonmagnetic and magnetic spacers.

- 2D materials, topological insulators, and oxide heterostructures provide large SOTs when interfaced with magnetic layers, consistently with the iSGE arising from spin-momentum locked interface states. Additional contributions to the SOT may result from the SHE in systems with residual bulk conductivity. The symmetry of the SOTs generated by single-crystal layers is determined by the current-injection direction relative to the crystal axes.

- Both dampinglike and fieldlike torques can be controlled through interface engineering, such as gate voltage, oxidation, or capping layer, which offers an efficient

way to improve charge-spin conversion in NM/FM as well as 2D systems.

SOT measurements in multilayer systems are often interpreted assuming either the SHE-SOT model or the Rashba-type iSGE. Such approaches are appealing because of their simplicity, but neglect important aspects of the generation of SOT. The one-dimensional drift-diffusion theory based on the bulk SHE (Sec. III.C) is the most commonly employed model to relate the torque amplitude to the spin Hall conductivity of the nonmagnetic metal. Such a model includes the probability of spin transmission at the interface through the spin mixing conductance parameter, but neglects the interface-generated spin density by either the iSGE or spin-dependent electron scattering as well as the spin-memory loss. Another major limitation of this model is that it assumes constant parameters σ_N, $\lambda_{\rm sf}$, and $\theta_{\rm sh}$ throughout the nonmagnetic metal layer, which is unjustified on both theoretical and experimental grounds. When the thickness of the nonmagnetic metal is comparable to the electronic mean free path (of the order of the grain size or t_N, i.e., a few nm in sputtered samples), semiclassical size effects become important and govern the current distribution in NM/FM bilayers (Camley and Barnas, 1989; Zhang and Levy, 1993). Neglecting these effects can lead to the wrong estimation of the SOT efficiency and $\lambda_{\rm sf}$ (Chen and Zhang, 2017). Moreover, *ab initio* calculations showed that the intrinsic spin Hall conductivity can strongly vary close to the interface, leading to an enhancement of the SOT (Freimuth, Blügel, and Mokrousov, 2015; Lei Wang *et al.*, 2016).

Most SOT models based on interfacial Rashba spin-orbit coupling assume a static spin polarization localized at a sharp interface between the nonmagnetic metal (or the oxide) and the ferromagnet. Considering the complexity of the real ultrathin magnetic multilayers involving complex orbital hybridization, disordered interfaces, and spin-dependent semiclassical size effects, it is quite unclear how these two models (bulk SHE and interfacial Rashba-like iSGE) apply to real systems. Spin-pumping experiments at Bi surfaces have been interpreted as evidence for either an interface-enhanced SHE (Hou *et al.*, 2012) or the iSGE (Rojas-Sánchez *et al.*, 2013). Angle-resolved photoemission studies, on the other hand, provide evidence that the iSGE is not a pure 2D effect in metallic thin films: the presence of magnetic exchange (Krupin *et al.*, 2005), out-of-plane spin polarization (Takayama *et al.*, 2011), spin-momentum locked quantum well states in the ferromagnet (Moras *et al.*, 2015), and topologically protected surface states (Thonig *et al.*, 2016; Marmolejo-Tejada *et al.*, 2017) significantly alter the Rashba effect at metallic interfaces compared to model semiconducting heterostructures.

Extrinsic effects such as impurity and interface scattering induce additional spin currents that propagate through or away from the magnetic layer and are polarized in directions different from the standard SHE and Rashba models, calling for a generalization of the spin current sources and spin mixing conductance (Chen and Zhang, 2015; Amin and Stiles, 2016a, 2016b; Saidaoui and Manchon, 2016; Humphries *et al.*, 2017; Baek *et al.*, 2018). For example, electron scattering from an interface with spins parallel and antiparallel to the local spin-orbit field have different reflection and transmission probabilities, leading to a net spin current polarized parallel to the $\mathbf{y} = \mathbf{z} \times \mathbf{j}_{\rm c}$ direction, identical to that of the spin current due to the SHE. Additionally, if the electrons carry a net spin polarization along $\mathbf{p}$, as in a ferromagnet, precession about the spin-orbit field results in a transverse spin current with polarization parallel to the $\mathbf{p} \times \mathbf{y}$ direction (Baek *et al.*, 2018). The interplay between all these effects makes it questionable to draw a clear separation between the SHE and iSGE in metallic structures, even when considering idealized theoretical models of these heterostructures.

Finally, the typical SOT bilayers are usually only a few nanometers thick. The phenomenological notion of an interface between bulk regions, as well as the interpretation in terms of bulk SHE, appears unjustified based on both theoretical and practical grounds. A full quantum-mechanical treatment of the SOT in realistic three-dimensional structures including disorder is therefore essential to reach consistency between experiments and theory.

D. Magnetization dynamics

It is well known that, due to the STT, a spin-polarized electric current injected into a ferromagnetic layer through a nanocontact leads to the emission of spin waves (Berger, 1996; Tsoi *et al.*, 1998). This effect provides a way to realize tunable spin-torque nano-oscillators, which can serve as active microwave components in integrated circuits (Tsoi *et al.*, 2000; Kiselev *et al.*, 2003; Rippard *et al.*, 2004; Demidov, Urazhdin, and Demokritov, 2010; Madami *et al.*, 2011). The discovery of SOT has led to new paradigms to control the high-frequency magnetization dynamics by means of dc and ac currents (Demidov *et al.*, 2017). In contrast to STT, SOTs allow for the compensation of magnetic damping and the generation of spin waves in spatially extended regions of a magnetic material. Moreover, since the spin and charge currents follow separate paths, the electrical current does not need to flow through the active magnetic layer, allowing for the excitation of both conducting and insulating magnetic materials. SOTs thus enable efficient and flexible device geometries for the generation and amplification of magnetic oscillations as well as for the propagation and manipulation of coherent spin waves, opening entirely new perspectives in the field of magnonics (Chumak *et al.*, 2015).

To a first approximation, the effects of the SOTs on the magnetization dynamics are described by Eqs. (1) and (2). Consequently, one expects that the fieldlike torque shifts the frequency spectrum of the magnetic layer, similar to an applied magnetic field, and that the dampinglike torque changes the magnitude of the magnetic damping. An early demonstration of the SOT-induced modification of magnetic damping was reported by Ando *et al.* (2008) in resonantly excited Pt/NiFe, in which the width of the FMR line decreased or increased depending on the sign of the dc current injected in the bilayer. This work evidenced variations of the damping constant α by an amount

$$\Delta\alpha = \frac{\gamma}{2\pi f M_s t_F} \frac{\hbar}{2e} \sin\psi \, \xi_{DL}^j j_c, \tag{68}$$

where f is the resonance frequency of the magnetic layer and ψ is the angle between the current and the precessional axis of the magnetization. Later measurements showed how the electrical control of magnetic damping can be used to enhance the spin wave propagation length in microwave guides (An *et al.*, 2014; Demidov, Urazhdin *et al.*, 2014). The variations of $\Delta\alpha$ reported in the literature range from a few percent to complete compensation of the damping, which eventually results in the onset of steady-state auto-oscillations of the magnetization (Demidov *et al.*, 2012; Liu, Pai, Ralph, and Buhrman, 2012). Note that the simple linear relationship between damping and current exemplified by Eq. (68) is observed only at low currents, whereas nonlinear phenomena and magnetic fluctuations lead to a more complex behavior as the damping compensation is approached (Demidov *et al.*, 2017).

A limiting factor for achieving self-sustained oscillations is the degeneracy of spin wave modes. If the sample is large, a significant amount of modes compete with each other to absorb the excitations induced by the SOT. In such a case, the degeneracy is high and only thermal excitations can be electrically controlled rather than current-driven coherent oscillations. Achieving self-sustained magnetic oscillations requires one to lift the degeneracy by reducing the size of the sample and thereby lowering the excitation threshold and excitation bandwidth. Current-driven magnetic oscillations were thus reported in a three-terminal CoFeB/MgO/CoFeB MTJ fabricated on top of a large Ta buffer layer [see Fig. 30(a)] (Liu, Pai, Ralph, and Buhrman, 2012). Because of the reduced size of the nanopillar ($\sim 50 \times 80$ nm^2), current-driven oscillations were detected electrically through the MTJ [see Fig. 30(b)] and independent control of the excitation via the currents injected into the Ta layer and through the MTJ was achieved. More recently, Duan, Boone *et al.* (2014) and Duan, Smith *et al.* (2014) achieved SOT-driven spin wave damping control and auto-oscillations in long and narrow nanowires ($\sim 1.6~\mu m \times 190$ nm), where both bulk modes and edge modes were identified.

Another successful configuration was realized by Demidov *et al.* (2012) by locally injecting a spin current in an extended ferromagnetic layer [see Fig. 30(c)]. The local injection creates a spin wave bullet, i.e., a spin wave packet localized in space through nonlinear energy losses (Slavin and Tiberkevich, 2005). This self-localization enables the selection of a small number of spin wave modes that reveal themselves in the coherent auto-oscillation. The microwave spectrum of such a nano-oscillator presents features similar to "traditional" STT point-contact oscillators (Slavin and Tiberkevich, 2005; Bonetti *et al.*, 2010), namely, a spin wave "bullet" and a propagating spin wave mode (Liu, Lim, and Urazhdin, 2013). These devices, similar to STT point-contact oscillators, are characterized by a strong nonlinearity, which enables their efficient synchronization to external rf signals over a broad frequency range (Demidov, Ulrichs *et al.*, 2014) as well as the synchronization of different oscillators placed next to each other at distances of up to several microns (Awad *et al.*, 2017).

A unique feature of SOTs is that they provide interconversion between the spin and charge currents in an electrical
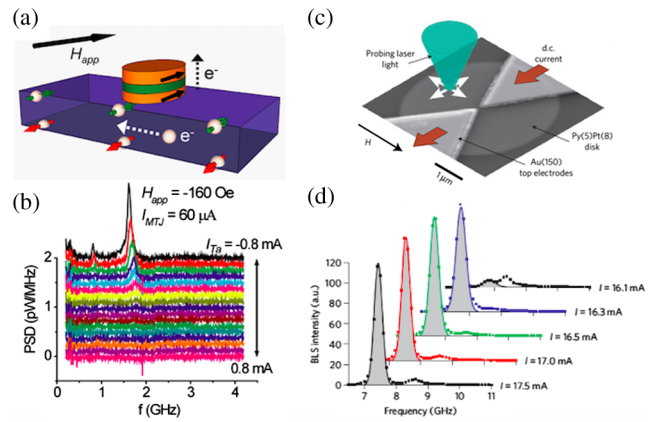

FIG. 30. (a), (c) Two configurations for the SOT-induced nano-oscillator and (b), (d) their corresponding excitation spectrum. (a), (b) Nanopillar deposited on top of a nonmagnetic metal. From Liu, Pai, Ralph, and Buhrman, 2012. (c), (d) Local injection into an extended ferromagnet. From Demidov *et al.*, 2012.

conductor and the magnon currents in a magnetic insulator. In an influential experiment, Kajiwara *et al.* (2010) proposed that SOTs can convert a dc electric current flowing in a Pt wire deposited on a yttrium iron garnet (YIG) film into a spin wave propagating through the YIG film, which can then be detected by a Pt electrode at a different location using spin pumping. In this experiment, which remains controversial, SOT needs to be large enough to compensate the damping of the fundamental FMR spin wave mode. This is particularly difficult to achieve in ultralow magnetic damping materials, as SOTs excite a broad range of modes. In YIG, Xiao and Bauer (2012) argued that surface spin waves are preferentially excited compared to bulk spin waves, which renders the observation of current-driven auto-oscillations very sensitive both to the size of the YIG layer and to the quality of the interface with Pt. Hamadeh *et al.* (2014) showed that the magnetic losses of spin wave modes in micron-sized YIG(20 nm)/Pt(8 nm) disks can be reduced or enhanced depending on the polarity and intensity of the dc current flowing through Pt, reaching complete compensation of the damping of the fundamental mode for a current density of 3×10^7 A cm^{-2} and eventually inducing coherent SOT-induced auto-oscillations (Collet *et al.*, 2016); see Fig. 31. By using Bi-substituted YIG films with perpendicular magnetic anisotropy, it is further possible to prevent the self-localization of the magnetization oscillations, thus leading to the propagation of coherent magnons into an extended magnetic insulator film (Evelt *et al.*, 2018).

An alternative strategy to circumvent the hurdles posed by the generation of coherent spin waves is to utilize thermal magnons in the same spirit as in spin caloritronics experiments (Uchida *et al.*, 2010; Bauer, Saitoh, and Wees, 2012). In this case, SOTs excite a broad range of magnons with characteristic frequencies much higher than the fundamental FMR mode ($\sim k_B T$ rather than a few GHz) and able to transmit information over long distances (Bender, Duine, and Tserkovnyak, 2012; Zhang and Zhang, 2012). Using a nonlocal setup consisting of two parallel Pt electrodes deposited
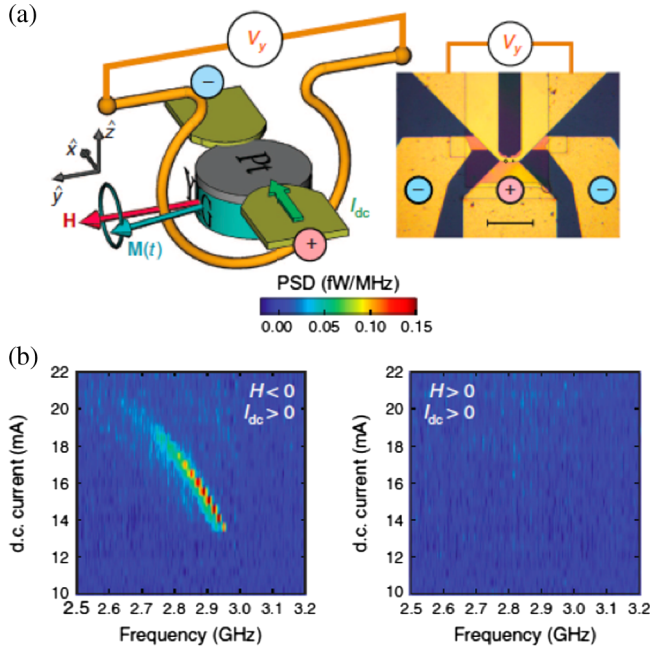
(a)

(b)

FIG. 31. (a) Sketch of the measurement configuration and microscopy image of a device with two connected microdisks (underneath the circles). The bias field $\mu_0 H$ is oriented transversely to the dc current I_{dc} flowing in Pt. The inductive voltage V_y produced in the antenna by the precession of the YIG magnetization $M(t)$ is amplified and monitored by a spectrum analyzer. (b) Power spectral density (PSD) maps measured on a 4 mm YIG/Pt disk at fixed $|\mu_0 H| = 47$ mT and variable I_{dc}. The two panels correspond to two different polarities of $\mu_0 H$. An auto-oscillation signal is detected above a threshold current of ± 13 mA if $\mu_0 H I_d < 0$, in agreement with the symmetry of the torque. Adapted from Collet *et al.*, 2016.

on an extended YIG film, Cornelissen *et al.* (2015) and Goennenwein *et al.* (2015) demonstrated SOT-driven injection, transmission, and detection of thermal magnons over distances up to 40 μm, with a crossover between a linear transport regime dominated by thermal exchange magnons at low current and nonlinear transport regime dominated by subthermal magnetostatic magnons at high current (Thiery *et al.*, 2018). These studies were recently extended to antiferromagnets, such as α-Fe$_2$O$_3$, where antiferromagnetic magnons can carry spin information over a few tens of microns (Lebrun *et al.*, 2018).

Overall, the SOT approach is attractive for controlling the magnetization dynamics of a broad class of ferromagnetic and antiferromagnetic materials, including both conducting and insulating systems. Because no electric current is required to flow between the magnetic layer and the spin-orbit coupled electrodes, low-damping magnetic dielectric materials can be used as the carriers of magnetic information over large distances. Moreover, SOTs can be applied to arbitrarily large areas of a magnetic film, unlike STT, which is limited to pillar-shaped nanostructures, allowing for spin wave amplification through the compensation of damping. SOTs can thus be utilized for the generation of propagating spin waves, the enhancement of their propagation range, and their detection in a single integrated nanomagnonic device, with the perspective of implementing coherent-wave computing and information processing.

E. Magnetization switching

The realization of current-driven magnetization switching has been a major milestone in the progress toward SOT devices. Miron, Garello *et al.* (2011), Liu, Lee *et al.* (2012), and Liu, Pai *et al.* (2012) demonstrated that, in the presence of a constant in-plane magnetic field, the magnetization direction of a perpendicularly magnetized ultrathin trilayer (Pt/Co/AlO$_x$ and Ta/CoFeB/MgO) can be reversibly switched by injecting bipolar current pulses at current densities of the order of 10^7–10^8 A/cm^2; see Fig. 32. This observation was soon confirmed by several groups using different magnetic stacks and heavy metal substrates (Avci *et al.*, 2012, 2014; Pai *et al.*, 2012; Emori *et al.*, 2013; Yu, Upadhyaya *et al.*, 2014), as well as antiferromagnets (Shunsuke Fukami *et al.*, 2016; Oh *et al.*, 2016; Wadley *et al.*, 2016), magnetic insulators (Li *et al.*, 2016; Avci, Quindeau *et al.*, 2017), and topological insulators (Han *et al.*, 2017; Wang *et al.*, 2017; Mahendra *et al.*, 2018). Notably, earlier investigations of Pt/Co/Pt and Pt/Co also reported an effect of very small current densities on the low temperature coercivity of Co, albeit mainly attributed to Joule heating (Lin *et al.*, 2006; Xie *et al.*, 2008; Riss *et al.*, 2010).

The switching of a perpendicularly magnetized layer can be qualitatively explained by considering the combined action of the dampinglike torque and in-plane field B_x in a simple macrospin picture, as shown in Fig. 32(e). In the Pt/Co/AlO$_x$ stack, a positive current pulse induces an effective field B_{DL}, such that the magnetization can rotate from up to down if B_{DL} is initially parallel to B_x, but cannot rotate from down to up if B_{DL} is antiparallel to B_x. When the current polarity is reversed, the sense of rotation changes, such that bipolar switching is achieved by either current or in-plane field reversal, as shown in Fig. 32(f). More generally, the transferred angular momentum is transverse to both the current direction and the normal to the plane, which alone cannot ensure reversible magnetization switching between the $+\mathbf{z}$ and $-\mathbf{z}$ directions. Hence, the dampinglike torque must be supplemented by the in-plane field B_x that breaks the symmetry along the current direction and determines the outcome of the switching process. In the macrospin approximation, the threshold switching current is given by (Lee *et al.*, 2013)

$$j_{\text{sw},\perp} = \frac{2e}{\hbar} \frac{M_s t_F}{\xi_{DL}^j} \left(\frac{B_{K,\perp}}{2} - \frac{B_x}{\sqrt{2}} \right), \tag{69}$$

where $B_{K,\perp}$ is the perpendicular anisotropy field. In-plane magnetized samples, on the other hand, switch at zero external field as long as the magnetization has a nonzero component in the $\mathbf{y}$ direction, which can be induced by shape anisotropy (Liu, Pai *et al.*, 2012; S. Fukami *et al.*, 2016). In this case, the threshold current has the same form as that of the conventional STT switching for free and fixed layers with in-plane magnetization (Sun, 2000) and is given by (Lee *et al.*, 2013)

$$j_{\text{sw},\parallel} = \alpha \frac{2e}{\hbar} \frac{M_s t_F}{\xi_{DL}^j} \left(B_{K,\parallel} + \frac{B_d}{2} \right), \tag{70}$$
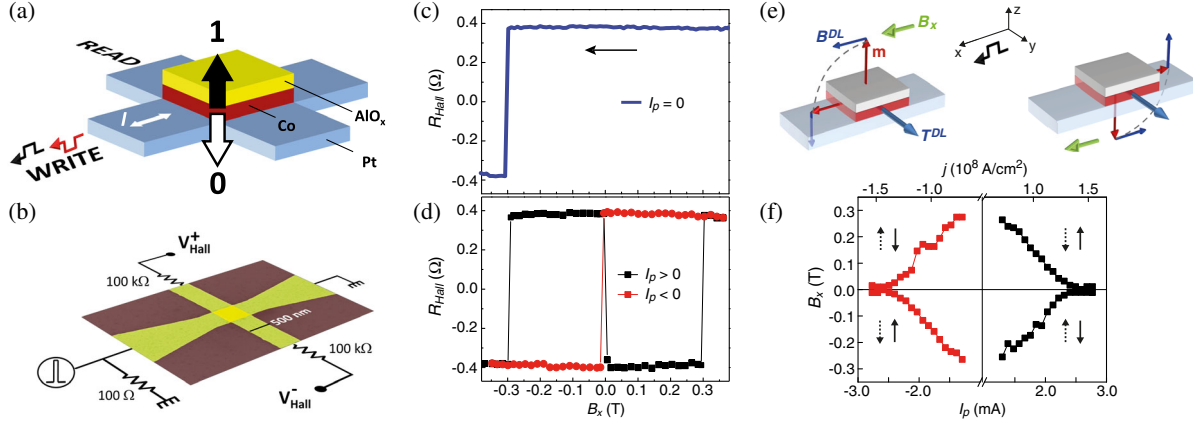
FIG. 32. (a) Schematic of a Co(0.6 nm)/AlO$_x$(2 nm) dot patterned on top of a 3-nm-thick Pt Hall cross. Black and white arrows indicate the equilibrium magnetization states of the Co layer. (b) Detection scheme and scanning electron micrograph of the sample. (c) m_z measured by the anomalous Hall resistance during a downward sweep of the external field B_x applied parallel to the current direction. The field has a 2° out-of-plane tilt to unambiguously define the residual z component. (d) The same measurement recorded after the injection of positive (black squares) and negative (red circles) current pulses of amplitude $I_p = 2.58$ mA, showing bipolar switching of m_z. (e) Macrospin model showing the stable (right) and unstable (left) magnetic configurations depending on the sign of B_{DL} relative to B_x. (f) Switching diagram: the dots show the minimum in-plane field at which switching becomes deterministic as a function of the injected current. Dashed (solid) arrows indicate the magnetization direction before (after) switching. Adapted from Miron *et al.*, 2011.

where $B_{K,\parallel}$ is the in-plane anisotropy field and B_d the demagnetizing field. Equations (69) and (70) exemplify the relationship between the power required for switching, the thermal stability of a magnet (determined by B_K) and ξ_{DL}^j. However, the actual mechanism of SOT switching is more complex than coherent magnetization reversal under the action of the dampinglike torque alone.

In realistic systems, j_{sw} depends on the factors appearing in Eqs. (69) and (70) as well as on the DMI, domain pinning field, device geometry, size, temperature, and duration of the current pulses. The temperature, which is determined by the current distribution in the bilayer as well as by the thermal conductivity of the different materials in the stack, plays a major role, both in activating the switching as well as in changing critical parameters such as M_s, B_K, α, and ξ_{DL}^j during switching. These factors vary significantly from experiment to experiment, so that a comparative estimate of the switching efficiency for different material systems can be highly misleading. Nonetheless, an approximate figure of merit for the switching efficiency can be calculated by taking the threshold power density $P_{sw} = j_{sw}^2 \rho \propto \rho/(\xi_{DL}^j)^2$ with j_{sw} estimated using the macrospin approximation, which is independent of the device size, temperature, and pulse length. Figure 33(a) presents a comparison of $\rho/(\xi_{DL}^j)^2$ for different nonmagnetic material systems (solid bars), based on the values of $(\xi_{DL}^j)^2$ and ρ reported in Figs. 33(b) and 33(c), respectively. Within the confines of such a comparison, Pt and W emerge as the best heavy metal elements, whereas topological insulators offer the largest gains in efficiency. Note that the current distribution in NM/FM bilayers can significantly alter the efficiency, especially if the resistivity of the ferromagnet is much smaller than that of the nonmagnetic material. By using a simple parallel resistor model, the threshold power density can be estimated as
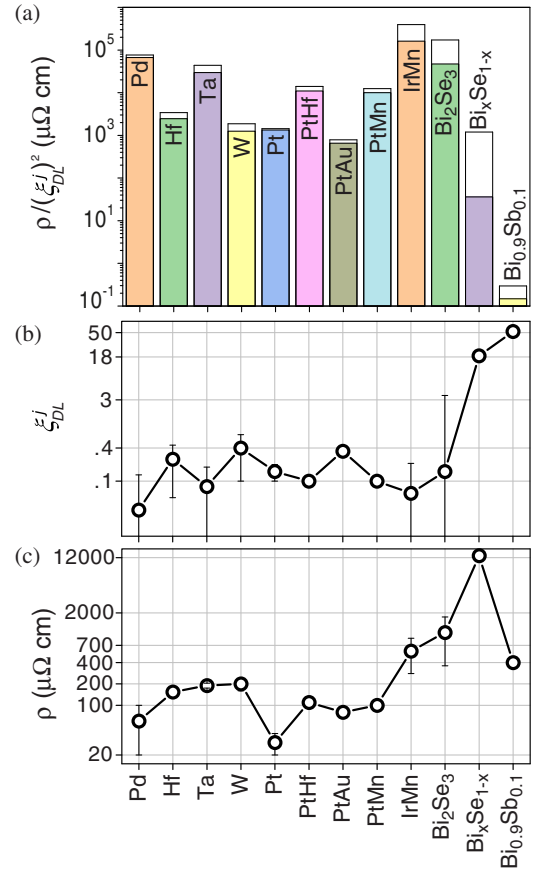

FIG. 33. (a) Power density $\rho/(\xi_{DL}^j)^2$ (solid bars) calculated using the (b) SOT efficiency and (c) resistivity of different nonmagnetic layers. The values are taken from Table II, with error bars representing experimental spreads, when available. The open bars represent the switching efficiency calculated for a NM/FM stack including a fictitious CoFeB layer according to Eq. (71).

$$P_{sw} \propto \left(\frac{\rho_N t_F}{\rho_F t_N} + 1 \right) \frac{\rho_N}{(\xi_{DL}^j)^2}. \tag{71}$$

The open bars in Fig. 33(a) show the change of the efficiency calculated using Eq. (71) for a bilayer with $t_N = 4$ nm, $t_F = 1$ nm, and $\rho_F = 100\ \mu\Omega$ cm, as typical, e.g., of CoFeB.

1. Switching mechanism

Although the macrospin model qualitatively reproduces the stability phase diagram of rather extended films (Liu, Lee *et al.*, 2012), magnetization switching in structures larger than the width of a domain wall ($\gtrsim 10$ nm) occurs by nucleation and expansion of magnetic domains. The magnetization reversal process is thus closely related to the SOT-driven dynamics of Néel-type domain wall in the presence of DMI (see Sec. VI). Different switching models have been proposed based on micromagnetic simulations (Finocchio *et al.*, 2013; Perez *et al.*, 2014; Martinez *et al.*, 2015; Mikuszeit *et al.*, 2015) and spatially resolved MOKE measurements (Emori *et al.*, 2013; Ryu *et al.*, 2013; Yu, Upadhyaya *et al.*, 2014; Safeer *et al.*, 2016). In such models, the domain nucleation is either random and thermally assisted (Finocchio *et al.*, 2013; O. J. Lee *et al.*, 2014; Perez *et al.*, 2014) or determined by the combined action of DMI, external field, and edge effects (Pizzini *et al.*, 2014; Martinez *et al.*, 2015; Mikuszeit *et al.*, 2015), followed by domain wall propagation across the magnetic layer driven by the dampinglike torque.

Time-resolved x-ray microscopy measurements of circular shaped Pt/Co/AlO$_x$ dots (Baumgartner *et al.*, 2017) eventually confirmed the edge nucleation models, further showing that the nucleation point is deterministic and alternates between the four quadrants of a dot depending on the sign of the magnetization, B_x, DMI, dampinglike and fieldlike torques, as illustrated in Fig. 34. These measurements also showed that switching is achieved within the duration of the current pulse with an incubation time below the time resolution of the experiment (≈ 100 ps) and fast propagation of a tilted domain wall across the dot (Baumgartner, 2018) with domain wall velocities of the order of 400 m/s. As the switching unfolds along a reproducible and deterministic

path, the timing and the extent of magnetization reversal can be reliably controlled by the amplitude and duration of the current pulses (Baumgartner *et al.*, 2017). Measurements performed by time-resolved MOKE on larger dots with a thinner Co layer, on the other hand, show significant after-pulse magnetic relaxation (Decker *et al.*, 2017), which is ascribed to long-lasting heating effects and weaker magnetic anisotropy compared to Baumgartner *et al.* (2017). After-pulse relaxation has been observed also in Ta/CoFeB/MgO dots for current pulses exceeding 2 ns, but was attributed to domain wall reflection at the sample edges that is favored by the lower DMI and Gilbert damping of Ta/CoFeB/MgO (Yoon *et al.*, 2017). These different results reveal how the reversal path is determined by the balance between damp-inglike and fieldlike torques, DMI, magnetic anisotropy, and temperature. For samples matching the width of the current line, the Oersted field can also facilitate or hinder the reversal (Aradhya *et al.*, 2016; Baumgartner *et al.*, 2017). In all cases, however, SOT switching is bipolar and robust with respect to multiple cycling events as well as to the presence of defects.

2. Switching speed

One of the most attractive features of SOT switching is the timescale of magnetization reversal. Because the switching speed scales with the lateral dimensions of the sample, and the domain wall velocity can attain up to 750 m/s (Miron, Garello *et al.*, 2011; Yang, Ryu, and Parkin, 2015), the reversal time can be reduced to well below 1 ns in dots of 100 nm size (Garello *et al.*, 2014). Figure 35(a) shows that the switching probability of perpendicularly magnetized Pt/Co/AlO$_x$ dots has a narrow distribution as a function of pulse length τ_p, which decreases to below 100 ps as the current density increases. In this study, a switching probability of 100% was demonstrated down to $\tau_p = 180$ ps, consistently with reversal due to domain nucleation and propagation. The critical switching current j_{sw} is characterized by a long and a short timescale regime, shown in Fig. 35(b), similar to STT-induced switching in metallic spin valves (T. Liu *et al.*, 2014). j_{sw} depends weakly on τ_p above 10 ns, as expected for a thermally activated reversal process (Bedau *et al.*, 2010), and
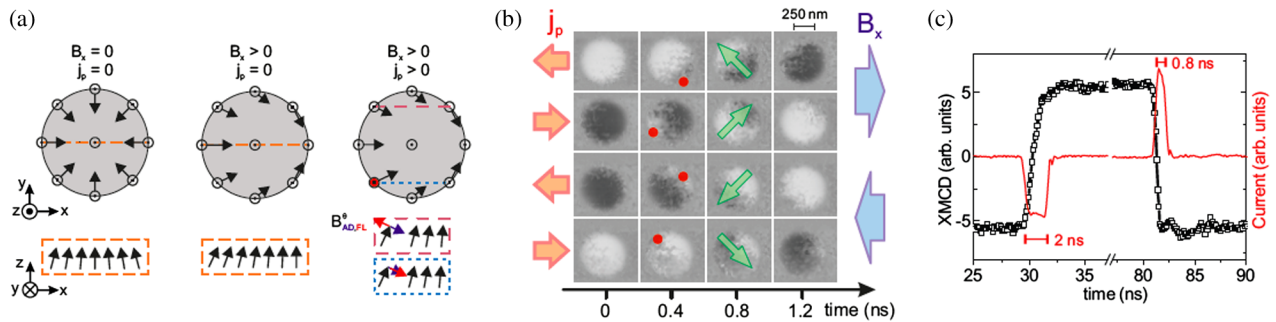
FIG. 34. (a) Schematics of the tilting of the magnetization at the edges of a Pt/Co/AlO$_x$ dot due to the DMI (left), DMI and external field B_x (middle), DMI, B_x, and current (right). The polar components of the dampinglike and fieldlike effective fields add up at the nucleation point. (b) Snapshots of the reversal process of a circular dot for different combinations of current and field measured by time-resolved scanning x-ray transmission microscopy. The red dots and green arrows indicate the nucleation point and the domain wall propagation direction, respectively. The pulse duration is 2 ns. (c) Time trace of the average out-of-plane magnetization (black squares) during current injection (red line). The amplitude of the first (second) pulse is $j_p = 3.1 \times 10^8$ (4.4×10^8) A/cm^2, and $B_x = 0.11$ T. Adapted from Baumgartner *et al.*, 2017.
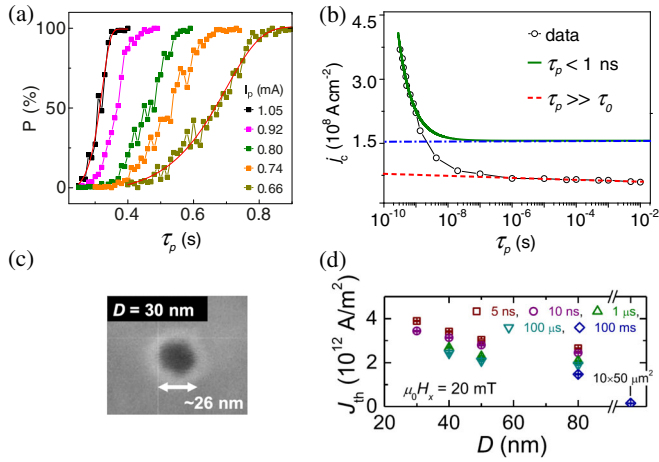
FIG. 35. (a) Switching probability P of a square $Pt(3 \text{ nm})/Co(0.6 \text{ nm})/AlO_x$ dot with a lateral size of 90 nm as a function of the current-pulse duration τ_p at fixed in-plane field $B_x = 91$ mT. (b) Critical current density as a function of pulse duration defined at $P = 90\%$. The green solid line is a fit to the data in the short-time regime ($\tau_p < 1$ ns), and the red dashed line is a fit in the thermally activated regime ($\tau_p \geq 1\ \mu s$). The blue dash-dotted line represents the intrinsic critical current j_{c0}. Adapted from Garello *et al.*, 2014. (c) Scanning electron microscope image of a $Ta(5 \text{ nm})/CoFeB(1.2)/MgO$ dot with a nominal diameter D of 30 nm. (d) Device diameter dependence of the critical current density at various τ_p. Adapted from C. Zhang *et al.*, 2015.

scales linearly with τ_p^{-1} below about 1 ns, as expected in the intrinsic regime where the reversal time is inversely proportional to the transferred angular momentum.

Studies of how j_{sw} scales as a function of dot size have been performed for Ta and $W/CoFeB/MgO$ dots (C. Zhang *et al.*, 2015; Zhang *et al.*, 2018). j_{sw} was found to increase by 1 order of magnitude going from micrometer-sized $Ta/CoFeB/MgO$ stripes to 80 nm dots, and to remain approximately constant upon further reduction of the dot size down to 30 nm; see Figs. 35(c) and 35(d)]. This behavior was interpreted as a signature of incipient monodomain behavior, even though no precessional switching was observed, contrary to the prediction of macrospin models (Lee *et al.*, 2013; Park *et al.*, 2014). An additional feature that makes SOT switching attractive for applications is that the incubation time required to start the process appears to be negligible (Garello *et al.*, 2014). The SOT geometry, in which $\mathbf{T}_{DL}$ can be made orthogonal to the quiescent magnetization, implies that the magnetization reacts immediately to the current, contrary to STT-induced switching, in which $\mathbf{T}_{DL}$ is initially zero for collinear magnetic layers until thermal fluctuations induce a misalignment of the free layer magnetization that is sufficient to trigger the reversal, leading to ns-long random delays (Devolder *et al.*, 2008; Hahn *et al.*, 2016).

3. Zero field switching

A critical issue for perpendicularly magnetized layers is the need to apply an external field B_x to uniquely define the switching polarity, as shown in Fig. 32. Although B_x by itself cannot switch the magnetization because it is orthogonal to

the easy axis, fields ranging from 1 to 100 mT are typically required to achieve deterministic reversal, depending on the current density as well as on the magnetic anisotropy of the layers (Avci *et al.*, 2014). Several approaches have been demonstrated to solve this issue by substituting B_x with a real or effective field embedded into a device. The first working concept by Miron *et al.* (2011) was to deposit two 50-nm-thick CoFe stripes on either side of the magnetic dot, providing a dipolar in-plane field parallel to the current. This solution, however, is not practical for device integration because it limits the scalability of a matrix of such dots or MTJs.

Yong-Chang Lau *et al.* (2016) showed that it is possible to embed an in-plane magnetized CoFe layer directly into the stack, and provide an effective B_x on the perpendicular CoFe free layer via interlayer exchange coupling mediated by nonmagnetic Ru or Pt spacers. Such an approach allows for varying the sign of B_x upon changing the spacer thickness, but may not be easily integrated into standard MTJ architectures. A more straightforward approach relies on the stray field projected by an in-plane magnetized layer placed on top of the free layer/barrier/reference layer stack (Zhao *et al.*, 2017), provided that such a field does not reduce the TMR. Alternatively, the ferromagnet can be deposited directly on top of a few nm-thick antiferromagnet like IrMn or PtMn; see Fig. 36 (van den Brink *et al.*, 2016; Shunsuke Fukami *et al.*, 2016; Oh *et al.*, 2016). The antiferromagnetic layer provides an in-plane exchange bias field but also the source of the spin density, which enables the switching of perpendicular ferromagnetic layers in zero field at current densities of the order of 3×10^7 A/cm². The switching process in ferromagnetic and antiferromagnetic systems takes place in a stepwise manner, as schematized in Fig. 36(c), depending on the microstructure of the antiferromagnetic layer and the local direction of the exchange bias field (van den Brink *et al.*, 2016; Shunsuke Fukami *et al.*, 2016; Kurenkov *et al.*, 2017a). This behavior can be also exploited to introduce analogue memristive properties into three-terminal MTJ devices (Shunsuke Fukami *et al.*, 2016).

Another practical solution consists of employing a magnetic spin valve composed of a bottom reference ferromagnet and a top recording free layer in the current-in-plane configuration (see Sec. IV.C.6). If the magnetization of the bottom ferromagnet points along the current direction, the spin current resulting from spin-orbit interfacial scattering has a component $\zeta \| \mathbf{p} \times (\mathbf{z} \times \mathbf{j}_c) \equiv \mathbf{z}$ polarized along the easy axis of the free layer, which has been shown to induce field-free switching in $CoFeB/NiFe/Ti/CoFeB/MgO$ spin valves (Baek *et al.*, 2018). The combination of STT and SOT in perpendicular MTJs also leads to field-free magnetization switching of the free layer, which is particularly promising for applications (Wang *et al.*, 2018).

Finally, an elegant approach to this problem is to introduce lateral symmetry breaking in the magnetic structure. Thickness gradients of the oxide and ferromagnetic layers have been shown to induce an out-of-plane fieldlike torque (Yu *et al.*, 2014; Yu, Upadhyaya *et al.*, 2014) or a tilted anisotropy (Torrejon *et al.*, 2015; You *et al.*, 2015), both conducive to zero field switching, whereas asymmetric
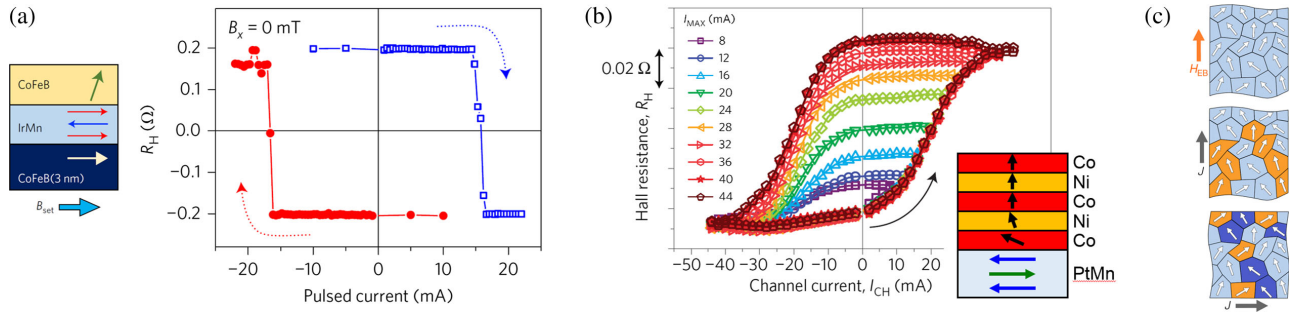
FIG. 36. (a) Left: schematic of the in-plane effective field induced by exchange bias. The colored arrows in the layers indicate the direction of the magnetic moments. Field-free switching of Ta(5 nm)/CoFeB(3 nm)/IrMn(3 nm)/CoFeB/MgO as a function of current. From Oh *et al.*, 2016. (b) Magnetization loops of a $[Co(0.3)/Ni(0.6)]_2/Co(0.3)$ multilayer on PtMn(8 nm) measured after the application of current pulses of increasing amplitude up to the maximum specified in the legend. The black arrow indicates the position from which the measurement starts after initialization by a negative pulse. Adapted from Shunsuke Fukami *et al.*, 2016. (c) Model representing the uncompensated spin direction in each grain of the antiferromagnet at the interface with the ferromagnet. Top: situation after field cooling showing an average exchange bias field (orange arrow). A current pulse along the exchange bias direction (middle) or perpendicular to it (bottom) switches the regions of the ferromagnetic layer coupled to only one type of antiferromagnetic domain. Switched regions are indicated in orange and blocked regions are indicated in dark blue. Adapted from van den Brink *et al.*, 2016.

patterning of the magnetic and conductive layers has been used to control the switching polarity via nonreciprocal domain wall propagation (Safeer *et al.*, 2016). Recently, artificial nanomagnets consisting of adjacent out-of-plane and in-plane magnetized regions coupled by the DMI have also been shown to exhibit field-free switching, with interesting implications to cascade linear and planar arrays of nanomagnets (Luo *et al.*, 2019).

F. Memory and logic devices

SOT-operated devices can find application in memory as well as logic architectures where current-induced switching is required to control the magnetization of one or several magnetic elements (Lee and Lee, 2016). MTJs with in-plane (Liu, Pai *et al.*, 2012; Pai *et al.*, 2012; Yamanouchi *et al.*, 2013) and perpendicular (Cubukcu *et al.*, 2014; Garello *et al.*, 2018) magnetization provided the first demonstration of three-terminal devices in which the write operation is performed by SOTs (Fig. 37).

MTJs constitute the building blocks of MRAMs, where the bit state is encoded in the high (low) TMR corresponding to antiparallel (parallel) alignment of the magnetization of the free and reference layers. The ever increasing need for faster data storage and retrieval has placed MRAMs in a prime position to replace or complement complementary metal-oxide semiconductor (CMOS)-based memory technologies, owing to the intrinsic nonvolatility, low write energy, low standby power, as well as superior endurance and resistance to radiation of MTJ bit cells compared to semiconductor memories (Apalkov, Dieny, and Slaughter, 2016; Hanyu *et al.*, 2016). State-of-the-art MRAMs incorporate STT as the writing mechanism (Kent and Worledge, 2015). STT brings great advantages in terms of scalability and integration with peripheral electronics, since the critical switching current scales with the area of the free layer and requires only two terminals to perform the read and write operations; see Fig. 37(a). However, as the write and read currents flow along the same path through the oxide tunnel

barrier, a compromise between conflicting requirements must be achieved, namely, a thin barrier for low current switching and a thick barrier for high TMR. Moreover, because the STT reversal process is thermally activated, a large overdrive current is required for fast switching, which can damage the tunnel barrier, while the finite probability to not switch at high currents and to switch at low current leads to write error rates that are larger than desired (Oh *et al.*, 2009).
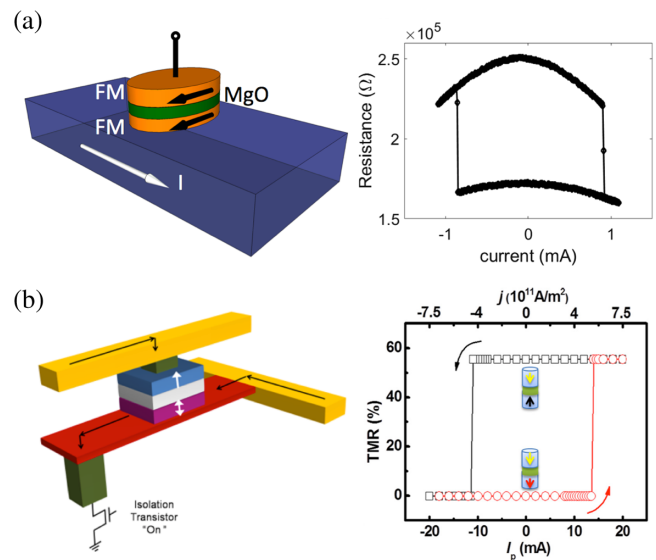
FIG. 37. (a) Left: Schematic of a three-terminal MTJ device with in-plane magnetization. Right: TMR of the device as a function of the applied dc current. An in-plane external field of 3.5 mT is applied to set the device at the center of the minor loop, although this is not required for switching the in-plane magnetized free layer. Courtesy of Luqiao Liu. (b) Left: Schematic of a three-terminal MTJ with perpendicular magnetization. Right: TMR as a function of current amplitude I_p injected in the Ta electrode using 50-ns-long pulses under an in-plane magnetic field of 40 mT. Adapted from Cubukcu *et al.*, 2014.

Three-terminal MTJ devices based on SOT offer critical advantages in this respect, as the free layer can be switched without passing a current through the oxide and reference layers; see Fig. 37(b). The separation of the read and write current paths in the MTJ allows for optimal tuning of the barrier independently of the write process and increases the endurance of the MTJ. Moreover, the deterministic character of SOT switching enables sub-ns reversal of perpendicular MTJs (Cubukcu *et al.*, 2018) and low error rates in in-plane MTJs down to 2-ns-long current pulses (Aradhya *et al.*, 2016). The three-terminal configuration of MTJs operated by SOT, on the other hand, implies a larger footprint of the bit cell compared to two-terminal MTJs. As the actual size of the bit cell depends on the size and number of the transistors required to control data flow, the area penalty depends on the particular cell architecture and may not be so large. Importantly, the three-terminal configuration also allows for voltage control of the magnetic anisotropy of the free layer, which enables write speed acceleration (Yoda *et al.*, 2017), lower current thresholds, as well as selective SOT switching of several MTJs sharing a single write line (Kato *et al.*, 2018). The analysis of SOT-MRAMs at the circuit and architecture levels (Oboril *et al.*, 2015; Prenat *et al.*, 2016) reveals that this technology can be advantageously introduced in the data cache of processors, offering a strong reduction of the power consumption relative to volatile memories, comparable performances to STT-MRAMs and significant gains in terms of reliability and speed.

SOTs hold great promise also for driving magnetic cellular automata (Cowburn and Welland, 2000), domain wall logic (Allwood *et al.*, 2005), and MTJ-based logic devices (Yao *et al.*, 2012; Guo, Prenat, and Dieny, 2014). In the first two types of devices, SOTs offer unique features such as the clocking of nanomagnetic logic arrays by in-plane current injection (Bhowmik, You, and Salahuddin, 2014) and the efficient manipulation of domain walls (Yang, Ryu, and Parkin, 2015; Safeer *et al.*, 2016). In hybrid CMOS and magnetic devices based on MTJs, SOTs can perform similar functions as STT (Yao *et al.*, 2012; Guo, Prenat, and Dieny, 2014), but also enable novel architectures. Recent proposals include MTJ devices that exploit gate-voltage-modulated SOT switching for the parallel initialization of programmable logic arrays (Lee and Lee, 2016), four terminal devices that allow for direct cascading at high operation gain and low switching power (Kang *et al.*, 2016), and nonvolatile flip-flops for power gating (Jabeur *et al.*, 2014; Kwon *et al.*, 2014; Hanyu *et al.*, 2016). More futuristic ideas concern "probabilistic spin logic" systems in which SOTs are used to control the stochastic switching of thermally activated nanomagnets (Camsari *et al.*, 2017) as well as neuromorphic computing architectures (Locatelli, Cros, and Grollier, 2014; Sengupta *et al.*, 2015; Borders, Fukami, and Ohno, 2018). Other unconventional memory and logic architectures can be envisaged based on purely planar structures. In such a case, the SOTs would provide the writing mechanism while the reading operation can be performed by the AHE (Moritz *et al.*, 2008) or the unidirectional SMR (Avci, Garello, Ghosh *et al.*, 2015; Olejník *et al.*, 2015; Avci *et al.*, 2018).

A critical issue in this wide range of applications is the dynamic power consumption relative to the thermal stability factor of nanomagnets, $\Delta = B_K M_s V_F / 2k_B T$, where V_F is the volume of the ferromagnet. In perpendicularly magnetized structures with $\Delta \gtrsim 500$, the critical current density ranges from 10^7 to a few times 10^8 A/cm^2 depending on the switching speed; see Fig. 35(b). However, because the critical current scales with the lateral cross section of a device, the switching of a 50-nm-wide dot is predicted to require less than 200 μA and a write energy smaller than 100 fJ at 1.5 ns (Cubukcu *et al.*, 2018), which is close to the best results obtained so far for perpendicular STT-MRAM devices.

Very promising figures of merit in this context have been obtained for in-plane CoFeB layers with $\Delta \gtrsim 35$ by dusting the W/CoFeB interface with Hf, which allows for critical current densities of the order of 5×10^6 A/cm^2 at 2 ns (Shengjie Shi *et al.*, 2018). The power dissipated in the current lines is also a matter of concern, as some of the most efficient NM/FM combinations are based on the high-resistive phase of W and Ta (Liu, Pai *et al.*, 2012; Pai *et al.*, 2012); see Fig. 23. The search for novel SOT materials is thus focusing on systems that combine large charge-spin conversion efficiency with low resistivity or whose magnetic properties can be strongly modulated by a gate voltage. While there are still margins of improvement, SOT devices already offer an unprecedented variety of applications and compatibility with different classes of materials, which extends the range of spintronics well beyond the prototypical spin valve and MTJ structures of the past two decades.

V. SPIN-ORBIT TORQUES IN NONCENTROSYMMETRIC MAGNETS

SHE and iSGE are known as distinct but companion phenomena from their initial observations in nonmagnetic semiconductor structures (Ganichev, Danilov *et al.*, 2004; Kato *et al.*, 2004a, 2004b; Silov *et al.*, 2004; Wunderlich *et al.*, 2004, 2005; Belkov and Ganichev, 2008; Ivchenko and Ganichev, 2008). As discussed in the previous section, both iSGE and SHE have been utilized for electrically generating SOTs in metallic magnetic multilayers. The primary focus of the present section is to discuss the experiments performed on bulk noncentrosymmetric magnets, including dilute magnetic semiconductors (Chernyshov *et al.*, 2009; Endo, Matsukura, and Ohno, 2010; Fang *et al.*, 2011; Kurebayashi *et al.*, 2014), magnetic half-heusler compounds (Ciccarelli *et al.*, 2016), and antiferromagnets (Wadley *et al.*, 2016; Bodnar *et al.*, 2018; Meinert, Graulich, and Matalla-Wagner, 2018; Zhou *et al.*, 2018). This type of system is particularly interesting as SHE is absent (there is no adjacent nonmagnetic metal), so that the observed SOTs are solely attributed to iSGE.

In analogy to the galvanic (voltaic) cell, the term SGE was coined for a phenomenon in which an externally induced nonequilibrium spin density generates an electrical current (voltage) (Ganichev *et al.*, 2002). Inversely the iSGE, sometimes also called the Rashba-Edelstein effect, then refers to an externally applied electrical current that generates a spin density (Ivchenko and Pikus, 1978; Aronov and Lyanda-Geller, 1989; Ivchenko, Lyanda-Geller, and Pikus, 1989;

Edelstein, 1990; Mal'shukov and Chao, 2002; Inoue, Bauer, and Molenkamp, 2003). The theory of iSGE was discussed in detail in Sec. III.D. We start in Sec. V.A with initial observations of the iSGE in nonmagnetic GaAs structures and continue in Sec. V.B by discussing the iSGE induced SOTs in bulk ferromagnets, namely, in the low Curie temperature, dilute-moment semiconductor (Ga,Mn)As, and in the high Curie temperature, dense-moment metal NiMnSb. The physics of staggered iSGE spin densities in locally non-centrosymmetric lattices and corresponding Néel SOTs is reviewed in Sec. V.C based on studies in antiferromagnetic CuMnAs and Mn_2Au. We conclude in Sec. V.E by discussing the SGE and spin-orbit-driven magnonic charge pumping phenomena that are reciprocal to the iSGE and SOT, respectively.

A. Nonmagnetic GaAs structures

Initial observations of the iSGE were made in parallel with the initial SHE experiments, in both cases in semiconductors and employing optical detection methods (Ganichev, Danilov *et al.*, 2004; Kato *et al.*, 2004a, 2004b; Silov *et al.*, 2004; Wunderlich *et al.*, 2004, 2005; Belkov and Ganichev, 2008; Ivchenko and Ganichev, 2008). Wunderlich *et al.* (2004, 2005) detected iSGE and SHE in the same asymmetrically confined hole gas in a AlGaAs/GaAs semiconductor heterostructure. The experiments are shown in Fig. 38. The current-induced
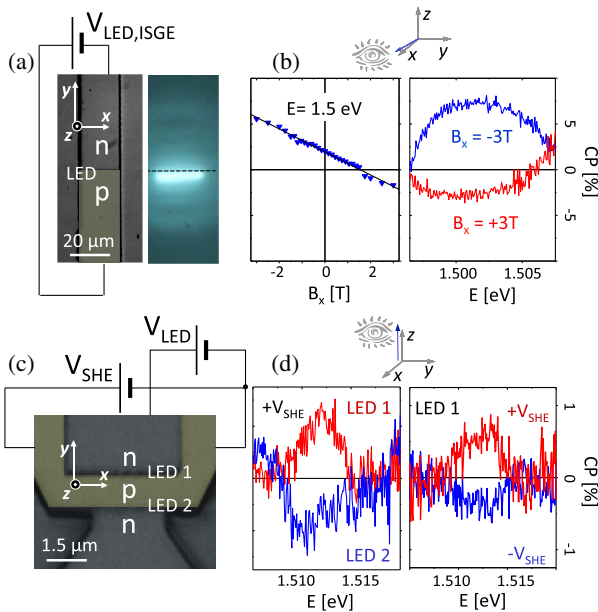

FIG. 38. (a) Electron micrograph of the device and an optical image of the emitted light in the experimental detection of the iSGE by circularly polarized electroluminescence. The net in-plane spin polarization is detected by placing the LED across the transport channel and using an in-plane observation angle. (b) Right: spectral dependence of the circular polarization of the emitted light. Left: the dependence of the circular polarization on the external in-plane magnetic field. (c), (d) Experimental detection of the SHE by two LEDs placed along the edges of the conduction channel and using an out-of-plane observation angle. Adapted from Wunderlich *et al.*, 2004, 2005.

spin density was measured by detecting the circularly polarized electroluminescence from a built-in planar *p-n* light emitting diode (LED). Since in this semiconductor heterostructure the iSGE has the Rashba symmetry and the corresponding in-plane polarization (perpendicular to the applied electric field) is uniform, the LED was placed across the hole transport channel and an in-plane observation angle was used; see Fig. 38(a). The measured nonzero circular polarization at zero magnetic field [see Fig. 38(b)] is then a signature of the iSGE spin density of current-carrying holes that radiatively recombined with electrons at the detection LED. For comparison, the SHE experiment is displayed in Figs. 38(c) and 38(d). Here opposite out-of-plane spin densities accumulate only at the edges and, correspondingly, the detecting LEDs are fabricated along the edges of the transport channel and the emitted light observation angle is out of plane.

The remarkable strength of these relativistic phenomena was already recognized in the initial experiments performed in the strongly spin-orbit coupled GaAs valence band. The effective iSGE fields inferred from Fig. 38(b) are in teslas. In other words, the ∼1%–10% spin polarization was achieved in the microchip at a ∼100 μA current, compared to a ∼100 A superconducting magnet that would generate the same degree of spin density in the semiconductor via an external magnetic field. Using Maxwell's equations physics one needs $10^6 \times$ larger equipment with $10^6 \times$ larger current than using Dirac equation physics in the iSGE (SHE) microchips to achieve the same polarization in the nominally nonmagnetic system.

When the current is switched off these large spin densities immediately vanish, which makes the iSGE and SHE phenomena in nonmagnetic crystals impractical for spintronic memory applications. However, shortly after their initial discovery, it was realized theoretically (Bernevig and Vafek, 2005; Manchon and Zhang, 2008; Garate and MacDonald, 2009; Železný *et al.*, 2014) and subsequently verified in experiments (Chernyshov *et al.*, 2009; Ciccarelli *et al.*, 2016; Wadley *et al.*, 2016) that iSGE represents uniquely efficient means for electrical writing of information when the nonequilibrium, spin-orbit-induced charge polarizations are exchange coupled to ferromagnetic or antiferromagnetic moments. These are discussed in the following sections.

B. Bulk ferromagnetic (Ga,Mn)As and NiMnSb

One can picture iSGE based on simple symmetry rules. Figure 39 represents the iSGE spin densities in three selected systems: (i) a Si diamond lattice, (ii) a GaAs zinc-blende crystal, and (iii) a NiMnSb noncentrosymmetric magnet. *A priori*, since a Si diamond lattice possesses inversion symmetry, iSGE vanishes globally at the level of the unit cell. But due to the local inversion-symmetry breaking, iSGE generates two spin densities $\mathbf{S}_A = -\mathbf{S}_B$ pointing in the opposite direction on the two noncentrosymmetric, inversion-partner sites of the Si diamond-lattice unit cell, as shown in Fig. 39(a) and discussed theoretically by Ciccarelli *et al.* (2016) and references therein. This staggered-symmetry spin density induced by the iSGE can generate an efficient SOT in collinear antiferromagnets as further discussed in Sec. V.C.
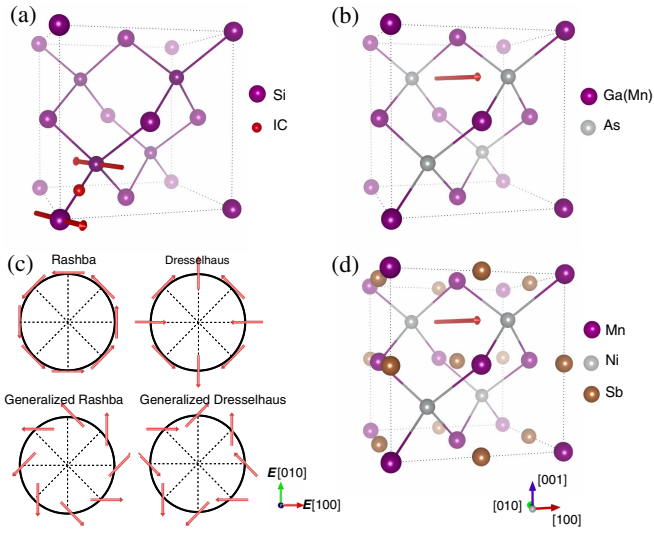
FIG. 39. (a) Cartoon representation of opposite iSGE spin densities generated at the locally noncentrosymmetric inversion-partner lattice cites of the Si lattice. (b) Cartoon representation of a net uniform iSGE spin density generated over a noncentrosymmteric unit cell of a zinc-blende GaAs lattice. Exchange coupling between the iSGE spin density of carriers and equilibrium dilute ferromagnetic moments on Mn atoms results in the SOT. (c) Different symmetries of iSGE spin density as a function of the electric field direction corresponding to different noncentrosymmetric crystal point groups. (d) Same as (b) for a room-temperature dense-moment ferromagnet NiMnSb. Adapted from Ciccarelli *et al.*, 2016.
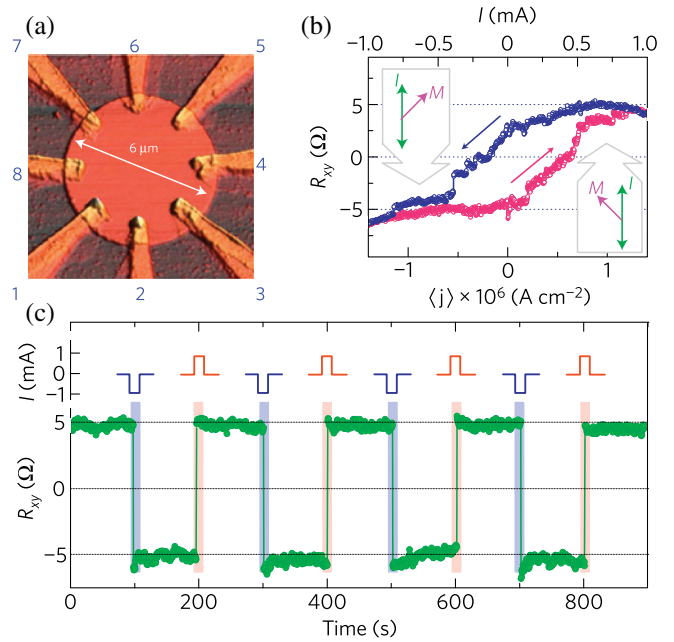

FIG. 40. (a) An atomic force micrograph of the sample used to detect the SOT in GaMnAs. (b) R_{xy} shows hysteresis as a function of the current for a fixed external magnetic field $H = 6$ mT applied at an angle $\phi_H = 72°$. (c) The magnetization switches between the [010] and [$\bar{1}$00] directions when alternating ± 1 mA current pulses are applied. The pulses have 100 ms duration and are shown schematically above the data curve. Adapted from Chernyshov *et al.*, 2009.

On the other hand, the zinc-blende lattices of GaAs [or (Ga, Mn)As] and the closely related half-heusler lattice of NiMnSb are examples of crystals that lack an inversion center in the unit cell. This can result in a nonzero net spin density, illustrated in Figs. 39(b) and 39(d), that generates an efficient SOT in ferromagnets, provided that the iSGE-induced spin density is exchange coupled to the ferromagnetic moments. As discussed earlier in detail in Sec. III.D, depending on the crystal symmetry, the iSGE can be composed of three distinct terms: generalized Rashba and Dresselhaus terms, shown in Fig. 39(c), and a term describing a response collinear to the electric field.

The experimental discovery of the iSGE-induced SOT was reported in a (Ga,Mn)As sample whose image is shown Fig. 40(a) (Chernyshov *et al.*, 2009; Endo, Matsukura, and Ohno, 2010). The experiment demonstrated not only the presence of the iSGE effective field of the expected Dresselhaus symmetry for the strained (Ga,Mn)As epilayer, but also demonstrated that iSGE was sufficiently strong to reversibly switch the direction of magnetization. Data in Fig. 40(b) were taken at external magnetic field magnitude and angle fixed close to the switching point between the [010] and [100] easy axes. The measured transverse AMR, used for the electrical readout, forms a hysteresis loop as the writing iSGE current is swept between ± 1 mA. The loop corresponds to the electrical switching between the [010] and [100] easy axes. Here 100 ms current pulses of a 1 mA amplitude and alternating polarity were sufficient to permanently rotate the direction of magnetization, as highlighted in Fig. 40(c).

A detailed analysis of the magnitude and symmetry of iSGE effective fields in (Ga,Mn)As was performed by employing an all-electrical ST-FMR technique, sketched in Fig. 41(a) (Fang *et al.*, 2011; Kurebayashi *et al.*, 2014) and presented in Sec. IV.B.2. Here an electric current oscillating at microwave frequencies is used to create an oscillating effective SOT field in the magnetic material being probed, which makes it possible to characterize individual nanoscale samples with uniform magnetization profiles (Fang *et al.*, 2011). For detection, a frequency mixing effect based on the AMR was used. When magnetization precession is driven, there is a time-dependent change $\Delta R(t)$ in longitudinal resistance from the equilibrium value R (owing to the AMR). The resistance oscillates with the same frequency as the microwave current, thus causing frequency mixing, and a directly measurable dc voltage V_{dc} is generated. This voltage provides a probe of the amplitude and phase of magnetization precession with respect to the microwave current.

The FMR vector magnetometry on the driving SOT fields revealed a dominant Dresselhaus and a weaker Rashba contribution [Fig. 41(a)] (Fang *et al.*, 2011). By separating the symmetric and antisymmetric parts of the mixing V_{dc} signal [Fig. 41(b)], it was possible to identify both the fieldlike and the dampinglike SOT components (Kurebayashi *et al.*, 2014). It was shown that the dampinglike SOT plays a comparably important role in driving the magnetization dynamics in (Ga,Mn)As as the fieldlike SOT; see Figs. 41(c) and 41(d).

The FMR technique was also employed in the study of the iSGE-induced SOT in the room-temperature, dense-moment
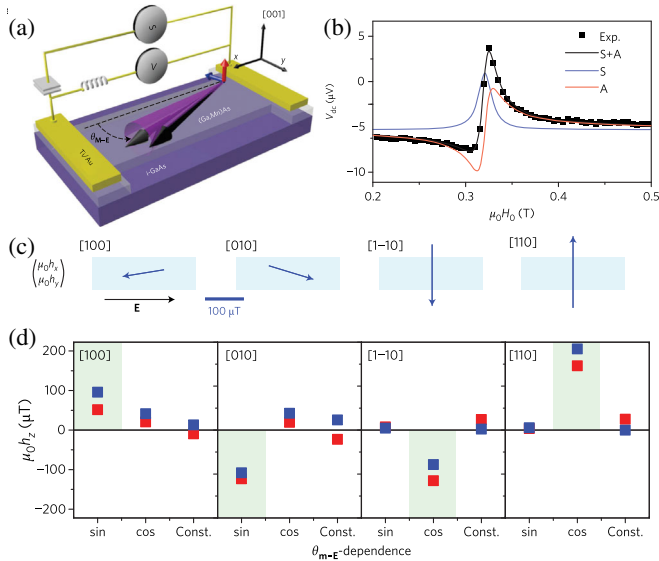
FIG. 41. Schematic of the (Ga,Mn)As sample, measurement setup, and magnetization precession. The injected microwave current drives FMR, which is detected via the dc voltage V_{dc} across the microbar. θ_{m-E} is the angle of the static magnetization direction measured from the current flow direction. Arrows represent in-plane (blue) and out-of-plane (red) components of the instantaneous nonequilibrium iSGE spin density induced by the microwave current that drives the magnetization. (b) A typical ST-FMR signal driven by an alternating current at 11 GHz and measured by V_{dc} as a function of external magnetic field. Data were fitted by a combination of symmetric (S) and antisymmetric (A) Lorentzian functions. (c) Direction and magnitude of the in-plane spin-orbit field (blue arrows) within the microbars (light blue rectangles). The direction of the electric field is represented by **E**. (d) Coefficients of the $\cos\theta_{m-E}$ and $\sin\theta_{m-E}$ fits to the angle dependence of the out-of-plane SOT field for the sample set. In these out-of-plane data, two samples are shown in each microbar direction and are distinguished by blue and red square data points. The symmetries expected for the dampinglike SOT, on the basis of the theoretical model for the Dresselhaus spin-orbit Hamiltonian [see Eq. (28)], are shown by light green shading. Adapted from Kurebayashi *et al.*, 2014.

metal ferromagnet NiMnSb, as shown in Fig. 42. In agreement with the symmetry expectations for the strained half-heusler lattice of the NiMnSb epilayer, and in agreement with the results in the directly related zinc-blende lattice of (Ga,Mn)As, the observed fieldlike component has a dominant Dresselhaus symmetry; see Fig. 42(d). Unlike (Ga,Mn)As, the damping-like SOT was not identified in NiMnSb; see Figs. 42(b) and 42(c). This is likely due to the higher conductivity of metallic NiMnSb. While the extrinsic fieldlike SOT scales with the conductivity, the intrinsic contribution to the dampinglike SOT is scattering independent to lowest order (see Sec. III.D), implying that the higher conductivity of the NiMnSb metal might favor the fieldlike SOT.

C. Collinear antiferromagnets

Compensated two-spin-sublattice antiferromagnets have north poles of half of the microscopic atomic moments
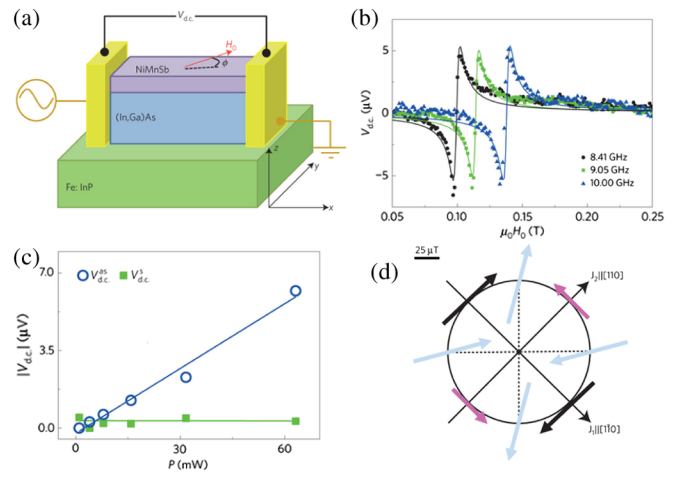

FIG. 42. (a) Schematic of the NiMnSb epilayer sample and measuring setup. A microwave current is passed in the bar and excites ST-FMR. By measuring the longitudinal dc voltage, the magnitude of the spin-orbit driving field is deduced. (b) The rectified voltage showing FMR for different frequencies of the microwave current. The Lorentzians are well fitted by an anti-symmetric line shape (continuous line) at all frequencies. (c) Power dependence of the symmetric and antisymmetric components of the rectified voltage. (d) Polar plot illustrating the direction of the spin-orbit field for current flowing along different crystal directions of NiMnSb. Adapted from Ciccarelli *et al.*, 2016.

pointing in one direction and the other half in the opposite direction. This makes the uniform external magnetic field inefficient for switching magnetic moments in antiferromagnets. The complete absence of electromagnets or reference permanent magnets in the SOT scheme for writing ferromagnetic memory bits has served as the key for introducing the physical concept for the efficient control of magnetic moments in antiferromagnets (Železný *et al.*, 2014).

Two distinct scenarios have been considered for the SOT on antiferromagnetic spin sublattices A/B, $(\partial/\partial t)\mathbf{m}_{A/B}\sim \mathbf{m}_{A/B} \times \mathbf{B}_{A/B}^{\text{eff}}$ (Železný *et al.*, 2014), one in which the crystal is globally noncentrosymmetric. Here an example is the half-heusler antiferromagnet CuMnSb (Forster, Johnston, and Wheeler, 1968) or any thin-film antiferromagnet with structural inversion asymmetry. The efficient torque in this case is the dampinglike SOT which, assuming, e.g., Rashba spin-orbit coupling, is driven by an effective field $\mathbf{B}_{A/B}^{\text{eff}} \sim (\mathbf{E} \times \mathbf{z}) \times \mathbf{m}_{A/B}$. Here $\mathbf{B}_{A/B}^{\text{eff}}$ is staggered due to the opposite magnetizations on the two spin sublattices of the antiferromagnet, $\mathbf{m}_A = -\mathbf{m}_B$. The fieldlike SOT in these globally noncentrosymmetric crystals is not efficient for antiferromagnets since the effective field driving the fieldlike torque $\mathbf{B}_{A/B}^{\text{eff}} \sim \mathbf{E} \times \mathbf{z}$ is not staggered.

Figure 39(a) illustrates that, in crystals with two inversion-partner lattice sites in the unit cell, the iSGE can generate a staggered spin density. This leads to the second scenario in which the fieldlike component of the SOT is efficient in an antiferromagnet whose magnetic spin sublattices A/B coincide with the two inversion-partner crystal sublattices. In this case the effective field driving the fieldlike SOT has
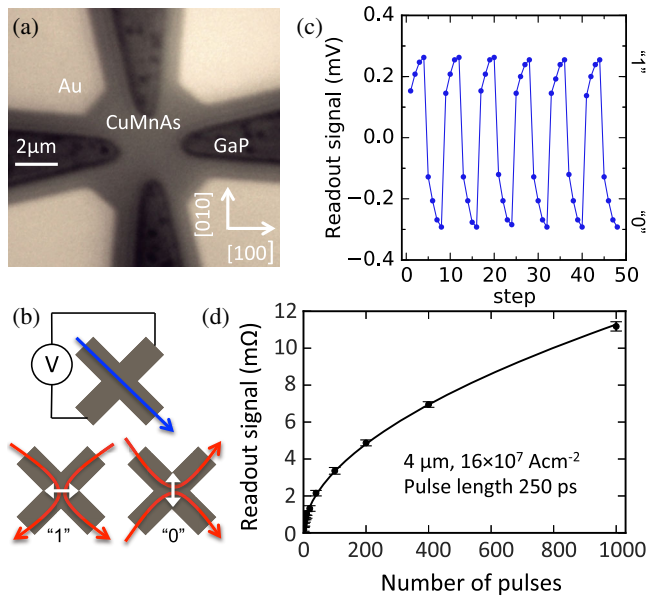
FIG. 43. (a) Optical microscopy image of the device containing Au contact pads and the antiferromagnet CuMnAs cross-shape cell on the GaP substrate. (b) Top: The readout current (blue arrow) and transverse voltage detection geometry. Bottom: Write pulse current lines (red arrows) labeled 1 (left) and 0 (right) and the corresponding preferred antiferromagnetic moment orientations (white double arrows). (c) Readout signals after repeated four write pulses with current lines along the [100] direction (0) followed by four pulses with current lines along the [010] direction (1). (d) Readout signal as a function of the number of pulses in the train of pulses for the individual pulse length of 250 ps. Adapted from Olejník *et al.*, 2017.

the staggered form (again assuming the Rashba symmetry): $\mathbf{B}_A^{\text{eff}} \sim \mathbf{E} \times \mathbf{z}$ and $\mathbf{B}_B^{\text{eff}} \sim -\mathbf{E} \times \mathbf{z}$. Mn_2Au and CuMnAs are examples of high Néel temperature antiferromagnetic crystals in which this scenario applies (Železný *et al.*, 2014; Wadley *et al.*, 2016).

Figure 43 illustrates the experimental realization of electrical switching by the staggered SOT field in a memory bit cell fabricated from a single-crystal epitaxial film of a CuMnAs antiferromagnet (Wadley *et al.*, 2016; Olejník *et al.*, 2017). Writing current pulses are sent through the four contacts of the bit cell to generate current lines in the central region of the cross along one of two orthogonal axes, representing "0" and "1"; see Fig. 43(b). The writing current pulses give preference to domains with antiferromagnetic moments aligned perpendicular to the current lines (Rashba-like symmetry). Electrical readout is performed by running the probe current along one of the arms of the cross and by measuring the antiferromagnetic transverse AMR across the other arm; see Fig. 43(b). The write and read functionality of the CuMnAs memory cells was verified to not be significantly perturbed in a superconducting magnet generating a magnetic field as strong as 12 T (Wadley *et al.*, 2016). This highlights the efficiency of the staggered SOT fields whose inferred magnitude allowing one to switch the antiferromagnetic moments is only in the mT range.

The bit-cell write and read signals can be sent at ambient conditions by placing the CuMnAs chip on a standard printed circuit board connected to a personal computer via a 5 V USB interface (Olejník *et al.*, 2017). Figure 43(c) shows an example of data obtained from this proof-of-concept antiferromagnetic memory device. Apart from demonstrating the application potential of antiferromagnets in spintronics thanks to the SOT, it also illustrates a deterministic multilevel switching of the antiferromagnetic bit cell. Here successive $\sim \mu$s writing pulses along one of the current path directions produce reproducible steplike changes in the memory readout signal. A photoemission electron microscopy study of CuMnAs has associated the multilevel electrical switching signal with the antiferromagnetic moment reorientations within multiple domains (Grzybowski *et al.*, 2017).

The observation of SOT-driven switching was recently extended to Mn_2Au, where a large AMR ratio up to 6% is obtained (Bodnar *et al.*, 2018; Meinert, Graulich, and Matalla-Wagner, 2018; Zhou *et al.*, 2018). The general switching features are quite similar to the ones observed in CuMnAs, revealing the multidomain magnetic structure of the system. Upon increasing the applied current, the Néel order of the different magnetic domains is progressively reoriented under thermal activation (Meinert, Graulich, and Matalla-Wagner, 2018), in sharp contrast with the fast switching obtained in NM/FM bilayers driven by domain wall nucleation or propagation (see Sec. IV.E). This progressive switching seems to be a specific property of antiferromagnetic materials, as it was also reported in the case of field-free switching in AF/FM metallic bilayers (van den Brink *et al.*, 2016; Shunsuke Fukami *et al.*, 2016; Oh *et al.*, 2016) (see Sec. IV.E.3). In agreement with the multidomain picture, experiments in the AF and FM bilayers showed that the number of intermediate levels decreases with the decreasing size of the device and finally evolves into a binary mode below a certain threshold (Kurenkov *et al.*, 2017).

The multilevel nature of antiferromagnetic bit cells opens the possibility for combining memory, logic, and neuromorphic functionalities (e.g., pulse counter) within the cell (Olejník *et al.*, 2017). Another unique merit of antiferromagnets is the THz scale of the internal spin dynamics which in combination with the SOT physics opens the door to ultrafast switching schemes. Figure 43(d) shows the initial results of experiments in this direction demonstrating a deterministic memory-counter functionality in a multilevel CuMnAs memory cell for ~ 1000 pulses with the individual pulse length scaled down to 250 ps. In these experiments, current pulses were delivered via wire-bonded contacts for which the pulse length ~ 100 ps is at the limit achievable with common current-pulse setups.

Subsequently, reversible switching with analogous characteristics was demonstrated using 1 ps long writing pulses (Olejník *et al.*, 2018). A noncontact technique was employed for generating the ultrashort current pulses in the antiferromagnetic memory cell via THz electromagnetic transients to overcome the limit of common contact current-pulse setups. Remarkably, the writing energy did not increase when downscaling the pulse length from ns to ps. This is in striking contrast to ferromagnetic STT (Bedau *et al.*, 2010) or SOT (Garello *et al.*, 2014) memories in which the theoretically extrapolated writing energy at ps would increase by 3 orders of magnitude compared to the state-of-the-art ns-switching

devices. While readily achievable in antiferromagnets, the ps range remains elusive for ferromagnets because, in frequency terms, it far exceeds the GHz scale of the FMR in typical ferromagnets.

All the SOT experiments on antiferromagnets employed 90° switching of the Néel vector. 180° switching was also recently demonstrated in CuMnAs by alternating the sign of the writing current. The readout of the reversed Néel vector memory states was performed electrically using a second-order magnetoresistance whose presence relies on the broken time-reversal and space-inversion symmetries in the antiferromagnetic crystal of CuMnAs (Godinho *et al.*, 2018). Microscopically, the mechanism of this second-order magnetoresistance in CuMnAs was ascribed to a transient tilt of the Néel vector due to the SOT combined with the AMR.

D. Antiferromagnetic topological Dirac fermions

Recently, a new concept was theoretically proposed. It follows from the observation that the staggered SOT fields can coexist with topological Dirac fermions in the band structure of antiferromagnets because of the serendipitous overlap of the key symmetry requirements (Šmejkal *et al.*, 2017). Therefore, one can use SOT to reorient the Néel vector in antiferromagnets in order to control such topological Dirac fermions. This is illustrated in Figs. 44(a) and 44(b) of
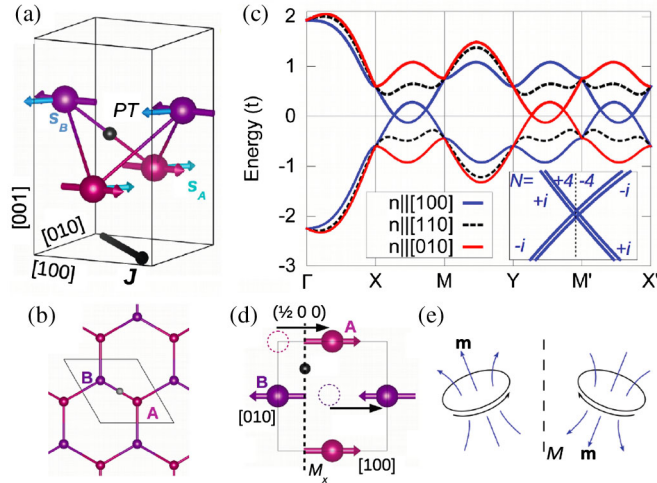

FIG. 44. (a) Mn antiferromagnetic spin sublattices of CuMnAs denoted by purple and pink balls with thick arrows. The antiferromagnet order breaks time-reversal symmetry ($\mathcal{T}$) and space-inversion symmetry ($\mathcal{P}$); however, the combined $\mathcal{PT}$ symmetry is preserved. Staggered current-induced spin density on the sublattices A and B is denoted by cyan and blue arrows. (b) Graphene crystal with two C sites per unit cell in analogy with the Mn sites in CuMnAs. (c) Band dispersion of the minimal antiferromagnet model based on CuMnAs illustrating the control of the Dirac points by the direction of the Néel vector **n**. Topological indices of the Dirac point are shown in the inset (for clarity the degenerate bands are slightly shifted). (d) Top view of the model quasi-2D-antiferromagnetic lattice of CuMnAs highlighting the nonsymmorphic glide mirror plane symmetry, combining mirror plane ($\mathcal{M}_x$) reflection with a half-unit-cell translation along the x axis. (e) An axial vector **m** under mirror ($\mathcal{M}$) reflection. Adapted from Šmejkal *et al.*, 2017.

examples of the CuMnAs where the SOT switching was experimentally verified and of the graphene lattice representing the Dirac systems (Castro Neto *et al.*, 2009): (i) The two-Mn-site primitive cell of CuMnAs favors band crossings in analogy with the two-C-site graphene lattice. (ii) In the paramagnetic phase, CuMnAs has time-reversal ($\mathcal{T}$) and space-inversion ($\mathcal{P}$) symmetries. It guarantees that each band is doubly degenerate forming a Kramer's pair, in analogy to graphene. In the antiferromagnetic phase, this degeneracy is not lifted because the combined $\mathcal{PT}$ symmetry is preserved, although the $\mathcal{T}$ symmetry and the $\mathcal{P}$ symmetry are individually broken (Herring, 1966; Chen, Niu, and MacDonald, 2014; Tang *et al.*, 2016; Šmejkal *et al.*, 2017). (iii) The combined $\mathcal{PT}$ symmetry is just another way of expressing that the two antiferromagnetic spin sublattices conincide with the two inversion-partner crystal sublattices. As explained, this condition leads to an efficient fieldlike SOT in bipartite antiferromagnets.

An additional crystal symmetry is needed to mediate the dependence of Dirac quasiparticles on the Néel vector orientation; see Fig. 44(c). In graphene there is no symmetry that protects the fourfold degeneracy of Dirac crossings of two Kramer's pair bands in the presence of spin-orbit coupling (Kane and Mele, 2005). In CuMnAs, on the other hand, the Dirac crossings are protected by a nonsymmorphic, glide mirror plane symmetry (Young and Kane, 2015) $\mathcal{G}_x = \{\mathcal{M}_x | \frac{1}{2} 00\}$ as long as the Néel vector is aligned with the [100] axis. $\mathcal{G}_x$ combines the mirror symmetry $\mathcal{M}_x$ along the (100) plane with the half-primitive cell translation along the [100] axis; see Fig. 44(d). Because of the mirror-reflection behavior of the axial vectors of magnetic moments [Fig. 44(e)], the $\mathcal{G}_x$ symmetry, and thus also the Dirac crossing protection, is broken when the antiferromagnetic moments are reoriented into a general crystal direction by the SOT.

E. Magnonic charge pumping in (Ga,Mn)As

We conclude this section by briefly discussing the SGE, which is a reciprocal phenomenon to the iSGE, and its counterpart in magnets termed the magnonic charge pumping (Ciccarelli *et al.*, 2015). The latter, in turn, is a reciprocal phenomenon to the SOT. Following theoretical predictions (Ivchenko and Pikus, 1978; Aronov and Lyanda-Geller, 1989; Ivchenko, Lyanda-Geller, and Pikus, 1989; Edelstein, 1990; Mal'shukov and Chao, 2002; Inoue, Bauer, and Molenkamp, 2003), the SGE was initially observed in an asymmetrically confined GaAs quantum well (Ganichev *et al.*, 2002). The key signature of the SGE is the electrical current induced by a nonequilibrium, but uniform, polarization of electron spins. In the nonequilibrium steady state, the spin-up and spin-down subbands have different populations, induced in the experiment of Ganichev *et al.* (2002) by a circularly polarized light excitation. Simultaneously, the two subbands for spin-up and spin-down electrons are shifted in momentum space due to the inversion asymmetry of the semiconductor structure which leads to an inherent asymmetry in the spin-flip scattering events between the two subbands. This results in the flow of the electrical current.

The Onsager reciprocity relations imply that there is also a reciprocal phenomenon of the iSGE induced SOT in which the
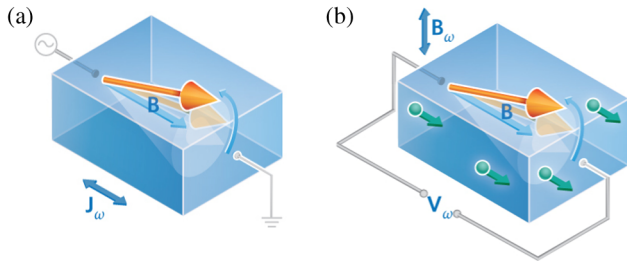
FIG. 45. (a) A charge current through (Ga,Mn)As results in a nonequilibrium spin polarization of the carriers, which exchange couples to the magnetization and exerts the SOT. An alternating current generates a time-varying torque, which drives magnetic precession resonantly when a magnetic field is applied. (b) The reciprocal effect of (a) termed the magnonic charge pumping. From Ciccarelli *et al.*, 2015.

electrical signal due to the SGE is generated from the magnetization precession in a uniform, spin-orbit coupled magnetic system with broken space inversion symmetry (see Fig. 45) (Hals, Brataas, and Tserkovnyak, 2010; Kim, Moon *et al.*, 2012; Tatara, Nakabayashi, and Lee, 2013). In this reciprocal SOT effect no secondary spin-charge conversion element is required and, as for the SOT, (Ga,Mn)As with broken inversion symmetry in its bulk crystal structure and strongly spin-orbit coupled holes represents a favorable model system to explore this phenomenon. The effect was observed in (Ga,Mn)As and termed the magnonic charge pumping (Ciccarelli *et al.*, 2015). This effect is physically similar to the SGE (or alternatively called the inverse Rashba-Edelstein effect) observed at Bi/Ag(111) (Rojas-Sánchez *et al.*, 2013) or topological insulator surfaces (Shiomi *et al.*, 2014).

F. Established features and open questions

SOTs in bulk noncentrosymmetric crystals are relatively well understood since here the iSGE mechanism is not complemented by the SHE, and ST-FMR experiments in external magnetic fields can provide a quantitatively accurate vector analysis of the SOT fields. Among the remaining open questions is what material parameters control the relative strengths of fieldlike and dampinglike SOTs. Regarding the crystal symmetries of the SOT, Rashba and Dresselhaus spin-orbit fields have already been identified whereas an experimental evidence of the Weyl symmetry SOT [Fig. 11(e)] is yet to be demonstrated.

Compared to ferromagnets, the research of SOTs in antiferromagnetic crystals is still in its infancy. The insensitivity to external magnetic fields makes the experimental calibration of the staggered SOT field strength difficult to perform. In experiments performed to date, the current-induced switching shows clear signatures of a heat-assisted mechanism (Bodnar *et al.*, 2018; Meinert, Graulich, and Matalla-Wagner, 2018; Olejník *et al.*, 2018). On the one hand, this is favorable for lowering the effective magnetic anisotropy barrier but, on the other hand, it may limit the accessible writing frequency and current amplitudes, and further complicates the experimental determination of the strength of the SOT fields. Therefore, only the experimental switching current amplitudes have been reported in antiferromagnets so far. In CuMnAs structures, the switching current densities are in the 10^8 A/cm^2 range for ~ns long writing pulses which is comparable to the common ferromagnetic Co/Pt SOT devices (Garello *et al.*, 2014; Olejník *et al.*, 2017).

SOT electrical writing speeds, defined as the inverse of the writing pulse length, in the CuMnAs antiferromagnet have been experimentally demonstrated to reach the THz range, which far exceeds the SOT writing speeds in ferromagnets. Antiferromagnets also offer the possibility to combinate the SOT with topological Dirac fermions, which are prohibited by symmetry in ferromagnets. An indication of the SOT-induced opening and closing of the Dirac crossing has already been reported in an experimental and theoretical study of the AMR in Mn$_2$Au (Bodnar *et al.*, 2018). The ultimate strength of this topological AMR, however, has been predicted for purely semimetallic antiferromagnets in which the Dirac points are at the Fermi level and no other trivial bands are crossing the Fermi energy (Šmejkal *et al.*, 2017). If experimentally demonstrated, it would have important implications not only for the basic research of topological phenomena in magnetic systems but may also provide the desired large magneto-resistance allowing for a better scalability of the readout signals in antiferromagnetic spintronic devices.

VI. SPIN-ORBIT TORQUES AND NONUNIFORM MAGNETIC TEXTURES

The electrical manipulation of magnetic textures using SOTs opens stimulating perspectives for applications. In Sec. IV, we already mentioned that domain wall nucleation and propagation play an important role in the context of SOT-driven switching. In addition, intentional and well-controlled domain wall manipulation constitutes the basis of alternative, domain wall-based racetrack memories (Parkin, Hayashi, and Thomas, 2008; Parkin and Yang, 2015) and logic concepts (Allwood *et al.*, 2005). In this context, a major breakthrough was the recent realization and control of individual metastable skyrmions at room temperatures (Fert, Reyren, and Cros, 2017; Jiang, Chen *et al.*, 2017), which show promising potential for such applications (Fert, Cros, and Sampaio, 2013; Zhang, Ezawa, and Zhou, 2015). Nonetheless, evaluating SOTs in magnetic textures poses a specific challenge compared to the magnetically uniform thin films discussed in Sec. IV. While SOTs induce a rotation of the magnetization that can be "simply" recorded through magnetometry (AMR, AHE, or MOKE), in magnetic textures one can evaluate only the *global* impact of the SOTs through the texture motion and deformation. This feature transforms the magnetometry issue to a magnetic microscopy issue. The present section addresses SOT-driven domain wall and skyrmion motion and dynamics in detail.

Starting with a phenomenological description of the influence of current-induced torques on domain wall motion in Sec. VI.A, we then discuss its experimental observation in in-plane and perpendicularly magnetized domain walls in Secs. VI.B and VI.C, respectively. Recent progress achieved on ferrimagnetic and antiferromagnetic systems is presented in Sec. VI.D. Note that the role of domain wall nucleation and propagation in SOT-driven switching was discussed in Sec. IV.E.

A. Domain wall dynamics under current

The dynamics of magnetic textures is governed by the LLG equation, Eq. (1), at the basis of the continuous theory of magnetic structures, called micromagnetics (Hubert and Schäfer, 1998). In this framework, the local magnetization vector is written $\mathbf{M}(\mathbf{r}, t) = M_s \mathbf{m}(\mathbf{r}, t)$, where the spontaneous magnetization modulus M_s depends on temperature, whereas the unit vector $\mathbf{m}$ specifies its local orientation as a function of space and time. The torques induced by an electrical current on the magnetic texture are of two forms. On the one hand, the STT is generally written, in its local version, as the sum of the so-called adiabatic and nonadiabatic terms (Beach, Tsoi, and Erskine, 2008)

$$(\gamma/M_s)\mathbf{T}_{STT} = -(\mathbf{u} \cdot \mathbf{\nabla})\mathbf{m} + \beta\mathbf{m} \times [(\mathbf{u} \cdot \mathbf{\nabla})\mathbf{m}], \quad (72)$$

where the velocity $\mathbf{u}$ is proportional to the electrical current density in the magnetic material, its spin polarization, etc., and where β is the nonadiabaticity factor (no dimensions). This torque is proportional to the gradient of magnetization along the current direction and thus vanishes in the domains. On the other hand, the SOT is expressed by Eq. (2). It does not depend on the gradient of the magnetization at the lowest order, hence acting also on the magnetization within the domains [for higher order expansion, see van der Bijl and Duine (2012)]. Note that in general when a current is applied to a NM/FM bilayer, it flows both into the magnet, leading to STT, and into the metal, leading to SOT in the magnet as well as to an Oersted field. We thus need to study the effect of these three torques on domain walls.

A qualitative analysis of these current-induced torques is instructive. For this we consider, for each torque term $\mathbf{T}$, the effective field $\mathbf{B_T}$ obtained by writing $\mathbf{T} = \mathbf{M} \times \mathbf{B_T}$, the evaluation being performed at the center of the domain wall. We emphasize that the proposed analysis is phenomenological in essence. In fact, the current-driven torques involved in the domain wall dynamics are different from a "real" magnetic field in the thermodynamics sense. In contrast with magnetic fields, spin torques are nonlocal, not necessarily conservative, and often exist only at the level of the domain wall. Hence, a more rigorous understanding of the effect of the spin torques on the domain wall motion can be obtained from a detailed analysis of the micromagnetic equations (see Sec. VI.C.2). That being said, interpreting the effect of the spin torque in terms of an effective magnetic field proves quite useful to explain the experimental observations. From the solved form of Eq. (1), i.e., with $\partial\mathbf{m}/\partial t$ only on the left-hand side, one sees that the magnetization dynamics is driven by the total effective field $\mathbf{B_M} - \mathbf{B_T}$ [where the minus sign is consistent with Eq. (1)], with a precession around it driven by the gyromagnetic ratio γ, and a relaxation toward it driven by the damping parameter α. To analyze the impact of current-induced torques on the domain wall motion, we need to know the types of magnetic domain walls in samples where large current pulses can be applied (typically 10^{11} A/m²). In order to promote large current densities while avoiding excessive sample Joule heating, these samples have the shape of nanostrips, with a width w of about a few hundreds of nanometers, and a thickness h of the order of a few
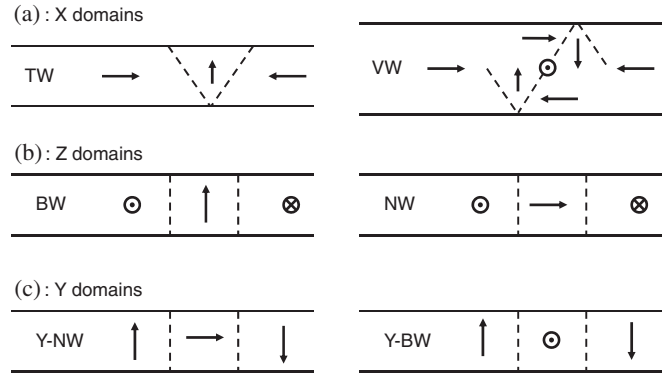

FIG. 46. Schematic of domain wall structures in nanostrips relevant for SOT studies. (a) When the magnetic easy axis is along the nanostrip (x axis), typically for small magnetic anisotropy, magnetostatics leads to two basic structures, the transverse wall at small width and thickness (left), and the vortex wall at larger lateral dimensions (right) (McMichael and Donahue, 1997; Nakatani, Thiaville, and Miltat, 2005). Note that these domain walls have a nonzero magnetostatic charge. (b) When the easy axis is perpendicular (z axis), typically for strong interface anisotropy, magnetostatics favors the Bloch wall (left) but the interfacial DMI can favor the Néel wall (Heide, Bihlmayer, and Blügel, 2008; Thiaville *et al.*, 2012) and fix its chirality (right). A "bulk" DMI would favor the Bloch wall and fix its chirality. (c) The last case of a transverse easy axis (y axis) is rare. The associated walls, known for a long time (Hubert and Schäfer, 1998), are the Néel wall (Y-Néel wall) at small thickness (left), and the Bloch wall (Y-Bloch wall) at larger thickness (right). In the absence of DMI, the domain wall magnetization is uncorrelated to the magnetization in the domains, so that domain or domain wall magnetization arrows can be reversed with no change of energy. The dashed lines outline the shape of the domain walls.

nanometers (the thickness being generally thinner for interfacial SOT). As shown in Fig. 46, a limited number of domain wall structures has to be considered, according to the magnetic anisotropy of the sample.

1. Steady-state domain wall dynamics

In order to get a *steady-state* current-induced domain wall motion (CIDM) under a torque $\mathbf{T}$, one needs the effective field $\mathbf{B_T}$ to be directed along the domains' magnetization (a subtlety exists for the vortex wall, as the magnetization is not uniform outside the vortex core, see later). This prescription derives from the analogy with the case of an applied magnetic field. It expresses a domain wall motion controlled by damping: if the effective field favors one domain, this domain steadily grows and hence the domain wall moves.

The STT torques, Eq. (72), depend on the magnetization gradient along the current direction, i.e., $\sim(\mathbf{u} \cdot \mathbf{\nabla})\mathbf{m}$ ($\equiv\partial\mathbf{m}/\partial x$ with the axes convention defined in Fig. 46). From Fig. 46 we see that at the domain wall center this derivative is along the magnetization of the domain on the right of the domain wall (an exception to this rule is afforded by the vortex wall, where the magnetization streamlines are reoriented by 90° through the vortex structure). By construction, the effective field $\mathbf{B_T}$ associated with the adiabatic STT is orthogonal to the domains' magnetization, so that it cannot lead to steady-state domain wall motion. On the other hand, the

TABLE III. Characteristics of the effective field $\mathbf{B_T}$ associated with the current-induced torques, evaluated at the center of the domain wall types shown in Fig. 46. For each case, the first line indicates (Y or N) whether or not this effective field drives the domain wall into steady-state motion. The second line indicates (null, odd, or even) if this field is zero and, when it is not, if it is even or odd with respect to the domain wall magnetization, the case "odd" leading to long-term precessional domain motion.

DW	Adiabatic STT	Nonadiabatic STT	FL SOT/Oersted	DL SOT
TW	N	Y	N	N
	Odd	Even	Even	Null
VW	N	Y	N	N
	Odd	Even	Even	Odd
BW	N	Y	N	N
	Odd	Even	Even	Null
NW	N	Y	N	Y
	Odd	Even	Even	Odd
Y-NW	N	Y	Y	N
	Odd	Even	Even	Odd
Y-BW	N	Y	Y	N
	Odd	Even	Even	Odd

effective field associated with the nonadiabatic STT lies along the domain magnetization. This explains qualitatively the rule for steady-state STT driven domain wall motion, given by the velocity formula $\mathbf{v} = (\beta/\alpha)\mathbf{u}$ in which domain walls move along the carriers for positive current polarization (majority spin polarization of the current) and positive β factor (Zhang and Li, 2004; Thiaville *et al.*, 2005). The same conclusions are reached for the vortex wall case, by considering the surrounding of the vortex core instead of the domains.

We now perform the same analysis for the SOTs. The effective field associated with the fieldlike SOT reads $\mathbf{B_{FL}} = -(\tau_{FL}/M_s)\boldsymbol{\zeta}$ with $\boldsymbol{\zeta}\|\mathbf{y}$ for a current along x, considering the Rashba symmetry of the spin-orbit coupling. This field is oriented like the main part of the Oersted field (as $w \gg h$ the y component of the stray field dominates the z component). The results for the various domain wall structures are summarized in Table III, a generalization of those of Khvalkovskiy *et al.* (2013): apart from the obvious case of the y easy axis (Obata and Tatara, 2008), no steady-state domain wall motion is expected. For the dampinglike SOT with $\mathbf{B_{DL}} = -(\tau_{DL}/M_s)\mathbf{m} \times \boldsymbol{\zeta}$, only the Néel wall for the z easy axis is expected to be set in steady-state motion.

2. Precessional domain wall dynamics

Another characteristic regime of domain wall motion is called *precessional*, meaning that the domain wall magnetization is rotating in a given direction around the domains' magnetization. Following very general arguments initially due to Slonczewski (1972) according to which the domain wall position and the angle of the domain wall magnetization are coupled variables in the Hamilton sense, a continuously precessing domain wall magnetization induces an overall domain wall motion.

The simplest known case of precession occurs under a large enough field applied along the domains' magnetization, the field being larger than the so-called Walker field. In that case, this precession-induced velocity opposes that due to the applied field, hence the term of Walker breakdown stressing that domain wall velocity drops above the Walker field. The Walker threshold occurs because the domain wall structure deformation by domain wall magnetization rotation around the applied field can be counterbalanced by internal energies (anisotropy, demagnetizing field, DMI, etc.), up to a certain limit. The same breakdown is therefore also expected when the effective field $\mathbf{B_T}$ is along the domains' magnetization and large enough [with the subtleties that for STT, the velocity increases above the threshold when $\beta < \alpha$ (Zhang and Li, 2004; Thiaville *et al.*, 2005), while for dampinglike SOT the threshold is never reached (Thiaville *et al.*, 2012)].

Domain wall magnetization rotation also occurs by relaxation toward the current-induced effective fields $\mathbf{B_T}$. If these fields are below the "breakdown" threshold, a domain wall position shift will appear as a result of the domain wall structure transformation when current is applied. When current goes back to zero, and provided the sample is perfect, the opposite domain wall position shift will however occur as the domain wall recovers its initial structure. Note that several devices based on an anticipated stick-slip domain wall motion under application of dissymmetric pulses with short rise time and long fall time have been proposed, based on this phenomenon. A partial list of cases with domain wall shift was presented by Khvalkovskiy *et al.* (2013). The full list is given in Table III. When the effective field related to a current-induced torque is large enough, the domain wall structure goes to its image where the domain wall magnetization has been reversed. Whether this process continues or not depends on the power to which the domain wall magnetization enters the expression of the effective field $\mathbf{B_T}$. If this power is odd, the opposite field will act on the opposite domain wall magnetization, leading to indefinite precession of domain wall magnetization and hence to long-term precessional domain wall motion. If the power is even, however, indefinite precession will not occur and only a domain wall position shift will occur. These cases are also indicated in Table III. The table shows that fieldlike SOT (and Oersted field) can drive only domain walls in the y-easy axis situation; see Y-domain walls in Fig. 46.

With this analysis in mind, we turn in the next sections to each situation, reviewing the experimental reports existing on the subject.

B. In-plane magnetized samples

1. Soft samples (*X* domains)

These samples have been the workhorse of the initial studies of the STT, leading to the definition of the adiabatic and nonadiabatic STT terms. As Table III shows, such samples are generally not adequate to test the SOT. The vortex wall is a special case in this picture, being a composite object that can easily deform by lateral motion of the vortex core, inducing a displacement of the whole wall along the nanostrip [see, e.g., Beach, Tsoi, and Erskine (2008), Clarke *et al.* (2008), and Tretiakov *et al.* (2008)]. As a result, under adiabatic STT, for example, the vortex core displaces laterally (along y), leading to a longitudinal domain wall displacement (along x). The effect is however transient as the core eventually stops or disappears at the nanostrip edge, transforming the vortex wall into a transverse wall. The same effect is expected under SOT.

Micromagnetic studies of the effect of disorder on CIDM by STT show that disorder induces, on top of the expected current threshold for domain wall motion, a modification of the linear regime (change of slope, offset), as well as a suppression of velocity breakdown (Nakatani, Thiaville, and Miltat, 2003; Thiaville *et al.*, 2005; Thiaville and Nakatani, 2009). The modification of the linear regime may be partly understood by introducing a larger effective damping constant for a magnetic texture (such as a domain wall) moving in a disordered medium (Min *et al.*, 2010).

Up until now, only two studies have considered *X* domains with adjacent heavy metal layers. An early study on Pt/NiFe (Vanhaverbeke, Bischof, and Allenspach, 2008) investigated the influence of the current direction on the domain wall polarity (i.e., the direction of the domain wall's transverse magnetization). Another more recent study addressed thermal effects in Ta/NiFe/Pt (Torrejon *et al.*, 2012). Moreover, typical thicknesses of the ferromagnetic film were 10 nm, so that the effect of the interfacial torques is strongly reduced. Note that the Oersted field effect was directly observed in the case of a bilayer sample (Uhlír *et al.*, 2011) by time-resolved photoelectron emission microscopy using x-ray magnetic circular dichroism, a technique that could be used to measure the fieldlike SOT *in situ*. Simulations showed that fieldlike SOT modifies the STT-driven dynamics (Seo *et al.*, 2012).

Trilayer samples, typically Co/Cu/NiFe where easier domain wall motion and higher velocities have been observed, are a special case that could not be understood in the frame of STT plus Oersted fields. It was thus proposed that perpendicular spin currents may play some role (Pizzini *et al.*, 2009; Uhlír *et al.*, 2010). Khvalkovskiy *et al.* (2009) performed a numerical exploration of the effect of various forms of SOT on both transverse wall and vortex wall, taking $\zeta = \mathbf{x}$ and $\zeta = \mathbf{z}$, i.e., the two cases that are not considered in standard SOT configuration [the latter case was investigated by Khvalkovskiy *et al.* (2013) for the transverse wall]. The results show that indeed in some cases domain wall sustained motion is expected (fieldlike SOT for $\zeta = \mathbf{x}$, dampinglike SOT for $\zeta = \mathbf{z}$ for a vortex wall), but their relation to the experimental situation is unclear. Another family of bilayer samples are the synthetic antiferromagnets. In CoFe/Ru/CoFe, a very low threshold for CIDM was measured (Lepadatu *et al.*, 2017) and attributed to the intrinsic dynamics of antiferromagnetically coupled transverse walls, driven by nonadiabatic STT (see Sec. VI.D).

2. Anisotropic samples with *Y* domains

In the case of *Y*-domain walls (see Fig. 46) the fieldlike SOT is directly active (Obata and Tatara, 2008). Such samples require an in-plane anisotropy that is stronger than the magnetostatic energy cost. This has been realized by growing epitaxial layers on single-crystal substrates. One example is (Ga,Mn)As grown on (001) GaAs (Thevenard *et al.*, 2017), where structures with *X* and *Y* domains were compared, on 50-nm-thick layers so that bulk SOT would be active. Large current-induced effects were observed, that strongly differed in the two cases, but no simple and global understanding of the observed effects could be found.

Another way to obtain such structures is to use large magnetostriction materials, as growth-induced stress is relaxed at the edges of a nanostrip, modifying the anisotropy locally. As a result, transverse *Y* domains were observed in $Ni_{80}Pd_{20}$ films (Chauleau *et al.*, 2011). No study of CIDM could however be realized on such samples, as the Curie temperature was rapidly reached.

C. Perpendicularly magnetized samples

A numerical micromagnetic study (Fukami *et al.*, 2008) demonstrated the interest of perpendicularly magnetized samples for CIDM: as the sample thickness is reduced, the energy cost of a Néel wall relative to the Bloch wall decreases linearly. Thus, the Walker breakdown field also decreases linearly, as well as the current threshold for domain wall motion under the adiabatic STT. In addition, microscopic STT theories predicted that the nonadiabatic torque might be larger in narrow domain walls (Tatara and Kohno, 2004; Waintal and Viret, 2004; Bohlens and Pfannkuche, 2010; Akosa *et al.*, 2015). Experimentally, studies first focused on the influence of the electric current on the domain wall depinning (Ravelosona *et al.*, 2005; Boulle *et al.*, 2008; Burrowes *et al.*, 2010). The results seemed encouraging, but there were only few systems exhibiting CIDM without the assistance of external field. One of these systems is the Co/Ni multilayers where the predictions of the adiabatic STT model were most clearly evidenced (Koyama *et al.*, 2011): (i) the existence of an intrinsic critical current that depends on the geometric structure of the domain wall rather than the extrinsic pinning, and (ii) the independence of the critical current on a perpendicular magnetic field.

1. Demonstrations of spin-orbit torques in current-induced domain wall motion

Among the materials with perpendicular anisotropy, the Pt/Co/AlOx trilayers, in particular, have attracted a lot of interest. The domain wall motion was found to be significantly faster (Moore *et al.*, 2008; Miron *et al.*, 2011; Baumgartner *et al.*, 2017) compared to the previous observations in NiFe or Co/Ni films; see Fig. 47(a). Besides the practical importance of fast domain wall motion, the physical parameter determining this improvement was the structural inversion asymmetry (Miron *et al.*, 2009). Indeed, while Pt/Co/AlOx supports fast CIDM, magnetically similar Pt/Co/Pt symmetric layers do not exhibit any CIDM at all (Miron *et al.*, 2009; Cormier *et al.*, 2010). These first observations were initially analyzed within the framework of the STT model, including the influence of the fieldlike SOT, which was discovered at the same time. It was proposed that the broken symmetry could accelerate the spin-flip rate and enhance the nonadiabatic torque, the fieldlike SOT stabilizing the Bloch wall structure to prevent the Walker breakdown (Miron *et al.*, 2011). This idea was pursued by several theoretical investigations of the ability of fieldlike SOT to delay (Jisu Ryu *et al.*, 2012) or suppress the Walker breakdown (Linder and Alidoust, 2013; Stier, Creutzburg, and Thorwart, 2014; Risinggård and Linder, 2017).

At that stage, there was still a major discrepancy between the STT model and the experiment: the domain walls move in
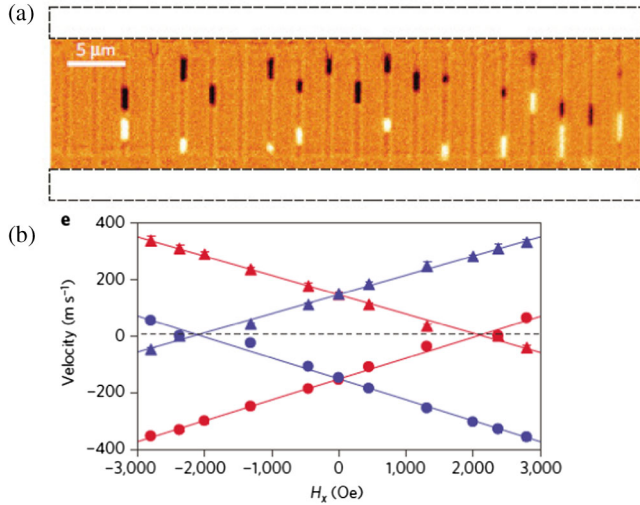
FIG. 47.   (a) Differential Kerr microscopy imaging of domain wall displacements (stripes of black or white contrast) in an array of Pt/Co 0.6 nm/AlOx 500-nm-wide nanostrips, after 20 current pulses ($J = 1.2 \times 10^{12}$ A/m^2, 3 ns duration). From Miron *et al.*, 2011. (b) Observation of chiral effects: the velocity of up and down and downand up domain walls (blue and red) is the same, but becomes different when an in-plane field is applied [sample Pt/CoNiCo/TaN, current density $J = 1.5 \times 10^{12}$ A/m^2, either positive (triangles) or negative (circles)]. Within the DMI-SOT model, the DMI field strength is indicated by the value of the crossing field, where the domain wall velocity changes sign. From Ryu *et al.*, 2013.

the direction of the electric current and not along that of the electron flow (Moore *et al.*, 2009). This intriguing observation motivated several theoretical studies, which found that the combination of STT and SOT could in certain cases produce backward motion (Kim, Seo *et al.*, 2012; Boulle *et al.*, 2014). However, these scenarios were not robust: the backward motion was obtained only for certain values of the physical parameters and only in a certain range of current density. In parallel, it was observed that nearly symmetric Pt/Co/Pt samples exhibit CIDM if an external in-plane field is applied parallel to the current, sufficiently large to convert Bloch walls to Néel walls (Haazen *et al.*, 2013) [the Néel wall structure under the in-plane field was later confirmed by anisotropic magnetoresistance measurements (Franken *et al.*, 2014)]. The dampinglike SOT mechanism was shown to be compatible with all observations, especially (i) the reversal of the domain wall motion upon locating the thicker Pt layer below or above the Co layer, (ii) the reversal of the domain wall motion upon change of sign of the in-plane field, and (iii) the fact that two successive domain walls always move in opposite directions. The latter point is of crucial importance: all Néel walls, having the same magnetization, feel the same dampinglike SOT and are hence displaced in opposite directions, as under an easy-axis (z here) field.

In this context, a breakthrough was the micromagnetic study (Thiaville *et al.*, 2012) of the dynamics of Néel walls under magnetic field and dampinglike SOT, in the case where such walls are stabilized by the interfacial DMI. The DMI (Dzyaloshinskii, 1957; Moriya, 1960) is an antisymmetric exchange interaction that is allowed when the medium does

not have inversion symmetry. The general form of the DMI energy density reads $W_{\mathrm{DMI}} = D_{ij}\mathbf{e}_i \cdot (\mathbf{m} \times \partial \mathbf{m}/\partial j)$, where the coefficient D_{ij} possesses the same symmetries as the SOT response function χ_{ij} discussed in Sec. III.B (Freimuth, Blügel, and Mokrousov, 2014a). Hence, the generalization of SOT symmetries suggested by Fig. 11 also applies to DMI. In an isotropic bulk material without inversion symmetry, to the lowest order in gradient expansion, DMI in continuous micromagnetic form is expressed by an energy density (Bogdanov and Yablonskii, 1989)

$$W_{3D} = D_{3D}\mathbf{m} \cdot (\boldsymbol{\nabla} \times \mathbf{m}). \tag{73}$$

Such an interaction favors helicoidal magnetization rotations of a given handedness. Referring to Fig. 46, this form of DMI stabilizes chiral Bloch walls or Y-Bloch walls.

On the other hand, at the interface between two dissimilar materials where inversion symmetry is structurally broken (Fert, 1990), assuming the highest symmetry ($C_{\infty v}$) and considering the lowest order in spatial gradient, one obtains (Bogdanov and Yablonskii, 1989; Heide, Bihlmayer, and Blügel, 2008)

$$W_{2D} = D_{2D}\mathbf{m} \cdot [(\mathbf{z} \times \boldsymbol{\nabla}) \times \mathbf{m}]. \tag{74}$$

This interaction, called interfacial DMI, favors cycloidal magnetization rotations of a given handedness. Again referring to Fig. 46, this form of DMI stabilizes chiral Néel walls (but none of the Y-Néel walls). The immediate consequence is that chiral Néel walls move under dampinglike SOT without any in-plane field, with successive walls moving in the same direction as their domain wall magnetizations are opposite. Such a motion, already obtained with STT, is required for domain wall race-track applications (Parkin, Hayashi, and Thomas, 2008). Another notable feature of the domain wall dynamics under DMI and dampinglike SOT is that the relative sign of domain wall velocity with respect to that of the current is given by the product of the sign of the dampinglike SOT and the sign of the DMI.

Interfacial DMI was already evidenced in magnetic atomic monolayers or bilayers by spin-polarized scanning tunneling microscopy that revealed magnetization cycloids of fixed handedness (Bode *et al.*, 2007; Meckler *et al.*, 2009). However, these were situations of very large DMI so that the uniform magnetic state was destabilized. For the Pt/Co/AlOx case, direct proof that domain walls are chiral Néel walls was obtained by NV-center magnetic microscopy (Tetienne *et al.*, 2015), and by x-ray magnetic circular dichroism (Boulle *et al.*, 2016). In addition, spin-polarized low-energy electron microscopy has shown the change of domain wall structure from chiral Néel wall to achiral Bloch wall as a function of the thickness of the magnetic layer (G. Chen *et al.*, 2013; Gong Chen *et al.*, 2013), confirming the interfacial DMI description.

The prediction of Thiaville *et al.* (2012) was immediately backed by two experimental papers (Emori *et al.*, 2013; Ryu *et al.*, 2013). As the sign of the SHE (hence of the dampinglike SOT) was known from other measurements, the direction of domain wall motion under current could be related to the sign of DMI; see Fig. 47(b). This sign was later obtained by several other techniques, so that presently estimates of interfacial

DMI for a fair number of NM/FM interfaces exist. In this picture, the Pt/Co interface stands out with one of the largest interfacial DMI constants $D_s \approx -1.7$ pJ/m (Belmeguenai *et al.*, 2015). One of the techniques for determining the DMI consists of applying an additional in-plane field in order to compensate the DMI effective field on the domain wall. At this compensation, the domain wall velocity crosses zero (Emori *et al.*, 2013); for an example see Fig. 47(b).

2. Domain wall motion under spin-orbit torque

We now describe in more detail the dynamics of domain walls under SOTs and DMI. Once the torques are known and quantified, the study of their impact on domain wall motion should ultimately be performed by numerical micromagnetic simulations, for the sample parameters and geometrical dimensions. For the physical understanding, however, simplified and as analytical as possible models are helpful. The simplest model was exposed in Sec. VI.A. The next level of complexity is addressed by the so-called $q - \Phi$ model that describes a 1D domain wall dynamics for an assumed domain wall profile described by only two variables, namely, the domain wall position q and the angle Φ of the domain wall magnetization within the plane orthogonal to the easy axis (Slonczewski, 1972; Schryer and Walker, 1974). For SOT-driven domain wall motion assisted by DMI, the model was established by Thiaville *et al.* (2012), and further developed to incorporate in-plane fields (Emori *et al.*, 2013) and STT (Torrejon *et al.*, 2014). At a higher level of complexity, a numerical micromagnetic calculation is performed assuming 1D structure and dynamics, i.e., the magnetization depends only on the x coordinate, the magnetostatic effects being computed for the nanostrip width w and thickness h. Finally, for ultrathin films the full model consists of 2D numerical micromagnetics.

Figure 48(a) shows the predicted velocity versus current curves $v(J)$ in the case of pure dampinglike SOT and for various values of the effective DMI energy density $D = D_s/h$. The domain wall velocity initially rises linearly with current, following a slope that does not depend on DMI and is given, for DMI dominating the magnetostatic energy associated with a Néel wall and using the notation of Eq. (2), by

$$v = -\gamma \frac{\pi \Delta_W}{2\alpha M_s} \tau_{DL}. \tag{75}$$

Here Δ_W is the micromagnetic domain wall width parameter. Upon further increase of the current density, the velocity saturates toward a plateau determined by the DMI strength $v_D = \gamma \pi D/(2M_s)$ (derived in the same limit). The velocity saturation is physically explained by the progressive rotation of the domain wall magnetization from Néel to Bloch around the effective field $\mathbf{B}_{DL}$ associated with the dampinglike SOT. This rotation leads to a reduction of the dampinglike SOT on the domain wall, as the torque vanishes for a Bloch wall. This behavior is in good overall agreement with experiments; see Fig. 48(b). With intrinsic curvature and no Walker breakdown, the velocity versus current behavior $v(J)$ is markedly different from that expected for STT.

When DMI is not much larger than the magnetostatic energy associated with the Néel wall, the situation is more complex to analyze, as the velocity v_D decreases and becomes
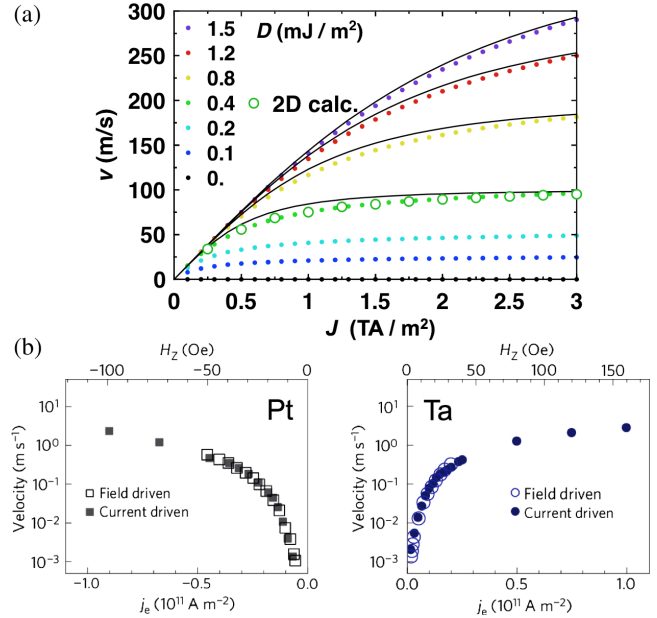

FIG. 48. Velocity of domain walls in ultrathin Pt/Co/oxide films with DMI under current. (a) Micromagnetic 1D calculations (points) of domain wall velocity vs current density, for various values of effective DMI in a 0.6 nm Co film (Thiaville *et al.*, 2012), considering only dampinglike SOT. Curves show the $q - \Phi$ model results for comparison. (b) Measured domain wall velocity under current for Pt/CoFe/MgO and Ta/CoFe/MgO (Emori *et al.*, 2013). The CoFe film has 80-20 atomic composition and is 0.6 nm thick. Note the log scale for velocities and the opposite current signs for the two heavy metal layers.

comparable to that induced by STT. Moreover, for the $q - \Phi$ model, the analytical expressions become much more complex. The analysis of the competition of DMI versus domain wall magnetostatics, together with that of dampinglike SOT versus STT, was performed by Torrejon *et al.* (2014) in the case of HM/CoFeB/MgO for HM = Hf, Ta, TaN, W, i.e., the beginning of the 5*d* series, using the $q - \Phi$ model to analyze the experiments. This showed that the determination of the DMI by the "crossing field" technique is strongly affected by the STT when DMI is not large.

3. Two-dimensional effects in current-induced domain wall motion

Unlike in-plane magnetized nanowires, where domain walls behave as quasi-1D objects, in perpendicular samples domain walls act more like 2D membranes. One of the first observations on the influence of the 2D character on the CIDM in materials with broken inversion symmetry was the occurrence of a domain wall tilt. When domain walls are displaced by sufficiently long current pulses, their end position is no longer perpendicular to the wire (at the energy minimum), but tilted at a certain angle (K. S. Ryu *et al.*, 2012; Baumgartner and Gambardella, 2018); see Fig. 49(a). The fact that this tilt is visible at rest is proof that domain wall pinning exists. Boulle *et al.* (2013) proposed that this tilting arises from the competition between the dampinglike SOT and the DMI. Because the DMI energy prefers that the domain wall magnetization is perpendicular to the domain wall, the
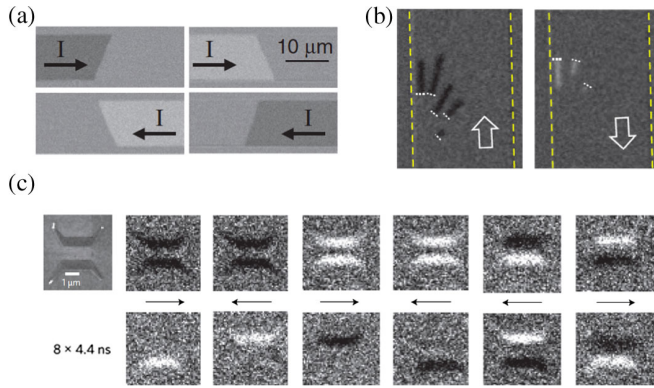
(a)

(b)

(c)

FIG. 49.   (a) Kerr imaging of domain wall tilting produced by current injection. From K. S. Ryu *et al.*, 2012. (b) Kerr images of current-induced domain wall motion in a noncollinear geometry. (c) Magnetization reversal controlled by geometry. From Safeer *et al.*, 2016.

dampinglike SOT acting on the domain wall magnetization modifies the domain wall angle [see also Martinez *et al.* (2014)]. A direct consequence of this current-driven tilting is an additional deformation of the $v(J)$ curve at large current density. For dampinglike SOT only, this gives rise to a velocity increase close to the threshold for domain stability given by $\tau_{\text{DL max}} = \gamma B_K^{\text{eff}}/2$ (B_K^{eff} being the effective perpendicular anisotropy that incorporates the demagnetizing field).

It was recently shown that the 2D character of CIDM can be exploited for domain wall manipulation. Since the domain wall magnetization is either aligned (Bloch wall) or perpendicular (Néel wall) to the domain wall direction, the control of the domain wall tilt allows for setting the SOT efficiency by modifying the angle between the electric current and the magnetization of the domain wall. Using this approach, Safeer *et al.* (2016) showed that the current-induced domain wall motion in the noncollinear geometry exhibits surprising features; see Fig. 49(b). Namely, depending on their polarity (up and down or down and up), the domain walls move faster for a certain sign of the electric current. This phenomenon links the polarity of the domain walls with their direction of motion. Therefore, by controlling the shape of a magnetic layer, one can control its magnetization reversal; see Fig. 49(c).

4. Domain wall motion under combined spin-transfer and spin-orbit torques

A detailed study of CIDM in $\text{Pt}/(\text{Co}/\text{Ni})_N/\text{Co}/\text{MgO}$ as a function of magnetic layer thickness (by varying the repetition number N) was realized by Ueda *et al.* (2014). The $(\text{Co}/\text{Ni})_N$ multilayer system is interesting since magnetic anisotropy arises from the internal Co/Ni interfaces, the total thickness of the multilayer can be changed while keeping the same magnetic anisotropy, which is not possible for a single Co layer. The domain walls were observed to move along the electron flow for large thicknesses ($N > 6$), but in the opposite direction at small thicknesses ($N < 3$). From the application of an additional easy-axis field, it was concluded that CIDM at large thickness is due to the adiabatic STT, but that the torque on the domain wall is like a bias field for low thickness. Applying then, in addition to current, in-plane fields in both orientations

(longitudinal x and transverse y), the crossing field effect [see Fig. 47(b)] was observed in the longitudinal case, in accord with the dampinglike SOT in the presence of DMI. The transverse field was observed to linearly modify the velocity of both up and down and down and up domain walls, in the same way. This is also consistent with the DMI and dampinglike SOT mechanism, as the magnetizations of two consecutive chiral Néel walls precess under the respective fields $\mathbf{B}_{\text{DL}}$ of the dampinglike SOT toward the same y direction. Thus, for not too large y fields, one polarity increases this rotation and hence decreases the domain wall velocities, whereas the other polarity decreases this rotation and increases the velocities. From the symmetry of the effects, they concluded that the fieldlike SOT effect was negligible. Direct measurements of the two components of the SOT confirmed the reduced value of the fieldlike SOT. This work clearly evidences the transition from bulk to interfacial CIDM and can serve as a guide for further studies of this physics. For example, the absence of domain wall motion for $3 \leq N \leq 6$ was interpreted by the fact that the interfacial DMI from the bottom Pt layer was raising the Walker field too much, so that the domain wall motion by adiabatic STT could not be reached for the applied currents. The same mechanism applies for the combination of adiabatic STT and fieldlike SOT, showing that these two mechanisms of CIDM can act in opposition. A similar transition from SOT to STT-driven domain wall motion was observed in $(\text{Co}/\text{Tb})_N$ multilayers (Bang *et al.*, 2016).

In another study in the same $(\text{Co}/\text{Ni})_N$ system, the structure was designed such that SOT acted as a perturbation with respect to STT (Yoshimura and Koyama, 2014). The sample was medium thick ($N = 4$) and the structure was nominally symmetric with Pt and Ta on both sides, with the same thicknesses. The domain wall motion, driven by STT, was modified by applying in-plane fields, both along the current (x) or transverse to it (y). As expected for adiabatic STT, the motion was suppressed by large in-plane fields, as these fields block the precession of the domain wall moment. The surprise was that the domain wall motion windows were not centered at zero field, with the x-field offset reversing sign between up-down and down-up domain walls. This could be qualitatively interpreted by (i) a precession dissymmetry under in-plane field that leads to different residence times for Néel walls of opposite chiralities, and (ii) a noncompensated dampinglike SOT due to a measured imbalance in the conduction of the top and bottom Pt layers. On the other hand, the independence of the y field offset on the domain wall type (up and down or down and up) is consistent with an effect of the Oersted field and/or the fieldlike SOT. This work, more generally, proposes a way to experimentally test the presence of the SOT and of the Oersted field, as any in-plane field affects the precession of the domain wall moment triggered by STT. Here we also refer to the numerical work by Martinez (2012) on the STT plus fieldlike SOT case, for various values on nonadiabaticity, and the micromagnetic simulations analysis by Martinez, Emori, and Beach (2013) and Boulle *et al.* (2014) of experimental results for Pt/Co/AlOx in terms of STT plus SOT.

5. Motion of magnetic skyrmions under spin-orbit torques

Magnetic skyrmions with nonzero spin winding number are compact magnetic textures with a nontrivial topology, so that

they cannot be removed by a continuous transformation, in the continuum limit. Although there are still arguments about the precise meaning of this terminology, we adopt here the definition agreed on by a large panel of authors (Hellman *et al.*, 2017). There is currently an increasing interest in the electrical manipulation of such objects as they could serve as fundamental building blocks for data storage and logic devices (Fert, Cros, and Sampaio, 2013; Tomasello *et al.*, 2014; Zhang, Ezawa, and Zhou, 2015). Skyrmions have, in addition to topology and compared to the magnetic bubbles extensively investigated in the past (Malozemoff and Slonczewski, 1979), a fixed chirality which is an important asset for SOT as can be inferred from the preceding considerations.

A physically appealing way to understand how the various characteristics of a skyrmion affect its response to current-induced torques is offered by Thiele's equation derived from the LLG equation to handle the steady-state motion of rigid textures (Thiele, 1973). Thiele's equation was generalized to include STT (Thiaville *et al.*, 2005) and, more recently, also SOT (Sampaio *et al.*, 2013). It reads

$$\mathbf{G} \times (\mathbf{v} - \mathbf{u}) - \overline{\overline{D}}(\alpha\mathbf{v} - \beta\mathbf{u}) + \mathbf{F}_{\text{SOT}} + \mathbf{F} = \mathbf{0}, \quad (76)$$

where $\mathbf{v}$ is the in-plane velocity of the skyrmion center, $\mathbf{u}$ is the spin-drift velocity, β is the nonadiabaticity parameter related to STT [see Eq. (72)], $\mathbf{G}$ is the so-called gyrovector, $\overline{\overline{D}}$ is the dissipation tensor introduced by Thiele (from which the damping coefficient α was factored out when generalizing to STT), $\mathbf{F}$ is the other force applied to the skyrmion (e.g., pinning), and finally $\mathbf{F}_{\text{SOT}}$ is the force that SOTs apply to the skyrmion. Topology appears in the gyrovector $\mathbf{G} = (M_s h/\gamma) 4\pi N_{\text{Sk}} \mathbf{z}$ that is along the film normal and proportional to the topological (or skyrmion) number N_{Sk}. The latter is simply, for a compact texture, $N_{\text{Sk}} = Sp$ with p the polarity of the magnetization of the skyrmion center ($+1$ for $+\mathbf{z}$) and S the winding number of the magnetization ($+1$ for the simple skyrmions). The dissipation tensor, diagonal for high symmetry textures, is related to the size of the skyrmion [see, e.g., Hrabec *et al.* (2017)]. The force $\mathbf{F}$ is nonzero, for example, when a confining potential exists, or a small z field gradient. The STT forces on a skyrmion are illustrated in Fig. 50(c).

The force from the SOT is computed by projecting the SOT on the skyrmion displacement (the procedure by which Thiele's equation is constructed), as a volume integral for each component

$$F_{i,\text{SOT}} = -\int d\mathcal{V} \mathbf{B}_{\text{SOT}} \cdot \frac{\partial}{\partial i} \mathbf{M} = \tau_{\text{DL}} \boldsymbol{\zeta} \cdot \int d\mathcal{V} \mathbf{m} \times \frac{\partial}{\partial i} \mathbf{m}. \quad (77)$$

The fieldlike SOT gives no contribution to the force as it acts like a constant in-plane field. As for the dampinglike SOT contribution, remembering that $\boldsymbol{\zeta} \| \mathbf{y}$ for current along x, Eq. (77) amounts to one term of the DMI energy density. For the x component of the force (along the current), it is the part of the interfacial DMI that involves the x gradients [Eq. (74)]. For the y component of the force (transverse to the current), it is the part of the bulk DMI that involves the y gradients [Eq. (73)]. Thus, the dampinglike SOT force on a skyrmion depends on its chirality and of its type (i.e., Bloch or
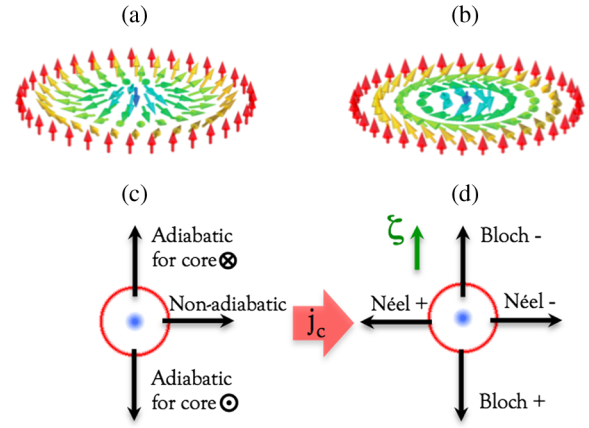

FIG. 50. (a) Néel and (b) Bloch skyrmions (both with negative polarity). Adapted from Fert, Reyren, and Cros, 2017. (c) Schematic of the forces (black arrows) applied to a skyrmion (circle) by a current density j_c, in the case of adiabatic and nonadiabatic STT. The forces are independent of the type of the skyrmion and depend only on its core polarity. (d) Schematic of the forces (black arrows) applied to a skyrmion (circle) by a dampinglike SOT with a spin polarization along $\boldsymbol{\zeta}$, as indicated by the green arrow. The forces depend on whether the skyrmion is Bloch or Néel.

Néel); see Fig. 50(d). Because of the gyrotropic term, both STTs and dampinglike SOT drive the skyrmion, at some angle between the x and y axes, so that skyrmion motion under current alone does not allow one to infer its internal structure. Nevertheless, conventional magnetic bubbles, whose lowest energy state is an achiral Bloch skyrmion because of the absence of significant DMI, would be sorted according to their Bloch chirality by dampinglike SOT. This is in contrast to skyrmions that have a definite chirality (fixed by DMI) and should all follow the same trajectory.

Metastable magnetic skyrmions have been recently obtained at room temperature in transition-metal multilayers (Gong Chen *et al.*, 2015; Jiang *et al.*, 2015; Boulle *et al.*, 2016; Moreau-Luchaire *et al.*, 2016; Woo *et al.*, 2016; Hrabec *et al.*, 2017; Pollard *et al.*, 2017). Many experiments revealed skyrmions motion under current, either along or against the direction of the electron flow, in most cases in agreement with the DMI and dampinglike SOT sign (Jiang *et al.*, 2015, 2017; Woo *et al.*, 2016; Guoqiang Yu *et al.*, 2016; Hrabec *et al.*, 2017; Litzius *et al.*, 2017). The influence of disorder and thermal fluctuations on the driven motion of single skyrmions has been investigated using either particle simulations (Lin *et al.*, 2013) or micromagnetic modeling (Sampaio *et al.*, 2013), demonstrating that skyrmions have the tendency to avoid pointlike defects (Iwasaki, Mochizuki, and Nagaosa, 2013a, 2013b). Remarkably, the angle of the gyrotropic deflection (sometimes also called the skyrmion Hall angle) observed in experiments is poorly reproduced by Thiele's equation. This discrepancy may be due to disorder effects, e.g., sliding along grain boundaries, as suggested by recent simulations (Reichhardt and Olson Reichhardt, 2016; Kim and Yoo, 2017; Legrand *et al.*, 2017; Salimath *et al.*, 2019). Moreover, the skyrmion dynamic deformation leads to an influence of the fieldlike SOT on the deflection angle

(Litzius *et al.*, 2017). Finally, the influence of the gradient of the *z* component of the Oersted field deserves further investigation (Hrabec *et al.*, 2017). Altogether, skyrmions appear as favorable objects to be controlled by either STT or SOT since their velocity reaches that of magnetic domain walls in the same structures. Further exploration of their robustness and scalability is currently ongoing (Bernand-Mantel *et al.*, 2018; Büttner, Lemesh, and Beach, 2018).

6. Impact of disorder

In sputtered ultrathin magnetic multilayers, disorder is so strong that CIDM occurs only at large (field or current) drive. At low drive, domain wall motion consists of thermally assisted hopping between pinning sites. This regime of domain wall motion is called creep, or depinning, depending on field magnitude and type of domain wall pinning (Metaxas *et al.*, 2007; Kim *et al.*, 2009; Gorchon *et al.*, 2014). Whereas field-driven and STT-driven creep seemed to be well understood (Chauve, Giamarchi, and Le Doussal, 2000; DuttaGupta *et al.*, 2016; Jeudy *et al.*, 2016), the situation has changed with the introduction of SOT and DMI. Several experiments of CIDM showed that the creep regime of domain wall motion deserves further study in order to be fully understood (Lavrijsen *et al.*, 2012, 2015; Vanatka *et al.*, 2015). For instance, it was recently proposed that structural inversion asymmetry could be responsible for a chiral dissipation mechanism affecting the domain wall dynamics, called chiral damping (Akosa *et al.*, 2016; Emilie Jué *et al.*, 2016). More recently it was shown that, as the domain wall energy becomes orientation dependent under the in-plane field (Pellegren, Lau, and Sokalski, 2017), an effect reinforced by DMI and strikingly evidenced by specific domain shapes (Derek Lau *et al.*, 2016), the simple creep model with uniform domain wall tension fails. Thus, the analysis of creep motion under the in-plane field has to be thoroughly reexamined.

In contrast, a thorough study of the influence of disorder on CIDM in the flow or precessional regimes is still missing. Similar to in-plane materials (see Sec. VI.B.1), one may expect a modification of the threshold values for domain wall motion, a change of slope and/or offset of velocity in the linear regime, and suppression of velocity breakdown. Regarding the apparent offset in velocity, a simple model considering the statistical average of the inverse velocities was shown to reproduce the feature (Feldtkeller, 1968; E. Jué *et al.*, 2016). The suppression of velocity breakdown has been observed and numerically reproduced for field-driven motion in the presence of interfacial DMI (E. Jué *et al.*, 2016; Pham *et al.*, 2016; Yoshimura *et al.*, 2016; Ajejas *et al.*, 2017). In fact, simulations reveal that this effect occurs even in the absence of disorder, as soon as the domain wall has a sufficient length to depart from 1D behavior. The novelty introduced by STT, SOT, and DMI is that the domain wall drive depends on the local domain wall orientation, which modifies the overall energetics and dynamics. In the creep regime under CIDM and field, these angle dependences are exemplified by the formation of triangular-shape domains pinned at nucleation sites (Moon *et al.*, 2013, 2018).

D. Antiferromagnetic and ferrimagnetic systems

The search for extremely high domain wall velocity has recently brought perpendicularly magnetized synthetic antiferromagnet strips, such as (Co/Ni)/Ru/(Co/Ni), to the forefront. In such systems, Yang, Ryu, and Parkin (2015) reported SOT-driven domain wall velocities as fast as 750 m/s and explained the results by the enhanced Walker breakdown threshold. Indeed, in the presence of Ru-mediated interlayer exchange coupling [Ruderman-Kittel-Kasuya-Yosida (RKKY)] the azimuthal angles of the two antiparallel domain walls stabilize each other such that the domain wall propagates in the flow regime over a larger range of driving current densities [see also Lepadatu *et al.* (2017)]. In a recent work Qiu *et al.* (2016) observed that the presence of the Ru spacer layer may affect the spin current, leading to different SOTs for such trilayers.

Similar ideas resulted in the proposition of antiferromagnetic skyrmions, either in the bilayer form or in bulk antiferromagnets, which display no skyrmion Hall effect and could also reach very high velocity in the latter case (Zhang, Zhou, and Ezawa, 2016; Barker and Tretiakov, 2016; Tomasello *et al.*, 2017). Bulk antiferromagnets are particularly interesting for their ability to support THz dynamics, and it was recently proposed that antiferromagnetic domain walls driven by SOT could reach extremely high velocities, while displaying a Lorentz contraction when reaching the spin wave group velocity (Gomonay, Jungwirth, and Sinova, 2016; Shiino *et al.*, 2016). The investigation of antiferromagnetic spintronics is still at its infancy though (Jungwirth *et al.*, 2016; Baltz *et al.*, 2018), and alternative materials are being explored. From this perspective, ferrimagnets such as FeGdCo offer an appealing platform due to the tunability of their compensation point. For instance, recent studies demonstrated a large enhancement of field-driven domain wall velocity and SOT efficiencies close to the angular momentum compensation point (Kab-jin Kim *et al.*, 2017; Mishra *et al.*, 2017).

VII. PERSPECTIVES

SOTs offer a powerful and versatile tool to manipulate and excite magnetic order parameters and efficiently control magnetic domain walls and skyrmions. A particularly attractive feature of these torques is their ability to excite any type of magnetic materials, ranging from metals to semiconductors and insulators, in both ferromagnetic and antiferromagnetic configurations. This versatility has led to groundbreaking accomplishments that could not be achieved with STT: the switching of single-layer ferromagnets, ferrimagnets, and antiferromagnets, as well as the excitation of spin waves and auto-oscillations in planar and vertical device geometries.

The discovery of topological materials as spin sources has opened appealing avenues for the realization of very large charge-to-spin conversion and low critical switching current. Topological insulators, Dirac semimetals, Weyl semimetals, Kondo topological insulators, as well as 2D materials (bismuth chalcogenides, graphene and its siblings, transition-metal dichalcogenides, transition-metal trihalides, etc.) present a unique opportunity for the exploitation of exotic spin-charge conversion mechanisms and chiral spin textures.

A number of questions remain open, which will have an impact on future developments and materials design.

(i) Whereas the basic mechanisms behind SOT seem to be understood, a robust and systematic quantitative agreement between theory and experiment is still lacking. In particular, understanding the interplay between interfacial, bulk, and orbital contributions to SOT as well as DMI and chiral damping in magnetic multilayers will indicate how to improve their efficiency.

(ii) Besides the two "flagship mechanisms" that control the current-induced dynamics (iSGE, SHE), novel phenomena have been identified recently: spin swapping (Saidaoui and Manchon, 2016), interfacial spin currents (Amin, Zemen, and Stiles, 2018), chiral damping (Emilie Jué *et al.*, 2016), etc. What is the actual magnitude of these effects and how do they influence the magnetization dynamics? How can they be best harvested to enhance the operability of SOT devices?

(iii) The electrical control of magnetic domain walls and skyrmions substantially benefits from SOTs. Nevertheless, their behavior in the presence of disorder, and particularly the creep and depinning regimes, need to be better understood. How can these regimes provide information about the nature of the chirality (dissipation and energy)? Several novel torques have been predicted in these textures (van der Bijl and Duine, 2012), but not observed yet. In addition, topological currents have been proposed to enhance the mobility of both ferromagnetic and antiferromagnetic skyrmions (Abbout *et al.*, 2018; Akosa *et al.*, 2018), which calls for experimental verification.

(iv) Antiferromagnets bear outstanding promises due to the zero net magnetization and their inherent THz dynamics (Jungwirth *et al.*, 2016, 2018; Baltz *et al.*, 2018). However, to date, only a few antiferromagnets have been electrically manipulated (CuMnAs, Mn_2Au, and NiO) (Wadley *et al.*, 2016; Bodnar *et al.*, 2018; X. Z. Chen *et al.*, 2018; Moriyama *et al.*, 2018). The next frontier is to extend these observations to more materials, including noncollinear antiferromagnets. The latter present the advantage of displaying AHE as well as MOKE response, enabling for the electrical and optical detection of their order parameter's orientation (Nakatsuji, Kiyohara, and Higo, 2015). A natural development direction will be to extend these ideas to frustrated magnets that support exotic magnetic behaviors (Balents, 2010).

(v) Finally, the search for the most efficient sources of SOTs raises the question about the nature of spin-orbit effects in the presence of very large spin-orbit coupling. How do concepts such as spin currents, SHE, iSGE, DMI, and magnetic damping evolve when the spin-orbit interaction is comparable to or larger than the crystal field? Is there a limit to the amount of angular momentum that can be transferred to the magnetic system, and if so, how can it be determined? What materials combination produces the largest torque? Similar questions can be asked when electronic correlations are important, such as in $(Ce, Ca)MnO_3$, $Yb_2Ti_2O_7$, SmB_6, etc.

Besides these important challenges, what makes SOTs attractive is their potential for efficient device operation. In a nutshell, SOTs can do everything STT can, with the crucial advantage of decoupling the injection and detection paths. This unique feature allows for the excitation and switching of large magnetic surface areas ($> \mu m^2$), but also the electrical control of magnetic insulators and antiferromagnets, which traditional STT cannot achieve. Its implementation does not enhance only the performance of devices (speed, power consumption) such as SOT-MRAMs, nano-oscillators, or magnetic racetrack data storage devices, but it also opens thrilling perspectives beyond conventional spintronics components (Sato *et al.*, 2018). For instance, SOT-driven memristors have been developed to be used as synapses for artificial neural networks (Lequeux *et al.*, 2016; Borders, Fukami, and Ohno, 2018), while the dampinglike SOT can be exploited to build stochastic parity bits for invertible logic (Camsari *et al.*, 2017). Finally, SOTs could be used to manipulate and explore more exotic magnetic excitations such as the ones emerging in spin liquids (Balents, 2010), i.e., spinons, magnetic monopoles, anyons, or even Majorana fermions.

LIST OF SYMBOLS AND ABBREVIATIONS

1D, 2D, 3D	one, two, and three dimensional
AHE	anomalous Hall effect
AMR	anisotropic magnetoresistance
ANE	anomalous Nernst effect
CIDM	current-induced domain wall motion
CMOS	complementary metal-oxide semiconductor
DMI	Dzyaloshinskii-Moriya interaction
FMR	ferromagnetic resonance
iSGE	inverse spin galvanic effect
LED	light emitting diode
LLG	Landau-Lifshitz-Gilbert (equation)
MOKE	magneto-optical Kerr effect
MRAM	magnetic random access memory
NM/FM	nonmagnetic metal/ferromagnet
NM/AF	nonmagnetic metal/antiferromagnet
rf	radio frequency
RKKY	Ruderman-Kittel-Kasuya-Yosida (interaction)
SGE	spin galvanic effect
SHE	spin Hall effect
SMR	spin Hall magnetoresistance
SOT	spin-orbit torque
ST-FMR	spin-torque ferromagnetic resonance
STT	spin-transfer torque
TMR	tunneling magnetoresistance
YIG	yttrium iron garnet

ACKNOWLEDGMENTS

REFERENCES

Abbout, A., Joseph Weston, Xavier Waintal, and A. Manchon, 2018, "Cooperative Charge Pumping and Enhanced Skyrmion Mobility," Phys. Rev. Lett. **121**, 257203.

Ajejas, Fernando, Viola Kžáková, Dayane De Souza Chaves, Jan Vogel, Paolo Perna, Ruben Guerrero, Adrian Gudin, Julio Camarero, and Stefania Pizzini, 2017, "Tuning domain wall velocity with Dzyaloshinskii-Moriya interaction," Appl. Phys. Lett. **111**, 202402.

Akosa, C. A., I. M. Miron, G. Gaudin, and A. Manchon, 2016, "Phenomenology of chiral damping in noncentrosymmetric magnets," Phys. Rev. B **93**, 214429.

Akosa, C. A., O. A. Tretiakov, G. Tatara, and A. Manchon, 2018, "Theory of Topological Spin Hall Effect in Antiferromagnetic Skyrmion: Impact on Current-induced Motion," Phys. Rev. Lett. **121**, 097204.

Akosa, Collins Ashu, Won-Seok Kim, André Bisig, Mathias Kläui, Kyung-Jin Lee, and Aurélien Manchon, 2015, "Role of spin diffusion in current-induced domain wall motion for disordered ferromagnets," Phys. Rev. B **91**, 094411.

Akyol, Mustafa, Wanjun Jiang, Guoqiang Yu, Yabin Fan, Mustafa Gunes, Ahmet Ekicibil, Pedram Khalili Amiri, and Kang L. Wang, 2016, "Effect of heavy metal layer thickness on spin-orbit torque and current-induced switching in Hf/CoFeB/MgO structures," Appl. Phys. Lett. **109**, 022403.

Allen, Gary, Sasikanth Manipatruni, Dmitri E. Nikonov, Mark Doczy, and Ian A. Young, 2015, "Experimental demonstration of the coexistence of spin Hall and Rashba effects in β-tantalum/ ferromagnet bilayers," Phys. Rev. B **91**, 144412.

Allwood, D. A., G. Xiong, C. C. Faulkner, D. Atkinson, D. Petit, and R. P. Cowburn, 2005, "Magnetic Domain-Wall Logic," Science **309**, 1688.

Amin, V. P., and M. D. Stiles, 2016a, "Spin transport at interfaces with spin-orbit coupling: Formalism," Phys. Rev. B **94**, 104419.

Amin, V. P., and M. D. Stiles, 2016b, "Spin transport at interfaces with spin-orbit coupling: Phenomenology," Phys. Rev. B **94**, 104420.

Amin, V. P., J. Zemen, and M. D. Stiles, 2018, "Interface-Generated Spin Currents," Phys. Rev. Lett. **121**, 136805.

An, Hongyu, Yuito Kageyama, Yusuke Kanno, Nagisa Enishi, and Kazuya Ando, 2016, "Spin-torque generator engineered by natural oxidation of Cu," Nat. Commun. **7**, 13069.

An, Hongyu, Yusuke Kanno, Akio Asami, and Kazuya Ando, 2018, "Giant spin-torque generation by heavily oxidized Pt," Phys. Rev. B **98**, 014401.

An, Hongyu, Takeo Ohno, Yusuke Kanno, Yuito Kageyama, Yasuaki Monnai, Hideyuki Maki, Ji Shi, and Kazuya Ando, 2018, "Current-induced magnetization switching using an electrically insulating spin-torque generator," Sci. Adv. **4**, eaar2250.

An, Kyongmo, Daniel R. Birt, Chi Feng Pai, Kevin Olsson, Daniel C. Ralph, R. A. Buhrman, and Xiaoqin Li, 2014, "Control of propagating spin waves via spin transfer torque in a metallic bilayer waveguide," Phys. Rev. B **89**, 140405(R).

An, Z., F. Q. Liu, Y. Lin, and C. Liu, 2012, "The universal definition of spin current," Sci. Rep. **2**, 388.

Ando, K., S. Takahashi, K. Harii, K. Sasage, J. Ieda, S. Maekawa, and E. Saitoh, 2008, "Electric Manipulation of Spin Relaxation Using the Spin Hall Effect," Phys. Rev. Lett. **101**, 036601.

Ando, Kazuya, 2014, "Dynamical generation of spin currents," Semicond. Sci. Technol. **29**, 043002.

Apalkov, D., B. Dieny, and J. M. Slaughter, 2016, "Magnetoresistive Random Access Memory," Proc. IEEE **104**, 1796.

Aradhya, S. V., G. E. Rowlands, J. Oh, D. C. Ralph, and R. A. Buhrman, 2016, "Nanosecond-Timescale Low Energy Switching of In-Plane Magnetic Tunnel Junctions through Dynamic Oersted-Field-Assisted Spin Hall Effect," Nano Lett. **16**, 5987.

Aronov, A. G., and Y. B. Lyanda-Geller, 1989, "Nuclear electric resonance and orientation of carrier spins by an electric field," JETP Lett. **50**, 398 [http://adsabs.harvard.edu/abs/1989JETPL..50.431A].

Avci, Can Onur, Kevin Garello, Mihai Gabureac, Abhijit Ghosh, Andreas Fuhrer, Santos F. Alvarado, and Pietro Gambardella, 2014, "Interplay of spin-orbit torque and thermoelectric effects in ferromagnet/normal-metal bilayers," Phys. Rev. B **90**, 224427.

Avci, Can Onur, Kevin Garello, Abhijit Ghosh, Mihai Gabureac, Santos F. Alvarado, and Pietro Gambardella, 2015, "Unidirectional spin Hall magnetoresistance in ferromagnet/normal metal bilayers," Nat. Phys. **11**, 570.

Avci, Can Onur, Kevin Garello, Johannes Mendil, Abhijit Ghosh, Nicolas Blasakis, Mihai Gabureac, Morgan Trassin, Manfred Fiebig, and Pietro Gambardella, 2015, "Magnetoresistance of heavy and light metal/ferromagnet bilayers," Appl. Phys. Lett. **107**, 192405.

Avci, Can Onur, Kevin Garello, Ioan Mihai Miron, Gilles Gaudin, S. Auffret, Olivier Boulle, and Pietro Gambardella, 2012, "Magnetization switching of an MgO/Co/Pt layer by in-plane current injection," Appl. Phys. Lett. **100**, 212404.

Avci, Can Onur, Johannes Mendil, Geoffrey S. D. Beach, and Pietro Gambardella, 2018, "Origins of the Unidirectional Spin Hall Magnetoresistance in Metallic Bilayers," Phys. Rev. Lett. **121**, 087207.

Avci, Can Onur, Andy Quindeau, Chi-Feng Pai, Maxwell Mann, Lucas Caretta, Astera S. Tang, Mehmet C. Onbasli, Caroline A. Ross, and Geoffrey S. D. Beach, 2017, "Current-induced switching in a magnetic insulator," Nat. Mater. **16**, 309.

Avci, Can Onur, Ethan Rosenberg, Manuel Baumgartner, Lukáš Beran, Andy Quindeau, Caroline A. Ross, and Geoffrey S. D. Beach, 2017, "Fast switching and signature of efficient domain wall motion driven by spin-orbit torques in a perpendicular anisotropy magnetic insulator/Pt bilayer," Appl. Phys. Lett. **111**, 072406.

Avci, Can Onur, *et al.*, 2014, "Fieldlike and antidamping spin-orbit torques in as-grown and annealed Ta/CoFeB/MgO layers," Phys. Rev. B **89**, 214419.

Awad, A. A., A. Houshang, M. Dvornik, E. Iacocca, and R. K. Dumas, 2017, "Long-range mutual synchronization of spin Hall nano-oscillators," Nat. Phys. **13**, 292.

Baek, Seung Heon C., Vivek P. Amin, Young Wan Oh, Gyungchoon Go, Seung Jae Lee, Geun Hee Lee, Kab Jin Kim, M. D. Stiles, Byong Guk Park, and Kyung Jin Lee, 2018, "Spin currents and spin-orbit torques in ferromagnetic trilayers," Nat. Mater. **17**, 509.

Baldrati, L., *et al.*, 2018, "Mechanism of Néel order switching in antiferromagnetic thin films revealed by magnetotransport and direct imaging," arXiv:1810.11326.

Balents, Leon, 2010, "Spin liquids in frustrated magnets," Nature (London) **464**, 199.

Baltz, V., A. Manchon, M. Tsoi, T. Moriyama, T. Ono, and Y. Tserkovnyak, 2018, "Antiferromagnetic spintronics," Rev. Mod. Phys. **90**, 015005.

Bang, Do, Jiawei Yu, Xuepeng Qiu, Yi Wang, Hiroyuki Awano, Aurelien Manchon, and Hyunsoo Yang, 2016, "Enhancement of spin Hall effect induced torques for current-driven magnetic domain wall motion: Inner interface effect," Phys. Rev. B **93**, 174424.

Barker, Joseph, and Oleg A. Tretiakov, 2016, "Static and Dynamical Properties of Antiferromagnetic Skyrmions in the Presence of Applied Current and Temperature," Phys. Rev. Lett. **116**, 147203.

Barnett, S. J., 1915, "Magnetization by rotation," Phys. Rev. **6**, 239.

Bass, Jack, and William P. Pratt, 2007, "Spin-diffusion lengths in metals and alloys, and spin-flipping at metal/metal interfaces: an experimentalist's critical review," J. Phys. Condens. Matter **19**, 183201.

Bauer, G. E. W., E. Saitoh, and Bart J. van Wees, 2012, "Spin caloritronics," Nat. Mater. **11**, 391.

Bauer, Uwe, Yao Lide, and Geoffrey S. D. Beach, 2015, "Magneto-ionic control of interfacial magnetism," Nat. Mater. **14**, 174.

Baumgartner, M., 2018, Spatially and time-resolved measurements of the magnetization dynamics driven by spin-orbit torques, Ph.D. thesis (ETH Zurich).

Baumgartner, M., and Pietro Gambardella, 2018, "Asymmetric velocity and tilt angle of domain walls induced by spin-orbit torques," Appl. Phys. Lett. **113**, 242402.

Baumgartner, Manuel, *et al.*, 2017, "Spatially and time-resolved magnetization dynamics driven by spin-orbit torques," Nat. Nanotechnol. **12**, 980.

Beach, G. S. D., M. Tsoi, and J. L. Erskine, 2008, "Current-induced domain wall motion," J. Magn. Magn. Mater. **320**, 1272.

Bedau, D., H. Liu, J. Z. Sun, J. A. Katine, E. E. Fullerton, S. Mangin, and A. D. Kent, 2010, "Spin-transfer pulse switching: From the dynamic to the thermally activated regime," Appl. Phys. Lett. **97**, 262502.

Belabbes, Abderrezak, Gustav Bihlmayer, Stefan Blügel, and Aurélien Manchon, 2016, "Oxygen-enabled control of Dzyaloshinskii-Moriya Interaction in ultra-thin magnetic films," Sci. Rep. **6**, 24634.

Belashchenko, K. D., Alexey A. Kovalev, and M. Van Schilfgaarde, 2016, "Theory of Spin Loss at Metallic Interfaces," Phys. Rev. Lett. **117**, 207204.

Belashchenko, K. D., Alexey A. Kovalev, and M. Van Schilfgaarde, 2019, "First-principles calculation of spin-orbit torque in a Co/Pt bilayer," Phys. Rev. Mater. **3**, 011401(R).

Belkov, V. V., and S. D. Ganichev, 2008, "Magneto-gyrotropic effects in semiconductor quantum wells," Semicond. Sci. Technol. **23**, 114003.

Belmeguenai, Mohamed, Jean Paul Adam, Yves Roussigne, Sylvain Eimer, Thibaut Devolder, Joo Von Kim, Salim Mourad Cherif, Andrey Stashkevich, and Andre Thiaville, 2015, "Interfacial Dzyaloshinskii-Moriya interaction in perpendicularly magnetized Pt/Co/AlOx ultrathin films measured by Brillouin light spectroscopy," Phys. Rev. B **91**, 180405.

Bender, Scott A., Rembert A. Duine, and Yaroslav Tserkovnyak, 2012, "Electronic pumping of quasiequilibrium Bose-Einstein-condensed magnons," Phys. Rev. Lett. **108**, 246601.

Berger, Andrew J., Eric R. J. Edwards, Hans T. Nembach, Alexy D. Karenowska, Mathias Weiler, and Thomas J. Silva, 2018, "Inductive detection of fieldlike and dampinglike ac inverse spin-orbit torques in ferromagnet / normal-metal bilayers," Phys. Rev. B **97**, 094407.

Berger, Andrew J., Eric R. J. Edwards, Hans T. Nembach, Olof Karis, Mathias Weiler, and T. J. Silva, 2018, "Determination of the spin Hall effect and the spin diffusion length of Pt from self-consistent fitting of damping enhancement and inverse spin-orbit torque measurements," Phys. Rev. B **98**, 024402.

Berger, L., 1996, "Emission of spin waves by a magnetic multilayer traversed by a current," Phys. Rev. B **54**, 9353.

Bernand-Mantel, Anne, Lorenzo Camosi, Alexis Wartelle, Nicolas Rougemaille, Michaël Darques, and Laurent Ranno, 2018, "The skyrmion-bubble transition in a ferromagnetic thin film," SciPost Phys. **4**, 027.

Bernevig, B. Andrei, and Oskar Vafek, 2005, "Piezo-magnetoelectric effects in p-doped semiconductors," Phys. Rev. B **72**, 033203.

Bhowmik, Debanjan, Long You, and Sayeef Salahuddin, 2014, "Spin Hall effect clocking of nanomagnetic logic without a magnetic field," Nat. Nanotechnol. **9**, 59.

Blügel, Stefan, and Gustav Bihlmayer, 2007, "Magnetism of Low-dimensional Systems: Theory," in *Handbook of Magnetism and Advanced Magnetic Materials*, edited by H. Kronmuller, and S. Parkin (John Wiley & Sons, New York), pp. 1–42.

Bobeck, A. H., P. I. Bonyhard, and J. E. Geusic, 1975, "Magnetic bubbles: An emerging new memory technology," Proc. IEEE **63**, 1176.

Bode, M., M. Heide, K. von Bergmann, P. Ferriani, Stefan Heinze, G. Bihlmayer, A. Kubetzka, O. Pietzsch, Stefan Blügel, and R. Wiesendanger, 2007, "Chiral magnetic order at surfaces driven by inversion asymmetry," Nature (London) **447**, 190.

Bodnar, S. Yu, L. Šmejkal, I. Turek, T. Jungwirth, O. Gomonay, J. Sinova, A. A. Sapozhnik, H. J. Elmers, M. Klaüi, and M. Jourdan, 2018, "Writing and reading antiferromagnetic Mn2Au by Néel spin-orbit torques and large anisotropic magnetoresistance," Nat. Commun. **9**, 348.

Bogdanov, A., and D. A. Yablonskii, 1989, "Thermodynamically stable vortices states in magnetically ordered crystals. The mixed state of magnets," Zh. Eksp. Teor. Fiz. **68**, 101 [http://www.jetp.ac.ru/cgi-bin/e/index/e/68/1/p101?a=list].

Bohlens, Stellan, and Daniela Pfannkuche, 2010, "Width Dependence of the Nonadiabatic Spin-Transfer Torque in Narrow Domain Walls," Phys. Rev. Lett. **105**, 177201.

Bonell, Frédéric, Marc G. Cuxart, Kenan Song, Roberto Robles, Pablo Ordejón, Stephan Roche, Aitor Mugarza, and Sergio O. Valenzuela, 2017, "Growth of Twin-Free and Low-Doped Topological Insulators on BaF2(111)," Cryst. Growth Des. **17**, 4655.

Bonetti, Stefano, Vasil Tiberkevich, Giancarlo Consolo, Giovanni Finocchio, Pranaba Muduli, Fred Mancoff, Andrei Slavin, and Johan Åkerman, 2010, "Experimental evidence of self-localized and propagating spin wave modes in obliquely magnetized current-driven nanocontacts," Phys. Rev. Lett. **105**, 217204.

Borders, William A., Shunsuke Fukami, and Hideo Ohno, 2018, "Characterization of spin-orbit torque-controlled synapse device

for artificial neural network applications," Jpn. J. Appl. Phys. **57**, 1002B2.

Bose, Arnab, D. D. Lam, S. Bhuktare, S. Dutta, H. Singh, Y. Jibiki, and M. Goto, 2018, "Observation of Anomalous Spin Torque Generated by a Ferromagnet," Phys. Rev. Applied **9**, 064026.

Boulle, O., L. D. Buda-Prejbeanu, E. Jué, I. M. Miron, and G. Gaudin, 2014, "Current induced domain wall dynamics in the presence of spin orbit torques," J. Appl. Phys. **115**, 17D502.

Boulle, O., J. Kimling, P. Warnicke, M. Kläui, U. Rüdiger, G. Malinowski, H. J. M. Swagten, B. Koopmans, C. Ulysse, and G. Faini, 2008, "Nonadiabatic spin transfer torque in high anisotropy magnetic nanowires with narrow domain walls," Phys. Rev. Lett. **101**, 216601.

Boulle, O., S. Rohart, L. D. Buda-Prejbeanu, E. Jué, I. M. Miron, S. Pizzini, J. Vogel, G. Gaudin, and A. Thiaville, 2013, "Domain Wall Tilting in the Presence of the Dzyaloshinskii-Moriya Interaction in Out-of-Plane Magnetized Magnetic Nanotracks," Phys. Rev. Lett. **111**, 217203.

Boulle, Olivier, *et al.*, 2016, "Room temperature chiral magnetic skyrmion in ultrathin magnetic nanostructures," Nat. Nanotechnol. **11**, 449.

Brataas, Arne, Andrew D. Kent, and Hideo Ohno, 2012, "Current-induced torques in magnetic materials," Nat. Mater. **11**, 372.

Brataas, Arne, Yaroslav Tserkovnyak, G. E. W. Bauer, and Bertrand Halperin, 2002, "Spin battery operated by ferromagnetic resonance," Phys. Rev. B **66**, 060404.

Brataas, Arne, Yaroslav Tserkovnyak, G. E. W. Bauer, and Paul J. Kelly, 2012, "Spin Pumping and Spin Transfer," arXiv:1108.0385v3.

Burrowes, C., *et al.*, 2010, "Non-adiabatic spin-torques in narrow magnetic domain walls," Nat. Phys. **6**, 17.

Buschow, K. H. J., 1984, *Handbook on the Physics and Chemistry of Rare Earths* (Elsevier, New York).

Büttner, Felix, Ivan Lemesh, and Geoffrey S. D. Beach, 2018, "Theory of isolated magnetic skyrmions: From fundamentals to room temperature applications," Sci. Rep. **8**, 4464.

Bychkov, Yu A., and E. I. Rashba, 1984, "Oscillatory effects and the magnetic susceptibility of carriers in inversion layers," J. Phys. C **17**, 6039.

Camley, R. E., and J. Barnas, 1989, "Theory of Giant Magnetoresistance Effects in Magnetic Layered Structures with Antiferromagnetic Coupling," Phys. Rev. Lett. **63**, 664.

Camsari, Kerem Yunus, Rafatul Faria, Brian M. Sutton, and Supriyo Datta, 2017, "Stochastic p-bits for invertible logic," Phys. Rev. X **7**, 031014.

Caretta, Lucas, *et al.*, 2018, "Fast current-driven domain walls and small skyrmions in a compensated ferrimagnet," Nat. Nanotechnol. **13**, 1154.

Castro Neto, A. H., N. M. R. Peres, K. S. Novoselov, and A. K. Geim, 2009, "The electronic properties of graphene," Rev. Mod. Phys. **81**, 109.

Caviglia, A. D., M. Gabay, S. Gariglio, N. Reyren, C. Cancellieri, and J.-M. Triscone, 2010, "Tunable Rashba Spin-Orbit Interaction at Oxide Interfaces," Phys. Rev. Lett. **104**, 126803.

Chang, Po Hao, Troels Markussen, Søren Smidstrup, Kurt Stokbro, and Branislav K. Nikolić, 2015, "Nonequilibrium spin texture within a thin layer below the surface of current-carrying topological insulator Bi2Se3: A first-principles quantum transport study," Phys. Rev. B **92**, 201406.

Chappert, Claude, A. Fert, and Frédéric Nguyen Van Dau, 2007, "The emergence of spin electronics in data storage," Nat. Mater. **6**, 813.

Chauleau, J. Y., *et al.*, 2011, "Magnetization textures in NiPd nanostructures," Phys. Rev. B **84**, 094416.

Chauve, Pascal, Thierry Giamarchi, and Pierre Le Doussal, 2000, "Creep and depinning in disordered media," Phys. Rev. B **62**, 6241.

Chen, G., *et al.*, 2013, "Novel Chiral Magnetic Domain Wall Structure in Fe/Ni/Cu(001) Films," Phys. Rev. Lett. **110**, 177204.

Chen, Gong, Tianping Ma, Alpha T. N'Diaye, Heeyoung Kwon, Changyeon Won, Yizheng Wu, and Andreas K. Schmid, 2013, "Tailoring the chirality of magnetic domain walls by interface engineering," Nat. Commun. **4**, 2671.

Chen, Gong, Arantzazu Mascaraque, Alpha T. N'Diaye, and Andreas K. Schmid, 2015, "Room temperature skyrmion ground state stabilized through interlayer exchange coupling," Appl. Phys. Lett. **106**, 242404.

Chen, Hua, Qian Niu, and A. H. MacDonald, 2014, "Anomalous Hall Effect Arising from Noncollinear Antiferromagnetism," Phys. Rev. Lett. **112**, 017205.

Chen, Kai, and Shufeng Zhang, 2015, "Spin pumping in the presence of spin-orbit coupling," Phys. Rev. Lett. **114**, 126602.

Chen, Kai, and Shufeng Zhang, 2017, "Roles of nonlocal conductivity on spin Hall angle measurement," Phys. Rev. B **96**, 134401.

Chen, L., M. Decker, M. Kronseder, R. Islinger, M. Gmitra, D. Schuh, D. Bougeard, J. Fabian, D. Weiss, and C. H. Back, 2016, "Robust spin-orbit torque and spin-galvanic effect at the Fe/GaAs (001) interface at room temperature," Nat. Commun. **7**, 13802.

Chen, L., M. Gmitra, M. Vogel, R. Islinger, M. Kronseder, D. Schuh, D. Bougeard, J. Fabian, D. Weiss, and C. H. Back, 2018, "Electric-field control of interfacial spin orbit fields," Nat. Electron. **1**, 350.

Chen, Wei, Manfred Sigrist, Jairo Sinova, and Dirk Manske, 2015, "Minimal model of spin-transfer torque and spin pumping caused by the spin hall effect," Phys. Rev. Lett. **115**, 217203.

Chen, X. Z., *et al.*, 2018, "Antidamping-Torque-Induced Switching in Biaxial Antiferromagnetic Insulators," Phys. Rev. Lett. **120**, 207204.

Cheng, Ran, Di Xiao, and Arne Brataas, 2016, "Terahertz Antiferromagnetic Spin Hall Nano-Oscillator," Phys. Rev. Lett. **116**, 207603.

Cheng, Ran, Jiang Xiao, Qian Niu, and Arne Brataas, 2014, "Spin pumping and spin-transfer torques in antiferromagnets," Phys. Rev. Lett. **113**, 057601.

Chernyshov, Alexandr, Mason Overby, Xinyu Liu, Jacek K. Furdyna, Yuli Lyanda-Geller, and Leonid P. Rokhinson, 2009, "Evidence for reversible control of magnetization in a ferromagnetic material by means of spin orbit magnetic field," Nat. Phys. **5**, 656.

Chumak, A. V., V. I. Vasyuchka, A. A. Serga, and Burkard Hillebrands, 2015, "Magnon spintronics," Nat. Phys. **11**, 453.

Ciccarelli, C., *et al.*, 2016, "Room-temperature spin-orbit torque in NiMnSb," Nat. Phys. **12**, 855.

Ciccarelli, Chiara, Kjetil M. D. Hals, A. C. Irvine, Vit Novak, Yaroslav Tserkovnyak, Hidekazu Kurebayashi, Arne Brataas, and Andrew Ferguson, 2015, "Magnonic charge pumping via spin orbit coupling," Nat. Nanotechnol. **10**, 50.

Clarke, D., O. Tretiakov, G.-W. Chern, Ya. Bazaliy, and O. Tchernyshyov, 2008, "Dynamics of a vortex domain wall in a magnetic nanostrip: Application of the collective-coordinate approach," Phys. Rev. B **78**, 134412.

Cohen, Aron J., Paula Mori-Sanchez, and Weito Yang, 2008, "Insights into Current Limitations of Density Functional Theory," Science **321**, 792.

Collet, M., *et al.*, 2016, "Generation of coherent spin-wave modes in yttrium iron garnet microdiscs by spin-orbit torque," Nat. Commun. **7**, 10377.

Cormier, M., A. Mougin, J. Ferré, A. Thiaville, N. Charpentier, F. Piéchon, R. Weil, V. Baltz, and B. Rodmacq, 2010, "Effect of electrical current pulses on domain walls in Pt/Co/Pt nanotracks with out-of-plane anisotropy: Spin transfer torque versus Joule heating," Phys. Rev. B **81**, 024407.

Cornelissen, L. J., J. Liu, R. A. Duine, J. Ben Youssef, and B. J. Van Wees, 2015, "Long-distance transport of magnon spin information in a magnetic insulator at room temperature," Nat. Phys. **11**, 1022.

Cowburn, R. P., and M. E. Welland, 2000, "Room Temperature Magnetic Quantum Cellular Automata," Science **287**, 1466.

Cubukcu, Murat, Olivier Boulle, Marc Drouard, Kevin Garello, Can Onur Avci, Ioan Mihai Miron, Juergen Langer, Berthold Ocker, Pietro Gambardella, and Gilles Gaudin, 2014, "Spin-orbit torque magnetization switching of a three-terminal perpendicular magnetic tunnel junction," Appl. Phys. Lett. **104**, 042406.

Cubukcu, Murat, *et al.*, 2018, "Ultra-fast perpendicular Spin Orbit Torque MRAM," IEEE Trans. Magn. **54**, 9300204.

Decker, M. M., M. S. Wörnle, A. Meisinger, M. Vogel, H. S. Körner, G. Y. Shi, C. Song, M. Kronseder, and C. H. Back, 2017, "Time Resolved Measurements of the Switching Trajectory of Pt/Co Elements Induced by Spin-Orbit Torques," Phys. Rev. Lett. **118**, 257201.

Demasius, Kai-Uwe, Timothy Phung, Weifeng Zhang, Brian P. Hughes, See-Hun Yang, Andrew Kellock, Wei Han, Aakash Pushp, and Stuart S. P. Parkin, 2016, "Enhanced spin orbit torques by oxygen incorporation in tungsten films," Nat. Commun. **7**, 10644.

Demidov, V. E., H. Ulrichs, S. V. Gurevich, S. O. Demokritov, V. S. Tiberkevich, A. N. Slavin, A. Zholud, and S. Urazhdin, 2014, "Synchronization of spin Hall nano-oscillators to external microwave signals," Nat. Commun. **5**, 3179.

Demidov, V. E., S. Urazhdin, G. De Loubens, O. Klein, V. Cros, and A. Anane, 2017, "Magnetization oscillations and waves driven by pure spin currents," Phys. Rep. **673**, 1.

Demidov, V. E., S. Urazhdin, A. B. Rinkevich, G. Reiss, and S. O. Demokritov, 2014, "Spin Hall controlled magnonic microwaveguides," Appl. Phys. Lett. **104**, 152402.

Demidov, V. E., Sergei Urazhdin, Henning Ulrichs, Vasyl Tiberkevich, Andrei Slavin, Dietmar Baither, Guido Schmitz, and S. O. Demokritov, 2012, "Magnetic nano-oscillator driven by pure spin current," Nat. Mater. **11**, 1028.

Demidov, Vladislav E., Sergei Urazhdin, and Sergej O. Demokritov, 2010, "Direct observation and mapping of spin waves emitted by spin-torque nano-oscillators," Nat. Mater. **9**, 984.

Deorani, Praveen, Jaesung Son, Karan Banerjee, Nikesh Koirala, Matthew Brahlek, Seongshik Oh, and Hyunsoo Yang, 2014, "Observation of inverse spin Hall effect in bismuth selenide," Phys. Rev. B **90**, 094403.

Devolder, T., J. Hayakawa, K. Ito, H. Takahashi, S. Ikeda, P. Crozat, N. Zerounian, Joo Von Kim, C. Chappert, and H. Ohno, 2008, "Single-shot time-resolved measurements of nanosecond-scale spin-transfer induced switching: Stochastic versus deterministic aspects," Phys. Rev. Lett. **100**, 057206.

Dieny, B., and M. Chshiev, 2017, "Perpendicular magnetic anisotropy at transition metal/oxide interfaces and applications," Rev. Mod. Phys. **89**, 025008.

Dolui, Kapildeb, and Branislav K. Nikolic, 2017, "Spin-memory loss due to spin-orbit coupling at ferromagnet/heavy-metal interfaces: Ab initio spin-density matrix approach," Phys. Rev. B **96**, 220403(R).

Duan, Zheng, Carl T. Boone, Xiao Cheng, Ilya N. Krivorotov, Nathalie Reckers, Sven Stienen, Michael Farle, and Jürgen Lindner, 2014, "Spin-wave modes in permalloy/platinum wires and tuning

of the mode damping by spin Hall current," Phys. Rev. B **90**, 024427.

Duan, Zheng, Andrew Smith, Liu Yang, Brian Youngblood, Jürgen Lindner, Vladislav E. Demidov, Sergej O. Demokritov, and Ilya N. Krivorotov, 2014, "Nanowire spin torque oscillator driven by spin orbit torques," Nat. Commun. **5**, 5616.

DuttaGupta, S., S. Fukami, C. Zhang, H. Sato, M. Yamanouchi, F. Matsukura, and H. Ohno, 2016, "Adiabatic spin-transfer-torque-induced domain wall creep in a magnetic metal," Nat. Phys. **12**, 333.

D'yakonov, M. I., and V. I. Perel, 1971, "Possibility of Orienting Electron Spins with Current," J. Exp. Theor. Phys. Lett. **13**, 467 [http://adsabs.harvard.edu/abs/1971JETPL..13..467D].

Dyakonov, M. I., 2008, Ed., *Spin Physics in Semiconductors*, Springer Series in Solid-State Sciences Vol. 157 (Springer-Verlag, Berlin) [https://www.springer.com/gp/book/9783540788195].

D'yakonov, M. I., V. A. Marushchak, V. I. Perel, and A. N. Titkov, 1986, "The effect of strain on the spin relaxation of conduction electrons in III-V semiconductors," Zh. Eksp. Teor. Fiz. **90**, 1123 [http://jetp.ac.ru/cgi-bin/dn/e_063_03_0655.pdf].

Dyakonov, M. I., and V. I. Perel, 1971, "Current-induced spin orientation of electrons in semiconductors," Phys. Lett. A **35**, 459.

Dyrdał, A., and J. Barnas, 2015, "Current-induced spin polarization and spin-orbit torque in graphene," Phys. Rev. B **92**, 165404.

Dzyaloshinskii, I. E., 1957, "Thermodynamic theory of weak ferromagnetism in antiferromagnetic substances," Sov. Phys. JETP **5**, 1259 [http://www.jetp.ac.ru/cgi-bin/e/index/e/5/6/p1259?a=list].

Edelstein, V. M., 1990, "Spin Polarization of conduction electrons induced by electric current in two-dimensional asymmetric electron systems," Solid State Commun. **73**, 233.

Einstein, A., and W. J. de Haas, 1915, "Experimenteller Nachweis der Ampereschen Molekularströme," Deutsche Physikalische Gesellschaft **17**, 152 [http://adsabs.harvard.edu/abs/1915DPhyG. .17..152E].

Emori, Satoru, Uwe Bauer, Sung-Min Ahn, Eduardo Martinez, and Geoffrey S. D. Beach, 2013, "Current-driven dynamics of chiral ferromagnetic domain walls," Nat. Mater. **12**, 611.

Emori, Satoru, Uwe Bauer, Seonghoon Woo, and Geoffrey S. D. Beach, 2014, "Large voltage-induced modification of spin-orbit torques in Pt/Co/GdOx," Appl. Phys. Lett. **105**, 222401.

Emori, Satoru, Tianxiang Nan, Amine M. Belkessam, Xinjun Wang, Alexei D. Matyushov, Christopher J. Babroski, Yuan Gao, Hwaider Lin, and Nian X. Sun, 2016, "Interfacial spin-orbit torque without bulk spin-orbit coupling," Phys. Rev. B **93**, 180402.

Endo, M., F. Matsukura, and H. Ohno, 2010, "Current induced effective magnetic field and magnetization reversal in uniaxial anisotropy (Ga,Mn)As," Appl. Phys. Lett. **97**, 222501.

Engel, H.-A., Bertrand Halperin, and Emmanuel Rashba, 2005, "Theory of Spin Hall Conductivity in n-Doped GaAs," Phys. Rev. Lett. **95**, 166605.

Eremeev, Sergey V., Stepan S. Tsirkin, Ilya A. Nechaev, and Pedro M. Echenique, 2015, "New generation of two- dimensional spintronic systems realized by coupling of Rashba and Dirac fermions," Sci. Rep. **5**, 12819.

Evelt, M., *et al.*, 2018, "Emission of Coherent Propagating Magnons by Insulator-Based Spin-Orbit-Torque Oscillators," Phys. Rev. Applied **10**, 041002.

Fan, Xin, Halise Celik, Jun Wu, Chaoying Ni, Kyung-Jin Lee, Virginia O. Lorenz, and John Q. Xiao, 2014, "Quantifying interface and bulk contributions to spin-orbit torque in magnetic bilayers," Nat. Commun. **5**, 3042.

Fan, Xin, Jun Wu, Yunpeng Chen, Matthew J. Jerry, Huaiwu Zhang, and John Q. Xiao, 2013, "Observation of the nonlocal spin-orbital effective field," Nat. Commun. **4**, 1799.

Fan, Yabin, and Kang L. Wang, 2016, "Spintronics Based on Topological Insulators," SPIN **06**, 1640001.

Fan, Yabin, *et al.*, 2014, "Magnetization switching through giant spin-orbit torque in a magnetically doped topological insulator heterostructure," Nat. Mater. **13**, 699.

Fan, Yabin, *et al.*, 2016, "Electric-field control of spin-orbit torque in a magnetically doped topological insulator," Nat. Nanotechnol. **11**, 352.

Fang, D., H. Kurebayashi, J. Wunderlich, K. Výborný, Liviu P. Zârbo, R. P. Campion, A. Casiraghi, B. L. Gallagher, T. Jungwirth, and A. J. Ferguson, 2011, "Spin-orbit-driven ferromagnetic resonance," Nat. Nanotechnol. **6**, 413.

Feldtkeller, E., 1968, "Magnetic Domain Wall Dynamics," Phys. Status Solidi B **27**, 161.

Fert, A., 1990, "Magnetic and Transport Properties of Metallic Multilayers," Mater. Sci. Forum **59–60**, 439.

Fert, Albert, Vincent Cros, and Joao Sampaio, 2013, "Skyrmions on the track," Nat. Nanotechnol. **8**, 152.

Fert, Albert, Nicolas Reyren, and Vincent Cros, 2017, "Magnetic skyrmions: advances in physics and potential applications," Nat. Rev. Mater. **2**, 17031.

Finley, Joseph, and Luqiao Liu, 2016, "Spin-Orbit-Torque Efficiency in Compensated Ferrimagnetic Cobalt-Terbium Alloys," Phys. Rev. Applied **6**, 054001.

Finocchio, G., M. Carpentieri, E. Martinez, and B. Azzerboni, 2013, "Switching of a single ferromagnetic layer driven by spin Hall effect," Appl. Phys. Lett. **102**, 212410.

Fischer, Mark H., Abolhassan Vaezi, Aurelien Manchon, and Eun-ah Kim, 2016, "Spin-torque generation in topological insulator based heterostructures," Phys. Rev. B **93**, 125303.

Forster, R. H., G. B. Johnston, and D. A. Wheeler, 1968, "Studies on the heusler alloys III. The antiferro-magnetic phase in the Cu-Mn-Sb system," J. Phys. Chem. Solids **29**, 855.

Franken, J. H., M. Herps, H. J. M. Swagten, and B. Koopmans, 2014, "Tunable chiral spin texture in magnetic domain-walls," Sci. Rep. **4**, 5248.

Freimuth, Frank, Stefan Blügel, and Yuriy Mokrousov, 2010, "Anisotropic Spin Hall Effect from First Principles," Phys. Rev. Lett. **105**, 246602.

Freimuth, Frank, Stefan Blügel, and Yuriy Mokrousov, 2014a, "Berry phase theory of Dzyaloshinskii-Moriya interaction and spin-orbit torques," J. Phys. Condens. Matter **26**, 104202.

Freimuth, Frank, Stefan Blügel, and Yuriy Mokrousov, 2014b, "Spin-orbit torques in Co/Pt(111) and Mn/W(001) magnetic bilayers from first principles," Phys. Rev. B **90**, 174423.

Freimuth, Frank, Stefan Blügel, and Yuriy Mokrousov, 2015, "Direct and inverse spin-orbit torques," Phys. Rev. B **92**, 064415.

Freimuth, Frank, Stefan Blügel, and Yuriy Mokrousov, 2017, "Chiral damping, chiral gyromagnetism, and current-induced torques in textured one-dimensional Rashba ferromagnets," Phys. Rev. B **96**, 104418.

Freimuth, Frank, Stefan Blügel, and Yuriy Mokrousov, 2018, "Spin-orbit torques and tunable Dzyaloshinskii-Moriya interaction in Co/Cu/Co trilayers," Phys. Rev. B **98**, 024419.

Fuchs, K., 1938, "The conductivity of thin metallic films according to the electron theory of metals," Math. Proc. Cambridge Philos. Soc. **34**, 100.

Fujimoto, Junji, and Hiroshi Kohno, 2014, "Transport properties of Dirac ferromagnet," Phys. Rev. B **90**, 214418.

Fujiwara, Kohei, Yasuhiro Fukuma, Jobu Matsuno, Hiroshi Idzuchi, Yasuhiro Niimi, Yoshichika Otani, and Hidenori Takagi, 2013, "5d Iridium Oxide As a Material for Spin-Current Detection," Nat. Commun. **4**, 2893.

Fukami, S., T. Anekawa, C. Zhang, and H. Ohno, 2016, "A spin-orbit torque switching scheme with collinear magnetic easy axis and current configuration," Nat. Nanotechnol. **11**, 621.

Fukami, S., T. Suzuki, N. Ohshima, K. Nagahara, and N. Ishiwata, 2008, "Micromagnetic analysis of current driven domain wall motion in nanostrips with perpendicular magnetic anisotropy," J. Appl. Phys. **103**, 07E718.

Fukami, Shunsuke, and Hideo Ohno, 2017, "Magnetization switching schemes for nanoscale three-terminal spintronics devices," Jpn. J. Appl. Phys. **56**, 0802A1.

Fukami, Shunsuke, Chaoliang Zhang, Samik DuttaGupta, and Hideo Ohno, 2016, "Magnetization switching by spin-orbit torque in an antiferromagnet/ferromagnet bilayer system," Nat. Mater. **15**, 535.

Gambardella, Pietro, and Ioan Mihai Miron, 2011, "Current-induced spin-orbit torques," Phil. Trans. R. Soc. A **369**, 3175.

Ganichev, S., E. Ivchenko, S. Danilov, J. Eroms, W. Wegscheider, D. Weiss, and W. Prettl, 2001, "Conversion of Spin into Directed Electric Current in Quantum Wells," Phys. Rev. Lett. **86**, 4358.

Ganichev, S. D., S. N. Danilov, Petra Schneider, V. V. Bel'kov, L. E. Golub, W. Wegscheider, D. Weiss, and W. Prettl, 2004, "Can an electric current orient spins in quantum wells?," arXiv:cond-mat/0403641.

Ganichev, S. D., E. L. Ivchenko, V. V. Bel'kov, S. A. Tarasenko, M. Sollinger, D. Weiss, W. Wegscheider, and W. Prettl, 2002, "Spin-galvanic effect," Nature (London) **417**, 153.

Ganichev, S. D., *et al.*, 2004, "Experimental Separation of Rashba and Dresselhaus Spin Splittings in Semiconductor Quantum Wells," Phys. Rev. Lett. **92**, 256601.

Garate, Ion, and M. Franz, 2010, "Inverse Spin-Galvanic Effect in the Interface between a Topological Insulator and a Ferromagnet," Phys. Rev. Lett. **104**, 146802.

Garate, Ion, and A. H. MacDonald, 2009, "Influence of a transport current on magnetic anisotropy in gyrotropic ferromagnets," Phys. Rev. B **80**, 134403.

Garello, K., F. Yasin, S. Couet, L. Souriau, J. Swerts, S. Rao, S. Van Beek, W. Kim, E. Liu, and S. Kundu, 2018, "SOT-MRAM 300 mm integration for low power and ultrafast embedded memories," *2018 IEEE Symposium on VLSI Circuits* (IEEE, New York), pp. 81–82 [https://doi.org/10.1109/VLSIC.2018.8502269].

Garello, Kevin, Can Onur Avci, Ioan Mihai Miron, Manuel Baumgartner, Abhijit Ghosh, S. Auffret, Olivier Boulle, Gilles Gaudin, and Pietro Gambardella, 2014, "Ultrafast magnetization switching by spin-orbit torques," Appl. Phys. Lett. **105**, 212402.

Garello, Kevin, Abhijit Ghosh, Can Onur Avci, and Pietro Gambardella, 2017 (unpublished).

Garello, Kevin, Ioan Mihai Miron, Can Onur Avci, Frank Freimuth, Yuriy Mokrousov, Stefan Blügel, S. Auffret, Olivier Boulle, Gilles Gaudin, and Pietro Gambardella, 2013, "Symmetry and magnitude of spin-orbit torques in ferromagnetic heterostructures," Nat. Nanotechnol. **8**, 587.

Géranton, Guillaume, Frank Freimuth, Stefan Blügel, and Yuriy Mokrousov, 2015, "Spin-orbit torques in L10-FePt/Pt thin films driven by electrical and thermal currents," Phys. Rev. B **91**, 014417.

Géranton, Guillaume, Bernd Zimmermann, Nguyen H. Long, Phivos Mavropoulos, Stefan Blügel, Frank Freimuth, and Yuriy Mokrousov, 2016, "Spin-orbit torques and spin accumulation in FePt/Pt and Co/Cu thin films from first principles: The role of impurities," Phys. Rev. B **93**, 224420.

Ghosh, Abhijit, Kevin Garello, Can Onur Avci, Mihai Gabureac, and Pietro Gambardella, 2017, "Interface-Enhanced Spin-Orbit

Torques and Current-Induced Magnetization Switching of Pd/Co/AlOx Layers," Phys. Rev. Applied **7**, 014004.

Ghosh, S., and A. Manchon, 2017, "Spin-orbit torque in two-dimensional antiferromagnetic topological insulators," Phys. Rev. B **95**, 035422.

Ghosh, Sumit, and Aurelien Manchon, 2018, "Spin-orbit torque in 3D topological insulator-ferromagnet heterostructure: crossover between bulk and surface transport," Phys. Rev. B **97**, 134402.

Go, Dongwook, Daegeun Jo, Changyoung Kim, and Hyun Woo Lee, 2018, "Intrinsic Spin and Orbital Hall Effects from Orbital Texture," Phys. Rev. Lett. **121**, 086602.

Go, Dongwook, and Hyun-woo Lee, 2019, "Orbital Torque: Torque Generation by Orbital Current Injection," arXiv:1903.01085v1.

Godinho, J., *et al.*, 2018, "Electrically induced and detected Néel vector reversal in a collinear antiferromagnet," Nat. Commun. **9**, 4686.

Goennenwein, Sebastian T. B., Richard Schlitz, Matthias Pernpeintner, Kathrin Ganzhorn, Matthias Althammer, Rudolf Gross, and Hans Huebl, 2015, "Non-local magnetoresistance in YIG/Pt nanostructures," Appl. Phys. Lett. **107**, 172405.

Gomonay, E. V., and Vadim Loktev, 2014, "Spintronics of antiferromagnetic systems (Review Article)," Low Temp. Phys. **40**, 17.

Gomonay, Helen V., Roman V. Kunitsyn, and Vadim M. Loktev, 2012, "Symmetry and the macroscopic dynamics of antiferromagnetic materials in the presence of spin-polarized current," Phys. Rev. B **85**, 134446.

Gomonay, Helen V. , and Vadim M. Loktev, 2010, "Spin transfer and current-induced switching in antiferromagnets," Phys. Rev. B **81**, 144427.

Gomonay, Olena, T. Jungwirth, and J. Sinova, 2016, "High Antiferromagnetic Domain Wall Velocity Induced by Néel Spin-Orbit Torques," Phys. Rev. Lett. **117**, 017202.

Gorchon, J., S. Bustingorry, J. Ferré, V. Jeudy, A. B. Kolton, and T. Giamarchi, 2014, "Pinning-Dependent Field-Driven Domain Wall Dynamics and Thermal Scaling in an Ultrathin Pt/Co/Pt Magnetic Film," Phys. Rev. Lett. **113**, 027205.

Gould, C., C. Rüster, T. Jungwirth, E. Girgis, G. Schott, R. Giraud, K. Brunner, G. Schmidt, and L. Molenkamp, 2004, "Tunneling Anisotropic Magnetoresistance: A Spin-Valve-Like Tunnel Magnetoresistance Using a Single Magnetic Layer," Phys. Rev. Lett. **93**, 117203.

Grimmer, H., 1993, "General relations for transport properties in magnetically ordered crystals," Acta Crystallogr. Sect. A **49**, 763.

Grytsyuk, Sergiy, Abderrezak Belabbes, Paul M. Haney, Hyun Woo Lee, Kyung Jin Lee, M. D. Stiles, Udo Schwingenschlögl, and Aurelien Manchon, 2016, "k-asymmetric spin splitting at the interface between transition metal ferromagnets and heavy metals," Phys. Rev. B **93**, 174421.

Grzybowski, M. J., *et al.*, 2017, "Imaging current-induced switching of antiferromagnetic domains in CuMnAs," Phys. Rev. Lett. **118**, 057701.

Guo, Wei, Guillaume Prenat, and Bernard Dieny, 2014, "A novel architecture of non-volatile magnetic arithmetic logic unit using magnetic tunnel junctions," J. Phys. D **47**, 165001.

Gweon, Hyung Keun, Kyung-jin Lee, and Sang Ho Lim, 2019, "Influence of MgO Sputtering Power and Post annealing on Strength and Angular Dependence of Spin-Orbit Torques in Pt/Co/MgO Trilayers," Phys. Rev. Applied **11**, 014034.

Haazen, P. P. J., E. Murè, J. H. Franken, R. Lavrijsen, H. J. M. Swagten, and B. Koopmans, 2013, "Domain wall depinning governed by the spin Hall effect," Nat. Mater. **12**, 299.

Hahn, Christian, Georg Wolf, Bartek Kardasz, Steve Watts, Mustafa Pinarbasi, and Andrew D. Kent, 2016, "Time-Resolved Studies of the Spin-Transfer Reversal Mechanism in Perpendicularly Magnetized Magnetic Tunnel Junctions," Phys. Rev. B **94**, 214432.

Hals, Kjetil, and Arne Brataas, 2013a, "Phenomenology of current-induced spin-orbit torques," Phys. Rev. B **88**, 085423.

Hals, Kjetil, and Arne Brataas, 2013b, "Spin-transfer torques in helimagnets," Phys. Rev. B **87**, 174409.

Hals, Kjetil, Arne Brataas, and Yaroslav Tserkovnyak, 2010, "Scattering theory of charge-current induced magnetization dynamics," Europhys. Lett. **90**, 47002.

Ham, Woo Seung, Sanghoon Kim, Duck-Ho Kim, Kab-Jin Kim, Takaya Okuno, Hiroki Yoshikawa, Arata Tsukamoto, Takahiro Moriyama, and Teruo Ono, 2017, "Temperature dependence of spin-orbit effective fields in Pt/GdFeCo bilayers," Appl. Phys. Lett. **110**, 242405.

Hamadeh, A., *et al.*, 2014, "Electronic control of the spin-wave damping in a magnetic insulator," Phys. Rev. Lett. **113**, 197203.

Han, Jiahao, A. Richardella, Saima A. Siddiqui, Joseph Finley, N. Samarth, and Luqiao Liu, 2017, "Room-Temperature Spin-Orbit Torque Switching Induced by a Topological Insulator," Phys. Rev. Lett. **119**, 077702.

Haney, P. M., H.-W. Lee, K.-J. Lee, A. Manchon, and M. D. Stiles, 2013, "Current induced torques and interfacial spin-orbit coupling: Semiclassical modeling," Phys. Rev. B **87**, 174411.

Haney, Paul M., R. A. Duine, A. S. Núñez, and A. H. MacDonald, 2008, "Current-induced torques in magnetic metals: Beyond spin-transfer," J. Magn. Magn. Mater. **320**, 1300.

Haney, Paul M., Hyun Woo Lee, Kyung Jin Lee, Aurélien Manchon, and M. D. Stiles, 2013, "Current-induced torques and interfacial spin-orbit coupling," Phys. Rev. B **88**, 214417.

Haney, Paul M., and M. D. Stiles, 2010, "Current-Induced Torques in the Presence of Spin-Orbit Coupling," Phys. Rev. Lett. **105**, 126602.

Hanyu, Takahiro, Tetsuo Endoh, Daisuke Suzuki, Hiroki Koike, Yitao Ma, Naoya Onizawa, Masanori Natsui, Shoji Ikeda, and Hideo Ohno, 2016, "Standby-Power-Free Integrated Circuits Using MTJ-Based VLSI Computing," Proc. IEEE **104**, 1844.

Hao, Qiang, and Gang Xiao, 2015, "Giant Spin Hall Effect and Switching Induced by Spin-Transfer Torque in a W/Co40Fe40B20/MgO Structure with Perpendicular Magnetic Anisotropy," Phys. Rev. Applied **3**, 034009.

Harder, M., Z. X. Cao, Y. S. Gui, X. L. Fan, and C.-M. Hu, 2011, "Analysis of the line shape of electrically detected ferromagnetic resonance," Phys. Rev. B **84**, 054423.

Harder, Michael, Yongsheng Gui, and Can-ming Hu, 2016, "Electrical detection of magnetization dynamics via spin rectification effects," Phys. Rep. **661**, 1.

Hasan, M. Z., and C. Kane, 2010, "Colloquium: Topological insulators," Rev. Mod. Phys. **82**, 3045.

Hasan, M. Zahid, and Joel E. Moore, 2011, "Three-Dimensional Topological Insulators," Annu. Rev. Condens. Matter Phys. **2**, 55.

Hayashi, Masamitsu, Junyeon Kim, Michihiko Yamanouchi, and Hideo Ohno, 2014, "Quantitative characterization of the spin-orbit torque using harmonic Hall voltage measurements," Phys. Rev. B **89**, 144425.

He, Liang, Xufeng Kou, and Kang L. Wang, 2013, "Review of 3D topological insulator thin-film growth by molecular beam epitaxy and potential applications," Phys. Status Solidi RRL **7**, 50.

Heide, M., G. Bihlmayer, and Stefan Blügel, 2008, "Dzyaloshinskii-Moriya interaction accounting for the orientation of magnetic domains in ultrathin films: Fe/W(110)," Phys. Rev. B **78**, 140403.

Hellman, Frances, *et al.*, 2017, "Interface-induced phenomena in magnetism," Rev. Mod. Phys. **89**, 025006.

Herring, C., 1966, "Magnetism: Exchange interactions among itinerant electrons," in *Magnetism*, edited by George Tibor Rado and Harry Suhl (Academic Press, New York), p. 407.

Hibino, Y., T. Hirai, K. Hasegawa, T. Koyama, and D. Chiba, 2017, "Enhancement of the spin-orbit torque in a Pt/Co system with a naturally oxidized Co layer," Appl. Phys. Lett. **111**, 132404.

Hirata, Yuushou, *et al.*, 2018, "Correlation between compensation temperatures of magnetization and angular momentum in GdFeCo ferrimagnets," Phys. Rev. B **97**, 220403.

Hiroshi, Idzuchi, Yasuhiro Fukuma, and Yoshichika Otani, 2015, "Spin transport in non-magnetic nano-structures induced by non-local spin injection," Physica E (Amsterdam) **68**, 239.

Hirsch, J., 1999, "Spin Hall Effect," Phys. Rev. Lett. **83**, 1834.

Honolka, J., *et al.*, 2012, "In-plane magnetic anisotropy of Fe atoms on Bi2Se3(111)," Phys. Rev. Lett. **108**, 256811.

Hou, Dazhi, *et al.*, 2012, "Interface induced inverse spin Hall effect in bismuth/permalloy bilayer," Appl. Phys. Lett. **101**, 042403.

Hrabec, Ales, Joao Sampaio, Mohamed Belmeguenai, Isabell Gross, Raphael Weil, Salim Mourad Chérif, Andrei Stachkevitch, Vincent Jacques, Andre Thiaville, and Stanislas Rohart, 2017, "Current-induced skyrmion generation and dynamics in symmetric bilayers," Nat. Commun. **8**, 15765.

Hubert, A., and R. Schäfer, 1998, *Magnetic Domains* (Springer-Verlag, Berlin).

Humphries, Alisha M., Tao Wang, Eric R. J. Edwards, Shane R. Allen, Justin M. Shaw, Hans T. Nembach, John Q. Xiao, T. J. Silva, and Xin Fan, 2017, "Observation of spin-orbit effects with spin rotation symmetry," Nat. Commun. **8**, 911.

Hupfauer, T., A. Matos-Abiague, M. Gmitra, F. Schiller, J. Loher, D. Bougeard, C. H. Back, J. Fabian, and D. Weiss, 2015, "Emergence of spin orbit fields in magnetotransport of quasi-two-dimensional iron on gallium arsenide," Nat. Commun. **6**, 7374.

Inoue, Jun-ichiro, G. E. W. Bauer, and Laurens Molenkamp, 2004, "Suppression of the persistent spin Hall current by defect scattering," Phys. Rev. B **70**, 041303.

Inoue, Jun-ichiro, Gerrit E. W. Bauer, and Laurens W. Molenkamp, 2003, "Diffuse transport and spin accumulation in a Rashba two-dimensional electron gas," Phys. Rev. B **67**, 033104.

Isasa, Miren, *et al.*, 2016, "Origin of inverse Rashba-Edelstein effect detected at the Cu/Bi interface using lateral spin valves," Phys. Rev. B **93**, 014420.

Ivchenko, E. L., and S. D. Ganichev, 2008, "Spin-photogalvanic," in *Spin Physics in Semiconductors*, edited by M. I. Dyakonov (Springer, New York), p. 245.

Ivchenko, E. L., Y. B. Lyanda-Geller, and G. E. Pikus, 1989, "Photocurrent in structures with quantum wells with an optical orientation of free carriers," JETP Lett. **50**, 175 [http://adsabs.harvard.edu/abs/1989JETPL..50..175I].

Ivchenko, E. L., and G. E. Pikus, 1978, "New photogalvanic effect in gyrotropic crystals," Pis'ma Zh. Eksp. Teor. Fiz. **27**, 604 [http://adsabs.harvard.edu/abs/1978JETPL..27..604I].

Iwasaki, Junichi, Masahito Mochizuki, and Naoto Nagaosa, 2013a, "Current-induced skyrmion dynamics in constricted geometries," Nat. Nanotechnol. **8**, 742.

Iwasaki, Junichi, Masahito Mochizuki, and Naoto Nagaosa, 2013b, "Universal current-velocity relation of skyrmion motion in chiral magnets," Nat. Commun. **4**, 1463.

Jabeur, Kotb, G. Di Pendina, F. Bernard-Granger, and G. Prenat, 2014, "Spin Orbit Torque Non-Volatile Flip-Flop for High Speed and Low Energy Applications," IEEE Electron Device Lett. **35**, 408.

Jamali, Mahdi, Joon Sue Lee, Jong Seok Jeong, Farzad Mahfouzi, Yang Lv, Zhengyang Zhao, Branislav Nikolic, K. Andre Mkhoyan, Nitin Samarth, and Jian-Ping Wang, 2015, "Giant Spin Pumping and Inverse Spin Hall Effect in the Presence of Surface Spin-Orbit Coupling of Topological Insulator Bi2Se3," Nano Lett. **15**, 7126.

Jamali, Mahdi, Kulothungasagaran Narayanapillai, Xuepeng Qiu, Li Ming Loong, Aurelien Manchon, and Hyunsoo Yang, 2013, "Spin-orbit torques in Co/Pd multilayer nanowires," Phys. Rev. Lett. **111**, 246602.

Je, Soong-Geun, *et al.*, 2018, "Spin-orbit torque-induced switching in ferrimagnetic alloys: Experiments and modeling," Appl. Phys. Lett. **112**, 062401.

Jenkins, D., *et al.*, 2003, "Advanced optical and magneto-optical recording techniques: a review," Microsyst. Technol. **10**, 66.

Jeudy, V., A. Mougin, S. Bustingorry, W. Savero Torres, J. Gorchon, A. B. Kolton, A. Lemaître, and J. P. Jamet, 2016, "Universal Pinning Energy Barrier for Driven Domain Walls in Thin Ferromagnetic Films," Phys. Rev. Lett. **117**, 057201.

Jiang, Wanjun, Gong Chen, Kai Liu, Jiadong Zang, Suzanne G. E. te Velthuis, and Axel Hoffmann, 2017, "Skyrmions in magnetic multilayers," Phys. Rep. **704**, 1.

Jiang, Wanjun, *et al.*, 2015, "Blowing magnetic skyrmion bubbles," Science **349**, 283.

Jiang, Wanjun, *et al.*, 2017, "Direct Observation of the Skyrmion Hall Effect," Nat. Phys. **13**, 162.

Jones, R. O., 2015, "Density functional theory: Its origins, rise to prominence, and future," Rev. Mod. Phys. **87**, 897.

Jonietz, F., *et al.*, 2010, "Spin transfer torques in MnSi at ultralow current densities," Science **330**, 1648.

Jué, E., *et al.*, 2016, "Domain wall dynamics in ultrathin Pt/Co/AlOx microstrips under large combined magnetic fields," Phys. Rev. B **93**, 014403.

Jué, Emilie, C. K. Safeer, Marc Drouard, Alexandre Lopez, and Paul Balint, 2016, "Chiral damping of magnetic domain walls," Nat. Mater. **15**, 272.

Jungfleisch, M. B., W. Zhang, J. Sklenar, W. Jiang, J. E. Pearson, J. B. Ketterson, and A. Hoffmann, 2016, "Interface-driven spin-torque ferromagnetic resonance by Rashba coupling at the interface between non-magnetic materials," Phys. Rev. B **93**, 224419.

Jungwirth, T., X. Marti, P. Wadley, and J. Wunderlich, 2016, "Antiferromagnetic spintronics," Nat. Nanotechnol. **11**, 231.

Jungwirth, T., J. Sinova, A. Manchon, X. Marti, J. Wunderlich, and C. Felser, 2018, "The multiple directions of antiferromagnetic spintronics," Nat. Phys. **14**, 200.

Kajiwara, Y., *et al.*, 2010, "Transmission of electrical signals by spin-wave interconversion in a magnetic insulator," Nature (London) **464**, 262.

Kane, C. L., and E. J. Mele, 2005, "Quantum Spin Hall Effect in Graphene," Phys. Rev. Lett. **95**, 226801.

Kang, Wang, Zhaohao Wang, Youguang Zhang, Jacques-Olivier Klein, Weifeng Lv, and Weisheng Zhao, 2016, "Spintronic logic design methodology based on spin Hall effect driven magnetic tunnel junctions," J. Phys. D **49**, 065008.

Karube, Shutaro, Kouta Kondou, and Yoshi Chika Otani, 2016, "Experimental observation of spin-to-charge current conversion at non-magnetic metal/Bi2O3 interfaces," Appl. Phys. Express **9**, 033001.

Katmis, Ferhat, *et al.*, 2016, "A high-temperature ferromagnetic topological insulating phase by proximity coupling," Nature (London) **533**, 513.

Kato, Y., Y. Saito, H. Yoda, T. Inokuchi, S. Shirotori, N. Shimomura, S. Oikawa, and A. Tiwari, 2018, "Improvement of Write Efficiency in Voltage-Controlled Spintronic Memory by development of a Ta-B Spin Hall Electrode," Phys. Rev. Applied **10**, 044011.

Kato, Y. K., R. Myers, A. Gossard, and D. D. Awschalom, 2004a, "Current-Induced Spin Polarization in Strained Semiconductors," Phys. Rev. Lett. **93**, 176601.

Kato, Y. K., R. C. Myers, A. C. Gossard, and D. D. Awschalom, 2004b, "Observation of the spin Hall effect in semiconductors," Science **306**, 1910.

Kato, Yuichiro K., and David D. Awschalom, 2008, "Electrical manipulation of spins in nonmagnetic semiconductors," J. Phys. Soc. Jpn. **77**, 031006.

Kent, A. D., B. Özyilmaz, and E. Del Barco, 2004, "Spin-transfer-induced precessional magnetization reversal," Appl. Phys. Lett. **84**, 3897.

Kent, Andrew D., and Daniel C. Worledge, 2015, "A new spin on magnetic memories," Nat. Nanotechnol. **10**, 187.

Khang, Nguyen Huynh Duy, Yugo Ueda, and Pham Nam Hai, 2018, "A conductive topological insulator with large spin Hall effect for ultralow power spin orbit torque switching," Nat. Mater. **17**, 808.

Khvalkovskiy, A. V., V. Cros, D. Apalkov, V. Nikitin, M. Krounbi, K. A. Zvezdin, A. Anane, J. Grollier, and A. Fert, 2013, "Matching domain-wall configuration and spin-orbit torques for efficient domain-wall motion," Phys. Rev. B **87**, 020402.

Khvalkovskiy, A. V., K. A. Zvezdin, Ya V. Gorbunov, V. Cros, J. Grollier, A. Fert, and A. K. Zvezdin, 2009, "High Domain Wall Velocities due to Spin Currents Perpendicular to the Plane," Phys. Rev. Lett. **102**, 067206.

Khymyn, Roman, Ivan Lisenkov, Vasyl Tiberkevich, Boris A. Ivanov, and Andrei Slavin, 2017, "Antiferromagnetic THz-frequency Josephson-like Oscillator Driven by Spin Current," Sci. Rep. **7**, 43705.

Kim, Joo Von, and Myoung Woo Yoo, 2017, "Current-driven skyrmion dynamics in disordered films," Appl. Phys. Lett. **110**, 132404.

Kim, Junyeon, Peng Sheng, Saburo Takahashi, Seiji Mitani, and Masamitsu Hayashi, 2016, "Spin Hall Magnetoresistance in Metallic Bilayers," Phys. Rev. Lett. **116**, 097201.

Kim, Junyeon, Jaivardhan Sinha, Masamitsu Hayashi, Michihiko Yamanouchi, Shunsuke Fukami, Tetsuhiro Suzuki, Seiji Mitani, and Hideo Ohno, 2013, "Layer thickness dependence of the current-induced effective field vector in Ta/CoFeB/MgO," Nat. Mater. **12**, 240.

Kim, Junyeon, Jaivardhan Sinha, Seiji Mitani, Masamitsu Hayashi, Saburo Takahashi, S. Maekawa, Michihiko Yamanouchi, and Hideo Ohno, 2014, "Anomalous temperature dependence of current-induced torques in CoFeB/MgO heterostructures with Ta-based underlayers," Phys. Rev. B **89**, 174424.

Kim, Kab-jin, *et al.*, 2017, "Fast domain wall motion in the vicinity of the angular momentum compensation temperature of ferrimagnets," Nat. Mater. **16**, 1187.

Kim, Kab-Jin, Jae-Chul Lee, Sung-Min Ahn, Kang-Soo Lee, Chang-Won Lee, Young Jin Cho, Sunae Seo, Kyung-Ho Shin, Sug-Bong Choe, and Hyun-Woo Lee, 2009, "Interdimensional universality of dynamic interfaces," Nature (London) **458**, 740.

Kim, Kyoung Whan, Kyung Jin Lee, Jairo Sinova, Hyun Woo Lee, and M. D. Stiles, 2017, "Spin-orbit torques from interfacial spin-orbit coupling for various interfaces," Phys. Rev. B **96**, 104438.

Kim, Kyoung-Whan, Hyun-Woo Lee, Kyung-Jin Lee, and M. D. Stiles, 2013, "Chirality from Interfacial Spin-Orbit Coupling Effects in Magnetic Bilayers," Phys. Rev. Lett. **111**, 216601.

Kim, Kyoung-Whan, Jung-Hwan Moon, Kyung-Jin Lee, and Hyun-Woo Lee, 2012, "Prediction of Giant Spin Motive Force due to Rashba Spin-Orbit Coupling," Phys. Rev. Lett. **108**, 217202.

Kim, Kyoung-Whan, Soo-Man Seo, Jisu Ryu, Kyung-Jin Lee, and Hyun-Woo Lee, 2012, "Magnetization dynamics induced by in-plane currents in ultrathin magnetic nanostructures with Rashba spin-orbit coupling," Phys. Rev. B **85**, 180404.

Kimata, Motoi, *et al.*, 2019, "Magnetic and magnetic inverse spin Hall effects in a non-collinear antiferromagnet," Nature (London) **565**, 627.

King, P. D. C., *et al.*, 2011, "Large Tunable Rashba Spin Splitting of a Two-Dimensional Electron Gas in Bi2Se3," Phys. Rev. Lett. **107**, 096802.

Kiselev, S. I., J. C. Sankey, I. N. Krivorotov, N. C. Emley, R. J. Schoelkopf, R. a. Buhrman, and D. C. Ralph, 2003, "Microwave oscillations of a nanomagnet driven by a spin-polarized current," Nature (London) **425**, 380.

Kobayashi, Tadashi, Hideaki Hayashi, Yuji Fujiwara, and Shigeru Shiomi, 2005, "Damping Parameter and Wall Velocity of RE-TM Films," IEEE Trans. Magn. **41**, 2848.

Kobs, A., S. Heße, W. Kreuzpaintner, G. Winkler, D. Lott, P. Weinberger, A. Schreyer, and H. P. Oepen, 2011, "Anisotropic Interface Magnetoresistance in Pt/Co/Pt Sandwiches," Phys. Rev. Lett. **106**, 217207.

Kondou, K., R. Yoshimi, A. Tsukazaki, Y. Fukuma, J. Matsuno, K. S. Takahashi, M. Kawasaki, Y. Tokura, and Y. Otani, 2016, "Fermi level dependent charge-to-spin current conversion by Dirac surface state of topological insulators," Nat. Phys. **12**, 1027.

Koyama, T., *et al.*, 2011, "Observation of the intrinsic pinning of a magnetic domain wall in a ferromagnetic nanowire," Nat. Mater. **10**, 194.

Krupin, O., G. Bihlmayer, K. Starke, S. Gorovikov, J. Prieto, K. Döbrich, Stefan Blügel, and G. Kaindl, 2005, "Rashba effect at magnetic metal surfaces," Phys. Rev. B **71**, 201403.

Kubota, Hitoshi, *et al.*, 2008, "Quantitative measurement of voltage dependence of spin-transfer torque in MgO-based magnetic tunnel junctions," Nat. Phys. **4**, 37.

Kurebayashi, H., *et al.*, 2014, "An antidamping spin-orbit torque originating from the Berry curvature," Nat. Nanotechnol. **9**, 211.

Kurenkov, A., C. Zhang, S. DuttaGupta, S. Fukami, and H. Ohno, 2017, "Device-size dependence of field-free spin-orbit torque induced magnetization switching in antiferromagnet / ferromagnet structures," Appl. Phys. Lett. **110**, 092410.

Kuroda, K., *et al.*, 2010, "Hexagonally Deformed Fermi Surface of the 3D Topological Insulator Bi 2 Se 3," Phys. Rev. Lett. **105**, 076802.

Kwon, Kon Woo, Sri Harsha Choday, Yusung Kim, Xuanyao Fong, Sang Phill Park, and Kaushik Roy, 2014, "SHE-NVFF: Spin hall effect-based nonvolatile flip-flop for power gating architecture," IEEE Electron Device Lett. **35**, 488.

Laczkowski, P., *et al.*, 2017, "Large enhancement of the spin Hall effect in Au by side-jump scattering on Ta impurities," Phys. Rev. B **96**, 140405(R).

Lang, Murong, *et al.*, 2014, "Proximity induced high-temperature magnetic order in topological insulator—Ferrimagnetic insulator heterostructure," Nano Lett. **14**, 3459.

Lau, Derek, Vignesh Sundar, Jian Gang Zhu, and Vincent Sokalski, 2016, "Energetic molding of chiral magnetic bubbles," Phys. Rev. B **94**, 060401(R).

Lau, Yong-Chang, Davide Betto, Karsten Rode, J. M. D. Coey, and Plamen Stamenov, 2016, "Spin-orbit torque switching without an external field using interlayer exchange coupling," Nat. Nanotechnol. **11**, 758.

Lavrijsen, R., P. P. J. Haazen, E. Murè, J. H. Franken, J. T. Kohlhepp, H. J. M. Swagten, B. Koopmans, R. Lavrijsen, P. P. J. Haazen, and E. Mure, 2012, "Asymmetric Pt/Co/Pt-stack induced sign-control

of current-induced magnetic domain-wall creep," Appl. Phys. Lett. **100**, 262408.

Lavrijsen, R., D. M. F. Hartmann, A. van den Brink, Y. Yin, B. Barcones, R. A. Duine, M. A. Verheijen, H. J. M. Swagten, and B. Koopmans, 2015, "Asymmetric magnetic bubble expansion under in-plane field in Pt/Co/Pt: Effect of interface engineering," Phys. Rev. B **91**, 104414.

Lebrun, R., A. Ross, S. A. Bender, A. Qaiumzadeh, L. Baldrati, J. Cramer, A. Brataas, R. A. Duine, and M. Kläui, 2018, "Tunable long-distance spin transport in a crystalline antiferromagnetic iron oxide," Nature (London) **561**, 222.

Lee, Hwang-Rae, Kyujoon Lee, Jaehun Cho, Young-Ha Choi, Chun-Yeol You, Myung-Hwa Jung, Frédéric Bonell, Yoichi Shiota, Shinji Miwa, and Yoshishige Suzuki, 2014, "Spin-orbit torque in a bulk perpendicular magnetic anisotropy Pd/FePd/MgO system," Sci. Rep. **4**, 6548.

Lee, Ki-Seung, Dongwook Go, Aurélien Manchon, Paul M. Haney, M. D. Stiles, Hyun-Woo Lee, and Kyung-Jin Lee, 2015, "Angular dependence of spin-orbit spin-transfer torques," Phys. Rev. B **91**, 144401.

Lee, Ki-Seung, Seo-Won Lee, Byoung-Chul Min, and Kyung-Jin Lee, 2013, "Threshold current for switching of a perpendicular magnetic layer induced by spin Hall effect," Appl. Phys. Lett. **102**, 112410.

Lee, O. J., L. Q. Liu, C. F. Pai, Y. Li, H. W. Tseng, P. G. Gowtham, J. P. Park, D. C. Ralph, and R. A. Buhrman, 2014, "Central role of domain wall depinning for perpendicular magnetization switching driven by spin torque from the spin Hall effect," Phys. Rev. B **89**, 024418.

Lee, S.-W., and K.-J. Lee, 2016, "Emerging Three-Terminal Magnetic Memory Devices," Proc. IEEE **104**, 1831.

Legrand, William, Davide Maccariello, Nicolas Reyren, Karin Garcia, Christoforos Moutafis, Constance Moreau-Luchaire, Sophie Collin, Karim Bouzehouane, Vincent Cros, and Albert Fert, 2017, "Room-Temperature Current-Induced Generation and Motion of sub-100 nm Skyrmions," Nano Lett. **17**, 2703.

Lepadatu, Serban, *et al.*, 2017, "Synthetic ferrimagnet nanowires with very low critical current density for coupled domain wall motion," Sci. Rep. **7**, 1640.

Lequeux, Steven, Joao Sampaio, Vincent Cros, Kay Yakushiji, Akio Fukushima, Rie Matsumoto, Hitoshi Kubota, Shinji Yuasa, and Julie Grollier, 2016, "A magnetic synapse: Multilevel spin-torque memristor with perpendicular anisotropy," Sci. Rep. **6**, 31510.

Lesne, E., *et al.*, 2016, "Highly efficient and tunable spin-to-charge conversion through Rashba coupling at oxide interfaces," Nat. Mater. **15**, 1261.

Levy, P. M., 1994, "Giant Magnetoresistance in Magnetic Layered and Granular Materials," Solid State Phys. **47**, 367.

Li, Hang, and Aurelien Manchon, 2016, "Tunable spin-charge conversion through topological phase transitions in zigzag nano-ribbons," Phys. Rev. B **93**, 235317.

Li, Hang, Xuhui Wang, Fatih Doan, and Aurelien Manchon, 2013, "Tailoring spin-orbit torque in diluted magnetic semiconductors," Appl. Phys. Lett. **102**, 192411.

Li, Hang, Xuhui Wang, and A. Manchon, 2016, "Valley-dependent spin-orbit torques in two-dimensional hexagonal crystals," Phys. Rev. B **93**, 035417.

Li, Hang, *et al.*, 2015, "Intraband and interband spin-orbit torques in noncentrosymmetric ferromagnets," Phys. Rev. B **91**, 134402.

Li, Mingda, *et al.*, 2015, "Proximity-Driven Enhanced Magnetic Order at Ferromagnetic-Insulator-Magnetic-Topological-Insulator Interface," Phys. Rev. Lett. **115**, 087201.

Li, Peng, *et al.*, 2016, "Spin-orbit torque-assisted switching in magnetic insulator thin films with perpendicular magnetic anisotropy," Nat. Commun. **7**, 12688.

Li, Xiaopeng, W. Vincent Liu, and Leon Balents, 2014, "Spirals and Skyrmions in Two Dimensional Oxide Heterostructures," Phys. Rev. Lett. **112**, 067202.

Lifshits, Maria, and Michel Dyakonov, 2009, "Swapping Spin Currents: Interchanging Spin and Flow Directions," Phys. Rev. Lett. **103**, 186601.

Lin, Shi-Zeng, Charles Reichhardt, Cristian D. Batista, and Avadh Saxena, 2013, "Particle model for skyrmions in metallic chiral magnets: Dynamics, pinning, and creep," Phys. Rev. B **87**, 214419.

Lin, W. W., H. Sang, D. Liu, Z. S. Jiang, A. Hu, and X. S. Wu, 2006, "Magnetization switching induced by in-plane current with low density in sandwich," J. Appl. Phys. **99**, 08G518.

Linder, Jacob, 2014, "Improved domain-wall dynamics and magnonic torques using topological insulators," Phys. Rev. B **90**, 041412.

Linder, Jacob, and Mohammad Alidoust, 2013, "Asymmetric ferromagnetic resonance, universal Walker breakdown, and counterflow domain wall motion in the presence of multiple spin-orbit torques," Phys. Rev. B **88**, 064420.

Litzius, Kai, *et al.*, 2017, "Skyrmion Hall Effect Revealed by Direct Time-Resolved X-Ray Microscopy," Nat. Phys. **13**, 170.

Liu, Luqiao, O. Lee, T. J. Gudmundsen, D. C. Ralph, and R. A. Buhrman, 2012, "Current-Induced Switching of Perpendicularly Magnetized Magnetic Layers Using Spin Torque from the Spin Hall Effect," Phys. Rev. Lett. **109**, 096602.

Liu, Luqiao, Takahiro Moriyama, D. C. Ralph, and R. A. Buhrman, 2011, "Spin-Torque Ferromagnetic Resonance Induced by the Spin Hall Effect," Phys. Rev. Lett. **106**, 036601.

Liu, Luqiao, Chi-Feng Pai, Y. Li, H. W. Tseng, D. C. Ralph, and R. A. Buhrman, 2012, "Spin-torque switching with the giant spin Hall effect of tantalum," Science **336**, 555.

Liu, Luqiao, Chi-Feng Pai, D. C. Ralph, and R. A. Buhrman, 2012, "Magnetic Oscillations Driven by the Spin Hall Effect in 3-Terminal Magnetic Tunnel Junction Devices," Phys. Rev. Lett. **109**, 186602.

Liu, R., W. Lim, and S. Urazhdin, 2013, "Spectral Characteristics of the Microwave Emission by the Spin Hall Nano-Oscillator," Phys. Rev. Lett. **110**, 147601.

Liu, R. H., W. L. Lim, and S. Urazhdin, 2014, "Control of current-induced spin-orbit effects in a ferromagnetic heterostructure by electric field," Phys. Rev. B **89**, 220409(R).

Liu, T., Y. Zhang, J. W. Cai, and H. Y. Pan, 2014, "Thermally robust Mo/CoFeB/MgO trilayers with strong perpendicular magnetic anisotropy," Sci. Rep. **4**, 5895.

Locatelli, N., V. Cros, and J. Grollier, 2014, "Spin-torque building blocks," Nat. Mater. **13**, 11.

Luo, Z., *et al.*, 2019, "Chirally Coupled Nanomagnets," Science **363**, 1435.

MacDonald, A. H., and M. Tsoi, 2011, "Antiferromagnetic metal spintronics," Phil. Trans. R. Soc. A **369**, 3098.

MacNeill, D., G. M. Stiehl, M. H. D. Guimaraes, R. A. Buhrman, J. Park, and D. C. Ralph, 2017, "Control of spin-orbit torques through crystal symmetry in WTe2/ferromagnet bilayers," Nat. Phys. **13**, 300.

Madami, M., S. Bonetti, G. Consolo, S. Tacchi, G. Carlotti, G. Gubbiotti, F. B. Mancoff, M. A. Yar, and J. Åkerman, 2011, "Direct observation of a propagating spin wave induced by spin-transfer torque," Nat. Nanotechnol. **6**, 635.

Mahan, G. D., 2000, *Many-Particle Physics* (Plenum Publishers, New York), 3rd ed.

Mahendra, D. C., *et al.*, 2018, "Room-temperature high spin orbit torque due to quantum confinement in sputtered BixSe(1x) films," Nat. Mater. **17**, 800.

Mahfouzi, Farzad, and Nicholas Kioussis, 2018, "First-principles study of the angular dependence of the spin-orbit torque in Pt/Co and Pd/Co bilayers," Phys. Rev. B **97**, 224426.

Mahfouzi, Farzad, Naoto Nagaosa, and Branislav K. Nikolic, 2012, "Spin-orbit coupling induced spin-transfer torque and current polarization in topological-insulator/ferromagnet vertical hetero-structures," Phys. Rev. Lett. **109**, 166602.

Mahfouzi, Farzad, Naoto Nagaosa, and Branislav K. Nikolić, 2014, "Spin-to-charge conversion in lateral and vertical topological-insulator/ferromagnet heterostructures with microwave-driven pre-cessing magnetization," Phys. Rev. B **90**, 115432.

Mahfouzi, Farzad, Branislav K. Nikolic, Son-hsien Chen, and Ching-ray Chang, 2010, "Microwave-driven ferromagnet topological-insulator heterostructures: The prospect for giant spin battery effect and quantized charge pump devices," Phys. Rev. B **82**, 195440.

Mahfouzi, Farzad, Branislav K. Nikolić, and Nicholas Kioussis, 2016, "Antidamping spin-orbit torque driven by spin-flip reflection mechanism on the surface of a topological insulator: A time-dependent nonequilibrium Green function approach," Phys. Rev. B **93**, 115419.

Malozemoff, A. P., and J. C. Slonczewski, 1979, *Magnetic Domain Walls in Bubble Materials* (Academic, New York).

Mal'shukov, A. G., and K. A. Chao, 2002, "Optoelectric spin injection in semiconductor heterostructures without a ferromagnet," Phys. Rev. B **65**, 241308.

Manchon, A., 2011, "Interfacial spin-orbit splitting and current-driven spin torque in anisotropic tunnel junctions," Phys. Rev. B **83**, 172403.

Manchon, A., 2017, "Spin diffusion and torques in disordered antiferromagnets," J. Phys. Condens. Matter **29**, 104002.

Manchon, A., H. C. Koo, J. Nitta, S. M. Frolov, and R. A. Duine, 2015, "New Perspectives for Rashba Spin-Orbit Coupling," Nat. Mater. **14**, 871.

Manchon, A., and S. Zhang, 2008, "Theory of nonequilibrium intrinsic spin torque in a single nanomagnet," Phys. Rev. B **78**, 212405.

Manchon, A., and S. Zhang, 2011, "Spin Torque in Magnetic Systems: Theory," in *Handbook of Spin Transport and Magnetism*, edited by Evgeny Y. Tsymbal, and Igor Zutic (CRC Press, Boca Raton), Chap. 8, pp. 157–178.

Manchon, A., *et al.*, 2008, "Analysis of oxygen induced anisotropy crossover in Pt/Co/MOx trilayers," J. Appl. Phys. **104**, 043914.

Manchon, Aurelien, 2011, "Voltage-driven versus current-driven spin torque in anisotropic tunneling junctions," IEEE Trans. Magn. **47**, 2735.

Manchon, Aurelien, 2012, "Spin Hall effect versus Rashba torque: a Diffusive Approach," arXiv:1204.4869v1.

Manchon, Aurélien, and S. Zhang, 2009, "Theory of spin torque due to spin-orbit coupling," Phys. Rev. B **79**, 094422.

Mangin, S., *et al.*, 2014, "Engineered materials for all-optical helicity-dependent magnetic switching," Nat. Mater. **13**, 286.

Manna, Kaustuv, Yan Sun, Lukas Muechler, Jürgen Kübler, and Claudia Felser, 2018, "Heusler, Weyl and Berry 1," Nat. Rev. Mater. **3**, 244.

Marmolejo-Tejada, Juan Manuel, Kapildeb Dolui, Predrag Lazić, Po Hao Chang, Søren Smidstrup, Daniele Stradi, Kurt Stokbro, and Branislav K. Nikolić, 2017, "Proximity Band Structure and Spin Textures on Both Sides of Topological-Insulator/Ferromagnetic-Metal Interface and Their Charge Transport Probes," Nano Lett. **17**, 5626.

Martinez, Eduardo, 2012, "Micromagnetic analysis of the Rashba field on current-induced domain wall propagation," J. Appl. Phys. **111**, 033901.

Martinez, Eduardo, Satoru Emori, and Geoffrey S. D. Beach, 2013, "Current-driven domain wall motion along high perpendicular anisotropy multilayers: The role of the Rashba field, the spin Hall effect, and the Dzyaloshinskii-Moriya interaction," Appl. Phys. Lett. **103**, 072406.

Martinez, Eduardo, Satoru Emori, Noel Perez, Luis Torres, and Geoffrey S. D. Beach, 2014, "Current-driven dynamics of Dzyaloshinskii domain walls in the presence of in-plane fields: Full micromagnetic and one-dimensional analysis," J. Appl. Phys. **115**, 213909.

Martinez, Eduardo, Luis Torres, Noel Perez, Maria Auxiliadora Hernandez, Victor Raposo, and Simone Moretti, 2015, "Universal chiral-triggered magnetization switching in confined nanodots," Sci. Rep. **5**, 10156.

Maruyama, T., *et al.*, 2009, "Large voltage-induced magnetic anisotropy change in a few atomic layers of iron," Nat. Nano-technol. **4**, 158.

Matos-Abiague, A., and R. L. Rodriguez-Suárez, 2009, "Spin-orbit coupling mediated spin torque in a single ferromagnetic layer," Phys. Rev. B **80**, 094424.

McGuire, T., and R. Potter, 1975, "Anisotropic magnetoresistance in ferromagnetic 3d alloys," IEEE Trans. Magn. **11**, 1018.

McMichael, R. D., and M. J. Donahue, 1997, "Head to head domain wall structures in thin magnetic strips," IEEE Trans. Magn. **33**, 4167.

Meckler, S., N. Mikuszeit, A. Preßler, E. Vedmedenko, O. Pietzsch, and R. Wiesendanger, 2009, "Real-Space Observation of a Right-Rotating Inhomogeneous Cycloidal Spin Spiral by Spin-Polarized Scanning Tunneling Microscopy in a Triple Axes Vector Magnet," Phys. Rev. Lett. **103**, 157201.

Meinert, Markus, Dominik Graulich, and Tristan Matalla-Wagner, 2018, "Electrical Switching of Antiferromagnetic Mn2Au and the Role of Thermal Activation," Phys. Rev. Applied **9**, 064040.

Mellnik, A. R., *et al.*, 2014, "Spin-transfer torque generated by a topological insulator," Nature (London) **511**, 449.

Mendes, J. B. S., O. Alves Santos, J. Holanda, R. P. Loreto, C. I. L. de Araujo, Cui-Zu Chang, J. S. Moodera, A. Azevedo, and S. M. Rezende, 2017, "Dirac-surface-state-dominated spin to charge current conversion in the topological insulator (Bi 0. 22 Sb 0. 78) 2 Te 3 films at room temperature," Phys. Rev. B **96**, 180415(R).

Metaxas, P. J., J. P. Jamet, A. Mougin, M. Cormier, J. Ferré, V. Baltz, B. Rodmacq, B. Dieny, and R. L. Stamps, 2007, "Creep and Flow Regimes of Magnetic Domain-Wall Motion in Ultrathin Pt/Co/Pt Films with Perpendicular Anisotropy," Phys. Rev. Lett. **99**, 217208.

Mikuszeit, N., O. Boulle, I. M. Miron, K. Garello, P. Gambardella, G. Gaudin, and L. D. Buda-Prejbeanu, 2015, "Spin-orbit torque driven chiral magnetization reversal in ultrathin nanostructures," Phys. Rev. B **92**, 144424.

Min, Hongki, Robert D. McMichael, Michael J. Donahue, Jacques Miltat, and M. D. Stiles, 2010, "Effects of disorder and internal dynamics on vortex wall propagation," Phys. Rev. Lett. **104**, 217201.

Miron, I., P.-J. Zermatten, G. Gaudin, S. Auffret, B. Rodmacq, and A. Schuhl, 2009, "Domain Wall Spin Torquemeter," Phys. Rev. Lett. **102**, 137202.

Miron, Ioan Mihai, Kevin Garello, Gilles Gaudin, Pierre Jean Zermatten, Marius V. Costache, Stéphane Auffret, Sébastien Ban-diera, Bernard Rodmacq, Alain Schuhl, and Pietro Gambardella,

2011, "Perpendicular switching of a single ferromagnetic layer induced by in-plane current injection," Nature (London) **476**, 189.

Miron, Ioan Mihai, Gilles Gaudin, S. Auffret, Bernard Rodmacq, Alain Schuhl, Stefania Pizzini, Jan Vogel, and Pietro Gambardella, 2010, "Current-driven spin torque induced by the Rashba effect in a ferromagnetic metal layer," Nat. Mater. **9**, 230.

Miron, Ioan Mihai, *et al.*, 2011, "Fast current-induced domain-wall motion controlled by the Rashba effect," Nat. Mater. **10**, 419.

Mishra, Rahul, Jiawei Yu, Xuepeng Qiu, M. Motapothula, T. Venkatesan, and Hyunsoo Yang, 2017, "Anomalous Current-Induced Spin Torques in Ferrimagnets near Compensation," Phys. Rev. Lett. **118**, 167201.

Monso, S., B. Rodmacq, S. Auffret, G. Casali, F. Fettar, B. Gilles, B. Dieny, and P. Boyer, 2002, "Crossover from in-plane to perpendicular anisotropy in Pt/CoFe/AlOx sandwiches as a function of Al oxidation: A very accurate control of the oxidation of tunnel barriers," Appl. Phys. Lett. **80**, 4157.

Montazeri, Mohammad, *et al.*, 2015, "Magneto-optical investigation of spin orbit torques in metallic and insulating magnetic hetero-structures," Nat. Commun. **6**, 8958.

Moon, Kyoung Woong, Changsoo Kim, Jungbum Yoon, Jun Woo Choi, Dong Ok Kim, Kyung Mee Song, Dongseuk Kim, Byong Sun Chun, and Chanyong Hwang, 2018, "A spin torque meter with magnetic facet domains," Nat. Commun. **9**, 3788.

Moon, Kyoung Woong, Duck Ho Kim, Sang Cheol Yoo, Cheong Gu Cho, Sungmin Hwang, Byungnam Kahng, Byoung Chul Min, Kyung Ho Shin, and Sung Bong Choe, 2013, "Distinct universality classes of domain wall roughness in two-dimensional Pt/Co/Pt films," Phys. Rev. Lett. **110**, 107203.

Moore, T. A., I. M. Miron, G. Gaudin, G. Serret, S. Auffret, B. Rodmacq, A. Schuhl, S. Pizzini, J. Vogel, and M. Bonfim, 2008, "High domain wall velocities induced by current in ultrathin Pt/Co/AlOx wires with perpendicular magnetic anisotropy," Appl. Phys. Lett. **93**, 262504; **95**, 179902(E) (2009).

Moras, P., G. Bihlmayer, P. M. Sheverdyaeva, S. K. Mahatha, M. Papagno, J. Sánchez-Barriga, O. Rader, L. Novinec, S. Gardonio, and C. Carbone, 2015, "Magnetization-dependent Rashba splitting of quantum well states at the Co/W interface," Phys. Rev. B **91**, 195410.

Moreau-Luchaire, C., *et al.*, 2016, "Additive interfacial chiral interaction in multilayers for stabilization of small individual skyrmions at room temperature," Nat. Nanotechnol. **11**, 444.

Moritz, J., B. Rodmacq, S. Auffret, and B. Dieny, 2008, "Extraordinary Hall effect in thin magnetic films and its potential for sensors, memories and magnetic logic applications," J. Phys. D **41**, 135001.

Moriya, Toru, 1960, "Anisotropic superexchange interaction and weak ferromagnetism," Phys. Rev. **120**, 91.

Moriyama, Takahiro, Weinan Zhou, Takeshi Seki, Koki Takanashi, and Teruo Ono, 2018, "Spin-Orbit-Torque Memory Operation of Synthetic Antiferromagnets," Phys. Rev. Lett. **121**, 167202.

Morota, M., Y. Niimi, K. Ohnishi, D. H. Wei, T. Tanaka, H. Kontani, T. Kimura, and Y. Otani, 2011, "Indication of intrinsic spin Hall effect in 4d and 5d transition metals," Phys. Rev. B **83**, 174405.

Murakami, Shuichi, N. Nagaosa, and Shou-Cheng Zhang, 2003, "Dissipationless Quantum Spin Current at Room Temperature," Science **301**, 1348.

Nagaosa, Naoto, Jairo Sinova, Shigeki Onoda, A. H. MacDonald, and N. P. Ong, 2010, "Anomalous Hall effect," Rev. Mod. Phys. **82**, 1539.

Nagaosa, Naoto, and Yoshinori Tokura, 2013, "Topological properties and dynamics of magnetic skyrmions," Nat. Nanotechnol. **8**, 899.

Nakatani, Yoshinobu, André Thiaville, and Jacques Miltat, 2003, "Faster magnetic walls in rough wires," Nat. Mater. **2**, 521.

Nakatani, Yoshinobu, André Thiaville, and Jacques Miltat, 2005, "Head-to-head domain walls in soft nano-strips: A refined phase diagram," J. Magn. Magn. Mater. **290**–**291 PA**, 750.

Nakatsuji, Satoru, Naoki Kiyohara, and Tomoya Higo, 2015, "Large anomalous Hall effect in a non-collinear antiferromagnet at room temperature," Nature (London) **527**, 212.

Nakayama, H., *et al.*, 2013, "Spin Hall Magnetoresistance Induced by a Nonequilibrium Proximity Effect," Phys. Rev. Lett. **110**, 206601.

Nakayama, Hiroyasu, Yusuke Kanno, Hongyu An, Takaharu Tashiro, Satoshi Haku, Akiyo Nomura, and Kazuya Ando, 2016, "Rashba-Edelstein Magnetoresistance in Metallic Heterostructures," Phys. Rev. Lett. **117**, 116602.

Nan, Tianxiang, Satoru Emori, Carl T. Boone, Xinjun Wang, Trevor M. Oxholm, John G. Jones, Brandon M. Howe, Gail J. Brown, and Nian X. Sun, 2015, "Comparison of spin-orbit torques and spin pumping across NiFe/Pt and NiFe/Cu/Pt interfaces," Phys. Rev. B **91**, 214416.

Ndiaye, Papa B., C. A. Akosa, M. H. Fischer, A. Vaezi, E. A. Kim, and A. Manchon, 2017, "Dirac spin-orbit torques and charge pumping at the surface of topological insulators," Phys. Rev. B **96**, 014408.

Nguyen, Anh Kiet, Hans Joakim Skadsem, and Arne Brataas, 2007, "Giant current-driven domain wall mobility in (Ga,Mn)As," Phys. Rev. Lett. **98**, 146602.

Nguyen, Minh Hai, Chi Feng Pai, Kayla X. Nguyen, David A. Muller, D. C. Ralph, and R. A. Buhrman, 2015, "Enhancement of the anti-damping spin torque efficacy of platinum by interface modification," Appl. Phys. Lett. **106**, 222402.

Nguyen, Minh Hai, D. C. Ralph, and R. A. Buhrman, 2016, "Spin Torque Study of the Spin Hall Conductivity and Spin Diffusion Length in Platinum Thin Films with Varying Resistivity," Phys. Rev. Lett. **116**, 126601.

Nielsen, J. W., 1976, "Bubble Domain Memory Materials," IEEE Trans. Magn. **12**, 327.

Nikolić, Branislav K., Kapildeb Dolui, Marko D. Petrović, Petr Plecháč, Troels Markussen, and Kurt Stokbro, 2018, "*First-Principles Quantum Transport Modeling of Spin-Transfer and Spin-Orbit Torques in Magnetic Multilayers*," in *Handbook of Materials Modeling: Applications: Current and Emerging Materials*, edited by Wanda Andreoni and Sidney Yip (Springer International Publishing, Cham), Chap. 34, pp. 1–35.

Nistor, C., T. Balashov, J. J. Kavich, A. Lodi Rizzini, B. Ballesteros, G. Gaudin, S. Auffret, B. Rodmacq, S. S. Dhesi, and P. Gambardella, 2011, "Orbital moment anisotropy of Pt/Co/AlOx heterostructures with strong Rashba interaction," Phys. Rev. B **84**, 054464.

Nomura, Kentaro, and Naoto Nagaosa, 2011, "Surface-Quantized Anomalous Hall Current and the Magnetoelectric Effect in Magnetically Disordered Topological Insulators," Phys. Rev. Lett. **106**, 166802.

Nozaki, T., Y. Jiang, Y. Kaneko, A. Hirohata, N. Tezuka, S. Sugimoto, and K. Inomata, 2004, "Spin-dependent quantum oscillations in magnetic tunnel junctions with Ru quantum wells," Phys. Rev. B **70**, 172401.

Núñez, A. S., R. A. Duine, Paul Haney, and A. H. MacDonald, 2006, "Theory of spin torques and giant magnetoresistance in antiferro-magnetic metals," Phys. Rev. B **73**, 214426.

Obata, Katsunori, and G. Tatara, 2008, "Current-induced domain wall motion in Rashba spin-orbit system," Phys. Rev. B **77**, 214429.

Oboril, Fabian, Rajendra Bishnoi, Mojtaba Ebrahimi, and Mehdi B. Tahoori, 2015, "Evaluation of Hybrid Memory Technologies Using SOT-MRAM for On-Chip Cache Hierarchy," IEEE Trans. Magn. **34**, 367.

Oh, Se-Chung, *et al.*, 2009, "Bias-voltage dependence of perpendicular spin-transfer torque in asymmetric MgO-based magnetic tunnel junctions," Nat. Phys. **5**, 898.

Oh, Young-Wan, *et al.*, 2016, "Field-free switching of perpendicular magnetization through spin-orbit torque in antiferromagnet/ ferromagnet/oxide structures," Nat. Nanotechnol. **11**, 878.

Ohtomo, A., and H. Y. Hwang, 2004, "A high-mobility electron gas at the LaAlO3/SrTiO3 heterointerface," Nature (London) **427**, 423.

Olejník, K., V. Schuler, X. Marti, and V. Nova, 2017, "Antiferromagnetic CuMnAs multi-level memory cell with microelectronic compatibility," Nat. Commun. **8**, 15434.

Olejník, K., V. Novák, J. Wunderlich, and T. Jungwirth, 2015, "Electrical detection of magnetization reversal without auxiliary magnets," Phys. Rev. B **91**, 180402(R).

Olejník, Kamil, *et al.*, 2018, "Terahertz electrical writing speed in an antiferromagnetic memory," Sci. Adv. **4**, eaar3566.

Ou, Yongxi, D. C. Ralph, and R. A. Buhrman, 2018, "Strong Enhancement of the Spin Hall Effect by Spin Fluctuations near the Curie Point of Fe x Pt 1 x Alloys," Phys. Rev. Lett. **120**, 097203.

Ou, Yongxi, Shengjie Shi, D. C. Ralph, and R. A. Buhrman, 2016, "Strong spin Hall effect in the antiferromagnet PtMn," Phys. Rev. B **93**, 220405(R).

Pai, Chi Feng, Yongxi Ou, Luis Henrique Vilela-Leao, D. C. Ralph, and R. A. Buhrman, 2015, "Dependence of the efficiency of spin Hall torque on the transparency of Pt/ferromagnetic layer interfaces," Phys. Rev. B **92**, 064426.

Pai, Chi-Feng, Luqiao Liu, Y. Li, H. W. Tseng, D. C. Ralph, and R. A. Buhrman, 2012, "Spin transfer torque devices utilizing the giant spin Hall effect of tungsten," Appl. Phys. Lett. **101**, 122404.

Pai, Chi-Feng, Minh-Hai Nguyen, Carina Belvin, Luis Henrique Vilela-Leão, D. C. Ralph, and R. A. Buhrman, 2014, "Enhancement of perpendicular magnetic anisotropy and transmission of spin-Hall-effect-induced spin currents by a Hf spacer layer in W/Hf/CoFeB/MgO layer structures," Appl. Phys. Lett. **104**, 082407.

Park, B. G., J. Wunderlich, D. A. Williams, S. J. Joo, K. Y. Jung, K. H. Shin, K. Olejník, A. B. Shick, and T. Jungwirth, 2008, "Tunneling Anisotropic Magnetoresistance in Multilayer-(Co/Pt)/AlOx/Pt Structures," Phys. Rev. Lett. **100**, 087204.

Park, Junbo, G. E. Rowlands, O. J. Lee, D. C. Ralph, and R. A. Buhrman, 2014, "Macrospin modeling of sub-ns pulse switching of perpendicularly magnetized free layer via spin-orbit torques for cryogenic memory applications," Appl. Phys. Lett. **105**, 102404.

Parkin, S. S. P., 1993, "Origin of enhanced magnetoresistance of magnetic multilayers: Spin-dependent scattering from magnetic interface states," Phys. Rev. Lett. **71**, 1641.

Parkin, Stuart, and See-Hun Yang, 2015, "Memory on the racetrack," Nat. Nanotechnol. **10**, 195.

Parkin, Stuart S. P., Masamitsu Hayashi, and Luc Thomas, 2008, "Magnetic domain-wall racetrack memory," Science **320**, 190.

Pauyac, Christian Ortiz, Mairbek Chshiev, Aurelien Manchon, and Sergey A. Nikolaev, 2018, "Spin Hall and Spin Swapping Torques in Diffusive Ferromagnets," Phys. Rev. Lett. **120**, 176802.

Pauyac, Christian Ortiz, Xuhui Wang, Mairbek Chshiev, and Aurelien Manchon, 2013, "Angular dependence and symmetry of Rashba spin torque in ferromagnetic heterostructures," Appl. Phys. Lett. **102**, 252403.

Pellegren, J. P., D. Lau, and V. Sokalski, 2017, "Dispersive Stiffness of Dzyaloshinskii Domain Walls," Phys. Rev. Lett. **119**, 027203.

Perez, N., E. Martinez, L. Torres, S.-H. Woo, S. Emori, and G. S. D. Beach, 2014, "Chiral magnetization textures stabilized by the Dzyaloshinskii-Moriya interaction during spin-orbit torque switching," Appl. Phys. Lett. **104**, 092403.

Pesin, D. A., and A. H. MacDonald, 2012a, "Quantum kinetic theory of current-induced torques in Rashba ferromagnets," Phys. Rev. B **86**, 014416.

Pesin, D. A., and A. H. MacDonald, 2012b, "Spintronics and pseudospintronics in graphene and topological insulators," Nat. Mater. **11**, 409.

Pham, Van Tuong, Laurent Vila, Gilles Zahnd, Alain Marty, Williams Savero-Torres, Matthieu Jamet, and Jean Philippe Attané, 2016, "Ferromagnetic/Nonmagnetic Nanostructures for the Electrical Measurement of the Spin Hall Effect," Nano Lett. **16**, 6755.

Pi, Ung Hwan, Kee Won Kim, Ji Young Bae, Sung Chul Lee, Young Jin Cho, Kwang Seok Kim, and Sunae Seo, 2010, "Tilting of the spin orientation induced by Rashba effect in ferromagnetic metal layer," Appl. Phys. Lett. **97**, 162507.

Pizzini, S., *et al.*, 2009, "High Domain Wall Velocity at Zero Magnetic Field Induced by Low Current Densities in Spin Valve Nanostripes," Appl. Phys. Express **2**, 023003.

Pizzini, S., *et al.*, 2014, "Chirality-Induced Asymmetric Magnetic Nucleation in Pt/Co/AlOx Ultrathin Microstructures," Phys. Rev. Lett. **113**, 047203.

Pollard, Shawn D., Joseph A. Garlow, Jiawei Yu, Zhen Wang, Yimei Zhu, and Hyunsoo Yang, 2017, "Observation of stable Néel skyrmions in Co/Pd multilayers with Lorentz transmission electron microscopy," Nat. Commun. **8**, 14761.

Prenat, Guillaume, *et al.*, 2016, "Ultra-Fast and High-Reliability SOT-MRAM: From Cache Replacement to Normally-Off Computing," IEEE Trans. Multi-Scale Comput. Syst. **2**, 49.

Qaiumzadeh, A., R. A. Duine, and M. Titov, 2015, "Spin-orbit torques in two-dimensional Rashba ferromagnets," Phys. Rev. B **92**, 014402.

Qi, Xiao-Liang, Taylor L. Hughes, and Shou-Cheng Zhang, 2008, "Topological field theory of time-reversal invariant insulators," Phys. Rev. B **78**, 195424.

Qi, Xiao-Liang, and Shou-Cheng Zhang, 2011, "Topological insulators and superconductors," Rev. Mod. Phys. **83**, 1057.

Qiao, Junfeng, Jiaqi Zhou, Zhe Yuan, and Weisheng Zhao, 2018, "Calculation of intrinsic spin Hall conductivity by Wannier interpolation," Phys. Rev. B **98**, 214402.

Qiu, Xuepeng, Praveen Deorani, Kulothungasagaran Narayanapillai, Ki-Seung Lee, Kyung-Jin Lee, Hyun-Woo Lee, and Hyunsoo Yang, 2014, "Angular and temperature dependence of current induced spin-orbit effective fields in Ta/CoFeB/MgO nanowires," Sci. Rep. **4**, 4491.

Qiu, Xuepeng, William Legrand, Pan He, Yang Wu, Jiawei Yu, Rajagopalan Ramaswamy, Aurelien Manchon, and Hyunsoo Yang, 2016, "Enhanced Spin-Orbit Torque via Modulation of Spin Current Absorption," Phys. Rev. Lett. **117**, 217206.

Qiu, Xuepeng, Kulothungasagaran Narayanapillai, Yang Wu, Praveen Deorani, Dong-Hyuk Yang, Woo-suk Noh, Jae-hoon Park, Kyung-Jin Lee, Hyun-woo Lee, and Hyunsoo Yang, 2015, "Spin orbit-torque engineering via oxygen manipulation," Nat. Nanotechnol. **10**, 333.

Qiu, Z. Q., and S. D. Bader, 2000, "Surface magneto-optic Kerr effect," Rev. Sci. Instrum. **71**, 1243.

Ralph, D. C., and M. D. Stiles, 2008, "Spin transfer torques," J. Magn. Magn. Mater. **320**, 1190.

Ramaswamy, Rajagopalan, Xuepeng Qiu, Tanmay Dutta, Shawn David Pollard, and Hyunsoo Yang, 2016, "Hf thickness dependence of spin-orbit torques in Hf/CoFeB/MgO heterostructures," Appl. Phys. Lett. **108**, 202406.

Rammer, S., and H. Smith, 1986, "Quantum field theoretical methods in transport theory of metals," Rev. Mod. Phys. **58**, 323.

Rashba, E. I., and V. I. Sheka, 1991, "Electric-Dipole Spin Resonances," in *Landau Level Spectroscopy*, edited by G. Landwehr and E. I. Rashba (Elsevier Science Publishers, New York), Chap. 4, p. 133.

Rashba, Emmanuel I., 2003, "Spin currents in thermodynamic equilibrium: The challenge of discerning transport currents," Phys. Rev. B **68**, 241315(R).

Ravelosona, D., D. Lacour, J. A. Katine, B. D. Terris, and C. Chappert, 2005, "Nanometer scale observation of high efficiency thermally assisted current-driven domain wall depinning," Phys. Rev. Lett. **95**, 117203.

Reichhardt, C., and C. J. Olson Reichhardt, 2016, "Noise fluctuations and drive dependence of the skyrmion Hall effect in disordered systems," New J. Phys. **18**, 095005.

Reichlova, H., *et al.*, 2015, "Current-induced torques in structures with ultrathin IrMn antiferromagnets," Phys. Rev. B **92**, 165424.

Reynolds, Neal, Priyamvada Jadaun, John T. Heron, Colin L. Jermain, Jonathan Gibbons, Robyn Collette, R. A. Buhrman, D. G. Schlom, and D. C. Ralph, 2017, "Spin Hall torques generated by rare-earth thin films," Phys. Rev. B **95**, 064412.

Richardella, Anthony, Abhinav Kandala, Joon Sue Lee, and Nitin Samarth, 2015, "Characterizing the structure of topological insulator thin films," APL Mater. **3**, 083303.

Rippard, W., M. Pufall, S. Kaka, S. Russek, and T. Silva, 2004, "Direct-Current Induced Dynamics in Co90Fe10/Ni80Fe20 Point Contacts," Phys. Rev. Lett. **92**, 027201.

Risinggård, Vetle, and Jacob Linder, 2017, "Universal absence of Walker breakdown and linear current-velocity relation via spin-orbit torques in coupled and single domain wall motion," Phys. Rev. B **95**, 134423.

Riss, O., A. Gerber, I. Ya Korenblit, and M. Karpovsky, 2010, "Nonthermal magnetization reversal assisted by unpolarized current," Phys. Rev. B **82**, 144417.

Roche, Stephan, *et al.*, 2015, "Graphene spintronics: The European Flagship perspective," 2D Mater. **2**, 030202.

Rodmacq, B., A. Manchon, C. Ducruet, S. Auffret, and B. Dieny, 2009, "Influence of thermal annealing on the perpendicular magnetic anisotropy of Pt/Co/AlOx trilayers," Phys. Rev. B **79**, 024423.

Rojas-Sánchez, J. C., P. Laczkowski, J. Sampaio, S. Collin, K. Bouzehouane, N. Reyren, H. Jaffrès, A. Mougin, and J. M. George, 2016, "Perpendicular magnetization reversal in Pt/[Co/Ni]3/Al multilayers via the spin Hall effect of Pt," Appl. Phys. Lett. **108**, 082406.

Rojas-Sánchez, J. C., L. Vila, G. Desfonds, S. Gambarelli, J.-P. Attane, J. M. De Teresa, C. Magén, and A. Fert, 2013, "Spin-to-charge conversion using Rashba coupling at the interface between non-magnetic materials," Nat. Commun. **4**, 2944.

Rojas-Sánchez, J. C., *et al.*, 2016, "Spin to Charge Conversion at Room Temperature by Spin Pumping into a New Type of Topological Insulator: α -Sn Films," Phys. Rev. Lett. **116**, 096602.

Rojas-Sánchez, J.-C., N. Reyren, P. Laczkowski, W. Savero, J.-P. Attane, C. Deranlot, M. Jamet, J.-M. George, L. Vila, and H. Jaffrès, 2014, "Spin Pumping and Inverse Spin Hall Effect in Platinum: The Essential Role of Spin-Memory Loss at Metallic Interfaces," Phys. Rev. Lett. **112**, 106602.

Roschewsky, Niklas, Charles-henri Lambert, and Sayeef Salahuddin, 2017, "Spin-orbit torque switching of ultralarge-thickness ferrimagnetic GdFeCo," Phys. Rev. B **96**, 064406.

Ryu, Jisu, Soo-Man Seo, Kyung-Jin Lee, and Hyun-Woo Lee, 2012, "Rashba spin orbit coupling effects on a current-induced domain wall motion," J. Magn. Magn. Mater. **324**, 1449.

Ryu, K. S., L. Thomas, S. Yang, and Stuart S. P. Parkin, 2012, "Current induced tilting of domain walls in high velocity motion along perpendicularly magnetized micron-sized Co/Ni/Co racetracks," Appl. Phys. Express **5**, 093006.

Ryu, Kwang-Su, Luc Thomas, See-Hun Yang, and Stuart Parkin, 2013, "Chiral spin torque at magnetic domain walls," Nat. Nanotechnol. **8**, 527.

Safeer, C. K., Emilie Jué, Alexandre Lopez, Liliana Buda-Prejbeanu, Stéphane Auffret, Stefania Pizzini, Olivier Boulle, Ioan Mihai Miron, and Gilles Gaudin, 2016, "Spin-orbit torque magnetization switching controlled by geometry," Nat. Nanotechnol. **11**, 143.

Safranski, Christopher, Eric A. Montoya, and Ilya N. Krivorotov, 2019, "Spin orbit torque driven by a planar Hall current," Nat. Nanotechnol. **14**, 27.

Saidaoui, Hamed Ben Mohamed, and Aurélien Manchon, 2016, "Spin-Swapping Transport and Torques in Ultrathin Magnetic Bilayers," Phys. Rev. Lett. **117**, 036601.

Saitoh, E., M. Ueda, H. Miyajima, and G. Tatara, 2006, "Conversion of spin current into charge current at room temperature: Inverse spin-Hall effect," Appl. Phys. Lett. **88**, 182509.

Sakai, Akio, and Hiroshi Kohno, 2014, "Spin torques and charge transport on the surface of topological insulator," Phys. Rev. B **89**, 165307.

Salimath, A., A. Abbout, A. Brataas, and A. Manchon, 2019, "Current-driven skyrmion Depinning in Magnetic Granular Films," Phys. Rev. B **99**, 104416.

Sambles, J. R., 1983, "The resistivity of thin metal lms—some critical remarks," Thin Solid Films **106**, 321.

Sampaio, J., V. Cros, S. Rohart, A. Thiaville, and A. Fert, 2013, "Nucleation, stability and current-induced motion of isolated magnetic skyrmions in nanostructures," Nat. Nanotechnol. **8**, 839.

Sankey, J. C., P. M. Braganca, A. G. F. Garcia, I. N. Krivorotov, R. A. Buhrman, and D. C. Ralph, 2006, "Spin-transfer-driven ferromagnetic resonance of individual nanomagnets," Phys. Rev. Lett. **96**, 227601.

Sankey, Jack C., Yong-Tao Cui, Jonathan Z. Sun, John C. Slonczewski, R. A. Buhrman, and Daniel C. Ralph, 2008, "Measurement of the spin-transfer-torque vector in magnetic tunnel junctions," Nat. Phys. **4**, 67.

Sato, Noriyuki, Fen Xue, Robert M. White, Chong Bi, and Shan X. Wang, 2018, "Two-terminal spin orbit torque magnetoresistive random access memory," Nat. Electron. **1**, 508.

Scholz, M. R., J. Sánchez-Barriga, D. Marchenko, A. Varykhalov, A. Volykhov, L. V. Yashina, and O. Rader, 2012, "Tolerance of topological surface states towards magnetic moments: Fe on Bi2Se3," Phys. Rev. Lett. **108**, 256810.

Schryer, N. L., and L. R. Walker, 1974, "The motion of 180 domain walls in uniform dc magnetic fields," J. Appl. Phys. **45**, 5406.

Seibold, Götz, Sergio Caprara, Marco Grilli, and Roberto Raimondi, 2017, "Theory of the Spin Galvanic Effect at Oxide Interfaces," Phys. Rev. Lett. **119**, 256801.

Sengupta, A., S. H. Choday, Y. Kim, and K. R. Schooll, 2015, "Spin orbit torque based electronic neuron," Appl. Phys. Lett. **106**, 143701.

Seo, Soo Man, Kyoung Whan Kim, Jisu Ryu, Hyun Woo Lee, and Kyung Jin Lee, 2012, "Current-induced motion of a transverse

magnetic domain wall in the presence of spin Hall effect," Appl. Phys. Lett. **101**, 022405.

Shao, Qiming, Guoqiang Yu, Yann-wen Lan, Yumeng Shi, Ming-Yang Li, Cheng Zheng, Xiaodan Zhu, Lain-Jong Li, Pedram Khalili Amiri, and Kang L. Wang, 2016, "Strong Rashba-Edelstein Effect-Induced Spin-Orbit Torques in Monolayer Transition Metal Dichalcogenide/Ferromagnet Bilayers," Nano Lett. **16**, 7514.

Shao, Qiming, *et al.*, 2018, "Role of dimensional crossover on spin-orbit torque efficiency in magnetic insulator thin films," Nat. Commun. **9**, 3612.

Shchelushkin, R., and Arne Brataas, 2005, "Spin Hall effects in diffusive normal metals," Phys. Rev. B **71**, 045123.

Shen, Ka, R. Raimondi, and G. Vignale, 2014, "Theory of coupled spin-charge transport due to spin-orbit interaction in inhomogeneous two-dimensional electron liquids," Phys. Rev. B **90**, 245302.

Shi, Junren, Ping Zhang, Di Xiao, and Qian Niu, 2006, "Proper definition of spin current in spin-orbit coupled systems," Phys. Rev. Lett. **96**, 076604.

Shi, Shengjie, Yongxi Ou, S. V. Aradhya, D. C. Ralph, and R. A. Buhrman, 2018, "Fast, low-current spin-orbit torque switching of magnetic tunnel junctions through atomic modifications of the free layer interfaces," Phys. Rev. Applied **9**, 011002.

Shi, Shuyuan, Aizhu Wang, Yi Wang, Rajagopalan Ramaswamy, Lei Shen, Jisoo Moon, Dapeng Zhu, and Jiawei Yu, 2018, "Efficient charge-spin conversion and magnetization switching through the Rashba effect at topological-insulator / Ag interfaces," Phys. Rev. B **97**, 041115(R).

Shiino, Takayuki, Se-hyeok Oh, Paul M. Haney, Seo-won Lee, Gyungchoon Go, Byong-guk Park, and Kyung-jin Lee, 2016, "Antiferromagnetic Domain Wall Motion Driven by Spin-Orbit Torques," Phys. Rev. Lett. **117**, 087203.

Shiomi, Y., K. Nomura, Y. Kajiwara, K. Eto, M. Novak, Kouji Segawa, Yoichi Ando, and E. Saitoh, 2014, "Spin-Electricity Conversion Induced by Spin Injection into Topological Insulators," Phys. Rev. Lett. **113**, 196601.

Shiota, Yoichi, Takayuki Nozaki, Frédéric Bonell, Shinichi Murakami, Teruya Shinjo, and Yoshishige Suzuki, 2012, "Induction of coherent magnetization switching in a few atomic layers of FeCo using voltage pulses," Nat. Mater. **11**, 39.

Siddiqui, Saima A., Jiahao Han, Joseph T. Finley, Caroline A. Ross, and Luqiao Liu, 2018, "Current-Induced Domain Wall Motion in a Compensated Ferrimagnet," Phys. Rev. Lett. **121**, 057701.

Silov, A. Yu., P. A. Blajnov, J. H. Wolter, R. Hey, K. H. Ploog, and N. S. Averkiev, 2004, "Current-induced spin polarization at a single heterojunction," Appl. Phys. Lett. **85**, 5929.

Sinova, Jairo, Dimitrie Culcer, Qian Niu, N. A. Sinitsyn, T. Jungwirth, and A. H. MacDonald, 2004, "Universal intrinsic spin Hall effect," Phys. Rev. Lett. **92**, 126603.

Sinova, Jairo, and Tomas Jungwirth, 2017, "Surprises from the spin Hall effect," Phys. Today **70**, No. 7, 38.

Sinova, Jairo, Sergio O. Valenzuela, J. Wunderlich, C. H. Back, and T. Jungwirth, 2015, "Spin Hall effect," Rev. Mod. Phys. **87**, 1213.

Skinner, T. D., K. Olejnik, L. K. Cunningham, H. Kurebayashi, R. P. Campion, B. L. Gallagher, T. Jungwirth, and A. J. Ferguson, 2015, "Complementary spin-Hall and inverse spin-galvanic effect torques in a ferromagnet/semiconductor bilayer," Nat. Commun. **6**, 6730.

Skinner, T. D., M. Wang, A. T. Hindmarch, A. W. Rushforth, A. C. Irvine, D. Heiss, H. Kurebayashi, and A. J. Ferguson, 2014, "Spin-orbit torque opposing the Oersted torque in ultrathin Co/Pt bilayers," Appl. Phys. Lett. **104**, 062401.

Slavin, Andrei, and Vasil Tiberkevich, 2005, "Spin wave mode excited by spin-polarized current in a magnetic nanocontact is a standing self-localized wave bullet," Phys. Rev. Lett. **95**, 237201.

Slonczewski, J. C., 1972, "Dynamics of magnetic domain walls," AIP Conf. Proc. **5**, 170.

Slonczewski, J. C., 1996, "Current-driven excitation of magnetic multilayers," J. Magn. Magn. Mater. **159**, L1.

Šmejkal, Libor, Jakub Železný, Jairo Sinova, and Tomáš Jungwirth, 2017, "Electric control of Dirac quasiparticles by spin-orbit torque in an antiferromagnet," Phys. Rev. Lett. **118**, 106402.

Soleimani, M., S. Jalili, F. Mahfouzi, and N. Kioussis, 2017, "Spin-orbit torque-driven magnetization switching in 2D-topological insulator heterostructure Spin-orbit torque-driven magnetization switching in 2D-topological insulator heterostructure," Europhys. Lett. **117**, 37001.

Sondheimer, E. H., 2001, "The mean free path of electrons in metals," Adv. Phys. **50**, 499.

Song, Qi, Hongrui Zhang, Tang Su, Wei Yuan, Yangyang Chen, Wenyu Xing, Jing Shi, Jirong Sun, and Wei Han, 2017, "Observation of inverse Edelstein effect in Rashba-split 2DEG between SrTiO3 and LaAlO3 at room temperature," Sci. Adv. **3**, e1602312.

Soumyanarayanan, Anjan, Nicolas Reyren, Albert Fert, and Christos Panagopoulos, 2016, "Spin-Orbit Coupling Induced Emergent Phenomena at Surfaces and Interfaces," Nature (London) **539**, 509.

Srivastava, Titiksha, *et al.*, 2018, "Route toward Dynamic Control of Skyrmion Chirality," Nano Lett. **18**, 4871.

Stamm, C., C. Murer, M. Berritta, J. Feng, M. Gabureac, P. M. Oppeneer, and P. Gambardella, 2017, "Magneto-Optical Detection of the Spin Hall Effect in Pt and W Thin Films," Phys. Rev. Lett. **119**, 087203.

Stanciu, C. D., F. Hansteen, A. V. Kimel, A. Kirilyuk, A. Tsukamoto, A. Itoh, and Th Rasing, 2007, "All-Optical Magnetic Recording with Circularly Polarized Light," Phys. Rev. Lett. **99**, 047601.

Stanciu, C. D., A. V. Kimel, F. Hansteen, A. Tsukamoto, A. Itoh, and A. Kirilyuk, 2006, "Ultrafast spin dynamics across compensation points in ferrimagnetic GdFeCo: The role of angular momentum compensation," Phys. Rev. B **73**, 220402(R).

Stier, Martin, Marcus Creutzburg, and Michael Thorwart, 2014, "Rashba-induced chirality switching of domain walls and suppression of the Walker breakdown," Phys. Rev. B **90**, 014433.

Stier, Martin, Reinhold Egger, and Michael Thorwart, 2013, "Non-equilibrium Rashba field driven domain wall motion in ferromagnetic nanowires," Phys. Rev. B **87**, 184415.

Stier, Martin, and Michael Thorwart, 2015, "Nonlocal spin torques in Rashba quantum wires with steep magnetic textures," Phys. Rev. B **92**, 220406.

Stiles, M., and A. Zangwill, 2002, "Anatomy of spin-transfer torque," Phys. Rev. B **66**, 014407.

Stöhr, J., and H. C. Siegmann, 2006, *Magnetism: from fundamentals to nanoscale dynamics* (Springer, New York).

Sun, J. Z., 2000, "Spin-current interaction with a monodomain magnetic body: A model study," Phys. Rev. B **62**, 570.

Sunko, Veronika, *et al.*, 2017, "Maximal Rashba-like spin splitting via kinetic energy-driven inversion symmetry breaking," Nature (London) **549**, 492.

Taguchi, Katsuhisa, Kunitaka Shintani, and Yukio Tanaka, 2015, "Spin-charge transport driven by magnetization dynamics on the disordered surface of doped topological insulators," Phys. Rev. B **92**, 035425.

Takayama, A., T. Sato, S. Souma, and T. Takahashi, 2011, "Giant out-of-plane spin component and the asymmetry of spin polarization in surface rashba states of bismuth thin film," Phys. Rev. Lett. **106**, 166401.

Tan, S. G., M. B. A. Jalil, and X.-J. Liu, 2007, "Local spin dynamics arising from the non-perturbative SU(2) gauge field of the spin-orbit coupling effect," arXiv:0705.3502v1.

Tanaka, T., H. Kontani, M. Naito, T. Naito, D. Hirashima, K. Yamada, and J. Inoue, 2008, "Intrinsic spin Hall effect and orbital Hall effect in 4d and 5d transition metals," Phys. Rev. B **77**, 165117.

Tang, Chi, *et al.*, 2018, "Dirac surface state modulated spin dynamics in a ferrimagnetic insulator at room temperature," Sci. Adv. **4**, eaas8660.

Tang, Peizhe, Quan Zhou, Gang Xu, and Shou-Cheng Zhang, 2016, "Dirac Fermions in Antiferromagnetic Semimetal," Nat. Phys. **12**, 1100.

Taniguchi, Tomohiro, J. Grollier, and M. D. Stiles, 2015, "Spin-Transfer Torques Generated by the Anomalous Hall Effect and Anisotropic Magnetoresistance," Phys. Rev. Applied **3**, 044001.

Tao, Xinde, Qi Liu, Bingfeng Miao, Rui Yu, Zheng Feng, Liang Sun, and Biao You, 2018, "Self-consistent determination of spin Hall angle and spin diffusion length in Pt and Pd: The role of the interface spin loss," Sci. Adv. **4**, eaat1670.

Tatara, G., and Hiroshi Kohno, 2004, "Theory of Current-Driven Domain Wall Motion: Spin Transfer versus Momentum Transfer," Phys. Rev. Lett. **92**, 086601.

Tatara, G., Noriyuki Nakabayashi, and Kyung-Jin Lee, 2013, "Spin motive force induced by Rashba interaction in the strong sd coupling regime," Phys. Rev. B **87**, 054403.

Tetienne, J., *et al.*, 2015, "The nature of domain walls in ultrathin ferromagnets revealed by scanning nanomagnetometry," Nat. Commun. **6**, 6733.

Theodonis, Ioannis, Alan Kalitsov, and Nicholas Kioussis, 2007, "Enhancing spin-transfer torque through the proximity of quantum well states," Phys. Rev. B **76**, 224406.

Thevenard, L., B. Boutigny, N. Güsken, L. Becerra, C. Ulysse, S. Shihab, A. Lemaître, J. V. Kim, V. Jeudy, and C. Gourdon, 2017, "Spin transfer and spin-orbit torques in in-plane magnetized (Ga,Mn)As tracks," Phys. Rev. B **95**, 054422.

Thiaville, A., Y. Nakatani, J. Miltat, and Y. Suzuki, 2005, "Micromagnetic understanding of current-driven domain wall motion in patterned nanowires," Europhys. Lett. **69**, 990.

Thiaville, A., and Y. Nakatani, 2009, "Micromagnetics of Domain-Wall Dynamics in Soft Nanostripss," in *Nanomagnetism and Spintronics*, edited by T. Shinjo (Elsevier, New York), Chap. 6, pp. 231–276.

Thiaville, André, Stanislas Rohart, Émilie Jué, Vincent Cros, and Albert Fert, 2012, "Dynamics of Dzyaloshinskii domain walls in ultrathin magnetic films," Europhys. Lett. **100**, 57002.

Thiele, A. A., 1973, "Steady-State Motion of Magnetic Domains," Phys. Rev. Lett. **30**, 230.

Thiery, N., *et al.*, 2018, "Nonlinear spin conductance of yttrium iron garnet thin films driven by large spin-orbit torque," Phys. Rev. B **97**, 060409(R).

Thonig, Danny, Tomas Rauch, Hossein Mirhosseini, Jurgen Henk, Ingrid Mertig, Henry Wortelen, Bernd Engelkamp, Anke B. Schmidt, and Markus Donath, 2016, "Existence of topological nontrivial surface states in strained transition metals: W, Ta, Mo, and Nb," Phys. Rev. B **94**, 155132.

Tölle, Sebastian, Ulrich Eckern, and Cosimo Gorini, 2017, "Spin-charge coupled dynamics driven by a time-dependent magnetization," Phys. Rev. B **95**, 115404.

Tomasello, R., E. Martinez, R. Zivieri, L. Torres, M. Carpentieri, and G. Finocchio, 2014, "A strategy for the design of skyrmion racetrack memories," Sci. Rep. **4**, 6784.

Tomasello, R., V. Puliafito, E. Martinez, A. Manchon, M. Ricci, M. Carpentieri, and G. Finocchio, 2017, "Performance of synthetic antiferromagnetic racetrack memory: domain wall versus skyrmion," J. Phys. D **50**, 325302.

Torrejon, J., G. Malinowski, M. Pelloux, R. Weil, A. Thiaville, J. Curiale, D. Lacour, F. Montaigne, and M. Hehn, 2012, "Unidirectional thermal effects in current-induced domain wall motion," Phys. Rev. Lett. **109**, 106601.

Torrejon, Jacob, Felipe Garcia-Sanchez, Tomohiro Taniguchi, Jaivardhan Sinha, Seiji Mitani, Joo Von Kim, and Masamitsu Hayashi, 2015, "Current-driven asymmetric magnetization switching in perpendicularly magnetized CoFeB/MgO heterostructures," Phys. Rev. B **91**, 214434.

Torrejon, Jacob, Junyeon Kim, Jaivardhan Sinha, Seiji Mitani, Masamitsu Hayashi, Michihiko Yamanouchi, and Hideo Ohno, 2014, "Interface control of the magnetic chirality in CoFeB/MgO heterostructures with heavy-metal underlayers," Nat. Commun. **5**, 4655.

Tretiakov, O., D. Clarke, Gia-Wei Chern, Ya. Bazaliy, and O. Tchernyshyov, 2008, "Dynamics of Domain Walls in Magnetic Nanostrips," Phys. Rev. Lett. **100**, 127204.

Tserkovnyak, Yaroslav, Arne Brataas, and G. E. W. Bauer, 2002a, "Enhanced Gilbert Damping in Thin Ferromagnetic Films," Phys. Rev. Lett. **88**, 117601.

Tserkovnyak, Yaroslav, Arne Brataas, and G. E. W. Bauer, 2002b, "Spin pumping and magnetization dynamics in metallic multilayers," Phys. Rev. B **66**, 224403.

Tserkovnyak, Yaroslav, D. A. Pesin, and Daniel Loss, 2015, "Spin and orbital magnetic response on the surface of a topological insulator," Phys. Rev. B **91**, 041121.

Tshitoyan, V., C. Ciccarelli, A. P. Mihai, M. Ali, A. C. Irvine, T. A. Moore, T. Jungwirth, and A. J. Ferguson, 2015, "Electrical manipulation of ferromagnetic NiFe by antiferromagnetic IrMn," Phys. Rev. B **92**, 214406.

Tsoi, M., A. G. Jansen, J. Bass, W. C. Chiang, V. Tsoi, and P. Wyder, 2000, "Generation and detection of phase-coherent current-driven magnons in magnetic multilayers," Nature (London) **406**, 46.

Tsoi, M., A. Jansen, J. Bass, W.-C. Chiang, M. Seck, V. Tsoi, and P. Wyder, 1998, "Excitation of a Magnetic Multilayer by an Electric Current," Phys. Rev. Lett. **80**, 4281.

Tulapurkar, A. A., Y. Suzuki, A. Fukushima, H. Kubota, H. Maehara, K. Tsunekawa, D. D. Djayaprawira, N. Watanabe, and S. Yuasa, 2005, "Spin-torque diode effect in magnetic tunnel junctions," Nature (London) **438**, 339–42.

Uchida, K., *et al.*, 2010, "Spin Seebeck insulator," Nat. Mater. **9**, 894.

Ueda, Hiroaki T., Akihito Takeuchi, Gen Tatara, and Takehito Yokoyama, 2012, "Topological charge pumping effect by the magnetization dynamics on the surface of three-dimensional topological insulators," Phys. Rev. B **85**, 115110.

Ueda, Kohei, Kab-jin Kim, Yoko Yoshimura, Ryo Hiramatsu, Takahiro Moriyama, Daichi Chiba, Hironobu Tanigawa, Tetsuhiro Suzuki, Eiji Kariyada, and Teruo Ono, 2014, "Transition in mechanism for current-driven magnetic domain wall dynamics," Appl. Phys. Express **7**, 053006.

Ueda, Kohei, Maxwell Mann, Paul W. P. De Brouwer, David Bono, and Geoffrey S. D. Beach, 2017, "Temperature dependence of spin-orbit torques across the magnetic compensation point in a ferrimagnetic TbCo alloy film," Phys. Rev. B **96**, 064410.

Uhlír, V., *et al.*, 2010, "Current-induced motion and pinning of domain walls in spin-valve nanowires studied by XMCD-PEEM," Phys. Rev. B **81**, 224418.

Uhlír, V., *et al.*, 2011, "Direct observation of Oersted-field-induced magnetization dynamics in magnetic nanostripes," Phys. Rev. B **83**, 020406(R).

Valenzuela, S. O., and M. Tinkham, 2006, "Direct electronic measurement of the spin Hall effect," Nature (London) **442**, 176.

Vanatka, M., J.-C. Rojas-Sánchez, J. Vogel, M. Bonfim, M. Belmeguenai, Y. Roussigné, A. Stashkevich, A. Thiaville, and S. Pizzini, 2015, "Velocity asymmetry of Dzyaloshinskii domain walls in the creep and flow regimes," J. Phys. Condens. Matter **27**, 326002.

van den Brink, Arno, Guus Vermijs, Aurélie Solignac, Jungwoo Koo, Jurgen T. Kohlhepp, Henk J. M. Swagten, and Bert Koopmans, 2016, "Field-free magnetization reversal by spin-Hall effect and exchange bias," Nat. Commun. **7**, 10854.

van der Bijl, E., and R. A. Duine, 2012, "Current-induced torques in textured Rashba ferromagnets," Phys. Rev. B **86**, 094406.

Vanhaverbeke, A., A. Bischof, and R. Allenspach, 2008, "Control of Domain Wall Polarity by Current Pulses," Phys. Rev. Lett. **101**, 107202.

Vasko, F. T., 1979, "Spin splitting in the spectrum of two-dimensional electrons due to the surface potential," Pis'ma Zh. Eksp. Teor. Fiz. **30**, 574 [http://www.jetpletters.ac.ru/ps/1368/article_20698.shtml].

Vedyayev, A., N. Ryzhanova, B. Dieny, and N. Strelkov, 2006, "Resonant spin-torque in double barrier magnetic tunnel junctions," Phys. Lett. A **355**, 243.

Vélez, Saül, *et al.*, 2019, "High-speed domain wall racetracks in a magnetic insulator," arXiv:1902.05639.

Verhagen, T. G. A., I. Leermakers, J. M. Van Ruitenbeek, and J. Aarts, 2015, "Detecting Rashba fields at the interface between Co and Si oxide by ferromagnetic resonance," Phys. Rev. B **91**, 184402.

Vorobev, L. E., E. L. Ivchenko, G. E. Pikus, I. I. Farbshtein, V. A. Shalygin, and A. V. Shturbin, 1979, "Optical activity in tellurium induced by a current," JETP Lett. **29**, 485 [http://adsabs.harvard.edu/abs/1979JETPL..29..441V].

Wadley, Peter, *et al.*, 2016, "Electrical switching of an antiferromagnet," Science **351**, 587.

Waintal, X., and M. Viret, 2004, "Current-induced distortion of a magnetic domain wall," Europhys. Lett. **65**, 427.

Walsh, Lee A., Christopher M. Smyth, Adam T. Barton, Qingxiao Wang, Zifan Che, Ruoyu Yue, Jiyoung Kim, Moon J. Kim, Robert M. Wallace, and Christopher L. Hinkle, 2017, "Interface Chemistry of Contact Metals and Ferromagnets on the Topological Insulator Bi2Se3," J. Phys. Chem. C **121**, 23551.

Wan, Xiangang, Ari M. Turner, Ashvin Vishwanath, and Sergey Y. Savrasov, 2011, "Topological semimetal and Fermi-arc surface states in the electronic structure of pyrochlore iridates," Phys. Rev. B **83**, 205101.

Wang, Hailong, James Kally, Joon Sue Lee, Tao Liu, Houchen Chang, Danielle Reifsnyder Hickey, K. Andre Mkhoyan, Mingzhong Wu, Anthony Richardella, and Nitin Samarth, 2016, "Surface-State-Dominated Spin-Charge Current Conversion in Topological-insulator Ferromagnetic-insulator Heterostructures," Phys. Rev. Lett. **117**, 076601.

Wang, Lei, R. J. H. Wesselink, Yi Liu, Zhe Yuan, Ke Xia, and Paul J. Kelly, 2016, "Giant Room Temperature Interface Spin Hall and Inverse Spin Hall Effects," Phys. Rev. Lett. **116**, 196602.

Wang, Mengxing, *et al.*, 2018, "Field-free switching of a perpendicular magnetic tunnel junction through the interplay of spin-orbit and spin-transfer torques," Nat. Electron. **1**, 582.

Wang, P., *et al.*, 2016, "Spin rectification induced by spin Hall magnetoresistance at room temperature," Appl. Phys. Lett. **109**, 112406.

Wang, Wei-Gang, Mingen Li, Stephen Hageman, and C. L. Chien, 2012, "Electric-field-assisted switching in magnetic tunnel junctions," Nat. Mater. **11**, 64.

Wang, Wenrui, *et al.*, 2019, "Anomalous Spin-Orbit Torques in Magnetic Single-Layer Films," Nature Nanotechnology.

Wang, Xuhui, and Aurelien Manchon, 2012, "Diffusive Spin Dynamics in Ferromagnetic Thin Films with a Rashba Interaction," Phys. Rev. Lett. **108**, 117201.

Wang, Xuhui, Christian Ortiz Pauyac, and Aurélien Manchon, 2014, "Spin-orbit-coupled transport and spin torque in a ferromagnetic heterostructure," Phys. Rev. B **89**, 054405.

Wang, Yi, Praveen Deorani, Karan Banerjee, Nikesh Koirala, Matthew Brahlek, Seongshik Oh, and Hyunsoo Yang, 2015, "Topological surface states originated spin-orbit torques in Bi2Se3," Phys. Rev. Lett. **114**, 257202.

Wang, Yi, Rajagopalan Ramaswamy, Mallikarjuna Motapothula, Kulothungasagaran Narayanapillai, Dapeng Zhu, Jiawei Yu, Thirumalai Venkatesan, and Hyunsoo Yang, 2017, "Room-Temperature Giant Charge-to-Spin Conversion at the SrTiO3-LaAlO3 Oxide Interface," Nano Lett. **17**, 7659.

Wang, Yi, *et al.*, 2017, "Room temperature magnetization switching in topological insulator-ferromagnet heterostructures by spin-orbit torques," Nat. Commun. **8**, 1364.

Wangsness, R. K., 1954, "Magnetic Resonance in Ferrimagnetics," Phys. Rev. **93**, 68.

Watanabe, Hikaru, and Youichi Yanase, 2018, "Symmetry analysis of current-induced switching of antiferromagnets," Phys. Rev. B **98**, 220412(R).

Wehling, T. O., A. M. Black-Schaffer, and A. V. Balatsky, 2014, "Dirac materials," Adv. Phys. **63**, 1–76.

Wei, Dahai, Martin Obstbaum, Mirko Ribow, C. H. Back, and Georg Woltersdorf, 2014, "Spin Hall voltages from a.c. and d.c. spin currents," Nat. Commun. **5**, 3768.

Weisheit, Martin, Sebastian Fähler, Alain Marty, Yves Souche, Christiane Poinsignon, and Dominique Givord, 2007, "Electric field-induced modification of magnetism in thin-film ferromagnets," Science **315**, 349.

Wen, Yan, Jun Wu, Peng Li, Qiang Zhang, Yuelei Zhao, Aurelien Manchon, John Q. Xiao, and Xixiang Zhang, 2017, "Temperature dependence of spin-orbit torques in Cu-Au alloys," Phys. Rev. B **95**, 104403.

Weyl, H., 1929, "Elektron und gravitation," Z. Phys. **56**, 330.

Wimmer, S., K. Chadova, M. Seemann, D. Ködderitzsch, and H. Ebert, 2016, "Fully relativistic description of spin-orbit torques by means of linear response theory," Phys. Rev. B **94**, 054415.

Winkler, R., 2003, *Spin-Orbit Coupling effects in Two-Dimensional Electron and Hole Systems*, Springer Tracts in Modern Physics, Vol. 191 [https://doi.org/10.1007/b13586].

Wolf, S. A., D. D. Awschalom, R. A. Buhrman, J. M. Daughton, S. von Molnár, M. L. Roukes, A. Y. Chtchelkanova, and D. M. Treger, 2001, "Spintronics: a spin-based electronics vision for the future," Science **294**, 1488.

Woo, S., *et al.*, 2016, "Observation of room-temperature magnetic skyrmions and their current-driven dynamics in ultrathin metallic ferromagnets," Nat. Mater. **15**, 501.

Woo, Seonghoon, Maxwell Mann, Aik Jun Tan, Lucas Caretta, and Geoffrey S. D. Beach, 2014, "Enhanced spin-orbit torques in Pt/Co/Ta heterostructures," Appl. Phys. Lett. **105**, 212404.

Wray, L. Andrew, Su-Yang Xu, Yuqi Xia, David Hsieh, Alexei V. Fedorov, Yew San Hor, R. J. Cava, Arun Bansil, Hsin Lin, and M. Z. Hasan, 2011, "A topological insulator surface under strong Coulomb, magnetic and disorder perturbations," Nat. Phys. **7**, 32.

Wu, Di, *et al.*, 2016, "Spin-orbit torques in perpendicularly magnetized Ir22Mn78/Co20Fe60*B*20/MgO multilayer," Appl. Phys. Lett. **109**, 222401.

Wunderlich, Joerg, Bernd Kaestner, Jairo Sinova, and Tomas Jungwirth, 2004, "Experimental discovery of the spin-Hall effect in Rashba spin-orbit coupled semiconductor systems," arXiv:cond-mat/0410295v1.

Wunderlich, Joerg, Bernd Kaestner, Jairo Sinova, and Tomas Jungwirth, 2005, "Experimental observation of the spin-Hall effect in a two dimensional spin-orbit coupled semiconductor system," Phys. Rev. Lett. **94**, 047204.

Xiao, Jiang, and G. E. W. Bauer, 2012, "Spin-Wave Excitation in Magnetic Insulators by Spin-Transfer Torque," Phys. Rev. Lett. **108**, 217204.

Xiao, Jiang, G. E. W. Bauer, K. Uchida, E. Saitoh, and S. Maekawa, 2010, "Theory of magnon-driven spin Seebeck effect," Phys. Rev. B **81**, 214418.

Xie, K. X., W. W. Lin, H. C. Sun, Y. Nie, and H. Sang, 2008, "Time dependence of magnetization reversal influenced by current in perpendicularly magnetized Co/Pt thin film," J. Appl. Phys. **104**, 083907.

Xu, Xiaodong, Wang Yao, Di Xiao, and Tony F. Heinz, 2014, "Spin and pseudospins in layered transition metal dichalcogenides," Nat. Phys. **10**, 343.

Yamanouchi, Michihiko, Lin Chen, Junyeon Kim, Masamitsu Hayashi, Hideo Sato, Shunsuke Fukami, Shoji Ikeda, Fumihiro Matsukura, and Hideo Ohno, 2013, "Three terminal magnetic tunnel junction utilizing the spin Hall effect of iridium-doped copper," Appl. Phys. Lett. **102**, 212408.

Yang, H. X., M. Chshiev, B. Dieny, J. H. Lee, A. Manchon, and K. H. Shin, 2011, "First-principles investigation of the very large perpendicular magnetic anisotropy at Fe/MgO and Co/MgO interfaces," Phys. Rev. B **84**, 054401.

Yang, See-Hun, Kwang-Su Ryu, and Stuart Parkin, 2015, "Domain-wall velocities of up to 750 m/s driven by exchange-coupling torque in synthetic antiferromagnets," Nat. Nanotechnol. **10**, 221.

Yao, Xiaofeng, Jonathan Harms, Andrew Lyle, Farbod Ebrahimi, Yisong Zhang, and Jian Ping Wang, 2012, "Magnetic tunnel junction-based spintronic logic units operated by spin transfer torque," IEEE Trans. Nanotechnol. **11**, 120.

Yasuda, K., A. Tsukazaki, R. Yoshimi, K. Kondou, K. S. Takahashi, Y. Otani, M. Kawasaki, and Y. Tokura, 2017, "Current-Nonlinear Hall Effect and Spin-Orbit Torque Magnetization Switching in a Magnetic Topological Insulator," Phys. Rev. Lett. **119**, 137204.

Yasuda, K., A. Tsukazaki, R. Yoshimi, K. S. Takahashi, M. Kawasaki, and Y. Tokura, 2016, "Large Unidirectional Magnetoresistance in a Magnetic Topological Insulator," Phys. Rev. Lett. **117**, 127202.

Ye, L., D. B. Gopman, L. Rehm, D. Backes, G. Wolf, T. Ohki, A. F. Kirichenko, I. V. Vernik, O. A. Mukhanov, and A. D. Kent, 2014, "Spin-transfer switching of orthogonal spin-valve devices at cryogenic temperatures," J. Appl. Phys. **115**, 17C725.

Ye, M., *et al.*, 2012, "Quasiparticle interference on the surface of Bi2Se3 induced by cobalt adatom in the absence of ferromagnetic ordering," Phys. Rev. B **85**, 205317.

Yoda, H., *et al.*, 2017, "High-Speed Voltage-Control Spintronics Memory (High-Speed VoCSM)," *2017 IEEE International Memory Workshop (IMW)*, pp. 1–4.

Yoda, Taiki, Takehito Yokoyama, and Shuichi Murakami, 2018, "Orbital Edelstein Effect as a Condensed-Matter Analog of Solenoids," Nano Lett. **18**, 916.

Yokoyama, Takehito, Jiadong Zang, and N. Nagaosa, 2010, "Theoretical study of the dynamics of magnetization on the topological surface," Phys. Rev. B **81**, 241410.

Yoon, Jungbum, Seo-Won Lee, Jae Hyun Kwon, Jong Min Lee, Jaesung Son, Xuepeng Qiu, Kyung-Jin Lee, and Hyunsoo Yang, 2017, "Anomalous spin-orbit torque switching due to field-like torque-assisted domain wall reflection," Sci. Adv. **3**, e1603099.

Yoshimura, Yoko, Kab-jin Kim, Takuya Taniguchi, Takayuki Tono, Kohei Ueda, Ryo Hiramatsu, Takahiro Moriyama, Keisuke Yamada, Yoshinobu Nakatani, and Teruo Ono, 2016, "Soliton-like magnetic domain wall motion induced by the interfacial Dzyaloshinskii Moriya interaction," Nat. Phys. **12**, 157.

Yoshimura, Yoko, and Tomohiro Koyama, 2014, "Effect of spin Hall torque on current-induced precessional domain wall motion," Appl. Phys. Express **7**, 033005.

You, Long, OukJae Lee, Debanjan Bhowmik, Dominic Labanowski, Jeongmin Hong, Jeffrey Bokor, and Sayeef Salahuddin, 2015, "Switching of perpendicularly polarized nanomagnets with spin orbit torque without an external magnetic field by engineering a tilted anisotropy," Proc. Natl. Acad. Sci. U.S.A. **112**, 10310.

Young, Steve M., and Charles L. Kane, 2015, "Dirac Semimetals in Two Dimensions," Phys. Rev. Lett. **115**, 126803.

Yu, Guoqiang, Pramey Upadhyaya, Xiang Li, Wenyuan Li, Se Kwon Kim, Yabin Fan, Kin L. Wong, Yaroslav Tserkovnyak, Pedram Khalili Amiri, and Kang L. Wang, 2016, "Room-Temperature Creation and Spin-Orbit Torque Manipulation of Skyrmions in Thin Films with Engineered Asymmetry," Nano Lett. **16**, 1981.

Yu, Guoqiang, Pramey Upadhyaya, Kin L. Wong, Wanjun Jiang, Juan G. Alzate, Jianshi Tang, Pedram Khalili Amiri, and Kang L. Wang, 2014, "Magnetization switching through spin-Hall-effect-induced chiral domain wall propagation," Phys. Rev. B **89**, 104421.

Yu, Guoqiang, *et al.*, 2014, "Switching of perpendicular magnetization by spin-orbit torques in the absence of external magnetic fields," Nat. Nanotechnol. **9**, 548.

Yu, Jiawei, Xuepeng Qiu, William Legrand, and Hyunsoo Yang, 2016, "Large spin-orbit torques in Pt/Co-Ni/W heterostructures," Appl. Phys. Lett. **109**, 042403.

Yu, Jiawei, *et al.*, 2019, "Long spin coherence length and bulk-like spin orbit torque in ferrimagnetic multilayers," Nat. Mater. **18**, 29.

Yuan, Zhe, and Paul J. Kelly, 2016, "Spin-orbit-coupling induced torque in ballistic domain walls: Equivalence of charge-pumping and non-equilibrium magnetization formalisms," Phys. Rev. B **93**, 224415.

Železný, J., 2017, "symcode," https://bitbucket.org/zeleznyj/linear-response-symmetry.

Železný, J., Y. Zhang, C. Felser, and B. H. Yan, 2017, "Spin-Polarized Current in Noncollinear Antiferromagnets," Phys. Rev. Lett. **119**, 187204.

Železný, J., H. Gao, Aurélien Manchon, Frank Freimuth, Yuriy Mokrousov, J. Zemen, J. Mašek, Jairo Sinova, and T. Jungwirth, 2017, "Spin-orbit torques in locally and globally non-centrosymmetric crystals: Antiferromagnets and ferromagnets," Phys. Rev. B **95**, 014403.

Železný, J., H. Gao, K. Výborný, J. Zemen, J. Mašek, A. Manchon, J. Wunderlich, J. Sinova, and T. Jungwirth, 2014, "Relativistic Néel-Order Fields Induced by Electrical Current in Antiferromagnets," Phys. Rev. Lett. **113**, 157201.

Zhang, C., S. Fukami, H. Sato, F. Matsukura, and H. Ohno, 2015, "Spin-orbit torque induced magnetization switching in nano-scale Ta/CoFeB/MgO," Appl. Phys. Lett. **107**, 012401.

Zhang, H. J., S. Yamamoto, Y. Fukaya, M. Maekawa, H. Li, A. Kawasuso, T. Seki, E. Saitoh, and K. Takanashi, 2014, "Current-induced spin polarization on metal surfaces probed by spin-polarized positron beam," Sci. Rep. **4**, 4844.

Zhang, Jia, Julian P. Velev, Xiaoqian Dang, and Evgeny Y. Tsymbal, 2016, "Band structure and spin texture of Bi2Se3 3d ferromagnetic metal interface," Phys. Rev. B **94**, 014435.

Zhang, Jinsong, Cui-zu Chang, Zuocheng Zhang, Jing Wen, Xiao Feng, Kang Li, Minhao Liu, and Ke He, 2011, "Band structure engineering in (Bi1-xSbx)2Te3 ternary topological insulators," Nat. Commun. **2**, 574.

Zhang, S., P. Levy, and A. Fert, 2002, "Mechanisms of Spin-Polarized Current-Driven Magnetization Switching," Phys. Rev. Lett. **88**, 236601.

Zhang, S., and Z. Li, 2004, "Roles of Nonequilibrium Conduction Electrons on the Magnetization Dynamics of Ferromagnets," Phys. Rev. Lett. **93**, 127204.

Zhang, Shufeng, and Peter M. Levy, 1993, "Conductivity and magnetoresistance in magnetic granular films (invited)," J. Appl. Phys. **73**, 5315.

Zhang, Steven S. L., and Shufeng Zhang, 2012, "Magnon mediated electric current drag across a ferromagnetic insulator layer," Phys. Rev. Lett. **109**, 096603.

Zhang, W., Wei Han, S.-H. Yang, Yan Sun, Yang Zhang, Binghai Yan, and Stuart S. P. Parkin, 2016, "Giant facet-dependent spin-orbit torque and spin Hall conductivity in the triangular antiferromagnet IrMn3," Sci. Adv. **2**, e1600759.

Zhang, Wei, Matthias B. Jungfleisch, Wanjun Jiang, John E. Pearson, and Axel Hoffmann, 2015, "Spin pumping and inverse Rashba-Edelstein effect in NiFe/Ag/Bi and NiFe/Ag/Sb," J. Appl. Phys. **117**, 17C727.

Zhang, Wei, *et al.*, 2016, "Research Update: Spin transfer torques in permalloy on monolayer MoS2," APL Mater. **4**, 032302.

Zhang, Weifeng, Wei Han, Xin Jiang, See Hun Yang, and Stuart S. P. Parkin, 2015, "Role of transparency of platinum-ferromagnet interfaces in determining the intrinsic magnitude of the spin Hall effect," Nat. Phys. **11**, 496.

Zhang, Wenxu, Bin Peng, Fangbin Han, Qiuru Wang, Wee Tee Soh, Chong Kim Ong, and Wanli Zhang, 2016, "Separating inverse spin Hall voltage and spin rectification voltage by inverting spin injection direction," Appl. Phys. Lett. **108**, 102405.

Zhang, Xichao, Motohiko Ezawa, and Yan Zhou, 2015, "Magnetic skyrmion logic gates: conversion, duplication and merging of skyrmions," Sci. Rep. **5**, 9400.

Zhang, Xichao, Yan Zhou, and Motohiko Ezawa, 2016, "Magnetic bilayer-skyrmions without skyrmion Hall effect," Nat. Commun. **7**, 10293.

Zhang, Yang, J. Zelezny, Yan Sun, Jeroen Van Den Brink, and Binghai Yan, 2018, "Spin Hall effect emerging from a noncollinear magnetic lattice without spin orbit coupling Spin Hall effect emerging from a noncollinear magnetic lattice without spin orbit coupling," New J. Phys. **20**, 073028.

Zhao, Zhengyang, M. Jamali, A. Klemm, and Jian-Ping Wang, 2015, "Spin Hall switching of the magnetization in Ta / TbFeCo structures with bulk perpendicular anisotropy," Appl. Phys. Lett. **106**, 132404.

Zhao, Zhengyang, Angeline K. Smith, Mahdi Jamali, and Jian-ping Wang, 2017, "External-Field-Free Spin Hall Switching of Perpendicular Magnetic Nanopillar with a Dipole-Coupled Composite Structure," arXiv:1603.09624.

Zhou, X. F., *et al.*, 2018, "Strong Orientation-Dependent Spin-Orbit Torque in Thin Films of the Antiferromagnet Mn2Au," Phys. Rev. Applied **9**, 054028.

Zhu, Lijun, Daniel C. Ralph, and Robert A. Buhrman, 2018, "Highly Efficient Spin-Current Generation by the Spin Hall Effect in Au 1 x Pt x," Phys. Rev. Applied **10**, 031001.

Zubko, Pavlo, Stefano Gariglio, Marc Gabay, Philippe Ghosez, and Jean-marc Triscone, 2011, "Interface Physics in Complex Oxide Heterostructures," Annu. Rev. Condens. Matter Phys. **2**, 141.

Zutic, Igor, Jaroslav Fabian, and S. Das Sarma, 2004, "Spintronics: Fundamentals and applications," Rev. Mod. Phys. **76**, 323.